Fission and *r*-process nucleosynthesis in neutron star mergers

Kernspaltung und r-Prozess Nukleosynthese bei Neutronensternverschmelzungen
Zur Erlangung des Grades eines Doktors der Naturwissenschaften (Dr. rer. nat.)
genehmigte Dissertation von M.Sc. Samuel Andrea Giuliani aus Rom, Italien
Tag der Einreichung: 13.06.2017, Tag der Prüfung: 05.07.2017
Darmstadt 2018 — D 17

1. Gutachten: Prof. Dr. Gabriel Martínez-Pinedo
2. Gutachten: Prof. Dr. Robert Roth

TECHNISCHE
UNIVERSITÄT
DARMSTADT

Fachbereich Physik
Institut für Kernphysik
Theoretische Nukleare Astrophysik

Fission and r-process nucleosynthesis in neutron star mergers
Kernspaltung und r-Prozess Nukleosynthese bei Neutronensternverschmelzungen

Genehmigte Dissertation von M.Sc. Samuel Andrea Giuliani aus Rom, Italien

1. Gutachten: Prof. Dr. Gabriel Martínez-Pinedo
2. Gutachten: Prof. Dr. Robert Roth

Tag der Einreichung: 13.06.2017
Tag der Prüfung: 05.07.2017

Darmstadt — D 17

Bitte zitieren Sie dieses Dokument als:
URN: urn:nbn:de:tuda-tuprints-71610
URL: http://tuprints.ulb.tu-darmstadt.de/7161

Dieses Dokument wird bereitgestellt von tuprints,
E-Publishing-Service der TU Darmstadt
http://tuprints.ulb.tu-darmstadt.de
tuprints@ulb.tu-darmstadt.de

Die Veröffentlichung steht unter folgender Creative Commons Lizenz:
Namensnennung – Keine kommerzielle Nutzung – Keine Bearbeitung 4.0 International
https://creativecommons.org/licenses/by-nc-nd/4.0/

Ai miei genitori,
che mi hanno cresciuto come meglio non potevano
e il cui amore non sapró mai come ricambiare.

But this long run is a misleading guide to current affairs.
In the long run we are all dead.

J. M. Keynes

Abstract

Fission plays a crucial role for the *r*-process nucleosynthesis in neutron star mergers. Due to the high neutron densities achieved in this astrophysical scenario the sequence of neutron captures and beta decays that constitutes the *r* process produces superheavy neutron rich nuclei that become unstable against fission. Fission determines thus the heaviest nuclei that can be produced by the *r* process and the fission yields shape the abundances of lighter nuclei. But despite the key role of fission the sensitivity of the *r*-process nucleosynthesis to uncertainties in fission predictions has not been explored. Nowadays there are only few set of fission rates suited for *r*-process calculations and most of them rely on a simplified treatment of the fission process.

In this thesis we go beyond these approximations and compute the fission properties of *r*-process nuclei using the energy density functional approach. Fission is described as a tunneling process where the nucleus "moves" in a collective space characterized by coordinates describing the nuclear shape. Thus fission depends on the evolution of the energy with the deformation but also on the inertia due to the motion in the collective space. This is analogous to the quantum mechanical tunneling of a particle inside a potential well. In our study the relevant quantities for the description of the fission process are consistently computed for 3642 nuclei following the Hartree-Fock-Bogolyubov theory with constraining operators. We perform an extensive benchmark against the available experimental data and explore the variations of the fission properties along the superheavy landscape. We find that while collective inertias have a strong impact in the fission probabilities of light nuclei their role becomes less relevant in *r*-process nuclei. Within the statistical model we compute the neutron induced stellar reaction rates relevant for the *r*-process nucleosynthesis. These sets of stellar reaction rates are used in *r*-process calculations for matter dynamically ejected in neutron star mergers and we compare our results with those obtained from a more conventional set of reaction rates. We find that all the models predict the onset of fission above the shell closure $N = 184$ and $Z = 100$ due to the sudden decrease in fission barriers. However, the amount of material accumulated at $N = 184$ turns out to be very sensitive to the height of the fission barriers and the shell gap.

Finally, we have also explored the impact of recent advances in fission calculations on the theoretical estimation of spontaneous fission lifetimes. We find that performing dynamical approaches based on the minimization of the integral action with nontraditional collective degrees of freedom has a strong impact in the fission barriers and the spontaneous fission lifetimes. The possible consequences of this new approach for the calculation of neutron induced fission rates has to be addressed.

Zusammenfassung

Kernspaltung spielt eine wesentliche Rolle bei der sogenannten r-Prozess Nukleosynthese im Rahmen von Neutronenstern-Verschmelzungen. Aufgrund der hohen Neutronendichte, welche in diesen astrophysikalischen Ereignissen erreicht wird, erzeugt der r-Prozess, eine Abfolge von Neutroneneinfängen und Beta-Zerfällen, superschwere neutronenreiche Kerne, die wiederum instabil in Bezug auf Kernspaltung sind. Folglich bestimmt Kernspaltung welches die schwersten Elemente sind, die durch den r-Prozess erzeugt werden können. Zudem beeinflusst die Verteilung der Spaltprodukte die Häufigkeitsverteilung vieler leichterer Kerne. Trotz dieser Schlüsselrolle wurde die Sensititvität der r-Prozess Nukleosynthese bezüglich Unsicherheiten in der Beschreibung der Kernspaltung bisher noch nicht untersucht. So gibt es bis heute nur wenige Sätze von Kernspaltungsraten die für R-Prozess Berechnungen geeignet sind, und die meisten von diesen basieren auf einer vereinfachten Behandlung des Spaltungsprozesses.

In dieser Arbeit gehen wir über solch eine Vereinfachung hinaus und berechnen die Spalt-Eigenschaften von r-Prozess-Kernen mittels Energiedichtefunktionalen. Kernspaltung wird dabei als quantenmechanischer Tunnel-Prozess beschrieben, bei dem sich der Kern in einem kollektiven Raum "bewegt". Dieser Raum ist charakterisiert durch Koordinaten, die die Verformung des Kerns beschreiben. Folglich hängt die Kernspaltung sowohl vom Verhalten der Energie als Funktion der nuklearen Verformung als auch von der Trägheit der Bewegung im kollektiven Raum ab. Dies stellt eine Analogie zum Tunneleffekt eines Teilchen in einem Potentialtopf dar. In unserer Arbeit berechnen wir die relevanten Größen zur Beschreibung der Kernspaltung konsistent für 3462 Kerne im Rahmen der Hartree-Fock-Bogolyubov Theorie mit einschränkenden Operatoren. Wir führen einen umfassenden Vergleich mit experimentellen Daten durch und untersuchen, wie sich die Spalteigenschaften für die unterschiedlichen superschweren Elemente verändern. Dabei stellen wir fest, dass die kollektiven Trägheitsmomente, die einen starken Einfluss auf die Spaltwahrscheinlichkeiten leichterer Kerne haben, bei r-Prozess Kernen weniger relevant sind. Weiter berechnen wir die durch Neutronen induzierten, stellaren Reaktionsraten, die für den r-Prozess wichtig sind, mit dem statistischen Modell. Diese Reaktionsraten nutzen wir schließlich in r-Prozess Berechnungen für Materie, die bei Neutronenstern-Verschmelzungen dynamischen ausgestoßen wird. Unsere Ergebnisse vergleichen wir mit anderen, die über einen konventionelleren Satz von Reaktionsraten berechnet wurden. Es zeigt sich, dass alle von uns betrachteten Modelle das Einsetzen von Kernspaltung jenseits des Schalenabschlusses $N = 184$ aufgrund einer plötzlichen Reduktion der Spaltbarrieren vorhersagen. Die Menge des akkumulierten Materials bei $N = 184$ zeigt jedoch eine deutliche Abhängigkeit von der Höhe der Spaltbarrieren und der Schalenlücke.

Abschließend haben wir auch den Einfluss jüngster Fortschritte bei der Berechnung von Kernspaltung auf die theoretische Bestimmung Halbwertszeit spontaner Spaltung untersucht. Dabei haben wir herausgefunden, dass die Verwendung dynamischer Ansätze basierend auf der Minimierung des Wirkungsintegrals mit unkonventionellen kollektiven Freiheitsgraden große Auswirkungen auf die Spaltbarrieren und die Halbwertszeiten von spontanen Zerfällen hat. Mögliche Konsequenzen dieses neuen Ansatzes für die Berechnung der Raten für neutroneninduzierte Spaltung müssen noch untersucht werden.

Contents

1 Introduction **1**
1.1 Thesis outline . . . 4

2 The energy density functional formalism **5**
2.1 Many-body systems and the independent particle model . . . 5
  2.1.1 Second quantization formalism . . . 6
  2.1.2 Matrix elements in second quantization . . . 7
  2.1.3 The particle density operator . . . 8
2.2 The Hartree-Fock-Bogoliubov theory (HFB) . . . 8
  2.2.1 The Hartree-Fock-Bogolyubov equation . . . 9
  2.2.2 Representation in the quasiparticle basis . . . 11
  2.2.3 The effective Hamiltonian . . . 11
  2.2.4 Constraints . . . 12
2.3 The nuclear energy density functional formalism . . . 12
  2.3.1 Gogny energy functional . . . 13
  2.3.2 Barcelona Catania Paris Madrid energy functional . . . 14
  2.3.3 Kinetic energy . . . 16
  2.3.4 Coulomb energy . . . 16
  2.3.5 Restoration of broken symmetries and zero-point energy corrections . . . 17
2.4 Description of odd nuclei . . . 18

3 Fission within the energy density functional formalism **21**
3.1 A semiclassical picture for fission . . . 21
3.2 Action integral and fission transmission coefficient . . . 22
  3.2.1 The Wentzel–Kramers–Brillouin (WKB) approximation . . . 22
  3.2.2 Extension of the WKB approach to spontaneous fission . . . 22
  3.2.3 Fission from excited states . . . 23
3.3 Collective inertias . . . 23
  3.3.1 The Generator Coordinate Method (GCM) . . . 23
  3.3.2 The Adiabatic Time Dependent Hartree Fock Bogolyubov theory (ATDHFB) . . . 26
  3.3.3 Semiempirical mass formula and reduced mass . . . 28
3.4 Potential energy surface . . . 29
  3.4.1 Shape parametrization of the nucleus . . . 29
  3.4.2 Pairing correlations . . . 31
  3.4.3 Energy corrections . . . 31
  3.4.4 The effective potential energy . . . 32
3.5 Dynamic vs static fission paths . . . 32
  3.5.1 The role of pairing correlations . . . 34
  3.5.2 Study of the ^{234}U . . . 34

4 Reaction rates within the Hauser-Feshbach theory **39**
4.1 Statistical nuclear reactions . . . 39
  4.1.1 Reaction channels . . . 39
  4.1.2 Hauser-Feshbach theory for cross sections . . . 40

4.2 Ingredients of the statistical theory . . . 41
    4.2.1 Transmission coefficients . . . 41
    4.2.2 Level densities . . . 43
4.3 Stellar reaction rates . . . 46
    4.3.1 Stellar cross sections . . . 46
    4.3.2 Stellar rates . . . 46
4.4 Limits of the statistical theory . . . 48

5 Reaction network for r-process calculations 49
5.1 Basics of reaction networks . . . 49
    5.1.1 The nuclear statistical equilibrium (NSE) . . . 49
    5.1.2 Abundances evolution . . . 50
5.2 Network calculations for r-process nucleosynthesis . . . 51
    5.2.1 The $(n,\gamma) \rightleftarrows (\gamma,n)$ equilibrium . . . 52
    5.2.2 The steady flow approximation . . . 53
    5.2.3 Dynamic calculations . . . 53
5.3 Energy generation . . . 54
5.4 Characteristic quantities in r-process nucleosynthesis . . . 55
5.5 Hydrodynamical trajectories . . . 55

6 Benchmark against experimental data 57
6.1 General considerations on fission observables . . . 57
6.2 Binding energies . . . 57
6.3 Fission barriers and isomer excitation energies . . . 62
6.4 Spontaneous fission lifetimes . . . 64
6.5 Neutron induced cross sections . . . 70
    6.5.1 Sensitivity to level densities and gamma-ray strengths . . . 71
    6.5.2 Sensitivity to collective inertias . . . 72
    6.5.3 Sensitivity to fission barriers . . . 73
6.6 α decay of superheavy nuclei . . . 74

7 Fission properties of r-process nuclei 79
7.1 Fission barriers . . . 79
7.2 Spontaneous fission lifetimes . . . 82
    7.2.1 Sensitivity to different energy density functionals . . . 83
    7.2.2 Sensitivity to collective inertias . . . 85
    7.2.3 Sensitivity to the collective ground state energy and zero-point energy correction 86
7.3 Reaction rates . . . 89

8 Impact of fission on r-process nucleosynthesis in neutron star mergers 93
8.1 The role of fission in r-process nucleosynthesis . . . 93
8.2 r-process abundances from BCPM rates . . . 95
    8.2.1 BCPM vs FRDM+TF . . . 97
    8.2.2 Sensitivity to collective inertias . . . 100
8.3 Competition between fission channels . . . 100
8.4 Production of radioactive energy . . . 102
8.5 Further work to be addressed . . . 103

9 Conclusions & Outlook 105

List of Figures 109

List of Tables 110

Bibliography 111

Index 118

Curriculum Vitæ 122

1 Introduction

The main goal of nuclear astrophysics is to describe how the chemical elements that we observe in the Universe are produced in astrophysical objects and how nuclear reactions influence the evolution of these environments. The possibility that the stellar origin was a promising method to describe the synthesis of elements (nucleosynthesis) was contemporaneously introduced in 1957 by Burbidge *et al.* [1] and Cameron [2]. These pioneering works exploited the idea that the changing structure of stars provide a large variety of conditions where nuclear reactions can take place. Nowadays we know that several astrophysical processes contributed and contribute to the nucleosynthesis of elements, from the production of hydrogen and helium during the bing-bang nucleosynthesis up to the long-lived thorium and uranium isotopes synthesized in the r process.

Despite the long time that passed from the first studies exploring the nuclear generation in stars [3] until nowadays, there are still several and important questions that nuclear astrophysics has to address [4]. One of those is the identification of the astrophysical site for the rapid neutron capture process, or r process. The r process is invoked in order to explain the existence of around half of the nuclei heavier than iron that are observed in stars of different metallicities as well as in the solar system. In the r-process nucleosynthesis the neutron captures are faster than β decays, allowing for the synthesis of extremely neutron rich nuclei. When this r-process flow reaches nuclei with a neutron magic number the material moves closer to stability, where the half-lives are longer. The halt of the r process at these "waiting points" produces then an accumulation of material resulting in the observed peak structure of the r-process abundances, as it is shown in Fig. 1.1.

The search of the r-process astrophysical scenario started sixty years ago and it is still going on. Historically, the proposed scenarios have been divided in two main categories: the high and low entropy scenario [6]. The former one include the neutrino-driven wind, that during several years has been considered the favored site [7]. This scenario occurs in core-collapse supernova, where the freshly born protoneutron star cools by emitting a large amount of neutrinos. These neutrinos heat the material in the surface of the neutron star and create an outflow of baryonic matter. For long time it was speculated that ejected matter in this scenario will allow for an r process. However, recent simulations show that the material ejected in this in neutrino-driven winds does not fulfill the conditions for producing a successful r process [8].

As an alternative to the high entropy conditions in supernovae, a low entropy scenario was proposed in 1974 [9]. It is based on the idea that at high neutron densities the material is neutronised due to continuous electron capture. When this material undergoes a sudden decompression, the existing nuclei will start to capture neutrons producing neutron-rich elements. If the ratio of neutron to seed nuclei is large enough, the seed nuclei are converted by successive neutron captures and beta decays to heavier and heavier elements until the point when they become unstable against fission. The astrophysical plausibility of this process remained unanswered for several years, until the first studies of the decompression of material during the merger of two neutron stars (NSM) and a NS with a black hole (BH) predicted the ejecta of r-process material [9–11].

Mergers of compact objects involving a NS not only produce gravitational waves that are detectable by ground-state interferometers [12] but also a large variety of electromagnetic signals [13–15]. One of these electromagnetic transients is produced by the radioactive decay of r-process elements, triggering a signal in the optical and infrared band that peaks at times from days to weeks after the ejecta [14, 16]. Since these electromagnetic signatures known as "macronova" or "kilonova" derive their energy directly from the radioactive decay of r-process nuclei, they can be used as a constraint to determine the astrophysical origin of the r-process elements. A possible recent observation of this event associated to the short γ-ray

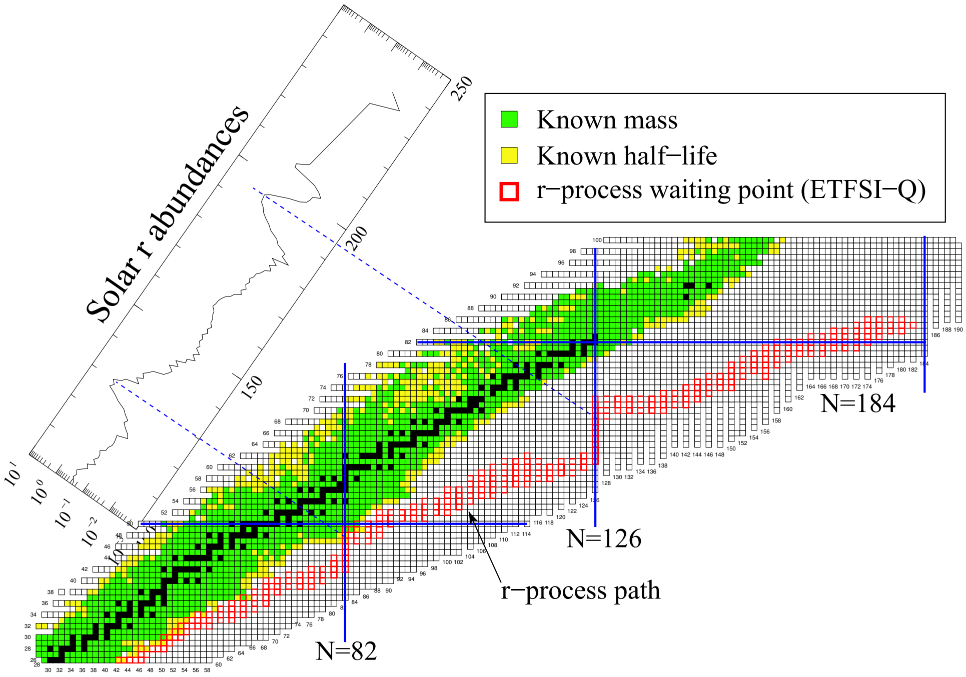

Figure 1.1: A variety of *r*-process paths defined by their waiting-point nuclei. The *r*-process path proceeds through neutron rich nuclei, where masses and half-lives are unknown. After decaying to stability the abundances reproduce the observed solar *r*-process abundance distribution. Adapted from [5].

burst GRB130603B [17, 18] raised a lot of excitement and if confirmed it will represent the first detection of *r*-process material in situ.

Focusing on NSM, another important aspect is that recent simulations show that a large amount of neutron-rich material is ejected during the dynamical phase of the merger [19–21]. The final abundances produced in these events have a distribution that closely follows the solar one. This "robustness" of the *r* process in NSM is a very appealing feature, since it may explain the solar-like distribution of *r*-process elements found in metal-poor stars [22].

As we already touched before, fission is unavoidable if the *r*-process occurs in high entropy scenarios with large enough neutron-to-seed ratio and plays a key role during the evolution. Foremost, fission determines the heaviest nuclei than can be synthesized during the *r* process. The fragments emitted by the fissioning nuclei populate the region of lighter elements shaping the distribution of abundances of *r*-process nuclei that we observe nowadays. For high neutron-to-seed ratios the fission fragments can capture neutrons giving raise to a fission cycling. Moreover, fission is an important source of radioactive energy and therefore it may contribute to the heating of the material during the *r*-process nucleosynthesis.

These aspects justify the argument that a proper description of the fission process is required to perform realistic *r*-process calculations. Actually, in order to understand and quantify the impact of fission, we should be able to answer three different, yet related, questions:

- Where does fission occur?
- How much material accumulates in the fissioning region?
- What are the yields of these fissioning nuclei?

Nowadays fission models predict very different fission properties for superheavy neutron-rich nuclei, and therefore answering these questions is not a straightforward task. It is therefore important to address the sensitivity of the r-process calculations to different sets of fission rates. However, while doing this one has to ensure that the calculation of all the reaction rates is as consistent as possible. This implies that ideally we would like to compute neutron-induced, photo-induced, spontaneous, β-delayed and neutrino-induced fission using always the same model. However, keeping this consistency can become very cumbersome due to the large number of nuclei that one has to cover and the different types of decay that are involved.

The additional problem is that the theoretical description of the fission process is already challenging *per se*. The evolution of the nucleus from its initial compact configuration to the scission point is driven by the competition between the long-range Coulomb repulsion of protons inside the nucleus and the short-range strong interaction binding the nucleons together. This competition produces quantum mechanical shell effects giving raise to the stability of the superheavy elements. But since the probability of such an event to occur cannot be computed using pure quantum mechanical rules, we are forced to introduce some approximations. By assuming that the time-scales at which fission occurs are longer than the average velocity of nucleons inside the neutrons [23], we can assume that the fission process can be described using a reduced set of collective coordinates. We can therefore compute the evolution of the energy as a function of these collective coordinates, that usually describe the shape of the nucleus, and the corresponding collective inertia associated to the "motion" inside this collective space. Within this picture fission is analogous to the quantum tunneling of a particle inside a potential, and this potential is the so-called fission barrier.

Nowadays exist two main nuclear structure models to describe the fission process: microscopic-macroscopic (mic-mac) model and the energy density functional approach (EDF). The mic-mac models pioneered the description of the fission process already in the late seventies [24, 25]. Within this model the energy of the nucleus is essentially given by the sum of three different terms: a deformed liquid drop describing the bulk properties of the nucleus, the shell corrections accounting for the role of single particle levels and a pairing contribution reproducing the two-body effects. This nuclear model has been applied to several calculations exploring the systematic binding energies and fission properties along the nuclear chart, and nowadays fission calculations can be performed in multidimensional space using up to 5 collective degrees of freedom [26, 27].

The main problem of mic-mac methods is that they require a large number of independent parameters that have to be fitted independently for each energy contribution. The energy density functional theory emerged as an alternative scheme based on more microscopic assumptions. Within this model the energy is expressed as a function of intrinsic densities of the nucleus and the ground state is obtained by seeking for the minimum of this energy. This method allows the description of nuclei along the whole chart using a single effective interaction modeling the energy density functional. As in the case of the mic-mac models, the evolution of the energy in obtained by constraining the nucleus to a particular configuration. The typical and most basic example is the sampling of the energy while constraining the nucleus to higher and higher quadrupole deformations. This will give a one dimensional fission path where each point is obtained by minimizing the energy to a particular quadrupole deformation. Since 1974 [28] fission has been used as a test to verify the microscopic description of collectivity obtained within the EDF approach. Nowadays the fission properties of superheavy nuclei are commonly used in the benchmark of the functionals against experimental data [29–33] and several models have been adjusted in order to reproduce the fission barriers and isomer excitation energies of superheavy nuclei [34, 35], converting the EDF in a solid scheme for the microscopic description of fission [36].

1.1 Thesis outline

This thesis is organized as follows. In Chapter 2 we revise the energy density functional formalism (EDF) based on the Hartree-Fock-Bogoliubov (HFB) theory. We will start from the independent particle model at the basis of the mean-field approach, and we will then introduce the HFB theory. The second part of this Chapter is dedicated to explain the different EDF's used in this thesis for the calculation of the fission properties of superheavy nuclei and the approach used in the calculation of odd nuclei.

Chapter 3 is devoted to the theoretical description of fission within the energy density functional formalism. In this Chapter we describe the approaches used for the calculations of the spontaneous fission lifetimes, collective inertias and potential energy surfaces. The last part is devoted to the results obtained for the spontaneous fission using a recent development in the theoretical calculation of the fission path.

In Chapter 4 we will introduce the Hauser-Feshbach statistical model used for the calculation of the stellar reaction rates. The different ingredients required by the statistical calculation are revised, with a special emphasis to the description of the neutron induced fission. Chapter 5 belongs to the description of the basics features of the nuclear network employed in the r-process calculations and the general considerations regarding the evolution of the r process.

In Chapter 6 we present the benchmark of our results against the experimental data. We will show the comparison for binding energies, fission barriers and spontaneous fission lifetimes. Afterwards we will discuss the results for the neutron induced fission and neutron capture cross sections and study the sensitivity of our predictions to variations in nuclear level densities, γ-ray strengths, fission barriers and collective inertias. Finally, we will introduce our α-decay calculations and study the competition with the spontaneous fission process.

Chapter 7 is devoted to study the fission properties of nuclei along the whole superheavy landscape. The predictions of fission barriers and spontaneous fission lifetimes obtained from the different models are discussed. We will also present the first calculations of stellar reaction rates obtained from a microscopic evaluation of the collective inertias.

In Chapter 8 we will present the r-process calculations obtained from trajectories simulating the dynamical ejecta in neutron star mergers. We will compare our results with those predicted by other models employing a traditional calculation of the fission process, and we will discuss the sensitivity of the abundances to different collective inertias. The last part of this Chapter is dedicated to the study of the radioactive energy emitted at timescales relevant for macronova observations.

Finally, Chapter 9 summarizes the main results obtained in this work, highlights the consequences for our findings and suggests the relevant questions that should be addressed in the future.

2 The energy density functional formalism

Energy density functionals (EDF's) allow the calculation of nuclear properties throughout the whole nuclear chart. This possibility of performing systematic nuclear structure calculations using a unique model is an appealing feature for studies exploring the impact of nuclear inputs on the *r*-process nucleosynthesis. This Chapter is thus devoted to a general introduction to the EDF formalism that we used for the calculation of binding energies and fission properties of superheavy nuclei. We will start from the independent particle model at the basis of any mean field theory and afterwards we will present the Hartree-Fock-Bogolyubov theory. The second part is dedicated to the description of the two models used in our calculations (the Barcelona-Catania-Paris-Madrid and the Gogny EDF) and the treatment of odd nuclei employed in this thesis.

2.1 Many-body systems and the independent particle model

In a system of N non-interacting and indistinguishable particles the total Hamiltonian is given by the sum of the N single particle Hamiltonians that, by definition, are identical. The time-independent Schrödinger equation can be written then as:

$$\hat{H}_0|\Phi\rangle = \sum_{i=1}^{N}\hat{h}(\boldsymbol{r}_i)|\Phi\rangle \,. \tag{2.1}$$

where the single-particle Hamiltonian $\hat{h}$ defines the eigenvalue equation for the single-particle energies ε and the single-particle states φ_i:

$$\hat{h}(\boldsymbol{r})\varphi_i(\boldsymbol{r}) = \varepsilon_i\varphi_i(\boldsymbol{r}) \,. \tag{2.2}$$

The wave function $|\Phi\rangle$ representing the N-particle system has to fulfill the requirement of its particles being indistinguishable. This condition can be imposed by requiring the many-body wave function to be an eigenstate of the unitary and Hermithian exchange operator $\hat{P}_{ij}$:

$$\hat{P}_{ij}|\Phi(\boldsymbol{r}_1,\ldots,\boldsymbol{r}_i,\ldots,\boldsymbol{r}_j,\ldots,\boldsymbol{r}_N)\rangle = \pm|\Phi(\boldsymbol{r}_1,\ldots,\boldsymbol{r}_j,\ldots,\boldsymbol{r}_i,\ldots,\boldsymbol{r}_N)\rangle \,. \tag{2.3}$$

The Hilbert space $\mathscr{H}$ of the N indistinguishable particles system can then be divided in two subspaces each of them formed by eigenfunctions with either a positive or negative eigenvalue p_{ij}. Experimental evidences and the spin statistic theory tell us that particles living in the symmetric subspace $\mathscr{H}^+$ have an integer spin (and they are called bosons), while particles living in the antisymmetric space $\mathscr{H}^-$ have a half-integer spin (and they are called fermions).

If the N-particles system is a representation of a nucleus formed by N nucleons, we have to construct our basis from the $\mathscr{H}^-$ space in order to deal only with antisymmetric states. The wave function of the system $|\Phi\rangle$ is then given by a Slater determinant of single particle states:

$$\Phi_{\alpha_1,\ldots,\alpha_N} = \frac{1}{\sqrt{N!}}\begin{vmatrix} \varphi_{\alpha_1}(\boldsymbol{r}_1) & \varphi_{\alpha_1}(\boldsymbol{r}_2) & \cdots & \varphi_{\alpha_1}(\boldsymbol{r}_N) \\ \varphi_{\alpha_2}(\boldsymbol{r}_1) & \varphi_{\alpha_2}(\boldsymbol{r}_2) & \cdots & \varphi_{\alpha_2}(\boldsymbol{r}_N) \\ \vdots & \vdots & \ddots & \vdots \\ \varphi_{\alpha_N}(\boldsymbol{r}_1) & \varphi_{\alpha_N}(\boldsymbol{r}_2) & \cdots & \varphi_{\alpha_N}(\boldsymbol{r}_N) \end{vmatrix} \,. \tag{2.4}$$

This Chapter is based on Ref. [36], [37] and [38].

The energy of the ground state $|\Phi_0\rangle$ is the sum of the N lowest single particle energies $E_{\mathrm{GS}} = \sum_i^N \varepsilon_i$. Furthermore, the $\mathscr{H}^-$ subspace is fully spanned by the set of all Slater determinants. It is important to recall that the symmetry of the system is a constant of motion, which implies that the reduced eigenspace $\mathscr{H}^-$ can be treated as the actual Hilbert space since its eigenvectors are not allow to range over the $\mathscr{H}^+$ space (and vice versa).

We can then restrict our discussion to the $\mathscr{H}^-$ space defined by antisymmetric eigenfunctions. Considering the antisymmetric Fock space:

$$\mathcal{F}^- = \mathbb{C} \oplus \mathscr{H}_1^- \oplus \mathscr{H}_2^- \oplus \cdots \oplus \mathscr{H}_N^- \oplus \cdots , \tag{2.5}$$

the creator (annhilitation) $a_\mu^\dagger$ (a_μ) operator is defined as the operator creating (destroying) a particle in the single particle state μ. The creation and annihilation operators must obey the anticommutation rules:

$$\{\hat{a}_\mu, \hat{a}_\nu\} = 0\,, \quad \{\hat{a}_\mu^\dagger, \hat{a}_\nu^\dagger\} = 0\,, \quad \{\hat{a}_\mu^\dagger, \hat{a}_\nu\} = \delta_{\mu\nu}\,, \tag{2.6}$$

from which one can obtain the Pauli exclusion principle by showing that $a_\mu^\dagger a_\mu^\dagger = 0$. Using the creation and annihilation operators we can now define the particle (Fock) vacuum as:

$$\langle 0|0\rangle = 1; \quad \hat{a}_\mu|0\rangle = 0 \quad \forall\ \mu\,, \tag{2.7}$$

corresponding to a state without particles, and an arbitrary N-particle state as:

$$|\Phi_{\alpha_1,\ldots,\alpha_N}\rangle = \prod_{i=1}^{N} \hat{a}_i^\dagger |0\rangle\,. \tag{2.8}$$

Since the anticommutation rules enforce the wave function to be antisymmetric, the expression above defines an orthonormal set of states and is equivalent to the Slater determinant expression of Eq. (2.4). The antisymmetrization of a many-body wave function via creation and annihilation operators is a direct application of the so-called "second quantization" formalism.

2.1.1 Second quantization formalism

The second quantization formalism allows to describe a many-body state without requiring an explicitly (anti)symmetrization of the wave function. Within the second quantization the many-body state is represented in the occupation number basis and any A-body operator $\hat{F}$ can be written in terms of its antysimmetrized matrix elements and the creation and annihilation operators:

$$\hat{F} = \frac{1}{(A!)^2} \sum_{\substack{\mu_1\ldots\mu_A \\ \nu_1\ldots\nu_A}} F_{\mu_1\ldots\mu_A\nu_1\ldots\nu_A} \hat{a}_{\mu_1}^\dagger \cdots \hat{a}_{\mu_A}^\dagger \hat{a}_{\nu_A} \cdots \hat{a}_{\nu_1}\,. \tag{2.9}$$

Using the expression above, the one-body operator in coordinate space representation:

$$\hat{F} = \sum_{i=1}^{N} \hat{f}(\boldsymbol{r}_i)\,, \tag{2.10}$$

can be written as:

$$\hat{F} = \sum_{\mu\nu} f_{\mu\nu} \hat{a}_\mu^\dagger \hat{a}_\nu\,, \tag{2.11}$$

where $f_{\mu\nu} = (\mu|\hat{f}|\nu)$ is the one-body matrix element obtained from the single particle states $|\mu) = \hat{a}_\mu^\dagger\,|0\rangle \equiv \varphi_\mu$, which general expression in the coordinate space representation will be derived in the next section. A typical example of one-body operator is the particle number operator $\hat{N}$ counting the total number of fermions in the system:

$$\hat{N} = \sum_{\nu=1}^{\infty} \hat{a}_{\nu}^{\dagger} \hat{a}_{\nu} \quad \text{with} \quad \hat{N} |\Phi_{\alpha_1,\ldots,\alpha_N}\rangle = N |\Phi_{\alpha_1,\ldots,\alpha_N}\rangle \,, \tag{2.12}$$

where $|\Phi_{\alpha_1,\ldots,\alpha_N}\rangle$ is a N-particle state of the form (2.8).

Similarly to the one-body case, the second quantization formalism can be applied to a two-body operator (and so-on):

$$\hat{G} = \frac{1}{2} \sum_{i \neq j}^{N} \hat{g}(\boldsymbol{r}_i, \boldsymbol{r}_j) = \frac{1}{4} \sum_{\substack{\mu_1 \mu_2 \\ \nu_1 \nu_2}} g_{\mu_1 \mu_2 \nu_1 \nu_2} \hat{a}_{\mu_1}^{\dagger} \hat{a}_{\mu_2}^{\dagger} \hat{a}_{\nu_1} \hat{a}_{\nu_2} \,, \tag{2.13}$$

where now $G_{\alpha\beta\gamma\delta}$ is the two-body matrix element between normalized antisymmetric two-particle states $|\alpha\beta) = \hat{a}_{\alpha}^{\dagger} \hat{a}_{\beta}^{\dagger} |0\rangle$:

$$g_{\alpha\beta\gamma\delta} = (\alpha\beta|\hat{g}|\delta\gamma) \,. \tag{2.14}$$

In nuclear physics we want to describe a system of N-interacting particles, whose most general Hamiltonian has the form:

$$\hat{H} = \sum_{i} \hat{h}_i + \sum_{i \leq j} \hat{v}_{ij} + \sum_{i \leq j \leq k} \hat{V}_{ijk} + \cdots \,, \tag{2.15}$$

where the sum can continue up to the N-nucleon interaction. Within the second quantization the Hamiltonian can be written in the elegant expression:

$$\hat{H} = \sum_{\mu} \varepsilon_{\mu} \hat{a}_{\mu}^{\dagger} \hat{a}_{\mu} + \frac{1}{4} \sum_{\substack{\mu_1 \mu_2 \\ \nu_2 \nu_1}} v_{\mu_1 \mu_2 \nu_1 \nu_2} \hat{a}_{\mu_1}^{\dagger} \hat{a}_{\mu_2}^{\dagger} \hat{a}_{\nu_2} \hat{a}_{\nu_1} + \frac{1}{36} \sum_{\substack{\mu_1 \mu_2 \mu_3 \\ \nu_1 \nu_2 \nu_3}} V_{\mu_1 \mu_2 \mu_3 \nu_1 \nu_2 \nu_3} \hat{a}_{\mu_1}^{\dagger} \hat{a}_{\mu_2}^{\dagger} \hat{a}_{\mu_3}^{\dagger} \hat{a}_{\nu_3} \hat{a}_{\nu_2} \hat{a}_{\nu_1} + \cdots \,, \tag{2.16}$$

being ε_i the energy of the single particle state $|i)$:

$$\hat{H}_0 |i) = \sum_{\mu} \varepsilon_{\mu} \hat{a}_{\mu}^{\dagger} \hat{a}_{\mu} \hat{a}_{i}^{\dagger} |0\rangle = \varepsilon_i |i) \,. \tag{2.17}$$

2.1.2 Matrix elements in second quantization

The second quantization requires the definition of single particle states φ_i. Given a complete basis of orthonormal wave functions the connection between single particle wavefunctions and operators in second quantization is given by the field operators:

$$\hat{\phi}^{\dagger}(\boldsymbol{r}) = \sum_{\mu} \varphi_{\mu}^{*}(\boldsymbol{r}) \hat{a}_{\mu}^{\dagger} \,; \quad \hat{\phi}(\boldsymbol{r}) = \sum_{\mu} \varphi_{\mu}(\boldsymbol{r}) \hat{a}_{\mu} \,, \tag{2.18}$$

that satisfy the anticommutation rules:

$$\{\hat{\phi}(\boldsymbol{r}), \hat{\phi}(\boldsymbol{r}')\} = \{\hat{\phi}^{\dagger}(\boldsymbol{r}), \hat{\phi}^{\dagger}(\boldsymbol{r}')\} = 0 \,, \quad \{\hat{\phi}^{\dagger}(\boldsymbol{r}), \hat{\phi}(\boldsymbol{r}')\} = \delta(\boldsymbol{r} - \boldsymbol{r}') \,. \tag{2.19}$$

Equations (2.18) allow to get an expression of the creation and annihilation in the coordinate space representation as:

$$\hat{a}_{\mu}^{\dagger} = \int d^3\boldsymbol{r} \, \hat{\phi}^{\dagger}(\boldsymbol{r}) \varphi_{\mu}(\boldsymbol{r}) \,; \quad \hat{a} = \int d^3\boldsymbol{r} \, \hat{\phi}(\boldsymbol{r}) \varphi_{\mu}^{*}(\boldsymbol{r}) \,. \tag{2.20}$$

Any one-body operator given in first-quantized form can then be written in second-quantized form by replacing Eqs. (2.18) in the expression of the one-body operator Eq. (2.11):

$$\hat{F} = \sum_{i=1}^{N} \hat{f}(\boldsymbol{r}_i) = \sum_{\mu\nu} \hat{f}_{\mu\nu} \hat{a}_{\mu}^{\dagger} \hat{a}_{\nu} = \int d^3\boldsymbol{r} \, \hat{\phi}^{\dagger}(\boldsymbol{r}) \hat{f}(\boldsymbol{r}) \hat{\phi}(\boldsymbol{r}) \,, \tag{2.21}$$

where the matrix element of the operator $\hat{F}$ in coordinate representation reads:

$$\hat{f}_{\mu\nu} = (\mu|\hat{f}|\nu) = \langle 0| \hat{a}_{\mu} \hat{f} \hat{a}_{\nu}^{\dagger} |0\rangle = \int d^3\boldsymbol{r} \varphi_{\mu}^{*}(\boldsymbol{r}) \hat{f}(\boldsymbol{r}) \varphi_{\nu}(\boldsymbol{r}) \,. \tag{2.22}$$

2.1.3 The particle density operator

In the nuclear mean-field model a central role is played by the particle density operator, that in the N-body Hilbert space is defined as:

$$\hat{\rho}(\boldsymbol{r}) = \sum_{i=1}^{N} \delta(\boldsymbol{r} - \hat{\boldsymbol{r}}_i)\,. \tag{2.23}$$

This operator counts the particle density at a given position $\boldsymbol{r}$. Using Eq. (2.11) and Eq. (2.21) one can rewrite it in second quantization form as:

$$\begin{aligned}\hat{\rho}(\boldsymbol{r}) &= \sum_{\mu\nu} \langle\mu|\,\delta(\boldsymbol{r} - \hat{\boldsymbol{r}})\,|\nu\rangle\, \hat{a}^\dagger_\mu \hat{a}_\nu = \sum_{\mu\nu} \int d^3\boldsymbol{r}'\, \varphi^*_\mu(\boldsymbol{r}')\delta(\boldsymbol{r} - \boldsymbol{r}')\varphi_\nu(\boldsymbol{r}')\hat{a}^\dagger_\mu \hat{a}_\nu \\ &= \int d^3\boldsymbol{r}' \hat{\phi}^\dagger(\boldsymbol{r}')\delta(\boldsymbol{r} - \boldsymbol{r}')\hat{\phi}(\boldsymbol{r}) = \hat{\phi}^\dagger(\boldsymbol{r})\hat{\phi}(\boldsymbol{r})\,,\end{aligned} \tag{2.24}$$

where the sum in the first equality run over all the single particle spectrum. Since $\hat{\rho}(\boldsymbol{r})$ only involves combinations of particle creators and annihilators operators is usually referred as a particle-hole (ph) operator. Using the equation above together with Eq. (2.9) and (2.12) one has that:

$$\int \rho(\boldsymbol{r})\, d^3\boldsymbol{r} = \int \hat{\phi}^\dagger(\boldsymbol{r})\hat{\phi}(\boldsymbol{r})\, d^3\boldsymbol{r} = \sum_{\mu\nu} \int \varphi^*_\mu(\boldsymbol{r})\varphi_\nu(\boldsymbol{r})\hat{a}^\dagger_\mu \hat{a}_\nu\, d^3\boldsymbol{r} = \sum_{\mu} \hat{a}^\dagger_\mu \hat{a}_\mu = \hat{N}\,, \tag{2.25}$$

showing the relation between particle number density and total particle number operators.

2.2 The Hartree-Fock-Bogoliubov theory (HFB)

The aim of any mean fields model is to find the ground-state wavefunction $|\Phi\rangle$ of the many-body system that minimizes the expectation value of the total energy:

$$\delta E = \delta \langle\Phi|\, \hat{H}\, |\Phi\rangle = 0\,. \tag{2.26}$$

In the Hartree-Fock formalism one restricts the variational Hilbert space to the subspace given by Slater determinants obtained from a complete set of orthonormal single-particle states $\{\varphi\}$. As we have seen in the previous section a Slater determinant defined in the Fock space can be written as a product of creation operators:

$$|\Phi\rangle = \prod_{i=1}^{N} \hat{a}^\dagger_i\, |0\rangle\ . \tag{2.27}$$

The goal of the HF formalism is then to find a single particle basis $\{\chi(\boldsymbol{r})\}$ related to the original orthonormal basis $\{\varphi(\boldsymbol{r})\}$ by a unitary transformation

$$\chi_i(\boldsymbol{r}) = \sum_{\mu\nu} U_{\mu\nu}\varphi_\nu(\boldsymbol{r})\,, \tag{2.28}$$

defining the Slater determinant $|\Phi_0\rangle$ that minimizes the expected value of the energy:

$$\delta E = \delta \langle\Phi_0|\, \hat{H}\, |\Phi_0\rangle = 0\,. \tag{2.29}$$

The many-body ground-state wavefunction is then defined as a product of the new creation operators $\hat{c}^\dagger$:

$$|\Phi_0\rangle = \prod_{i=1}^{N} \hat{c}^\dagger_i\, |0\rangle\ , \tag{2.30}$$

that are related to the original creation operators by the same unitary trasformation of the single-particle wave functions:

$$\hat{c}^{\dagger}_{\mu} = \sum_{\mu\nu} U_{\mu\nu} \hat{a}^{\dagger}_{\nu} \, . \tag{2.31}$$

In the Hartree-Fock method the nuclear potential is truncated at the level of the two-body term and reduced to a single-particle potential [39]:

$$V(i,\dots,A) = \sum_{i\leq j}^{A} V(i,j) \approx \sum_{i}^{A} V(i) \, , \tag{2.32}$$

which implicitly reduces the many-body problem of the nucleus to single nucleons moving independently in an average potential. In principle this approach is only justified if the gap between the last occupied level and the first empty one is large enough to forbid any particle-hole excitation. Therefore we can expect that in absence of shell closures the HF method is not valid anymore, and an explicitly treatment of the short-range correlations (also known as particle-particle or pairing correlations) has to be carried out. This is achieved by means of the Hartree-Fock-Bogoliubov theory which accounts for the most general product of wave functions describing independently moving “quasiparticles“.

2.2.1 The Hartree-Fock-Bogolyubov equation

The Hartree-Fock-Bogoliubov theory is based on a generalization of the Hartree-Fock equations, where pairing correlations are included via a Bogoliubov trasformation of the particle operators $(\hat{a}, \hat{a}^{\dagger})$ introducing the concept of independent quasiparticle:

$$\hat{\beta}_{\mu} = \sum_{i}^{N} U^{*}_{i\mu} \hat{a}_{i} + \sum_{i}^{N} V^{*}_{i\mu} \hat{a}^{\dagger}_{i} \, , \tag{2.33}$$

$$\hat{\beta}^{\dagger}_{\mu} = \sum_{i}^{N} U_{i\mu} \hat{a}^{\dagger}_{i} + \sum_{i}^{N} V_{i\mu} \hat{a}_{i} \, , \tag{2.34}$$

being N the dimension of the Hilbert space of the single-particle wave functions and U and V the Bogoliubov wave functions. Defining the Bogoliubov trasformation matrix W as

$$W = \begin{pmatrix} U & V^{*} \\ V & U^{*} \end{pmatrix} \, , \tag{2.35}$$

Eq. (2.33) can be written in the compact matrix form:

$$\begin{pmatrix} \hat{\beta} \\ \hat{\beta}^{\dagger} \end{pmatrix} = \begin{pmatrix} U^{+} & V^{+} \\ V^{T} & U^{T} \end{pmatrix} \begin{pmatrix} \hat{a} \\ \hat{a}^{\dagger} \end{pmatrix} = W^{+} \begin{pmatrix} \hat{a} \\ \hat{a}^{\dagger} \end{pmatrix} . \tag{2.36}$$

with W^{+} the hermitian conjugated of the W matrix. The orthonomalization of the quasiparticle states impose W to be a unitary matrix:

$$WW^{+} = W^{+}W = I \, . \tag{2.37}$$

In the HFB theory, the ground state wave function of the nucleus $|\Phi\rangle$ is assumed to be a state of independent quasiparticles:

$$|\Phi\rangle = \prod_{\mu} \hat{\beta}_{\mu} |0\rangle \, , \tag{2.38}$$

where $|0\rangle$ is the particle vacuum in the Fock space (2.7). When the ground state of the nucleus is described as a quasiparticle vacuum, the Wick theorem ensures that the degrees of freedom are the one-body density matrix ρ_{ij} and the pairing tensor κ_{ij} [39] defined as:

$$\rho_{ij} = \langle\Phi|\, \hat{a}_j^\dagger \hat{a}_i \,|\Phi\rangle = (V^* V^T)_{ij} = \rho_{ji}^*\,, \tag{2.39}$$

$$\kappa_{ij} = \langle\Phi|\, \hat{a}_i \hat{a}_j \,|\Phi\rangle = (V^* U^T)_{ij} = -\kappa_{ji}\,. \tag{2.40}$$

A generalised quasiparticle density matrix can be defined from ρ and κ as:

$$\mathcal{R} = \begin{pmatrix} \rho & \kappa \\ -\kappa^* & 1-\rho^* \end{pmatrix}, \tag{2.41}$$

with eigenvalues equal to either 1 or 0. This matrix allows to compact the notation by encapsulating the relevant degrees of freedom of the quasiparticle picture. For instance, the wave function of the HFB ground state $|\Phi\rangle$ is obtained by minimizing the total energy:

$$E = \langle\Phi|\hat{H}|\Phi\rangle = E[\rho, \rho^*, \kappa, \kappa^*] = E[\mathcal{R}]\,, \tag{2.42}$$

under the constraints on proton and neutron number ($\langle\Phi|\hat{N}|\Phi\rangle = N = \rho_{ii}$) and that the solution remains a quasiparticle vacuum ($\mathcal{R}^2 = \mathcal{R}$). This conditions are imposed by performing a minimization of the Routhian:

$$\delta\left\{\langle\Phi|\hat{H} - \lambda\hat{N}|\Phi\rangle - \mathrm{tr}[\Lambda(\mathcal{R}^2 - \mathcal{R})]\right\} = 0\,, \tag{2.43}$$

where Λ is the hermitian matrix of undetermined constraints whose elements are Lagrange multipliers λ. The variation must be performed in terms of $\delta\mathcal{R}$ and we have that:

$$\begin{aligned} \sum_{ab} \frac{(\partial\langle\Phi|\hat{H} - \lambda\hat{N}|\Phi\rangle)}{\partial\mathcal{R}_{ab}} \delta\mathcal{R}_{ab} - \sum_{ab} \frac{\partial}{\partial\mathcal{R}_{ab}} \mathrm{tr}\left[\Lambda(\mathcal{R}^2 - \mathcal{R})\right] \delta\mathcal{R}_{ab} = \\ \frac{1}{2}\mathcal{H} - (\mathcal{R}\Lambda + \Lambda\mathcal{R} - \Lambda) = 0\,, \end{aligned} \tag{2.44}$$

where on the LHS the first term was replaced by $\frac{1}{2}\mathcal{H}_{ba} = \frac{\partial\langle\Phi|\hat{H} - \lambda\hat{N}|\Phi\rangle}{\partial\mathcal{R}_{ab}}$ and the second term was obtained using $\partial\mathcal{R}_{ab}/\partial\mathcal{R}_{cd} = \delta_{ac}\delta_{bd}$. The equation above leads to the HFB equation [39]:

$$[\mathcal{H}, \mathcal{R}] = 0\,. \tag{2.45}$$

From the definition of the generalised density matrix in Eq. (2.41) the HFB matrix $\mathcal{H}$ can be written in terms of the one-body density matrix and the pairing tensor as:

$$\mathcal{H} = \begin{pmatrix} h & \Delta \\ -\Delta^* & -h^* \end{pmatrix}, \tag{2.46}$$

being h_{ij} and Δ_{ij} the mean and pairing field, respectively:

$$\begin{aligned} h_{ij} &= \frac{\partial\langle\Phi|\hat{H} - \lambda\hat{N}|\Phi\rangle}{\partial\rho_{ji}}\,, \quad & \Delta_{ij} &= 2\frac{\partial\langle\Phi|\hat{H}|\Phi\rangle}{\partial\kappa_{ij}^*}\,, \\ \Delta_{ij}^* &= 2\frac{\partial\langle\Phi|\hat{H}|\Phi\rangle}{\partial\kappa_{ij}}\,, \quad & h_{ij}^* &= \frac{\partial\langle\Phi|\hat{H} - \lambda\hat{N}|\Phi\rangle}{\partial\rho_{ji}^*}\,. \end{aligned} \tag{2.47}$$

Eq. (2.45) implies that exists a Bogolyubov transformation that diagonalizes both $\mathcal{R}$ and $\mathcal{H}$, which allows the formulation of the HFB equation in its standard form:

$$\mathcal{H}W = W\mathcal{E} \quad \text{with} \quad \mathcal{E} = \delta_{ii}E_i\,, \tag{2.48}$$

where $\mathcal{E}$ is the quasiparticle energy matrix formed by the quasiparticle energies E_i. The equation above is ensured by the fact that the generalised density matrix $\mathcal{R}$ is diagonalized by the matrix of Bogolyubov transformation W.

2.2.2 Representation in the quasiparticle basis

The trasformation of Eq. (2.33) can be inverted in order to express any operator in terms of the quasiparticle basis, that is, in terms of the Bogolyubov wavefunctions U and V. Given an Hermitian one-particle operator:

$$\hat{F} = \sum_{\mu\nu} f_{\mu\nu} + \frac{1}{2}\left(g_{\mu\nu}\hat{c}^{\dagger}_{\mu}\hat{c}^{\dagger}_{\nu} + \text{h.c.}\right), \tag{2.49}$$

its quasiparticle representation is given by the expression [39]:

$$\hat{F} = F^{0} + \sum_{\mu\nu} F^{11}_{\mu\nu}\hat{\beta}^{\dagger}_{\mu}\hat{\beta}_{\nu} + \frac{1}{2}\sum_{\mu\nu}\left(\hat{\beta}^{\dagger}_{\mu}\hat{\beta}^{\dagger}_{\nu} + \text{h.c.}\right), \tag{2.50}$$

with

$$F^{0} = \text{tr}(f\rho) + \text{tr}(g\kappa^{*} + g^{*}\kappa)\,, \tag{2.51a}$$

$$F^{11}_{\mu\nu} = (U^{\dagger}fU - V^{\dagger}f^{T}V + U^{\dagger}gV - V^{\dagger}g^{*}U)_{\mu\nu}\,, \tag{2.51b}$$

$$F^{20}_{\mu\nu} = (U^{\dagger}fV^{*} - V^{\dagger}f^{T}U^{*} + U^{\dagger}gU^{*} - V^{\dagger}g^{*}V^{*})_{\mu\nu}\,. \tag{2.51c}$$

In Chapter 3 we will use this notation to express the collective inertias in terms of the quasiparticle matrix elements of the collective variables.

2.2.3 The effective Hamiltonian

The solution of the non-linear system described by the HFB equation (2.45) or (2.48) requires an ansatz of the energy functional E. In nuclear physics this functional is usually obtained as the expectation value of an effective two-body Hamiltonian:

$$E = \langle\Phi|\hat{H}|\Phi\rangle \quad \text{with} \quad \hat{H} = \sum_{ij} t_{ij}\hat{a}^{\dagger}_{i}\hat{a}_{j} + \frac{1}{4}\sum_{ijkl}\bar{v}_{ijkl}\hat{a}^{\dagger}_{i}\hat{a}^{\dagger}_{j}\hat{a}_{l}\hat{a}_{k}, \tag{2.52}$$

being t_{ij} the one-body kinetic operator and $\bar{v}_{ijkl}$ the two-body potential. Making use of the Wick's theorem the energy functional can be written in terms of the one-body density matrix and pairing tensor density as [39]:

$$E = \text{tr}(t\rho) + \frac{1}{2}\text{tr}(\Gamma\rho) - \frac{1}{2}\text{tr}(\Delta\kappa^{*})\,. \tag{2.53}$$

where the mean field and pairing potentials are defined as:

$$\Gamma_{ij} = \sum_{kl}\overline{v}_{ijkl}\rho_{lk}\,, \qquad\qquad \Delta_{ij} = \frac{1}{2}\sum_{kl}\overline{v}_{ijkl}\kappa_{kl}\,. \tag{2.54}$$

and the Hartree-Fock Hamiltonian is obtained by replacing Eq. (2.53) in Eq. (2.47):

$$h = t - \lambda\delta_{ij} + \Gamma\,. \tag{2.55}$$

In nuclear structure calculations is very common to introduce density-dependent two-nucleon interactions $\hat{v}^{DD}(\mathbf{r_1} - \mathbf{r_2}, \rho(\mathbf{R}))$ with $\mathbf{R} = (\mathbf{r_1} + \mathbf{r_2})/2$. The energy functional $E[\mathcal{R}]$ is then obtained by computing the expected value of the potential $\hat{v}^{DD}$ on the quasiparticle vacuum $|\Phi\rangle$. The presence of a density-dependent interaction modifies the mean-field potential by introducing a term depending on the derivative $\partial\hat{v}^{DD}/\partial\rho$:

$$\Gamma_{ij} = \sum_{kl}\hat{v}^{DD}_{ij}\rho_{lk} + \frac{1}{4}\sum_{klmn}\langle mn|\frac{\partial\hat{v}^{DD}}{\partial\rho_{ij}}|kl\rangle\left(\rho_{ln}\rho_{km} + \frac{1}{2}\kappa_{lk}\kappa^{*}_{nm}\right)\rho_{ij}\,. \tag{2.56}$$

The second term on the right hand side is the so-called rearrangement term.

2.2.4 Constraints

Self-Consistent Mean-Field calculations usually rely on a solution of the HFB equation subject to constraints. The fundamental ones are the proton and neutron number already introduced in Eq. (2.43), that are made necessary by the fact that the HFB vacuum is not an eigenstate of the particle number operator. In fission calculations constraints are particularly important because allow the computation of the energy as a function of the collective coordinates caracterizing the multidimensional phase space of the fission process. The energy as a function of these collective coordinates is usually referred as potential energy surface and will be described in more detail in Sec. 3.4. In the HFB equation (2.45) constraints are introduced via Lagrange multipliers λ and the HFB matrix is replaced by the Routhian containing the matrix elements of the constraining operator $\hat{\mathcal{O}}$. The HFB equation becomes then:

$$(\mathcal{H} - \sum_{i}^{n} \lambda_i \hat{\mathcal{O}}_i - E)|\Phi\rangle = 0\,, \tag{2.57}$$

and the solution of this equation yields a HFB state $|\Phi(\lambda_1 \dots \lambda_n)\rangle$ that depends on the multipliers λ_i. The expectation value of the operator $\hat{\mathcal{O}}$ is then defined as

$$\langle\hat{\mathcal{O}}_i\rangle \equiv \langle\Phi(\lambda_1 \dots \lambda_n)|\hat{\mathcal{O}}_i|\Phi(\lambda_1 \dots \lambda_n)\rangle = \mathrm{tr}[\hat{\mathcal{O}}_i\rho] \quad \text{with} \quad i = 1, \dots, N\,, \tag{2.58}$$

where the last equality only holds for any one-body operator. If we assume that exists a unique relationship mapping the Lagrange multipliers with the expectation value of the constraining operators $\langle\hat{\mathcal{O}}_i(\lambda_1 \dots \lambda_n)\rangle \to \lambda_i(\langle\hat{\mathcal{O}}_1\rangle \dots \langle\hat{\mathcal{O}}_n\rangle)$ it is possible to obtain the expectation value of the energy as a function of the expectation value of the constraining operators $E(\langle\hat{\mathcal{O}}_1\rangle \dots \langle\hat{\mathcal{O}}_n\rangle)$, that for a fixed proton and neutron number is the potential energy surface of the nucleus.

2.3 The nuclear energy density functional formalism

The nuclear energy density functional formalism (EDF) is the application to atomic nuclei of the density functional theory (DFT) describing the electronic structure of many-body systems. The DFT roots in the Hohenberg-Kohn theorems relating a system of electrons moving under an external field. Given an external potential $v(\mathbf{r})$ governing the movement of an arbitrary number of electrons, and the electronic density $n(\mathbf{r})$ of the ground-state as a function of $v(\mathbf{r})$ the Hohenberg-Kohn theorem states that [40]:

Theorem 1 *The potential $v(\mathbf{r})$ is a unique functional of the electron density $n(\mathbf{r})$.*

Theorem 2 *If (and only if) $n(\mathbf{r})$ corresponds to the true ground-state density distribution of electrons, the resulting energy $E(n(\mathbf{r}))$ corresponds to the true ground state energy of the system E_{GS}.*

In practical formulations the electronic density $n(\mathbf{r})$ is determined by solving the Kohn-Sham equations that are formally equivalent to solving the Hartree-Fock equations using variational methods, where the many-body wavefunction is a Slater determinant built from an orthonormal basis of single particle states.

Despite the practical framework provided by the DFT theory one should be aware of the differences in the description of a system of interacting electrons and a system of interacting nucleons [36]. A nucleus is a self-bounded system made of compound particles (protons and neutrons), whose Hamiltonian is not known. In nucleons the internal charge distribution created by the constituent quarks results in a mismatch between and the charge distribution (that can be measured in scattering experiments) and the probability distribution. Finally correlations effects are weaker in electronic system than in nuclei, where the spontaneous symmetry breaking mechanism is required in order to include long-range correlations.

Despite all the difficulties expressed above, the EDF formalism resulted in a very powerful framework for computing the nuclear properties throughout the whole nuclear chart. The most common approach in nuclear calculations is to derive an energy density functional from the expectation value of an effective two-body density-dependent nuclear potential. The free parameters of such potential are adjusted in order to reproduce the bulk properties of several nuclei and once fixed the functional is uniquely defined for all the nuclei. Of this type are functionals based on Skyrme and Gogny potentials, which constitute the most popular choice in EDF calculations. But in principle the energy functional could be directly obtained as a parametrization of the density, without the definition of a nuclear potential. The Barcelona Catania Paris Madrid (BCPM) EDF used in this thesis is an example of such alternative approach, and it will be discussed in Sec. 2.3.2.

Within the EDF framework the total binding energy is thus obtained summing the contributions from the density functional (including spin-orbit and pairing terms), the Coulomb repulsion of protons in nuclei, the kinetic energy of nucleons and zero-point energy corrections stemming from spurious collectives modes:

$$E = E_{\text{edf}} + E_C + E_k + E_{\text{zpe}} \,, \tag{2.59}$$

where in our thesis E_{edf} will be computed using the BCPM (E_{BCPM}) or the Gogny (E_{Gogny}) EDF. The next sections of this thesis are devoted to a brief explanation of how the terms in Eq. (2.59) are derived.

2.3.1 Gogny energy functional

The Gogny force is an effective non-relativistic finite-range potential whose central part simulating the short and intermediate interaction is formed by a linear combination of two Gaussians. The original formulation of the potential reads [41]:

$$\begin{aligned} \hat{V}_{12}(\boldsymbol{r}_1, \boldsymbol{r}_2) = & \sum_{i=1,2} (W_i + B_i \hat{P}_\sigma - H_i \hat{P}_\tau - M_i \hat{P}_\sigma \hat{P}_\tau) e^{-\frac{(\boldsymbol{r}_1 - \boldsymbol{r}_2)^2}{\mu_i^2}} \\ & + i W_{LS} (\boldsymbol{\sigma}_1 + \boldsymbol{\sigma}_2) \cdot \left[\overleftarrow{\boldsymbol{\nabla}}_{12} \delta(\boldsymbol{r}_1 - \boldsymbol{r}_2) \times \overrightarrow{\boldsymbol{\nabla}}_{12} \right] \\ & + t_0 (1 + x_0 \hat{P}_\sigma) \rho^\alpha \left(\frac{\boldsymbol{r}_1 + \boldsymbol{r}_2}{2} \right) \delta(\boldsymbol{r}_1 - \boldsymbol{r}_2) \,, \end{aligned} \tag{2.60}$$

where W_i, B_i, H_i, M_i, μ_i, W_{LS}, t_0, x_0 and α form a set of 14 parameters that can be adjusted to reproduce properties of nuclear matter and finite nuclei. The first term on the right-hand side is the central part of the nuclear interaction including the spin-exchange $\hat{P}_\sigma$ and isospin-exchange $\hat{P}_\sigma$ operators combined in the Wigner, Majorana, Bartlett and Heisenberg terms of the bare nucleon-nucleon force. The second term is the spin-orbit coupling, being $(\boldsymbol{\sigma}_1 + \boldsymbol{\sigma}_2)$ the total spin and $\overrightarrow{\boldsymbol{\nabla}}_{12} = \overrightarrow{\boldsymbol{\nabla}}_1 - \overrightarrow{\boldsymbol{\nabla}}_2$ the relative momentum operator (by convention $\overleftarrow{\boldsymbol{\nabla}}_{12} = \overleftarrow{\boldsymbol{\nabla}}_1 - \overleftarrow{\boldsymbol{\nabla}}_2$ acts on the left). The last term is the phenomenological density-dependent term simulating the effect of three-body forces.

The spin-orbit and density-dependent terms of the Gogny potential are also found in the traditional formulation of the zero-range two-body Skyrme interaction [42, 43]. The main advantage of the Gogny potential is that due to its finite-range term the matrix elements of the pairing fields are free from ultraviolet divergences, allowing to treat on the same footing the particle-hole and the particle-particle channel without introducing an arbitrary truncation in the single particle space /citeBender2006. The energy density functional is obtained by taking the expectation value of the potential (2.60) on a Slater determinant:

$$E_{\text{Gogny}} = \langle \Phi | \hat{V}_{12} | \Phi \rangle = \int d^3\boldsymbol{r} \sum_{t=0,1} \left[\mathcal{H}_t^{\text{even}}(\boldsymbol{r}) + \mathcal{H}_t^{\text{odd}}(\boldsymbol{r}) \right] \,, \tag{2.61}$$

	i	W_i MeV	B_i MeV	H_i MeV	M_i MeV	μ_i fm	t_0 MeV fm^4	W_{LS} MeV fm^5
D1S	1	-1720.30	1300.00	-1813.53	1397.60	0.7	1390.60	-130
	2	103.64	-163.48	162.81	-223.93	1.2		
D1N	1	-2047.61	1700.00	-2414.93	1519.35	0.8	1609.46	115
	2	293.02	-300.78	414.59	-316.84	1.2		
D1M	1	$-12\,797.57$	14 048.85	$-15\,144.43$	11 963.89	0.5	1562.22	115.36
	2	490.95	-752.27	675.12	-693.57	1.0		

Table 2.1: Values of the D1S, D1N and D1M interactions for the Gogny potential (2.60). In all the interactions $x_0 = 1$ and $\alpha = 1/3$.

where the sum runs over the isoscalar ($t = 0$) and isovector ($t = 1$) energies. The energy densities $\mathcal{H}_t^{\text{even}}(\boldsymbol{r})$ and $\mathcal{H}_t^{\text{odd}}(\boldsymbol{r})$ collect the contributions from time-even and time-odd densities respectively, even though both terms have a positive time-parity, and they are expressed as integrals of the non-local density $\rho(\boldsymbol{r}, \boldsymbol{r}')$ over $\boldsymbol{r}'$. In stationary calculations of even-even nuclei the time-odd densities vanish, and therefore only $\mathcal{H}_t^{\text{even}}(\boldsymbol{r})$ contributes.

In this thesis we will explore the fission properties of the D1S [44], D1N [45] and D1M [46] parametrizations of the Gogny interaction. The D1S EDF is nowadays the most popular Gogny interaction in fission calculations. It was derived from the former D1 interaction in order to properly describe the fission barriers in actinides by reducing the surface energy, whose coefficient a_s was found to be too high in the D1 functional. Despite of the great improvement in describing the fission barriers, the D1S functional suffers from a “drift” in the difference between experimental and theoretical binding energies, which means that it underbinds the heavier nuclei compared to the lighter ones. The D1N and D1M interactions were then proposed in order to improve the prediction of the binding energies and remove this drift. Firstly, the D1N EDF was adjusted to reproduce the Equation of State (EoS) of neutron matter obtained from the Argonne bare nucleon-nucleon potential [47], with a fair agreement up to 1.5 times the saturation density $\rho_0 = 0.16\,\text{fm}^{-3}$. Afterwards, the D1M functional was fitted in order to reproduce all the experimental masses of the AME2013 mass table evaluation [48] with a total rms deviation of 0.8 MeV.

Table 2.1 shows the values of the 14 parameters used in the D1S, D1N and D1M parametrizations of the Gogny potential. It is important to recall that all the functionals were fitted to experimental data using mean-field calculations. On one hand this procedure should limit the selection of the possible observables used in the fit to those that are not strongly affected by beyond mean-fields correlations. At the same time, one should be aware of possible variations in the agreement between theoretical calculations and experimental data when beyond mean-field calculations are applied.

2.3.2 Barcelona Catania Paris Madrid energy functional

As we explained at the beginning of this section the traditional approach in NEDF is to derive the energy functional from the expectation value of an effective two-body potential. However nothing forbids to derive an expression of $E[\mathcal{R}]$ by directly parametrizing it as a function of the density. This alternative approach, closer to the spirit of the Kohn-Sham density functional theory (KS-DFT) [49], is at the heart of the Barcelona Catania Paris Madrid (BCPM) EDF [50] used in this thesis.

As it was introduced at the beginning of this section, in the KSDFT the density of a system of interacting particles is obtained from a configuration of non-interacting particles moving under an external local effective potential (the Kohn potential). The energy functional is then split in the uncorrelated kinetic energy of the nucleons $E_K[\rho]$ and the potential energy plus the correlated kinetic energy $W[\rho]$. In nuclear calculations the latter term is given by the sum of the spin-orbit contribution E_{so}, the Coulomb interaction between charges in the nucleus E_C and the nuclear contribution E_{int}. In order to properly describe the nuclear properties of open shell nuclei, pairing correlations are included using a zero-range density-dependent term. The forms of the kinetic and Coulomb contributions are the same as those used in the Gogny density functional and they will be treated explicitly in Sec. (2.3.3) and Sec. (2.3.4), where in this section we will restrict our discussion to the functional:

$$E_{\text{BCPM}} = E_{\text{int}} + E_{so} + E_{\text{pp}} \,. \tag{2.62}$$

The nuclear energy density functional

The nuclear energy density functional $E_{\text{int}}[\rho_p, \rho_n]$ contains the nuclear potential energy contribution and additional correlations of the potential energy. It is divided in a bulk term $E^{\infty}_{\text{int}}[\rho_p, \rho_n]$ given by a polynomial fit to realistic equations of state in both symmetric and nuclear matter and a surface term $E^{\text{FR}}_{\text{int}}[\rho_p, \rho_n]$ describing the finite size effect in nuclei

$$E_{\text{int}}[\rho_p, \rho_n] = E_{\text{int}}[\rho_p, \rho_n] + E^{\text{FR}}_{\text{int}}[\rho_p, \rho_n] \,. \tag{2.63}$$

The explicit expression of the EDF bulk part is:

$$E^{\infty}_{\text{int}}[\rho_p, \rho_n] = \int d^3\boldsymbol{r} \left[P_s(\rho(\boldsymbol{r}))(1-\beta^2) + P_n(\rho(\boldsymbol{r}))\beta^2 \right] \rho(\boldsymbol{r}) \tag{2.64}$$

where $\rho(\boldsymbol{r}) = \rho_n(\boldsymbol{r}) + \rho_p(\boldsymbol{r})$ is the total density and $\beta(\boldsymbol{r}) = (\rho_n(\boldsymbol{r}) - \rho_p(\boldsymbol{r}))/\rho(\boldsymbol{r})$ the asymmetry parameter. The interpolating polynomials to symmetric nuclear matter P_s ($\beta = 0$) and neutron matter P_n ($\beta = 1$) read:

$$P_s(\rho) = \sum_{n=1}^{5} a_n \left(\frac{\rho(\boldsymbol{r})}{\rho_0} \right)^n \; ; \quad P_n(\rho) = \sum_{n=1}^{5} b_n \left(\frac{\rho(\boldsymbol{r})}{\rho_{0n}} \right)^n \,, \tag{2.65}$$

being the nuclear saturation density $\rho_0 = 2/(3\pi^2)k_F^3 = 0.16\,\text{fm}^{-3}$ and $\rho_{0n} = 0.155\,\text{fm}^{-3}$. The coefficients a_n and b_n are adjusted in order to reproduce state-of-the-art microscopic Equation of State (EoS) in pure neutron and symmetric nuclear matter (see [51] and references therein).

The other term of the nuclear potential is a phenomenological finite-range Gaussian interaction that is included to account for finite-size effects:

$$E^{FR}_{\text{int}}[\rho_n, \rho_p] = \frac{1}{2} \sum_{t,t'} \iint d^3\boldsymbol{r}\, d^3\boldsymbol{r}'\, \rho_t(\boldsymbol{r})\, v_{t,t'}(\boldsymbol{r} - \boldsymbol{r}')\rho_{t'}(\boldsymbol{r}') \,, \tag{2.66}$$

where $t, t' = n, p$ run over the isospin channels and the form factor

$$v_{t,t'}(\boldsymbol{r}) = V_{t,t'} e^{-r^2/r^2_{t,t'}} \tag{2.67}$$

only distinguishes between like and unlike particles:

$$V_{n,n} = V_{p,p} = V_L = \frac{2\tilde{b}_1}{\pi^{3/2} r_L^3 \rho_0} \; ; \quad V_{n,p} = V_{p,n} = V_U = \frac{4a_1 - 2\tilde{b}_1}{\pi^{3/2} r_U^3 \rho_0} \,, \tag{2.68}$$

where a_1 and $\tilde{b}_1 = b_1\rho_0/\rho_{0n}$ are the first coefficients in Eq. (2.65). From the expressions above it turns out that the only free parameters in the BCPM EDF are the r_L and r_U ranges of the Gaussian interaction and the additional W_{LS} term of the spin-orbit term taken as in Eq. (2.60). However in [51] it was argued that W_{LS} is not a parameter that has to be adjusted since the spin-orbit strength depends on the major energy shells energy separation, that is inversely proportional to the inverse of the effective mass m^*. The value of W_{LS} can then be fixed from the beginning, and the effective free parameters in the BCPM interaction are then reduced to r_L and r_U.

r_L (fm)	r_U (fm)	W_{LS} (MeV fm^5)
0.659	0.659	90.58

Table 2.2: Values of the parameters of the BCPM energy density functional.

Pairing interaction

The term of the nuclear energy functional contributing to the particle-particle (pp) channel $E_{pp}[\rho, \kappa, \kappa^*]$ is usually obtained as the expectation value of an effective two-body potential. While functionals based in the Gogny potential are free from ultraviolet divergences in the pp channel and can use the same expression of the potential in both the pp and particle-hole (ph) channels, for BCPM as well as Skyrme models an explicit ansatz of this interaction describing the short-range correlations has to be guessed. The pairing functional used in the BCPM EDF is the widely used density-dependent zero-range force given by the potential [52]:

$$\hat{V}_{pp}(\rho(\boldsymbol{r}, \boldsymbol{r}')) = \frac{v_0}{2}(1 - \hat{P}_\sigma)\left[1 - \gamma\left(\frac{\rho((\boldsymbol{r}+\boldsymbol{r}')/2)}{\rho_0}\right)^\alpha\right]\delta(\boldsymbol{r}-\boldsymbol{r}')\,, \tag{2.69}$$

being $v_0 = 481\,\text{MeV fm}^3$, $\gamma = 0.70$ and $\alpha = 0.45$ the adjustable parameters used to reproduce the $T = 1$ pairing gap in nuclear matter computed with the Gogny D1 force [53]. The saturation density $\rho_0 = 0.16\,\text{fm}^3$ correspond to the average density distribution inside the nucleus, and therefore the γ parameter controls whether the pairing force is more active in the surface ($\gamma \to 0$ and therefore $\hat{V}_{pp} \approx 0$ if $\rho = \rho_0$) or in the volume ($\gamma \to 1$ with $\hat{V}_{pp} \approx v_0\delta(\boldsymbol{r}-\boldsymbol{r}')$) of the nucleus [37].

The free parameters r_L, r_U and V_{LS} of the BCPM EDF were fitted in order to reproduce the experimental binding energies of the even-even nuclei of the Atomic Mass table Evaluation (AME2003) of Audi and Wapstra [48]. Table 2.2 shows the value of the BCPM parameters leading to a root mean square deviation of 1.58 MeV for the masses and 0.027 fm for the radius of 579 nuclei. It is remarkable that this deviations are similar to those obtained by several Gogny and Skyrme models where several parameters (usually more than ten) where used in the fitting protocol of the interactions.

2.3.3 Kinetic energy

The uncorrelated kinetic energy functional reads:

$$E_k = \frac{\hbar^2}{2m}\sum_i \int d^3\boldsymbol{r}|\nabla\varphi_i(\boldsymbol{r})|^2\,, \tag{2.70}$$

where φ_i are the single particle wave functions defining the local density:

$$\rho(\boldsymbol{r}) = \sum_i |\varphi_i(\boldsymbol{r})|^2\,. \tag{2.71}$$

We are implicitly considering one type of nucleon, and therefore the total kinetic energy is obtained from the contribution of both protons and neutrons $\rho = \rho_p + \rho_n$ and $E_k = E_{k,p} + E_{k,n}$. This contribution is equivalent to the term $\text{tr}(t\rho)$ in Eq. (2.53), being t the one-body kinetic operator.

2.3.4 Coulomb energy

In nuclear structure calculations the modeling of the strong interaction has to be supplemented by the electrostatic interaction between protons in the nucleus:

$$E_C = \frac{e^2}{2}\int d^3\boldsymbol{r}\, d^3\boldsymbol{r}'\,\frac{|\rho_{\text{ch}}(\boldsymbol{r}, \boldsymbol{r}')|^2}{|\boldsymbol{r}-\boldsymbol{r}'|}\,, \tag{2.72}$$

being ρ_{ch} the charge density distribution. In nuclear structure calculations there are two main approximations that are commonly used in the evaluation of the Coulomb energy. The first approximation is to split the Coulomb interaction in a direct and an exchange term and compute the latter one in a local-density approximation using a Slater approximation. The reason for such approximation is that the calculation of the full exchange term is cumbersome, and it was argued that the contribution to the total energy is negligible at the precision of mean field calculations even though this argument is debatable [54].

The second approximation is to consider the protons as point-like particles, which allows to replace the charge density distribution for the proton density distribution $\rho_{\mathrm{ch}} \approx \rho_{\mathrm{p}}$. As we alread mentioned at the beginning of this section this approximation does not allow for a proper calculation of the charge form factor that is experimentally measured.

Taking these two approximations into account, the final expression of the Coulomb energy functional reads:

$$E_C = E_C^{\mathrm{dir}} + E_C^{\mathrm{exc}} = \frac{e^2}{2}\int d^3\boldsymbol{r}\, d^3\boldsymbol{r}'\, \frac{\rho_p(\boldsymbol{r})\rho_p(\boldsymbol{r}')}{|\boldsymbol{r}-\boldsymbol{r}'|} + \frac{3e^2}{4}\left(\frac{3}{\pi}\right)^{1/3}\int d^3\boldsymbol{r}\, \rho_p^{4/3}(\boldsymbol{r}). \tag{2.73}$$

It is important to recall that depending on the energy density functional the fitting of the free parameters can be done using either any of the approximations above described or the exact calculation of the Coulomb energy, and that the agreement with experimental data would change if calculations are not performed with the same prescription.

2.3.5 Restoration of broken symmetries and zero-point energy corrections

At the mean-field level long-range correlations are included in the many-body wavefunction by an explicit breaking of many nuclear symmetries. These broken symmetries should then be restored in beyond mean-field calculations by projecting the wave function on good quantum numbers $|\Phi_P\rangle = \prod_s \hat{P}_s |\Phi\rangle$, and the expectation value of any operator is then obtained using the projected wave functions. For example, the expectation value of energy now reads:

$$E_{\mathrm{PAV}} = \frac{\langle\Phi_0|\, \hat{P}^\dagger \hat{H} \hat{P}\, |\Phi_0\rangle}{\langle\Phi_0|\, \hat{P}^\dagger \hat{P}\, |\Phi_0\rangle}\,, \tag{2.74}$$

where $|\Phi_0\rangle$ is the many-body wavefunction obtained from the HFB equations minimizing the total energy. This method is known as Projection After Variation (PAV) since the variational space is formed by the wavefunctions obtained at the mean-field level. The PAV has the main drawback that the minimized HFB state Φ_0 may not correspond to the true ground-state if restoration of symmetries is taken into account before the projection. A more complete approach is then the Variation after Projection (VAP), where the projected wavefunctions are used as a variational space for the minimization of the energy:

$$\delta(E_{\mathrm{VAP}}) = \delta\left(\frac{\langle\Phi|\, \hat{P}^\dagger \hat{H} \hat{P}\, |\Phi\rangle}{\langle\Phi|\, \hat{P}^\dagger \hat{P}\, |\Phi\rangle}\right) = 0\,. \tag{2.75}$$

Obviously the variational space used in VAP is larger than in PAV, and therefore the VAP ground-state energy should be closer to the exact one than the PAV.

The restoration of symmetries is a daunting task in systematic calculations of nuclear properties. Moreover the projected states are a linear combination of HFB states which brings further complications like for instance the assignment of a density to those states. A less expensive approach is then to compute the demanded observable using the HFB wavefunctions as a variational space and afterwards subtract the contribution from the spurious modes related with the broken symmetries. In this thesis we will mainly deal with spurious modes contributing to the total energy stemming from the rotational and translational symmetries.

Translational symmetry restoration

The translational symmetry is broken because the mean field is localized in space, and in order to restore it one has to subtract the kinetic energy of the center-of-mass from the total energy. It is important to notice that this symmetry must be restored in all the nuclei obtained at the mean-field level. Its contribution is often computed using the expression

$$E_{cm} = \frac{\langle \Phi_0 | \hat{\boldsymbol{P}}^2 | \Phi_0 \rangle}{2mA} \quad \text{with} \quad \hat{\boldsymbol{P}} = \sum_i^N \hat{\boldsymbol{p}}_i \, , \tag{2.76}$$

where $\hat{\boldsymbol{P}}$ is the total momentum operator given as the sum of the single-particle momentum operators and m is the averaged nucleon mass. This expression is an approximation obtained from the real projection within the Gaussian Overloap Approximation that improves with increasing mass number, at the same time that the total energy correction decreases. Both Gogny and the BCPM EDF where fitted taking into account this approximation of the translational symmetry restoration.

Rotational symmetry restoration

The energy correction stemming from projecting the many-body state onto a good angular momentum can be computed using the expression [55]:

$$E_{\text{rot}} = -\frac{\langle \Phi_0 | \hat{\boldsymbol{J}}^2 | \Phi_0 \rangle}{2\mathcal{J}} \tag{2.77}$$

where $\mathcal{J}$ is the Yoccoz moment of inertia [56]. As we will see in the next chapter, this correction plays an important in fission calculations since it increases with the quadrupole deformation up to several MeV modifiyng the final shape of the barrier. The problem of the approximation Eq. (2.77) is that it can produce some artifacts in the binding energies of spherical nuclei close to the shell closures (see Sec. 6.2).

2.4 Description of odd nuclei

The estimation of nuclear properties of systems with an odd number of protons and/or neutrons is one of the most critical issues in self-consistent mean-field models. In such systems the HFB theory has to be extended in order to properly describe both bosonic degrees of freedom of nucleons pairing in Cooper pairs as well as fermionic degrees of freedom related to the unpaired nucleon. Blocking techniques are then required in order to properly compute the HFB wavefunction for the odd system $|\Phi_{\text{odd}}\rangle_\alpha = \beta_\alpha^\dagger |\Phi_{\text{even}}\rangle$ with an explicit breaking of the time reversal invariance [57]. Due to this, a self-consistent solution for odd-even and odd-odd nuclei obtained on the same footing of even-even nuclei becomes rather expensive from the computational point of view and therefore difficult to be implemented in systematic calculations.

For this reason, a good compromise in systematic calculations is to use a phenomenological approach aimed to reproduce the experimental bulk nuclear properties of odd-even and odd-odd nuclei. In this thesis, we computed the bulk nuclear properties of odd nuclei using the Perturbative Nucleon Addition Method (PNAM) [58]. Within this phenomenological scheme, the self-consistent energy of the nucleus is obtained by constraining the many-body wave function to have the desired particles number. After that, the overbinded energy is corrected by adding the lowest proton(neutron) quasiparticle excitation if the nucleus has an odd number of protons(neutrons). For odd-odd nuclei, both the proton and neutron lowest quasiparticle energies are added.

As it will be shown in Sec. 6.2, by adopting the PNAM method BCPM maintains the same level of accuracy achieved for even-even nuclei in the calculation of nuclear binding energies and fission properties when odd-even and odd-odd nuclei are included. However, this method has some severe limitations. The most important one in the framework of this thesis regards the calculation of the collective inertias extensively discussed in Chapter 3. Since the PNAM neglects the enhancement of collective inertias due to the quenching of pairing correlations in systems with unpaired nucleons [59], it may lead to a possible underestimation of spontaneous fission lifetimes of nuclei with an odd number of neutrons and/or protons.

3 Fission within the energy density functional formalism

Two of the main goals of this thesis were the study of the fission properties of superheavy nuclei and the improvement of the theoretical description of the fission process. The energy density functional provides nowadays the most microscopic framework for describing this process, and its wide applicability allows systematic calculations in a broad region of the nuclear chart. This Chapter is thus devoted to the current theoretical description of the fission process within the energy density functional model. We will start introducing the Wentzel–Kramers–Brillouin (WKB) approximation employed for the derivation of the action integral and the calculation of fission probabilities. Then we will present the derivation of the collective inertias within the different schemes employed in this thesis and the approximations used in their numerical calculations. Finally, the last part of the Chapter is devoted to the potential energy and the most common collective degrees of freedom used in fission calculations.

3.1 A semiclassical picture for fission

Despite its discovery dates almost 80 years ago, nowadays fission is one of the least understood nuclear processes. Defined as the process where a nucleus splits in two or more fragments with a comparable mass, fission is the consequence of the competition between the Coulomb repulsion of protons in the nucleus and the strong interaction acting against the increase of the mean distance between nucleons. It is a dynamical process, where the probability P of a nucleus in a state $|\Phi_i\rangle$ to evolve in time towards a two fragments configuration $|\Phi_f\rangle$ can be formally written as [36]:

$$P = \left| \langle \Psi_f | \, \hat{U}(t_f, t_i) \, | \Psi_i \rangle \right|^2 , \tag{3.1}$$

being $\hat{U}(t_i, t_f)$ the time evolution operator. As already introduced in the previous chapter, solving this kind of problems in nuclear physics using pure quantum mechanical rules is prohibitive due to the difficulties in describing a many-body system formed by a large number of interacting nucleons. Thus fission must be simplified to a more manageable problem and connected to the nuclear structure picture given by the self-consistent mean-field model.

The work presented in this thesis is grounded in two main approximations that are widely used in fission calculations. The most important one is the assumption that the huge number of internal degrees of freedom of the system can be reduced to a small set of collective variables. This simplification, known as "adiabatic approximation", is based on the separation of scales between the fast movement of nucleons inside the nucleus and the relative slow collective motion characterizing the fission process. The second main approximation is to assume that the fission probability can be obtained as the probability of the nucleus to penetrate a classically-forbidden potential barrier (the so-called "fission barrier") and this probability can be computed using the Wentzel–Kramers–Brillouin (WKB) approximation. This semiclassical approach allows to maximize the event probability by minimizing the action integral.

These two approximations are based on very strong assumptions and they basically forbid the description of fission from a pure microscopic ground. Some alternative approaches like the time dependent density functions theory are making inroads, but nowadays their application to systematic calculations is unworkable (see [36] for a general review of these methods). While waiting for the development of models based on a more microscopic ground, we shall rely on the WKB method to compute the probability of a nucleus to fission.

This Chapter is based on Ref. [38] and [36]

3.2 Action integral and fission transmission coefficient

3.2.1 The Wentzel–Kramers–Brillouin (WKB) approximation

The Wentzel–Kramers–Brillouin (WKB) approximation is a mathematical method allowing the calculation of an approximate solution to linear differential equation with spatially varying coefficients. For the problem of quantum tunneling in one dimension the starting point is the non-relativistic time-independent Schrödinger equation written in the form:

$$\left(-\frac{\hbar}{2m}\frac{\partial^2}{\partial x^2}+V(x)\right)\Psi(x)=E\Psi(x)\,, \tag{3.2}$$

being $p=\sqrt{2m[E-V(x)]}$ the classical momentum of a particle with energy E moving in a one-dimensional potential $V(x)$. Assuming that the wave function can be written in the exponential form

$$\Psi(x)=A(x)e^{i\varphi(x)}\,, \tag{3.3}$$

the WKB approximation allows to find an approximate solution by assuming that $V(x)$ varies slowly compared to the wavelength $\lambda=2\pi\hbar/p(x)$ (or, equivantely, to the decay length $l=\hbar/\sqrt{2m[V(x)-E]}$ if $E<V(x)$). The transmission coefficient T of a particle tunneling under the potential $V(x)$ is thus given by [60]:

$$T=|\Psi(b)|^2/|\Psi(a)|^2=\exp\left(-\frac{2}{\hbar}\int_a^b dx\sqrt{2m[V(x)-E]}\right)\equiv\exp(-2S), \tag{3.4}$$

where a and b are the classical turning points ($E=V(a)=V(b)$) and according to the initial definition the momentum $p=\sqrt{2m[E-V(x)]}=i\sqrt{2m[V(x)-E]}$ is now complex.

3.2.2 Extension of the WKB approach to spontaneous fission

The extension of the WKB approximation to fission is only possible when one considers a scale separation between the internal degrees of freedom of the nucleus and the collective variables determining the fission process. This hypothesis of adiabaticity allows to determine the fission path by minimizing the action integral S in the reduced multidimensional space given by the collective degrees of freedom. Within this semiclassical framework the least action principle is then invoked in order to maximize the tunneling probability of the nucleus. Another important aspect is the conversion of the quantities entering in Eq. (3.4) to their equivalent in the context of nuclear fission. In Sections 3.3 and 3.4 we will see that the role of the mass m is played by the collective inertia $\mathcal{M}$ which naturally arises in the context of the Generator Coordinate Method (GCM) and the Adiabatic Time Dependent HFB (ATDHFB) theory. The potential $V(x)$ is the HFB energy $\mathcal{V}$ of the nucleus computed along the fission path corrected by quantum effects stemming from symmetry restorations. Finally, the energy E is the ground-state energy of the nucleus E_{GS} plus an energy correction E_0 associated to the dynamics of the collective degrees of freedom.

Once all the quantities of the action integral S are established, the spontaneous fission lifetime can be computed as the inverse of the penetration probability P multiplied by the number of assaults n on the fission barrier per unit time [61, 62]:

$$t_{\mathrm{sf}}[s]=\frac{\ln 2}{nP}=2.86\times10^{-21}(1+\exp(2S))\,, \tag{3.5}$$

and the action integral S reads:

$$S(L) = \int_a^b ds \sqrt{2\mathcal{M}(s)[\mathcal{V}(s) - (E_0 + E_{\mathrm{GS}})]}\,. \tag{3.6}$$

The number of assaults n is given by the frequency of vibration in the fission degrees of freedom $n = \omega/2\pi$ and it is customary to assume $\hbar\omega = 1\,\mathrm{MeV}$ [61]. The action integral Eq. (3.6) is computed along the fission path $L(s)$ obtained by the least action principle and ds is the element length along L. As we will see in Sec. 3.5, the choice of the collective degrees of freedom as well as the approximations involving collective inertias and potential energy have a strong impact in determining the fission path L. Since the action integral enters in the exponential of the spontaneous fission lifetimes these variations may have a tremendous impact in the final value of t_{sf}, specially in nuclei that are stable against the spontaneous fission process and the value of $S(L)$ is large. Finally, when comparing theoretical calculations with experimental data, one should always keep in mind that the WKB formula (3.5) allows to compute the spontaneous fission lifetimes only with a logarithmic precision.

3.2.3 Fission from excited states

The neutron-, β- and photo- induced fission occurring during the r-process nucleosynthesis, the synthesis of superheavy nuclei in the laboratories and the experimental determination of the fission barriers are just some examples of nuclei undergoing fission from excited states. While there are several studies exploring the change of shape of the fission barriers at finite temperature, only few attempts investigated the dependence of the barriers with the excitation energy. Configuration-constrained calculations of the potential energy exploring multi-quasiparticle states [63] or the Time Dependent Density Functional Theory (TDDFT) methods [64] can consistently tackle the problem from a microscopic description, but their extension to systematic calculations is still not feasible. The alternative is then to use a simpler treatment and assume that the shape of the barrier does not change with the excitation energy of the nucleus. This approximation allows to obtain the probability of a nucleus to fission from an excited state with energy E^* by computing the fission barrier from the ground state and then replacing E_0 with E^* in Eq. (3.6). Besides the very strong assumption of a static barrier, one should keep in mind that the WKB is only valid for energies sufficiently below the potential barrier, and therefore its application to excited states close to the top of the barrier is rather uncertain [38].

3.3 Collective inertias

Collective inertias $\mathcal{M}$ are a key ingredient in the calculation of fission probabilities and in the case of spontaneous fission constitute one of the major source of uncertainties in the estimation of the lifetimes. They represent the resistance of the nucleus against deformations in the collective space and are associated to the momentum of the collective degrees of freedom mapping the fission path. Nowadays there exist two microscopic schemes devoted to the calculation of this quantity: the Generator Coordinate Method and the Adiabatic Time-Dependent Hartree-Fock-Bogolyubov approximation. In this section we will show how collective inertias can be derived from these two approaches, and the different approximations used for their numerical estimation. For the sake of comparison, we will also introduce the semiempirical mass formula employed in all the previous calculations of fission cross sections.

3.3.1 The Generator Coordinate Method (GCM)

In the Generator Coordinate Method (GCM) the correlated many-body states are constructed as a coherent superposition of independent particle states that are continuous functions of a finite set of coordinates. For this purpose the many body wavefunction is expanded in terms of known many-body states as:

$$|\Psi\rangle = \int d\boldsymbol{q}\, f(\boldsymbol{q})|\Phi(\boldsymbol{q})\rangle, \tag{3.7}$$

where $|\Phi(\boldsymbol{q})\rangle$ can be HFB states constrained by a finite set of collective variables such that:

$$\langle\Phi(\boldsymbol{q})|\,\hat{Q}_\alpha\,|\Phi(\boldsymbol{q})\rangle = q_\alpha \quad \text{with} \quad \{\boldsymbol{q}\} = \{q_1,\ldots,q_N\}\,. \tag{3.8}$$

The expansion coefficients $f(\boldsymbol{q})$ are obtained by means of the variational principle leading to the well-known Hill-Wheeler integral equation [65]:

$$\int d\boldsymbol{q}'\; h(\boldsymbol{q},\boldsymbol{q}')n(\boldsymbol{q},\boldsymbol{q}')f(\boldsymbol{q}') = E\int d\boldsymbol{q}'\; n(\boldsymbol{q},\boldsymbol{q}')f(\boldsymbol{q}')\,, \tag{3.9}$$

where the norm and energy kernels are given by:

$$n(\boldsymbol{q},\boldsymbol{q}') = \langle\Phi(\boldsymbol{q})|\Phi(\boldsymbol{q}')\rangle\,, \quad h(\boldsymbol{q},\boldsymbol{q}') = \frac{\langle\Phi(\boldsymbol{q})|\hat{H}|\Phi(\boldsymbol{q}')\rangle}{\langle\Phi(\boldsymbol{q})|\Phi(\boldsymbol{q}')\rangle}\,. \tag{3.10}$$

The GOA scheme and the collective Schrödinger equation

For the following discussion it will be useful to introduce the variables $\bar{\boldsymbol{q}} = (\boldsymbol{q}+\boldsymbol{q}')/2$ and $\boldsymbol{s} = \boldsymbol{q}-\boldsymbol{q}'$. The Gaussian Overlap Approximation consists in assuming that the norm kernel has the Gaussian form:

$$n(\boldsymbol{q},\boldsymbol{q}') = n(\bar{\boldsymbol{q}}+\boldsymbol{s}/2,\bar{\boldsymbol{q}}-\boldsymbol{s}/2) = \langle\Phi(\bar{\boldsymbol{q}})|\exp\left(-\frac{1}{2}\sum_{ij}G_{ij}(\bar{\boldsymbol{q}})s_is_j\right)|\Phi(\bar{\boldsymbol{q}})\rangle\;, \tag{3.11}$$

where G_{ij} is the overlap width that can be expressed in terms of the momentum operator $P_i = \partial/\partial q_i$:

$$G_{ij}(\boldsymbol{q}) = \langle\Phi(\boldsymbol{q})|\,\frac{\overleftarrow{\partial}}{\partial q_i}\frac{\overrightarrow{\partial}}{\partial q_j}\,|\Phi(\boldsymbol{q})\rangle \quad \text{with} \quad i,j=1,\ldots,N. \tag{3.12}$$

The GOA assumption is justified by the fact that the norm overlap $n(\boldsymbol{q},\boldsymbol{q}')$ is a sharply peaked function at $\boldsymbol{s}=0$ and that smoothly depends on $\bar{\boldsymbol{q}}$. This approximation allows to get an expression for the collective inertias from the GCM theory by reducing the Hill-Wheeler equation to a collective Schrödinger equation [65]:

$$\left(-\frac{\hbar^2}{2}\frac{\partial}{\partial\boldsymbol{q}}B_{\mathrm{GCM}}(\boldsymbol{q})\frac{\partial}{\partial\boldsymbol{q}} + V(\boldsymbol{q}) - \epsilon_{\mathrm{zpe}}(\boldsymbol{q})\right)g_\sigma(\boldsymbol{q}) = \epsilon_\sigma g_\sigma(\boldsymbol{q})\,, \tag{3.13}$$

being ϵ_σ the collective mode energies and $g_\sigma(\boldsymbol{q})$ the collective wavefunctions given by the amplitudes $f(\boldsymbol{q})$:

$$f_\sigma(\boldsymbol{q}) = \int d\boldsymbol{q}' n(\boldsymbol{q},\boldsymbol{q}')^{-1/2}g_\sigma(\boldsymbol{q}')\,. \tag{3.14}$$

The collective inertia B_{GCM} in Eq. (3.13) is a rank two tensor whose terms are given by the second derivative of the energy kernel [38]:

$$B^{ij}_{\mathrm{GCM}}(\boldsymbol{q}) = \frac{1}{2\hbar^2}G^{ij}(\boldsymbol{q})\left(\frac{\partial^2 h(\boldsymbol{q},\boldsymbol{q}')}{\partial q^k\partial q'^l} - \frac{\partial^2 h(\boldsymbol{q},\boldsymbol{q}')}{\partial q^k\partial q^l}\right)_{q=q'}G^{lj}(\boldsymbol{q})\,, \tag{3.15}$$

where we have assumed a constant value of the Gaussian width G_{ij} and defined its inverse as $\sum_i G_{ji}G^{ik} = \delta_j^k$. The term ϵ_{zpe} is an energy correction related to quantal fluctuations in the collective degrees of freedom $\boldsymbol{q}$:

$$\epsilon_{\text{zpe}}(\boldsymbol{q}) = \frac{1}{2} G^{ij}(\boldsymbol{q}) \frac{\partial^2 h(\boldsymbol{q}, \boldsymbol{q}')}{\partial q^i \partial q'^j}\bigg|_{q=q'} . \tag{3.16}$$

This energy is subtracted from the total HFB energy $V(q)$ and therefore can be interpreted similarly to the spurious contributions arising from the symmetry breaking described in Sec. 2.3.5.

The interesting analogy emerging from the comparison of Eqs. (3.2) and (3.13) is that if the degrees of freedom driving the evolution of the nucleus collective are the collective variables describing the fission process, then the probability to penetrate the potential barrier is given by the WKB formula where the mass of the system is the collective mass $\mathcal{M} \equiv B_{\text{GCM}}^{-1}$ and the potential barrier is the HFB energy with the zero-point energy correction ϵ_{zpe}, and the action integral can be written as Eq. (3.6).

Perturbative (local) cranking approximation

In order to evaluate the collective inertia B_{GCM} (3.15) one has to compute the derivatives defining the Gaussian width and those of the energy kernel. In the perturbative approximation, instead of performing a numerical differentiation the collective inertias (3.15) are reduced to a local expression in the coordinate space that only depends on $\boldsymbol{q}$ (for this reason the perturbative approximation is also known as local approximation). This is done by introducing the "momentum" operator of the collective variable q_α as:

$$\hat{P}_\alpha \left|\Phi\right\rangle = -i\hbar \frac{\partial}{\partial q_\alpha} \left|\Phi\right\rangle . \tag{3.17}$$

The action of the momentum operator on the HFB state is obtained by using the Ring and Schuck theorem [39] and expanding the HFB equation around $\boldsymbol{q} + \delta\boldsymbol{q}$ up to first order in $\delta\boldsymbol{q}$. Using the perturbative approximation we can thus reformulate the Gaussian width in terms of the quasiparticle matrix elements of the collective variables q_α^{20} defined in Eq. (2.51c):

$$G_{\alpha\beta}(\boldsymbol{q}) = \sum_{\kappa\lambda} \frac{1}{2} \left[M^{(-1)}(\boldsymbol{q})\right]^{-1}_{\alpha\kappa} M^{(-2)}_{\kappa\lambda}(\boldsymbol{q}) \left[M^{(-1)}(\boldsymbol{q})\right]^{-1}_{\lambda\beta} , \tag{3.18}$$

where the moments M^{-n} are defined as:

$$M^{(-n)}_{\alpha\beta} = \left(q_\alpha^{20\dagger}, q_\alpha^{20\,T}\right) \mathscr{M}^{-n} \begin{pmatrix} q_\beta^{20} \\ q_\beta^{20\,*} \end{pmatrix} . \tag{3.19}$$

In the equation above we have introduced the linear response matrix $\mathscr{M}$:

$$\mathscr{M} = \begin{pmatrix} A_{\mu\nu\mu'\nu'} & B_{\mu\nu\mu'\nu'} \\ B^*_{\mu\nu\mu'\nu'} & A^*_{\mu\nu\mu'\nu'} \end{pmatrix} , \tag{3.20}$$

whose elements are the quasiparticle energies E_i and the residual quasiparticle interaction:

$$A_{\mu\nu\mu'\nu'} = (E_\mu - E_\nu)\delta_{\mu\mu'}\delta_{\nu\nu'} + 2\frac{\partial^2 E}{\partial \rho_{\mu\nu} \rho_{\mu'\nu'}} , \tag{3.21a}$$

$$B_{\mu\nu\mu'\nu'} = 2\frac{\partial^2 E}{\partial \rho_{\mu\nu} \rho_{\mu'\nu'}} . \tag{3.21b}$$

The computation of the GCM collective inertia requires the inversion of the linear response matrix $\mathscr{M}$. Since the inversion of the full matrix is extremely expensive from a numerical point of view it is customary to alleviate this operation by neglecting the off-diagonal terms related to the residual interaction in Eq. (3.21):

$$\frac{\partial^2 E}{\partial \rho_{\mu\nu} \rho_{\mu'\nu'}} = 0\,. \tag{3.22}$$

This cranking approximation reduces the QRPA matrix (3.20) to a diagonal matrix whose elements are the single quasiparticle excitation energies:

$$\mathscr{M} = \begin{pmatrix} E_\mu - E_\nu & 0 \\ 0 & E_\mu - E_\nu \end{pmatrix}\,. \tag{3.23}$$

Within this approximation one can write the moments (3.19) as:

$$M^{(-n)}_{\alpha\beta} = \sum_{\mu<\nu} \frac{\langle \Phi | \hat{q}^\dagger_\alpha | \mu\nu \rangle \langle \mu\nu | \hat{q}_\beta | \Phi \rangle}{(E_\mu + E_\nu)^n}, \tag{3.24}$$

where $|\mu\nu\rangle = \beta^\dagger_\mu \beta^\dagger_\nu |\Phi\rangle$ is a two quasiparticle excitation with energy $E_\mu + E_\nu$ built on top of the quasiparticle vacuum $|\Phi\rangle$.

Finally, by using the perturbative approximation in addition to the cranking one the expressions of the derivatives of the energy kernels reduces to:

$$\frac{\partial^2 h(\boldsymbol{q},\boldsymbol{q}')}{\partial q_k \partial q'_l} = \frac{1}{2}\left[M^{(-1)}(\boldsymbol{q})\right]^{-1}_{kl}\ ; \quad \frac{\partial^2 h(\boldsymbol{q},\boldsymbol{q}')}{\partial q_k \partial q_l} = 0\,. \tag{3.25}$$

Replacing the equation above in Eq. (3.15) and (3.16) we finaly get the GCM collective inertias and zero-point energy correction in the perturbative cranking approximation:

$$\left(\mathcal{M}^{pc}_{\mathrm{GCM}}(\boldsymbol{q})\right)_{\alpha\beta} = \left(B^{pc}_{\mathrm{GCM}}(\boldsymbol{q})\right)^{-1}_{\alpha\beta} = 4 \sum_{\kappa,\lambda} G_{\alpha\kappa}(\boldsymbol{q}) M^{(-1)}_{\kappa\lambda}(\boldsymbol{q}) G_{\lambda\beta}(\boldsymbol{q})\,, \tag{3.26}$$

$$\epsilon(\boldsymbol{q}) = \frac{1}{2} \sum_\alpha G^{\alpha\beta}(\boldsymbol{q}) \left(B_{\mathrm{GCM}}(\boldsymbol{q})\right)_{\beta\alpha}\,. \tag{3.27}$$

In the systematic calculation of the fission properties of superheavy nuclei of Chapter 7 the only collective degree of freedom was the quadrupole deformation. In this case Eq. (3.26) and (3.27) simplify to:

$$\mathcal{M}^{pc}_{\mathrm{GCM}}(Q_{20}) = \frac{\left(M^{-2}(Q_{20})\right)^2}{2\left(M^{-1}(Q_{20})\right)^3}\,, \tag{3.28}$$

$$\epsilon^{\mathrm{GCM}}_{\mathrm{vib}}(Q_{20}) = \frac{G(Q_{20})}{\mathcal{M}^{pc}_{\mathrm{GCM}}(Q_{20})}\,. \tag{3.29}$$

3.3.2 The Adiabatic Time Dependent Hartree Fock Bogolyubov theory (ATDHFB)

In the Time Dependent Hartree-Fock-Bogolyubov Approximation (TDHFB), the many-body wave function describing the nuclear system is supposed to remain an HFB state at all times. This means that the dynamical evolution of the density can be written as [66]:

$$\dot{\mathcal{R}}(t) = -\frac{i}{\hbar}[\mathcal{H}, \mathcal{R}(t)]\,, \tag{3.30}$$

where the HFB matrix $\mathcal{H}$ (2.46) and the generalised density matrix $\mathcal{R}$ (2.41) are now time-dependent. The latter one is neither time-even nor time-odd, and therefore cannot play the role of a generalised collective coordinate or collective momentum [67]. In order to identify the matrix elements of $\mathcal{R}$ corresponding to the collective coordinates and momenta, we can decompose the density matrix in the following way:

$$\mathcal{R}(t) = e^{i\chi(t)/\hbar}\mathcal{R}_0(t)e^{-i\chi(t)/\hbar}\,, \tag{3.31}$$

where both $\chi(t)$ and $\mathcal{R}_0$ are time-even operators. From the properties of the generalised density matrix it follows that [67]:

$$\mathcal{R}_0^2 = \mathcal{R}; \quad \operatorname{tr}\mathcal{R}_0 = N\,, \tag{3.32}$$

being N the number of nucleons. In the adiabatic approximation, the one-body density $\mathcal{R}(t)$ is supposed to stay close to $\mathcal{R}_0(t)$ at all times. This means that χ and $\dot{\chi}$ are small, and we can expand the expression of the density matrix up to second order in χ:

$$\begin{aligned}\mathcal{R} &\cong \left(1+\frac{i\chi(t)}{\hbar}-\frac{\chi^2(t)}{\hbar^2}+\mathcal{O}(\chi^3)\right)\mathcal{R}_0\left(1-\frac{i\chi(t)}{\hbar}-\frac{\chi^2(t)}{\hbar^2}+\mathcal{O}(\chi^3)\right)\\ &= \mathcal{R}_0(t)+\frac{i}{\hbar}[\chi(t),\mathcal{R}_0(t)]+\frac{1}{2\hbar^2}\left[\chi(t),[\chi(t),\mathcal{R}_0(t)]\right] = \mathcal{R}_0(t)+\mathcal{R}_1(t)+\mathcal{R}_2(t)\,.\end{aligned} \tag{3.33}$$

By inserting the expression above in Eq. (3.30) we get the second-order expansion of the HFB matrix:

$$\mathcal{H}_{ab} \cong \mathcal{H}_0+\mathcal{H}_1+\mathcal{H}_2+\mathcal{O}(\chi^3)\,, \tag{3.34}$$

and by replacing both expansions (3.33) and (3.34) in the Time Dependent HFB equation (3.30) one gets the so-called ATDHFB equations:

$$i\hbar\dot{\mathcal{R}}_0 = [\mathcal{H}_0,\mathcal{R}_1]+[\mathcal{H}_1,\mathcal{R}_0]\,, \tag{3.35a}$$

$$i\hbar\dot{\mathcal{R}}_0 = [\mathcal{H}_0,\mathcal{R}_0]+[\mathcal{H}_0,\mathcal{R}_2]+[\mathcal{H}_1,\mathcal{R}_1]+[\mathcal{H}_2,\mathcal{R}_0]\,. \tag{3.35b}$$

In the ATDHFB basis the generalised density matrix $\mathcal{R}_0$ is diagonal and the parameter $\chi(t)$ can be written in the form:

$$\chi = \begin{pmatrix}\chi^{11} & \chi^{12}\\ \chi^{21} & \chi^{22}\end{pmatrix}, \tag{3.36}$$

where only the χ^{12} and χ^{21} blocks are relevant for the dynamics. In the ATDHFB basis the Eq. (3.35a) can thus be written as:

$$\hbar\begin{pmatrix}\dot{\mathcal{R}}_0^{12}\\ \dot{\mathcal{R}}_0^{12*}\end{pmatrix} = \begin{pmatrix}A & B\\ B^* & A^*\end{pmatrix}\begin{pmatrix}\chi^{12}\\ \chi^{12*}\end{pmatrix} = \mathscr{M}^{-1}\begin{pmatrix}\chi^{12}\\ \chi^{12*}\end{pmatrix}, \tag{3.37}$$

being $\mathscr{M}$ the QRPA linear response matrix of Eq. (3.20). Using the classical analogy of the velocity-momentum expression $\boldsymbol{p} = m\boldsymbol{v}$ one can associate the time-even density $\mathcal{R}(t)$ to the collective variable of the system and $\chi(t)$ to the associated collective momentum, being the inverse of the response matrix $\mathcal{R}$ the collective mass. Making use of the Wick's theorem we can now expand the energy in terms of $\mathcal{R}$ and χ [67]. By separating the terms depending on second order to χ to those depending on $\mathscr{M}$ we get an expression resembling the collective kinetic energy:

$$\begin{aligned}E(t) &= E^{(0)}(t)+E^{(1)}(t)+E^{(2)}(t)\\ &= E_{\text{HFB}}+\frac{1}{4}\left(\chi^{12\dagger}\quad\chi^{12T}\right)\mathscr{M}\begin{pmatrix}\chi^{12}\\ \chi^{12*}\end{pmatrix} = E_{\text{HFB}}+\frac{1}{4}\left(\dot{\mathcal{R}}_0^{12\dagger}\quad\dot{\mathcal{R}}_0^{12T}\right)\mathscr{M}^{-1}\begin{pmatrix}\dot{\mathcal{R}}_0^{12}\\ \dot{\mathcal{R}}_0^{12*}\end{pmatrix}\\ &\equiv E_{\text{HFB}}+\mathcal{K}\,.\end{aligned} \tag{3.38}$$

As it was already mention before, we are supposing that fission can be described using a finite set of collective variables $\mathcal{R}_0(t) = \mathcal{R}_0(\boldsymbol{q}(t)) = \mathcal{R}_0(q_1(t), \ldots, q_N(t))$. Within this assumption we can rewrite the time derivative of the density matrix in terms of the derivative respect to the collective coordinate q_α:

$$\dot{\mathcal{R}}_0 = \sum_{\alpha=1}^{N} \dot{q}_\alpha \frac{\partial \mathcal{R}_0}{\partial q_\alpha}, \tag{3.39}$$

and from the standard definition of the kinetic energy we can write the expression of the ATDHFB collective mass as:

$$\mathcal{K} = \frac{\partial \mathcal{R}_0}{\partial q_\alpha} \mathscr{M}^{-1} \frac{\partial \mathcal{R}_0}{\partial q_\beta} \dot{q}_\beta \equiv \sum_{\alpha\beta} \dot{q}_\alpha \mathcal{M}^{\mathrm{ATDHFB}}_{\alpha\beta} \dot{q}_\beta \sum_{\alpha\beta} \dot{q}_\alpha \,. \tag{3.40}$$

Perturbative cranking approximation

As in the GCM theory, the collective inertia obtained within the ATDHFB theory requires the inversion of the linear response matrix $\mathscr{M}$. The same approximations introduced in Sec. 3.3.1 can then be applied to the ATDHFB inertias in order to alleviate the computational effort in calculating such quantities. In the cranking approximation, the inversion of the linear response matrix can be simplified by neglecting the off-diagonal terms related to the residual interaction. In the perturbative approximation, the partial derivatives of the density $\mathcal{R}_0$ respect to the collective coordinate q_α are obtained applying the linear response theory, which result in an expression involving the momenta (3.19):

$$\left(\mathcal{M}^{pc}_{\mathrm{ATDHFB}}\right)_{\alpha\beta} = \hbar \sum_{\kappa\lambda} \left[M^{(-1)}\right]^{-1}_{\alpha\kappa} M^{(-3)}_{\kappa\lambda} \left[M^{(-1)}\right]^{-1}_{\lambda\beta} \,. \tag{3.41}$$

Since one part of this thesis will be devoted to study the one-dimensional case where the fission barrier is described as a function of the quadrupole operator, it is useful to write the explicit expression of the collective inertia for this particular case:

$$\mathcal{M}^{pc}_{\mathrm{ATDHFB}}(Q_{20}) = \frac{M^{-3}(Q_{20})}{2\left(M^{-1}(Q_{20})\right)^2} \,. \tag{3.42}$$

One should notice that in the derivation of the collective inertia within the ATDHFB theory there is not a term similar to the zero-point energy correction $\varepsilon_{\mathrm{zpe}}$ obtained in the GCM scheme (3.13). Since in the ATDHFB scheme the collective inertia is obtained from a classical picture involving generalised coordinates and momenta, a pure quantual correction like the Gaussian wave-packet energy cannot be extracted. However, in calculations involving the ATDHFB inertias it is customary to introduce a zero-point energy correction analogue to the term term of Eq. (3.29) obtained by replacing the GCM collective inertia with the ATDHFB one [36]:

$$\epsilon^{\mathrm{ATDHFB}}_{\mathrm{vib}}(Q_{20}) = \frac{G(Q_{20})}{\mathcal{M}^{pc}_{\mathrm{ATDHFB}}(Q_{20})} \,. \tag{3.43}$$

3.3.3 Semiempirical mass formula and reduced mass

In several calculations of fission cross sections the collective inertias are obtained from the semiempirical formula $\mu = 0.054 A^{5/3}$ MeV^{-1}, being β_{20} the collective variable of the action integral (3.6). This semiempirical expression was obtained in order to reproduce experimental data in the actinide region using a simplified prescription for the fission barriers [68]. The validity of μ for heavier nuclei and/or when different barriers to those of Moretto and Swiatecki are used, is rather uncertain and not fully tested. It is therefore interesting to compare the spontaneous fission lifetimes of this semiempirical expression with the results obtained using the ATDHFB and GOA-GCM approaches. Since the action integral is invariant under uniforming scaling, and $\beta_{20} = \frac{\sqrt{20\pi}}{5A}\frac{Q_{20}}{r^2}$ with $r = 1.2A^{1/3}$ fm, we have that:

$$\mathcal{M}_{\text{SEMP}} = \mu \left(\frac{d\beta_{20}}{dQ_{20}} \right)^2 = \frac{0.065}{A^{5/3}} \text{ MeV}^{-1}\text{fm}^{-4} . \tag{3.44}$$

The collective inertia of two separated fragments is given by the reduced mass $\mu = m_1 m_2/(m_1 + m_2)$. As a reference for the absolute magnitude of the collective inertia one can thus compare the results obtained from the microscopic and semiempirical schemes with the reduced mass. In the approximation of point-particles and expressing the distance between fragments in terms of the quadrupole deformation one gets the following expression for the reduced inertia:

$$\widetilde{\mathcal{M}} = \frac{m_n}{4\hbar^2 Q_{20}} , \tag{3.45}$$

being $m_n = 938.919$ MeV the averaged nucleon mass.

3.4 Potential energy surface

As it was already mentioned at the beginning of this chapter, the adiabatic approximation allows to study the fission process within a reduced set of collective variables. In order to determine the fission path is therefore necessary to compute the potential energy of the nucleus in the space given by the collective variables, and the evolution of the energy in this multidimensional space is usually referred as potential energy surface.

In fission calculations the choice of the collective variables is somehow arbitrary, but the traditional approach is to compute the evolution of the energy as a function of the deformation of the nucleus. The most important quantity is the quadrupole deformation Q_{20} related to the stretching of the nucleus, but the exploration of higher deformations is necessary to properly describe phenomena that are experimentally observed, like for instance the asymmetry of fission fragments.

Obviously the choice of the collective variables has an impact in the determination of the fission path. This is specially true when the fission path is determined by minimizing the action integral $S(L)$ instead of the potential energy $\mathcal{V}$. As we will see in the next section, the variation of quantities like pairing correlations may strongly modify the collective inertias and consequently the path followed by nucleus.

Usually fission calculations performed within the EDF framework employ between one and three collective degrees of freedom. One should notice that these numbers are lower than those commonly employed in macroscopic-microscopic (Mic-Mac) calculations, which nowadays explore up to seven collective variables. However, it is important to keep in mind that this higher dimensionality is somehow required in Mic-Mac calculations because all the deformations that are not explicitly explored are by construction equal to zero. This restriction does not apply to self-consistent mean field calculations, where all the parameters that are not constrained by the system symmetries are set in order to minimize the total (HFB) energy. This means that considering the full variational space, the potential energy surface is always given by the local minimum energy.

3.4.1 Shape parametrization of the nucleus

In EDF calculations the shape parametrization of the nucleus is done via the mass multipole moments defined as:

$$Q_{\mu\nu} = r^{\mu} Y_{\mu\nu}(\theta, \varphi) , \tag{3.46}$$

where $Y_{\mu\nu}$ are the standard spherical harmonics [69]. One should keep in mind that usually an arbitrary coefficient $C_{\mu\nu}$ is added to this definition for convenience and therefore the expected value of the multipole moments may have different definitions. The multiple operators are one-body operators, and therefore their expected valued can be written in terms of the density matrix (see Sec. 2.1.3):

$$\langle\Phi|\hat{Q}_{\mu\nu}|\Phi\rangle = \mathrm{tr}(\hat{Q}_{\mu\nu}\rho) = \int d^3\boldsymbol{r}\rho(\boldsymbol{r})r^{\mu}Y_{\mu\nu}(\theta,\varphi)\,. \tag{3.47}$$

Quadrupole deformations

The quadrupole mass moment given by the quadrupole moment operator:

$$\hat{Q}_{20} = \sum_{i=1}^{N}\hat{z}_i^2 - \frac{1}{2}(\hat{x}_i^2 + \hat{y}_i^2)\,, \tag{3.48}$$

represents the stretching of the nucleus and is the most important constraint in fission calculations. In the simplest EDF studies this is the only constraint used to study the evolution of the energy. Nuclei with a positive value of Q_{20} are defined prolate nuclei, while those with a negative Q_{20} are referred as oblate nuclei. The fission barrier solely obtained from the constraint of the quadrupole moment is actually a one-dimensional projection of the fission path in the multidimensional space of the collective variables. Since the configuration with the lowest energy is always chosen, one has that in the one-dimensional study the path connecting different configurations is neglected like for instance in the transition between one and two fragments. For a more realistic determination of the fission path is therefore necessary to increase the number of variational constraints including, for instance, higher multipole moments and/or pairing correlations.

Octupole deformations and hexadecapole deformations

The axial mass octupole moment Q_{30} describes the asymmetry of the nucleus under mirror reflection and is responsible for the appearance of asymmetric fission fragments. It is usually argued that the breaking of reflection symmetry is important to properly describe the region around the outer fission barrier, since this can be reduced by a couple of MeV. The hexadecapole moment Q_{40} is related to the scission mode of the nucleus and is widely used in neutron induced fission studies. Calculations using this multipole moment as a variational constraint showed that depending on the Q_{40} value the nucleus can follow either a compact fission path ($Q_{40} \approx 0$) or an elongated fission path ($Q_{40} \neq 0$), and the competition between these two fission modes determines the shape of the fission fragments distribution.

Neck operator

If the nucleus is in a very elongated configuration, the quadrupole moment operator may not capture the right shape evolution and therefore the neck operator $\hat{Q}_N$ is used instead. This is defined as [38]:

$$\hat{Q}_N = \sum_{i=1}^{N} e^{-\frac{(\hat{\boldsymbol{r}}_i - \boldsymbol{r}_N)^2}{C_0^2}}\,, \tag{3.49}$$

and represents a Gaussian distribution of nucleons centered at $\boldsymbol{r}_N$ (usually taken as the "neck" of the nucleus, i.e. the coordinate with the lowest nucleon density) with an arbitrary width C_0. Constraining the Q_N value is therefore equivalent to a variation in the number of nucleons placed around the neck of the nucleus, where obviously $Q_N \to 0$ correspond to a two-fragment configuration. In some studies [32, 33, 70, 71] this constraint is used in order to determine the lowest energy given by a two-fragment configuration of the system, which is also known as "quasi-fusion" path.

Triaxiality

Triaxial deformations can play a relevant role in determining the fission path by lowering the inner fission barrier by 2-3 MeV (see for example the discussion in Ref. [31, 33, 72]). This is particularly true for nuclei with an oblate ground-state, where the most favourable path towards scission is given by configurations breaking axial symmetry. However, it is important to point out that the collective inertia of triaxial configurations is usually higher than the axial ones. This means that in calculations where the fission path is determined by minimizing the action integral (3.6), triaxial paths may be less favourable than axial ones if the gain in energy is not high enough to compensate the higher collective inertia. This competitions was explored in some recent studies, showing that axial symmetry can be fully restored in dynamic calculations of the fission process [73, 74].

In this thesis, axial symmetry has been preserved in all the calculations in order to reduce the computational cost of solving the HFB equation. The imposition of axial symmetry allows to write the Bogoliubov wavefunctions, density matrix and pairing tensor in a block structure. This can be easily understood by the fact that any additional symmetry imposes an additional selection rule in calculation of the matrix elements matrix elements. We have therefore that to the preservation of this symmetry, the mean-value of the multipole operators, $\langle \hat{Q}_{\mu\nu} \rangle = 0$ for all $\nu \neq 0$.

3.4.2 Pairing correlations

In the last years several studies showed the extreme relevance of pairing correlations in fission. This renascence after the pioneering study of Moretto and Babinet [75] is strictly connected to the diffusion of dynamic studies, meaning calculations where the fission path is obtained by minimizing the action integral (3.6). As we will see in Sec. (3.5) the increase of pairing correlations lower the collective inertias separating the dynamic fission path from the one obtained by minimizing the total energy (static fission path).

In [76] the amount of pairing correlations was controlled by means of the particle number fluctuation mean value $\langle \Delta N^2 \rangle = N^2 - \langle \hat{N}^2 \rangle$, being N the total number of nucleons. For schematic pairing interactions one has that [39]:

$$\left(\langle \Delta N^2 \rangle \right)^2 = 4 \sum_{\mu>0} U_\mu^2 V_\mu^2 = \Delta^2 \sum_{\mu>0} \frac{1}{E_\mu}, \tag{3.50}$$

where E_μ is the quasiparticle energy and Δ the pairing gap measuring the amount of pairing correlations in the wavefunction [77]. When the particle number fluctuation is used as a variational parameter, one has to ensure that the self-consistent solution is a wave-function with the right number of proton (N_p) and neutrons (N_n). This is achieved by constraining the average particle number $\langle \hat{N}_\tau \rangle = N_\tau$, with $\tau = p, n$.

3.4.3 Energy corrections

There are two different types of energy corrections that enter in the calculation of the potential energy $\mathcal{V}(s)$ in Eq. (3.6). Corrections belonging to the first type were described in Sec. (2.3.5) and are related to the restoration of the broken symmetries at the mean-field level. These kind of corrections stem from the HFB calculation of the minimum energy for a given configuration and therefore are also considered in the estimation of the binding energies. The second kind of energy corrections are those stemming from the derivation of the collective Schrödinger equation (3.13) in the GCM framework. This are pure quantal corrections taking into account for fluctuations in the collective degrees of freedom, and therefore they are inherent to the description of the fission process within the adiabatic approximation.

Energy corrections belonging to this second type are the so-called zero-point energy corrections (ε_{ZPE}) that for the one-dimensional case with Q_{20} as a collective degree of freedom are denoted as vibrational zero-point energy correction (ε_{vib}). It is important to recall once again that the ZPE are only defined for the GCM approach, even though for the perturbative it is customary to reformulate an equation for the ATDHFB scheme by replacing the expression of the GCM collective inertias in Eq. (3.16) (see discussion in Sec. 3.3.2).

3.4.4 The effective potential energy

Taking into account the parametrization of the potential energy in terms of the reduced set of collective variables $\{\boldsymbol{q}\}$ together with the proper energy corrections, the effective potential energy $\mathcal{V}(s)$ in Eq. (3.6) can be written as:

$$\mathcal{V}(s) = E_{\text{HFB}}(s) - \epsilon_{\text{ZPE}}(s) - \epsilon_{\text{rot}}(s)\,, \tag{3.51}$$

being $s(\boldsymbol{q})$ the length in the space of the collective coordinates and E_{HFB} the HFB energy of Eq. (2.53). The term $\epsilon_{\text{rot}}(s)$ is the energy correction related to the restoration of the rotational symmetry described in Sec. 2.3.5 and $\epsilon_{\text{ZPE}}(s)$ the ZPE correction discussed before in Sec. 3.4.3. In Chapter 7 we will present the results for the one-dimensional case using the quadrupole moment as a collective degree of freedom:

$$\mathcal{V}(Q_{20}) = E_{\text{HFB}}(Q_{20}) - \epsilon_{\text{vib}}(Q_{20}) - \epsilon_{\text{rot}}(Q_{20})\,. \tag{3.52}$$

In this case the Routhian giving the minimum value of the HFB energy reads:

$$\hat{\mathcal{H}} = \hat{\mathcal{H}}_{\text{HFB}} + \sum_{\nu=1,2} \lambda_\nu \hat{Q}_{\nu 0} + \sum_{\tau=p,n} \lambda_\tau \hat{N}_\tau\,. \tag{3.53}$$

where $\hat{H}_{\text{HFB}}$ is the effective HFB Hamiltonian of Eq. (2.52), $\hat{N}_p(\hat{N}_n)$ the proton (neutron) number operator, λ_i the Lagrange multipliers and $\hat{Q}_{10}$ the center-of-mass constraint preventing spurious solutions arising from center-of-mass motion (see discussion in Sec. 2.3.5). The zero-point (vibrational) energy corrections ϵ_{vib} are computed in the perturbative cranking approximation (Eqs. (3.29) and (3.42)).

A typical outcome of the collective properties obtained in this kind of calculations is showed in Fig. 3.1 for the nucleus ^{244}U. The triple humped barrier of this nucleus is represented in the lower panel where each barrier height B_i is defined as the energy difference between the ground-state and the barrier peak. The different lines represents show the contributions of the energy corrections entering in Eq. (3.52). Clearly the major reduction to $\mathcal{V}(Q_{20})$ comes from the rotational correction $\epsilon_{\text{rot}}(Q_{20})$, while the vibrational correction $\epsilon_{\text{vib}}(Q_{20})$ produces a smaller, yet not constant, shift. From this plot it is clear that both the rotational and zero-point energy corrections introduced in Eq. (3.52) can modify the final height of the fission barriers B_i the isomer excitation energies E_i. The octupole and hexadecapole deformations plotted in the upper panel show that in self-consistent mean-field calculations all the deformations that are not restricted by the imposition of symmetries can be broken in order to minimize the HFB energy.

3.5 Dynamic vs static fission paths

As it was already mentioned before in this chapter, the expression dynamic calculations refers to fission calculations where the fission path is determined by minimizing the action integral 3.6. The alternative method is the so-called static approach, where the fission path is given by the minimization of the self-consistent energy. It is important to recall that the dynamic approach is formally the correct procedure to determine the fission path when the potential energy surface has a dimension larger than one, i.e. more than one collective degree of freedom is used as a variational parameter, by reason of

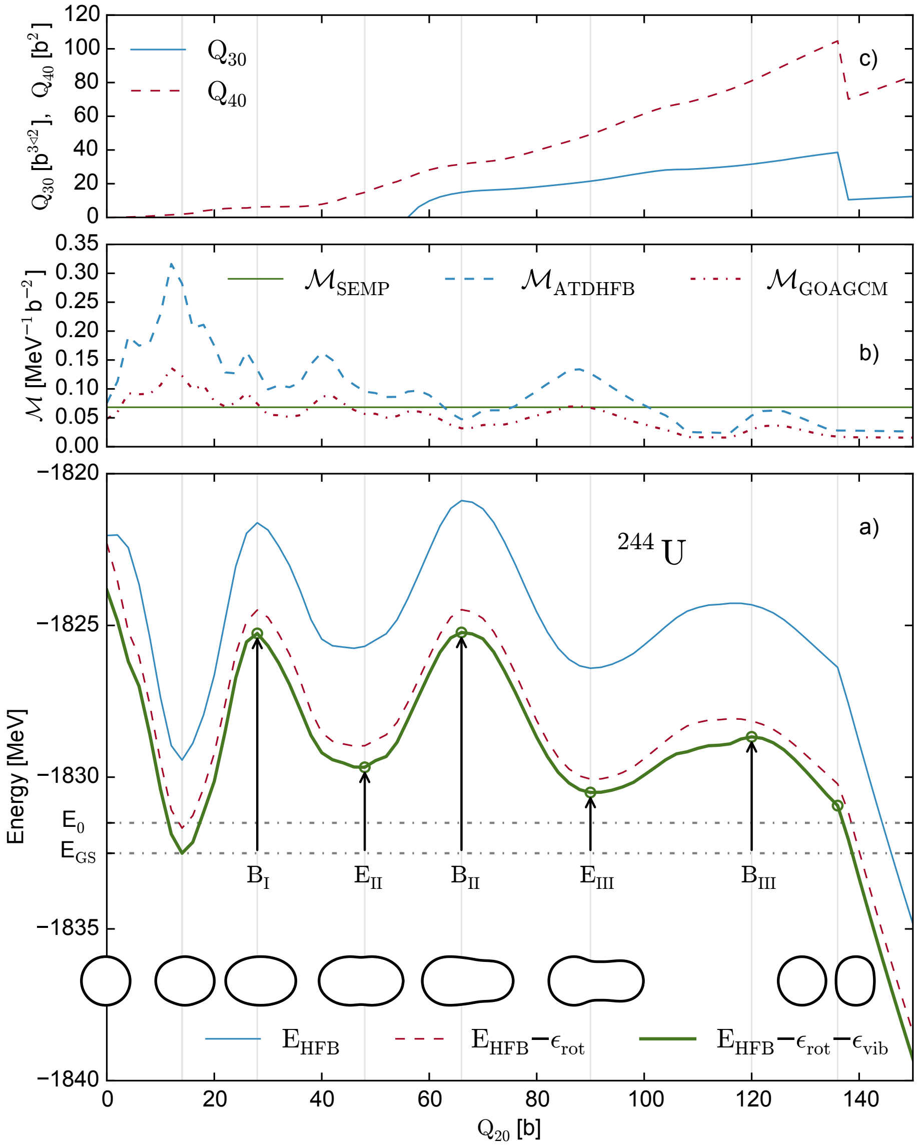

Figure 3.1: Collective properties of the ^{244}U as a function of the quadrupole moment Q_{20}. Panel a) shows the different contributions to the potential energy surface $\mathcal{V}(Q_{20})$ of Eq. (3.52), and the nuclear shape for different values of Q_{20}. Panel b) shows the inertias $\mathcal{M}(Q_{20})$ computed with the ATDHFB (dashed blue line, Eq. (3.42)), GCM (dash-dotted red line, Eq. (3.28)) and semiempirical inertia formula (solid green line, Eq. (3.44)) whithin the perturbative cranking approximation. The octupole (Q_{30}) and hexadecapole (Q_{40}) deformations are given in panel c).

the fact that the trajectory minimizing the action has the larger contribution to the path integral and it maximizes the fission probability. On the other hand, when only one collective variable is employed, the phase space is one-dimensional and obviously the least action and minimum energy paths line up.

The differences between static and dynamic calculations reside in the dependence of the collective inertias with the collective coordinates forming the potential energy surface. Looking at the Eq. (3.6) it is easy to understand that if $\mathcal{M}$ depends weakly on the collective variable q_i, then the dynamic and static fission paths will be very close to each other. Conversely, if the collective inertias have a strong dependence on the collective variable the minimization of the collective action can move the fission path towards configurations that do not correspond to the minimum energy configuration. This aspect stands out the extreme importance that the choice of the collective variables has in the description of the fission process.

3.5.1 The role of pairing correlations

Recent studies [32, 33] showed the large impact that pairing correlations have in spontaneous fission lifetimes. The large sensitivity of t_{sf} on this quantity lies on the fact that changes in pairing correlations modify the pairing gap and consequently the quasiparticle energies entering in the denominator of the collective inertias (see Eqs. (3.28) and (3.42)). This strong dependence of collective inertias on pairing correlations suggested that a measure of the amount of pairing correlations should be used as a collective variable in the minimization of the action integral. This idea was firstly introduced in 1974 by Moretto and Babinet [75], where the pairing gap Δ was used as a collective degree of freedom to compute the fission path. In this seminal paper the authors showed that the minimization of the action respect to the gap parameter is given by the competition between the decreasing of collective inertias ($\mathcal{M} \propto 1/\Delta^2$) and the increasing of the potential energy ($\mathcal{V} \propto \Delta^2$).

3.5.2 Study of the ^{234}U

In [76] we explored the impact of pairing correlations in the minimization of the action using realistic interactions and we compared the results to those obtained when other collective degrees of freedom are considered in the minimization. In this section we will present the outcome of our study obtained for the sample nucleus ^{234}U that was extensively benchmarked in several fission studies.

As it was already explained in Sec. 3.4.2, the amount of pairing correlations in a nucleus can be characterized by employing the particle number fluctuation mean value $\langle \Delta N^2 \rangle$. To find the $\langle \Delta N^2 \rangle$ value minimizing the action, we carry out constrained HFB calculations starting at the $\langle \Delta N^2 \rangle$ value minimizing the energy for each Q_{20} value of the fission path. In this way we obtain curves for the relevant physical quantities as a function of $\langle \Delta N^2 \rangle$ for each value of Q_{20}. An example of such curves is shown in Fig. 3.2, where the collective inertia, potential energy and action are depicted as a function of $\langle \Delta N^2 \rangle$ for $Q_{20} = 100\,\text{b}$. From this plot one can observe an almost parabolic behavior of the energy with the minimum located at the self-consistent solution, while the inertia decreases with the inverse of $\left(\langle \Delta N^2 \rangle\right)^2$, in accordance to the relation $\mathcal{M} \propto 1/\Delta^2$ [25, 75, 78]. After computing the action one finds that the corresponding minimum S_{min} is located at larger values of $\langle \Delta N^2 \rangle$ than the minimum energy solution E_{min}, and this displacement is obtained in all the values of the quadrupole moment operator [76].

This dynamical approach using pairing correlations as a collective degree of freedom resulted in a fission path that strongly differs from the one obtained by minimizing the energy, causing several changes in the fission properties of the nucleus:

- The t_{sf} in the dynamic description are strongly reduced when pairing correlations are included as a collective variable. This result is not straightforward since other dynamic calculations including only quadrupole-octupole and quadrupole-hexadecapole deformations do not show a significant difference with the corresponding static result (see Table 3.1). Obviously, the quenching of t_{sf}

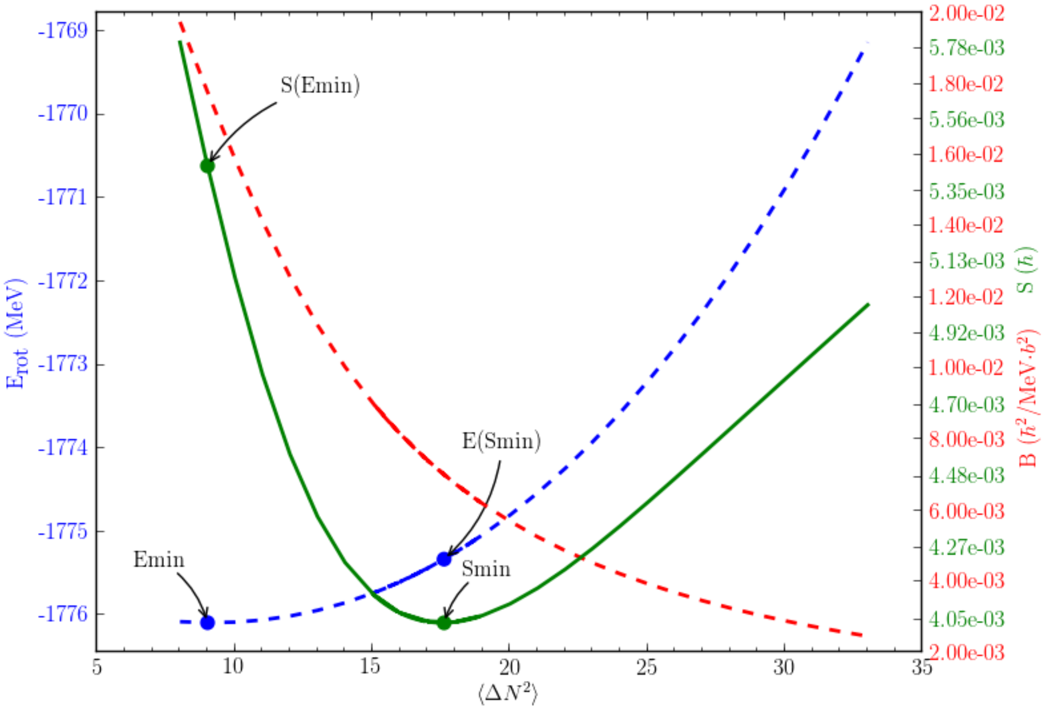

Figure 3.2: Variation of the potential energy $\mathcal{V}$ (blue dashed line), collective inertia $\mathcal{M}$ (red dashed line) and action (green solid line) as function of the particle number fluctuation for a fixed value of the quadrupole deformation $Q_{20} = 100\,\mathrm{b}$ of the ^{234}U computed with the BCPM EDF.

depends on the absolute value of the action, where for lower $S(L)$ one can expect a smaller impact of the dynamic approach.

- The displacement of the dynamic path toward larger $\langle \Delta N^2 \rangle$ values produces an increase of the fission barrier compared to the static result. The absolute change can be very large, as it is depicted in Fig. 3.3. Quoting a sentence of Shadukan *et. al.* in the context of a similar study, this result shows "*how limited the notion of fission barrier is*" [73].
- Within the perturbative cranking approximation, the ATDHFB collective inertias (3.42) are roughly two times larger than the one obtained with the GCM scheme (3.28). This difference enters in the exponential of the WKB formula, leading to a large variation of the SFL. However, Table 3.1 shows that the dynamical approach is less sensitive to the inertia scheme since the underlying differences are compensated by the searching of a minimum of the integral action.

Similar results tho those presented in this thesis were obtained by [73, 74], with the additional outcome that when traxiality is included as a collective variable some nuclei show a fission path restoring the axial symmetry, i.e., the nucleus prefers to penetrate a region with higher barrier as long as the triaxial region, where the collective inertias are higher, is avoided. The large variety of interactions used in these dynamic studies (BCPM, Gogny, Skyrme and relativisitic mean-field models [73, 74, 76]) showed that the impact of pairing correlations is not an artifact related to a particular interaction but a consequence of the fission description within the EDF formalism. These dynamic studies using pairing correlations as collective degrees of freedom gave new insights in the theoretical description of the fission process but they also opened new questions. The most important one is probably the role of symmetry restoration in fission calculations. As it was already mentioned in Chapter 2 the breaking of symmetries at the mean-field level is crucial to include long-range correlations and properly describe bulk properties of the nucleus. However a more realistic and precise results can be obtained only by including correlations from beyond mean-field calculations and these restorations can strongly modify pairing correlations in

Method	t_{sf} ATD (s)	t_{sf} GCM (s)
E_{min}	0.81×10^{43}	0.70×10^{30}
$S_{\mathrm{min}}(Q_{20}, Q_{30})$	0.44×10^{42}	0.64×10^{29}
$S_{\mathrm{min}}(Q_{20}, Q_{40})$	0.12×10^{43}	0.10×10^{29}
$S_{\mathrm{min}}(Q_{20}, \Delta N^2)$	0.18×10^{23}	0.21×10^{19}

Table 3.1: Spontaneous fission lifetimes (in seconds) of the ^{234}U obtained with the BCPM EDF for different fission paths and different choices of the collective variables. The second row shows the results obtained with the minimization of the potential energy. The remaining rows show the lifetimes obtained from the minimization of the action, using as a collective degree of freedom the quadrupole-octupole deformation (third row), the quadrupole-hexadecapole deformation (fourth row) and the quadrupole-particle number fluctuation (last row). The second and third column show the results obtained with the perturbative cranking collective inertias in the GCM (3.28) and the ATDHFB (3.42) scheme.

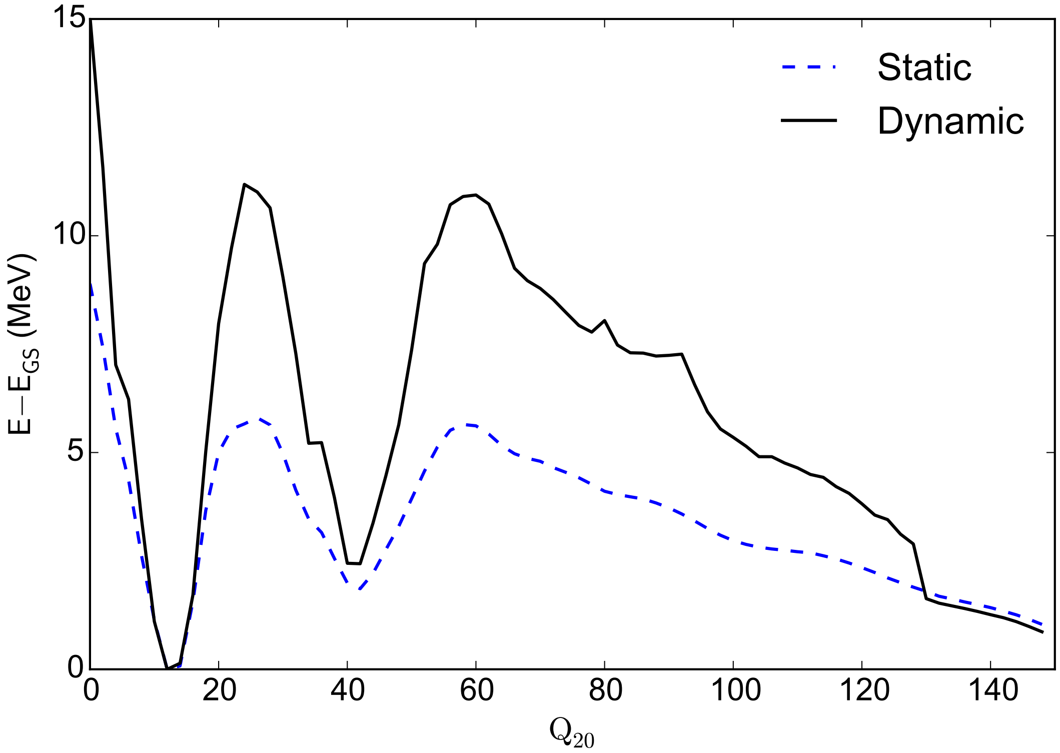

Figure 3.3: Fission barrier in MeV of ^{234}U as a function of the quadrupole moment Q_{20} obtained from dynamic calculations (solid black line) and static calculations (dashed blue line) of the fission path.

the nucleus. Fission calculations using a linear combinations of HFB states are challenging from both the theoretical and the computational point of view, but this effort has to be made in order to progress towards a more realistic description of the fission process.

4 Reaction rates within the Hauser-Feshbach theory

One of the goals of this thesis is the computation of fission and neutron-induced reaction rates relevant for r-process nucleosynthesis using the microscopic nuclear input obtained from our energy density functional (EDF) calculations. Since we are interested in nuclei with a large mass number, where the density of excited states is expected to be high, most of the reaction rates can be properly computed using Hauser-Feshbach statistical theory. This Chapter is thus devoted to the basics features of this model and its application to stellar reaction rates. We will start introducing the idea of compound nucleus being at the basis of the statistical theory and we will derive an expression for the nuclear reaction cross section. The next sections are devoted to the stellar reaction rates and the different ingredients required for their calculation. Finally, the last part of this Chapter is dedicated to the limits in the applicability of the statistical theory.

4.1 Statistical nuclear reactions

Nuclear reactions are commonly classified in terms of their timescales [81]. Fast reactions involving few intranuclear collisions, are called direct reactions, while reactions occurring at larger timescales, where several intranuclear collisions can take place, are known as compound reactions. Reactions whose timescales are in between of these two regimes are generally referred as pre-equilibrium reactions.

The work of this thesis is focused on r-process nucleosynthesis occurring in neutron star mergers, where the most important reactions are neutron captures, photo-dissociations, beta decays and fission decays. Except for beta-decays, all the other reactions can be treated within the statistical model describing compound nuclear reactions [82]. The main assumption of the statistical model is that the nuclear reaction between the projectile and the nucleus occurs via the formation of a compound system in an excited state. The excitation energy carried by the projectile is then shared among all the individual components of the compound nucleus, which has the time to fully equilibrate before decaying. This assumption, known as “Bohr independence hypothesis“ [83], implies that the decay of the compound nucleus is completely independent of its formation dynamics and it only depends on the energy, angular momentum and parity of the compound system. In the next sections we will see how the statistical hypothesis allows to derive an expression of the reactions cross sections of a general compound nuclear reaction.

4.1.1 Reaction channels

The main application of the statistical model is devoted to the description of binary reactions:

$$A + a \to CN \to B + b\,, \tag{4.1}$$

being A the target nucleus, a the projectile, CN the (excited) compound system, B the residual nucleus and b the ejectile. Instead of solving the Schrödinger equation of all the interacting particles one can assume that the interaction between the projectile and the target can be modeled by means of an effective potential called “optical potential”. The incident channel is then characterized by the coupling between

---

This Chapter is based on Ref. [79] and [80]

the angular momentum $\vec{l}_a$ and intrinsic spin $\vec{s}_a$ of the nucleus with the spin of the target $\vec{I}_A$. Reaction (4.1) has then to fulfill the conservation laws considering also the parity and total energy of the system:

$$
\begin{aligned}
E_A + E_a = E_{CN} = E_B + E_b & \quad \text{Total energy conservation,} && \text{(4.2a)} \\
\vec{p}_A + \vec{p}_a = \vec{p}_B + \vec{p}_b & \quad \text{Total momentum conservation,} && \text{(4.2b)} \\
\vec{l}_a + \vec{s}_a + \vec{I}_A = \vec{J}_{CN} = \vec{l}_b + \vec{s}_b + \vec{I}_B & \quad \text{Total angular momentum conservation,} && \text{(4.2c)} \\
(-)^{l_a} \pi_A \pi_a = (-)^{l_b} \pi_b \pi_B & \quad \text{Total parity conservation.} && \text{(4.2d)}
\end{aligned}
$$

being E_i the energy, $\vec{p}_i$ the linear momentum, $\vec{I}_i$ and $\vec{J}_i$ the total angular momentum and π_i the parity of the particles involved in the reaction and the compound nucleus.

Another important quantity in all nuclear reactions is the so-called Q-value given as the difference in the rest masses (or, equivalently, in the kinetic energies) after and before the reaction:

$$Q = (m_A + m_a)c^2 - (m_B + m_b)c^2 \, . \tag{4.3}$$

Nuclear reactions with a positive Q-value release energy and are called exothermic, while those with a negative Q-value consumes energy and are referred as endothermic. All reactions, with the exception of elastic scattering, have a Q-value different from zero.

4.1.2 Hauser-Feshbach theory for cross sections

The cross section of a reaction can be generally defined as:

$$\sigma = \frac{\text{number of interactions per time}}{\text{flux of incoming particles}} \, . \tag{4.4}$$

σ measures the probability of a certain reaction to occur, since all the particles passing through the area σ will undergo a reaction. In the case of spinless particles, the cross section of a reaction from an initial channel α decaying to the outgoing channel β can be written in terms of the scattering matrix element $S_{\alpha\beta}$ using the diffusion theory [84]:

$$\sigma_{\alpha\beta} = \frac{\pi}{k_\alpha^2} \langle |\delta_{\alpha\beta} - S_{\alpha\beta}|^2 \rangle \, , \tag{4.5}$$

being k_α the wave number of relative motion. The matrix element S_α is obtained from the optical potential effectively modeling the interaction between projectile and target nucleus. Using the Bohr's independence hypothesis one can rewrite Eq. (4.5) in terms of the compound nucleus formation cross section and the probability to decay into channel β:

$$\sigma_{\alpha\beta} = \sigma_\alpha^{CN} P_\beta = \frac{\pi}{k_\alpha^2} \frac{T_\alpha T_\beta}{\sum\limits_\gamma T_\gamma} \, , \tag{4.6}$$

being $T_i = 1 - |S_i|^2$ the transmission coefficient of the channel i and γ all the possible decay channels that are energetically allowed (including the entry channel α). Eq. (4.6) is the Hauser-Feshbach formula for spinless particles also known as statistical formula since considers the decay in the outgoing channel in terms of a statistical probabilities. This equation can be generalized to the case of several incident and outgoing channels taking place in the reaction by summing over all the possible channels contributing to the reaction. The final cross section will then result from the contribution of all the partial cross sections related to the compound levels $J_{CN}^{\pi_{CN}}$ [81]:

$$\begin{aligned}\sigma_{ab} = & \frac{\pi}{k^2}\frac{1+\delta_{Aa}}{(2I_A+1)(2I_a+1)} \sum_{J_{CN}} \sum_{\pi_{CN}=\pm} (2J_{CN}+1) \\ & \sum_{j_a=|J_{CN}-I_A|}^{J_{CN}+I_A} \sum_{l_a=|j_a-s_a|}^{j_a+s_a} \sum_{j_b=|J_{CN}-I_B|}^{J_{CN}+I_B} \sum_{l_b=|j_b-s_b|}^{j_b+s_b} \delta(a,\pi_{CN})\delta(b,\pi_{CN}) \frac{T^{J_{CN}}_{\alpha l_a j_a} T^{J_{CN}}_{\beta l_b j_b}}{\sum\limits_{\gamma} T_\gamma} .\end{aligned} \tag{4.7}$$

In the expression above the indices a and b contain all the relevant information regarding the conserved quantities of the system described in Eqs. (4.2). The first fraction on the LHS arises from the fact that we are interested on an averaged cross section over all the possible spin states of the compound nucleus and δ_{Aa} accounts for the case when the projectile and the target are the same particle ($A = a$). The summation over J_C is usually restricted up to $J_{CN} = I_A + s_a + l_a^{\max}$ since contributions from angular momenta higher than a certain value are negligible. For the case when the target nucleus and ejectile are in a particular state μ and ν $A_\mu(a,b)B_\nu$, we can rewrite Eq. (4.7) as:

$$\begin{aligned}\sigma_{ab}^{\mu\nu}(E) = & \frac{\pi\hbar^2}{2mE}\frac{1+\delta_{Aa}}{(2I_A^\mu+1)(2I_a+1)} \\ & \sum_{J_{CN},\pi_{CN}} (2J_{CN}+1) \frac{T_a^\mu(E_{CN},J_{CN},\pi_{CN};E_A^\mu,I_A^\mu,\pi_A^\mu)T_b^\nu(E_{CN},J_{CN},\pi_{CN};E_B^\nu,I_B^\nu,\pi_B^\nu)}{T_{\text{tot}}(E_{CN},J_{CN},\pi_{CN})} ,\end{aligned} \tag{4.8}$$

where E and m are the total energy and reduced mass of the initial system in the center-of-mass frame (and therefore $k = \sqrt{2mE}/\hbar$) and $\sum_\gamma T_\gamma \equiv T_{\text{tot}}$.

4.2 Ingredients of the statistical theory

In the previous section it was shown that the calculation of reaction cross section within the statistical model depends on the transmission coefficients. Later we will see that another crucial quantity for the computation of reaction rates is the nuclear level density. For the sake of completeness this section is devoted to a brief description of these two ingredients and the different approximations used in this thesis to compute them.

4.2.1 Transmission coefficients

Depending on the reaction it is possible to distinguish between three different transmission coefficients: particle transmission coefficients, describing the capture or emission of light particles; the gamma transmission coefficients, related to the emission of gamma rays; and the fission transmission coefficients for fissile nuclei.

Gamma transmission coefficients

The gamma transmission coefficients are obtained from the gamma-ray strength functions $f(x,\lambda)$:

$$T_{x\lambda}(\varepsilon_\gamma) = 2\pi f(x,\lambda)\varepsilon_\gamma^{2\lambda+1}, \tag{4.9}$$

being ε_γ the energy of the emitted gamma-ray, J^π the angular momentum of the compound nucleus and x the type of transition (either electric or magnetic) with a multipolarity λ. It exists different models describing the form of the gamma-ray strength. In this thesis we adopted the generalized Lorentzian form of Kopecky and Uhl for the $E1$ radiation [85]. Since the compound nucleus may decay to several final states it is necessary to introduce an effective gamma transmission coefficient summing over all the accessible states:

$$T_{\gamma}^{J^{\pi}}(E) = \sum_{x,\lambda} \sum_{J_f=|J-\lambda|}^{J+\lambda} \sum_{\pi_f} \int_0^E d\varepsilon_{\gamma}\, T_{x,\lambda}(\varepsilon_{\gamma}) \rho(E-\varepsilon_{\gamma}, J_f, \pi_f) \Theta(x,\lambda,\pi,\pi_f)\,, \tag{4.10}$$

where J^{π} is the initial level decaying to the final levels $J_f^{\pi_f}$ and a level density $\rho(E-\varepsilon_{\gamma}, J_f, \pi_f)$. The function $\Theta(x,\lambda,\pi,\pi_f)$ is equal to 1 if $\pi_f = (-1)^{\lambda}\pi$ for $E\lambda$ transitions or $\pi_f = (-1)^{\lambda+1}\pi$ for $M\lambda$ transitions and 0 otherwise.

Particle transmission coefficients

The transmission coefficients for light particles is obtained within the optical model assuming that the interaction between projectile and target can be modeled using a complex potential. As we already touched before, the optical potential allows the calculation of the scattering matrix $S_{\alpha\beta}$ and consequently the transmission coefficient for the entering channel α as:

$$T_{\alpha} = 1 - |S_{\alpha\alpha}|\,. \tag{4.11}$$

Once again, due to the large number of possible final states it is necessary to define an global transmission coefficient by summing over all the possible final states available within an arbitrary energy bin:

$$\left\langle T_{b,l_b,j_b}^{J^{\pi}} \right\rangle = \int dE\, \rho(E, I_B, \pi_B) \delta(b, \pi_{CN}) T_{b,l_b,j_b}^{J^{\pi}}\,. \tag{4.12}$$

The expression above, where $\rho(E, I_B, \pi_B)$ is the level density of the residual nucleus with an excitation energy E, implicitly assumes that all the decay channels contribute equally to the decay process, which a reasonable approximation if the size of the energy bins is small enough. In this thesis we used local and global parametrizations of the optical potential from Koning and Delaroche [86].

Fission transmission coefficients

The main difference in the calculation of the fission transmission coefficients and the gamma and light particle case is that for fission we cannot establish a connection to a particular residual nucleus, but rather we have to calculate a total fission probability given by a unique transmission coefficient. Due to this, the concept of nuclear level density of the residual nucleus is not applicable anymore and one should sum the probability of the nucleus to penetrate all the possible fission barriers. Obviously one cannot compute such probability because the number of fission barriers is extremely large and we do not know how to properly compute them, except (hopefully…) for the ground-state configuration. For this reason one introduces on top of each saddle point the so-called transition states miming all the possible fission barriers that might be tunneled through. Each transition state is then associated with one fission barrier, and if one assumes that the shape of the fission barrier does not change with excitation energy the probability of penetrating the transition state at energy ε above the (ground-state) fission barrier $\mathcal{V}$ from a compound energy E is equivalent to penetrate the fission barrier $\mathcal{V}$ from a compound energy $E-\varepsilon$:

$$P(E, \mathcal{V}+\varepsilon) = P(E-\varepsilon, \mathcal{V})\,. \tag{4.13}$$

The fission probability can then be computed using the WKB approximation described in Sec. 3.2:

$$P(E,\mathcal{V}) = \frac{1}{1+\exp(2S(E,\mathcal{V}))} \quad \text{with} \quad S(E,\mathcal{V}) = \int_b^a dQ_{20}\,\sqrt{2\mathcal{M}(Q_{20})[\mathcal{V}(Q_{20})-E]}\,, \tag{4.14}$$

where we assumed that the quadrupole deformation is the only relevant collective degree of freedom. Using Eq. (4.13) the fission transmission coefficient of a compound nucleus with energy E, spin J and parity π can be written as[1]:

$$T(E,J,\pi) = \int_0^\infty d\varepsilon\, P(E-\varepsilon)\rho_{\text{sad}}(B_f-\varepsilon,J,\pi)\,, \tag{4.15}$$

where $\rho_{\text{sad}}(B_f+\varepsilon,J,\pi)$ is the so-called saddle-point level density describing the density of levels on top of the fission barriers B_f. This level density is assumed to be the level density of the ground state $\rho(\varepsilon,J,\pi)$ with a slightly different calculation of collective effects [87].

The expressions introduced so far are in principle valid for any possible shape of the barrier, but they do not take into account for the so-called resonant class states effects [88]. The class states effects are sharp peaks observed in the fission probability which are associated to resonances induced by compound nuclei located in the deformed minima (see Fig. 4.1). The simplest method to account for these effects is assuming that the penetration through all the barriers can be factorized in terms of the penetration of the single barriers. In the case of a double humped barrier like the one sketched in Fig. 4.1, the total fission probability is given by the probability of crossing the first fission barrier (T_A) multiplied by the probability of fission from the second minimum (T_{II}). Since after tunneling the first barrier the nucleus can either penetrate the second barrier and fission (T_B) or cross back the first barrier (with a probability T_A), we have that the total fission cross section can be written as [89]:

$$T_{AB} = \frac{T_A \times T_B}{T_A + T_B} \times F_{AB}(E)\,, \tag{4.16}$$

where T_i is given by Eq. (4.15). The term $F_{AB}(E)$ is an empirical parameter depending on T_i, the depths of the wells and the compound nucleus energy E and it is introduced in order to enhance the fission probability according to the excited levels of the fission isomer (the resonant class II effects) [87, 90]. The previous approach can be easily extended to a triple humped fission barrier, that is the maximum amount of saddle points considered in most of the calculations:

$$T_{ABC} = \frac{T_{AB} \times T_C}{T_{AB} + T_C} \times F_{ABC}(E)\,, \tag{4.17}$$

where T_C is the transition coefficient of the third barrier and F_{ABC} the empirical parameter taking into account class III states effects. In this thesis we computed the transmission coefficients using a slightly different approach developed by [91], where the resonant class effects are included by adding a complex potential to the unidimensional multihumped barrier localized in the deformation range corresponding to the second minima. The fission probability is then decomposed in a direct part (T_d), where the class effects are mimicked by the complex potential, and an indirect term similar to Eq. (4.16) or (4.17) taking into account the possibility of fissioning from the isomer (T_{abs}).

4.2.2 Level densities

For excitation energies above 1-2 MeV, the mean spacing of the discrete nuclear excitation energies is so small that a description of the individual levels is not possible anymore and one has to rely upon

---

[1] For simplicity, in this equation as well as in (4.10) and (4.12) we have omitted the summation over the discrete levels that should replace the integral at low energies.

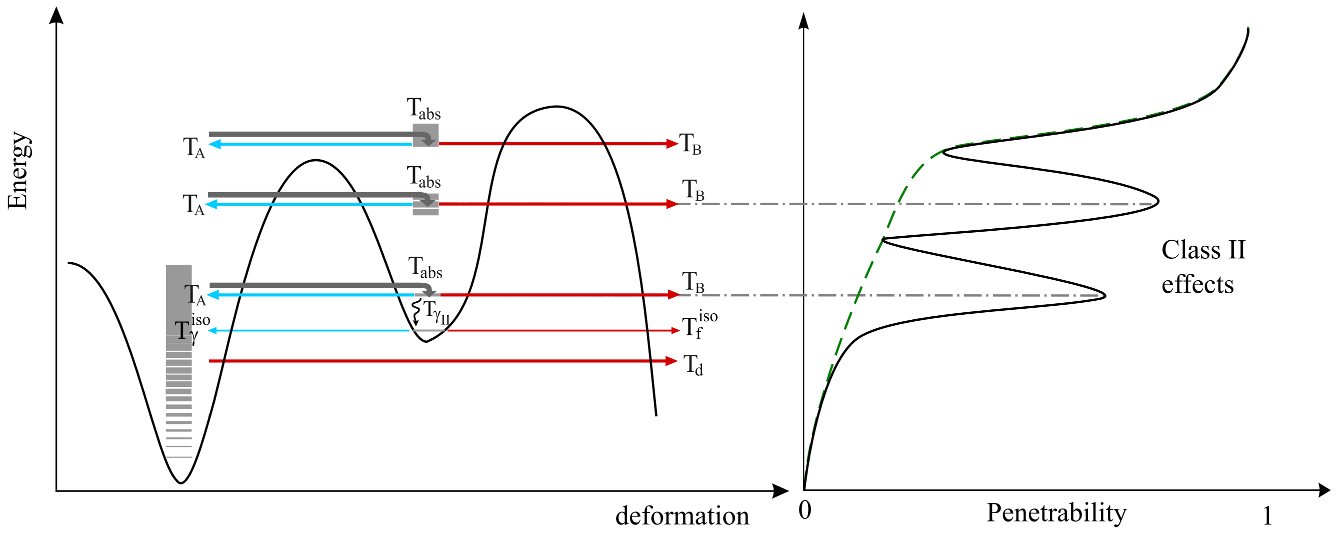

Figure 4.1: Illustration of effects of the class II states in the fission penetrability for a double humped barrier. The green dashed line on the left show the penetrability without class II effects. Modified from [91] and [79].

a global representation based on the nuclear level density function (NLD). The level densities can be computed either using phenomenological models (mostly based in the independent particle model) or more microscopic approaches within the self-consistent mean-field theory (see [92] for a recent comparison between both approaches). In this section we will briefly present the two main schemes used in this thesis, the back-shifted Fermi gas and the constant temperature models, both based on the Fermi Gas Model (FGM).

The Fermi Gas Model (FGM)

Generally we can define the level density function as the derivative of the total number of nuclear excited levels $N(E)$ below a certain excitation energy E:

$$\rho(E) = \frac{dN(E)}{dE}\,. \tag{4.18}$$

The FGM is derived from the independent particle model introduced in Chapter 2 with the additional assumption that the single-particle states are equally distributed. Using this model the level density function of a nucleus ${}^AZ$ for an excitation energy U reads [93]:

$$\rho_F(U) = \frac{\sqrt{\pi}}{12}\frac{\exp\left(2\sqrt{aU}\right)}{a^{1/4}U^{5/4}}\,, \tag{4.19}$$

where a is the so-called level density parameter depending on the density of single-particle states g:

$$a = \frac{\pi^2}{6}g = \frac{\pi^2}{4}\frac{A}{\varepsilon_f} \quad \text{with} \quad \varepsilon_f = \left(\frac{9\pi}{8}\right)^{2/3}\frac{\hbar^2}{2Mr_0^2}\,, \tag{4.20}$$

being M and r_0 the rest mass and radius of the nucleon, respectively. Eq. (4.19) can be extended to include a spin and parity distribution of the level densities. Analytically it is possible to show that in the FGM the dependence of the level density with the angular momentum projection follows a gaussian law [93]. On the other hand, the FGM does not contain any information regarding the parity of the states, and therefore it is often assumed that states with positive and negative parity are equally distributed. Thus the expression of the NLD (4.19) for a nucleus with spin J becomes:

$$\rho_F(U,J) = \frac{1}{2}\frac{\sqrt{\pi}}{12}\frac{\exp\left(2\sqrt{aU}\right)}{a^{1/4}U^{5/4}}\frac{2J+1}{2\sigma^3\sqrt{2\pi}}\exp\left[-\frac{(J+1/2)^2}{2\sigma^2}\right], \tag{4.21}$$

where $\sigma \propto \sqrt{U/a}$ is the spin-cut off parameter.

The main drawback of the FGM is that effects beyond the independent particle picture are not taken into account. Experiments showed that level densities exhibit odd-even effects arising from pairing correlation as well as collective enhancements (due to vibrations and rotations) and structural effects near the magic numbers. The odd-even effects can be partially reproduced by introducing in Eq. (4.21) an empirical correction Δ to the excitation energy U. This energy correction Δ is inspired by the pairing term in the semiempirical mass formula miming the spin-coupling effect and improves the agreement with experimental data. Unfortunately the other deficiencies described before cannot be cured with a similar simple prescription and semiempirical models (like the back-shifted Fermi gas or the constant temperature models) are in order to properly describe experimental data.

Semiempirical models

The most simple semiempirical models are the Back-Shifted Fermi-Gas (BSFGM) and the Constant Temperature (CTM) models, aiming to properly describe the density of nuclear levels at low excitation energies. The main idea behind both approaches it to use the level density parameter a and the spin cut-off parameter σ as free parameters that can be adjusted to reproduce experimental data. The difference between the two models lies in the ansatz adopted for the NLD at low energies.

In the CTM the level density at low energies is described by the constant temperature law [94]:

$$\rho_T(U,J) = \frac{1}{T}\exp\left(\frac{U-E_0}{T}\right)\frac{2J+1}{2\sigma^2}\exp\left[-\frac{(J+1/2)^2}{2\sigma^2}\right], \tag{4.22}$$

where the nuclear temperature T and energy E_0 are additional parameters that can be adjusted to reproduce the available experimental data. The reader shall notice that for the spin dependence the same prescription of the Fermi gas spin distribution of Eq. (4.21) has been adopted. The ansatz in Eq. (4.22) is used until an excitation energy U_M, above which the FGM applied:

$$\rho(U) = \begin{cases} \rho_T(U,J) & \text{if } U \leq U_M, \\ \rho_F(U,J) & \text{if } U \geq U_M; \end{cases} \tag{4.23}$$

where $\rho_F(U,J)$ is is the NLD for the FGM given by Eq. (4.21) including the pairing correction $U \to U - \Delta$. The unknowns E_0, E_M and T can be determined by imposing the continuity of the density and its derivative in Eq. (4.23) and the reproduction of the experimental discrete levels observed at low energies. When experimental data is not available the nuclear temperature can be obtained using a generic empirical prescription [87].

In the Back-Shifted Fermi Gas Model (BSFGM) [95] the Fermi-Gas expression Eq. (4.21) is used down to zero energy and the pairing correction Δ is treated as an additional adjustable parameter. The divergence of the equation when $U = 0$ can be cured writing the level densities as [96, 97]

$$\rho_B(U,J) = \frac{1}{2}\left[\frac{1}{\rho_F(U)} + \frac{1}{\rho_0(U)}\right]^{-1}\frac{2J+1}{2\sigma^2}\exp\left[-\frac{(J+1/2)^2}{2\sigma^2}\right] \tag{4.24}$$

being $\rho_0(U) = a\exp(1+aU)/(48\sigma)$ and $\rho_F(U)$ the level density from the Fermi gas model (4.19).

4.3 Stellar reaction rates

4.3.1 Stellar cross sections

For reactions occurring in stellar environments one has to consider that due to the finite temperature of the astrophysical plasma nuclei are thermally populated, i.e., they are present not only in their ground-state but also in excited states μ. The stellar cross section is then obtained by weighting Eq. (4.8) by the Boltzmann excitation probability:

$$\sigma^*_{ab} = \frac{\sum_\mu (2I^\mu_A + 1)e^{-E^\mu_A/kT^*} \sum_\nu \sigma^{\mu\nu}_{ab}}{\sum_\mu (2I^\mu_A + 1)e^{-E^\mu_A/kT^*}}\,, \tag{4.25}$$

being k the Boltzmann constant. The summation over the final states ν is added because now we are considering the probability of the compound nucleus to decay to any bound state. This requires the replacement of the partial transmission coefficient T^ν_b for the total transmission coefficients T_b:

$$\begin{aligned} T_b(E_{CN}, J_{CN}, \pi_{CN}) = & \sum_{\nu=0}^{\lambda} T^\nu_b(E_{CN}, J_{CN}, \pi_{CN}; E^\nu_B, I^\nu_B, \pi^\nu_B) \\ & + \int_{E_\lambda}^{E-S_b} dE_B \sum_{I_B,\pi_B} T^\nu_b(E_{CN}, J_{CN}, \pi_{CN}; E^\nu_B, I^\nu_B, \pi^\nu_B)\rho(E_B, J_B, \pi_B)\,. \end{aligned} \tag{4.26}$$

The summation over all the possible states is replaced above the highest experimentally known state λ by an integration over the nuclear level density $\rho(E_B, J_B, \pi_B)$, that is nothing else than the number of nuclear levels per energy interval. The limits of the integrations are given by the energy of the state λ and the difference between the total energy E and the channel separation energy S_b.

4.3.2 Stellar rates

The nuclear reaction rate, defined as the number of reactions occurring per volume and unit time, is given by the expression:

$$r_{Aa} = \int \sigma(v)\, v_{Aa} n_A(p_A) n_a(p_a)\, dp_A\, dp_a\,, \tag{4.27}$$

being $n_i(p_i)$ the particle distribution and $v_{Aa} = |\vec{v}_A - \vec{v}_a|$ the relative velocity between reactants. As we already introduced in Sec. 4.3.1 nuclei in typical astrophysical plasma follow a Maxwell-Boltzmann distribution:

$$n = \frac{G(T)}{(2\pi\hbar)^3} \int dp \exp\left(\frac{E-\mu}{kT}\right) 4\pi p^2\,, \tag{4.28}$$

with E the energy of the particle, μ its chemical potential and $G(T)$ the partition function measuring the internal degrees of freedom of nuclei considering all the excited state i:

$$G(T) = \sum_i (2J_i + 1) e^{-E_i/(kT)}\,. \tag{4.29}$$

Since nuclei are non-relativistic particles one has that

$$E = mc^2 - p^2/(2m)\,, \quad \mu = mc^2 + kT\eta\,, \tag{4.30}$$

where η is the degeneracy factor. This allows to integrate the Maxwell-Boltzmann distributions in Eq. (4.28) obtaining:

$$n = \frac{G(T)e^{\eta}}{\Lambda^3} \quad \text{with} \quad \Lambda = \sqrt{\frac{2\pi\hbar^2}{mkT}}\,, \tag{4.31}$$

where Λ is the so-called de Broglie wavelength.

Particles with similar mass

If the particles involved in the reaction have a similar mass one can use Eqs. (4.29) and (4.31) to express the reaction rate (4.27) as:

$$r_{aA} = \langle \sigma v \rangle_{A,a} n_a n_A\,, \tag{4.32}$$

being $\langle \sigma v \rangle$ the velocity integrated cross section:

$$\langle \sigma v \rangle_{A,a} = \left(\frac{8}{\pi \mu_{Aa}} \right)^{1/2} \frac{1}{(kT)^{3/2}} \int_0^{\infty} dE\, \sigma^*_{A,a}(E) E \exp\left(\frac{E}{kT} \right) . \tag{4.33}$$

In the expression above μ_{Aa} is the reduced mass, T the temperature of the astrophysical plasma and $\sigma_{A,a}$ the stellar cross section (4.25). In charged-particle reactions the cross sections strongly depend on the Coulomb barrier and for low energies the reactions occur via tunnel effect. In this case it is customary to extract out the penetration factor:

$$P(E) = \exp\left(-\frac{2\pi Z_A Z_a e^2}{\hbar v} \right) \equiv \exp(2\pi\eta(E))\,, \tag{4.34}$$

from the cross section:

$$\sigma(E) = \frac{S(E)}{E} \exp(2\pi\eta(E))\,, \tag{4.35}$$

and rewrite the velocity integrated cross section in terms of the S-factor $S(E)$ and the Sommerfeld paremeter $\eta(E) = b/\sqrt{E}$:

$$\langle \sigma v \rangle_{A,a} = \left(\frac{8}{\pi \mu_{Aa}} \right)^{1/2} \frac{1}{(kT)^{3/2}} \int_0^{\infty} dE\, S(E) \exp\left(-\frac{E}{kT} - \frac{b}{E^{1/2}} \right) . \tag{4.36}$$

The energy where the product of the two exponential peaks is the so-called Gamow energy and its width, the Gamow-window, determines the region where the process is more likely to take place.

Photodissociation and reverse rates

For reactions where one of the reactant is massless (e.g. photons) or much more lighter than the other (e.g. electrons reacting with a nucleus) the relative velocity v in Eq. (4.27) can be approximated by the speed of light, leading to an expression of the reaction rate that depends on the density and the effective decay rate of the target nucleus:

$$r_{Aa} = \lambda_A(T, \rho, \mu_A) n_a \quad \text{with} \quad \lambda_A = \int dp_a\, \sigma v_a n(p_a)\,. \tag{4.37}$$

The projectiles distribution depends on the type of particles. In case of photons it is the Bose-Einstein distribution and the disintegration rate reads:

$$\lambda_\gamma(T) = \frac{1}{\pi^2\hbar^3c^2}\int_0^\infty dE\,\frac{\sigma(E)E^2}{\exp(E/kT)-1}\,. \tag{4.38}$$

In practice calculations the photodisintegration rate is determined by detailed balance. If one assumes that the photodisintegration and its inverse reaction capture are in equilibrium:

$$A + a \rightleftarrows B + \gamma\,, \tag{4.39}$$

the photodisintegration rate can be written in terms of the capture rate as [80]:

$$\frac{n_A n_a}{1+\delta_{Aa}}\langle\sigma v\rangle_{A,a} = \lambda_\gamma n_B\,. \tag{4.40}$$

Using the equality of chemical potentials ($\mu_A + \mu_a = \mu_B$) together with Eqs. (4.30) and (4.31) one gets the following expression of the photodissociation rate:

$$\lambda_\gamma = \left(\frac{m_u kT}{2\pi\hbar^2}\right)^{3/2}\frac{G_A G_a}{G_B}\left(\frac{A_B}{A_A+A_a}\right)^{3/2}\exp(-Q/kT)\frac{\langle\sigma v\rangle_{Aa}}{1+\delta_{Aa}}\,, \tag{4.41}$$

being Q the reaction Q-value, A_i the atomic weight and m_u the unified atomic mass unit.

4.4 Limits of the statistical theory

The statistical Hauser-Feshbach theory is applicable whenever the number of nuclear levels per energy unit at the compound excitation energy is large enough ($\geq 5-10$ per MeV) to describe the cross section as an average over resonances [98]. Whenever this condition is fulfilled one has that $\Delta E \cdot \rho(E) \gg 1$ for an energy interval ΔE with a nuclear level density $\rho(E)$. Therefore the statistical theory can be applied regardless of the mass of the involved nuclei, as far as the level density is high enough to ensure that the compound nucleus can fully equilibrate before decaying. Thus what is extremely relevant for establishing whether a reaction can be described using the Hauser-Feshbach theory is the excitation energy of the compound nucleus E_{CN} that is given by the Q-value of the reaction (4.3) plus the kinetic energy of the projectile E_p:

$$E_{CN} = Q + E_p\,. \tag{4.42}$$

Since compound reactions dominate in the low regime of the projectile energy ($\leq$ 20 MeV), we have that a crucial role in determining the validity of the statistical model is played by the Q-value of the reaction. Reactions with large Q-value imply large excitation energies of the compound nucleus, where one may expect to have enough nuclear levels justifying the usage of the statistical theory. Also deformed and heavy nuclei have usually high level densities also at low excitation energies, allowing to properly describe reaction even if the Q-values are small.

For the particular case of the r-process nucleosynthesis, one of the most representative reactions is the neutron capture on heavy nuclei. At typical temperatures around 1 GK the kinetic energy of the neutrons is approximately 100 keV, which means that in this case the neutron separation energy has to be large enough to excite the compound nucleus at energies with a suitable number of levels for the statistical model. This restriction pose some doubts regarding the application of the statistical model to neutron captures on nuclei close to the dripline, where neutron separation energies are small. In [98] it was shown that for the neutron capture on neutron rich nuclei the statistical model can only be applied if the temperature of the stellar plasma is $\leq$ 2.5 GK even though this value may change depending on the nuclear mass model employed in the calculations. Another critical region are nuclei nearby close shell gaps, where the density of levels is lower than in deformed nuclei. In all these cases the reaction cross sections are dominated by direct capture and single resonances, and therefore a specific treatment beyond the statistical model should be applied.

5 Reaction network for r-process calculations

Stellar nucleosynthesis calculations are carried out by means of nuclear reaction networks. In these networks the system of differential equations determining the temporal evolution of nuclear abundances is solved for a given trajectory describing the change of the density and temperature of the stellar plasma with time. Since the final goal of this thesis is to study the impact of our fission calculations on the r-process abundances, this Chapter is devoted to explain the basic features of a reaction network, with a special emphasis in the application to the r-process nucleosynthesis. We will start introducing the system of equations for the abundance change rate and the computational schemes used for their solution. The second part of this Chapter is devoted to the definition of the most important quantities characterizing the evolution of the r process, while the final section is dedicated to a short description of the thermodynamical trajectories used in our calculations.

5.1 Basics of reaction networks

Reaction networks simulate the heating due to nuclear reactions and nucleosynthesis occurring in astrophysical scenarios. These phenomena can be related to a change in the number density of the different nuclear species n_i that in turn also depend on possible changes in the volume of the astrophysical plasma. Since in nucleosynthesis calculations we are mainly interested in studying changes due to nuclear reactions, we can decouple the dependence of nuclear changes on hydrodynamics effects by studying the variations of the ratio between the individual number densities n_i and the total nucleon density:

$$Y_i = \frac{n_i}{n}, \tag{5.1}$$

that is the definition of nuclear abundance of the nuclear specie i. The total nucleon density can be written in terms of the mass number A_i (number of nucleons of the specie i) as $n = n_i / \sum A_i n_i$ and is approximated by the expression $n \approx \rho / m_u$, being m_u the unified atomic mass unit. Defining the charge number (number of protons present in the specie i) as Z_i one can rewrite the conservation of the baryon number and charge as:

$$\sum_i A_i Y_i = 1\,, \quad \sum_i Z_i Y_i = Y_e\,, \tag{5.2}$$

where $Y_e = n_e / n$ is the electron fraction representing the number of electrons per nucleon.

5.1.1 The nuclear statistical equilibrium (NSE)

In several cases of interest for nuclear astrophysics, the temperature of the stellar plasma is high enough for reactions mediated by the electromagnetic and strong interaction to be in competition with their inverse reaction. If a certain critical temperature is exceeded all reactions mediated by these forces will be in equilibrium with their inverse and the matter will reach the state denoted as nuclear statistical equilibrium (NSE). In these conditions the nuclear composition is independent of the individual reaction rates and the nuclear abundances evolution is uniquely defined by the thermodynamic conditions and nuclear properties of the system taking into account the restrictions imposed by the mass conservation

---

This Chapter is based on Ref. [79] and [80]

and charge neutrality of Eqs. (5.2). We explicitly mentioned the electromagnetic and strong forces because weak interactions occur at longer timescales and therefore do usually not reach an equilibrium. Besides the thermodynamic quantities (ρ, T) it is therefore necessary to keep track of the weak interaction history determining the evolution of the electron abundance $\dot{Y}_e$.

Using the conservation of mass and charge neutrality in NSE, we can express the chemical potential of any nucleus ${}^AZ$ with Z protons and $A - Z$ neutrons in equilibrium with free neutrons in terms of the proton and neutron chemical potentials

$$\mu(A, Z) = Z\mu_p + (A - Z)\mu_n \,. \tag{5.3}$$

Since nuclei obey the Maxwell-Boltzmann statistics, we can use Eqs. (4.30) and (4.31) to rewrite the chemical potential in terms of the abundances:

$$\mu_i = m_i c^2 + kT \ln \left[\frac{\rho}{m_u} \frac{Y_i}{G_i} \left(\frac{2\pi\hbar^2}{m_i kT} \right)^{3/2} \right] , \tag{5.4}$$

and by substituting the equation above in Eq. (5.3) we can express any nuclear abundance in terms of the proton (Y_p) and neutron (Y_n) ones:

$$Y(Z, A) = \frac{G({}^AZ) A^{3/2}}{2^A} \left(\frac{\rho}{m_u} \right)^{A-1} Y_p^Z Y_n^{A-Z} \left(\frac{2\pi\hbar^2}{m_u kT} \right)^{3(A-1)/2} \exp \left[\frac{Be(Z, A)}{kT} \right] , \tag{5.5}$$

where $Be(Z, A) = Zm_p + (A - Z)m_n - M(Z, A)c^2$ is the nuclear binding energy. Eq. (5.5), known as Saha equation, tells that depending on the range of temperature where the NSE takes place the system will favour the presence of free nucleons (high temperatures), α particles (intermediate regime) or nuclei with $Z/A \sim Y_e$ (low temperatures).

The NSE can be applied whenever the nuclear reaction timescales are short compared to the evolution timescale of the system. The NSE is then a good approximation for many scenario with high temperatures (e.g. matter ejected during the initial phases of neutron stars merger) or in slowly evolving systems (like for instance cold neutrons stars). As soon as we start to explore different astrophysical conditions nuclear abundances become sensitive to reaction rates and individual species get connected. This interdependence between nuclear species results in a system of equations describing the variation of abundances, that has to be solved by means of network calculations.

5.1.2 Abundances evolution

Nuclear reactions occurring in network calculations are usually divided in three different categories depending in the number of nuclei involved as reactants:

- Reactions involving only one nucleus, like for instance spontaneous decays, photoabsortions, electron capture and neutrino induced reactions only depend in the density of the target nucleus n_i and the characteristic decay rate λ_i. As we have seen in Sec. 4.3.2, their reaction rate can be generally written as:

$$r_i = \lambda_i n_i = \frac{\rho}{m_u} \lambda_i Y_i \,. \tag{5.6}$$

- Reactions involving two nuclei or one nucleus and one nucleon depend on the densities of both reactants. In this case the reaction rate is given by the expression:

$$r_{ij} = n_i n_j \langle \sigma v \rangle_{ij} = \left(\frac{\rho}{m_u} \right)^2 \langle \sigma v \rangle_{ij} Y_i Y_j \,. \tag{5.7}$$

- Finally, in triple reactions like the triple-α process the rates depend on the densities of the three species:

$$r_{ijk} = n_i n_j n_k \langle ijk \rangle = \left(\frac{\rho}{m_u}\right)^3 \langle ijk \rangle Y_i Y_j Y_k \,. \tag{5.8}$$

Considering these three types of reactions we can write the time derivative of the densities as:

$$\dot{n}_i \equiv \left.\frac{\partial n_i}{\partial t}\right|_{\rho=\mathrm{const}} = \sum_j \mathcal{N}_j r_j + \sum_{jk} \mathcal{N}_{jk} r_{jk} + \sum_{jkl} \mathcal{N}_{jkl} r_{jkl} \,, \tag{5.9}$$

or to the equivalent expression for the nuclear abundances:

$$\begin{aligned} \dot{Y}_i \equiv \left.\frac{\partial Y_i}{\partial t}\right|_{\rho=\mathrm{const}} = \dot{n}_i \frac{m_u}{\rho} = \\ \sum_j \mathcal{N}_j^i \lambda_j Y_j + \sum_{jk} \mathcal{N}_{jk}^i \frac{\rho}{m_u} \langle \sigma v \rangle_{jk} Y_j Y_k + \sum_{jkl} \mathcal{N}_{jkl}^i \left(\frac{\rho}{m_u}\right)^2 \langle \sigma v \rangle_{jkl} Y_j Y_k Y_l \,. \end{aligned} \tag{5.10}$$

The coefficients $\mathcal{N}^i$ are added in order to account for the proper number of nuclei involved in the reactions and they are given by the expressions:

$$\mathcal{N}_j^i = \pm N_i \,, \tag{5.11a}$$

$$\mathcal{N}_{jk}^i = \frac{\pm N_i}{|N_j|!|N_k|!} \,, \tag{5.11b}$$

$$\mathcal{N}_{jkl}^i = \frac{\pm N_i}{|N_j|!|N_k|!|N_l|!} \,. \tag{5.11c}$$

The numerator represents the number of nuclei destroyed ($-$) or created ($+$) in the reaction, while the denominator avoids double counting in reactions involving identical particles.

5.2 Network calculations for *r*-process nucleosynthesis

In astrophysical scenarios allowing for *r*-process nucleosynthesis, the set of differential equations (5.10) has to be solved for all the (thousands) nuclei involved taking into account all the possible reactions between them. As a first, realistic approximation one shall consider that only neutron captures, photodisintegrations, beta decays and fission are relevant for the nuclear transformations. For simplification we will not consider fission at this stage of the discussion, which allows to write Eq. (5.10) as:

$$\begin{aligned} \frac{dY(Z,A)}{dt} &= n_n \langle \sigma v(Z,A-1) \rangle_{n,\gamma} Y(Z,A-1) + \lambda_\gamma(Z,A+1) Y(Z,A+1) \\ &+ \sum_{j=0}^{J} \lambda_{\beta j n}(Z-1,A+j) Y(Z-1,A+j) \\ &- \left(n_n \langle \sigma v(Z,A) \rangle_{n,\gamma} + \lambda_\gamma(Z,A) + \sum_{j=0}^{J} \lambda_{\beta j n}(Z,A) \right) Y(Z,A) \,. \end{aligned} \tag{5.12}$$

In the equation above $n_n = Y_n \rho / m_u$ is the neutron density, $\langle \sigma v \rangle_{n,\gamma}$ the stellar neutron-capture rate, λ_γ the photodisintegration rate and $\lambda_{\beta j n}$ the β-decay rate with the emission of j neutrons (up to a maximum of J neutrons). If the neutron density varies slowly enough that we can consider it constant over the integration time-step, the system of equations in (5.12) can be solved sequentially starting from species with lower Z. We want to recall here that the principle of detailed balance allows to relate the photodisintegration rate with the inverse neutron capture rate [99]:

$$\lambda_\gamma(Z,A+1) = \frac{2G(Z,A)}{G(Z,A+1)}\left(\frac{A}{A+1}\right)^{3/2}\left(\frac{m_u kT}{2\pi\hbar^2}\right)^{3/2}\langle\sigma v(Z,A)\rangle_{n,\gamma}\exp\left[-\frac{S_n(Z,A+1)}{kT}\right], \quad (5.13)$$

being $G(Z,A)$ the partition function and $S_n(Z,A) = Be(Z,A) - Be(Z,A-1)$ the neutron separation of the ${}^AZ$ nucleus.

For some particular conditions Eq. (5.12) can be further simplified. The most relevant situations are the nucleosynthesis occurring in a $(n,\gamma) \rightleftarrows (\gamma,n)$ equilibrium and the steady flow approximation that we will explain in the next sections. These approximations correspond to particular situations of the r process and they can give some relevant insights about its general properties. However, realistic r-process calculations must be carried using dynamic calculations in order to deal with a larger variety of thermodynamical conditions.

5.2.1 The $(n,\gamma) \rightleftarrows (\gamma,n)$ equilibrium

If both the neutron density and temperature are high enough to provide enough reaction partners, we may expect that photodissociations and neutron captures occur on shorter timescales than the β decays that are mediated by the weak interaction. This assumption implies that we can neglect the contribution from β decay in Eq. (5.12):

$$\dot{Y}(Z,A) = \lambda_\gamma(Z,A+1)Y(Z,A+1) - \langle\sigma v(Z,A)\rangle Y(Z,A)n_n\,. \quad (5.14)$$

Since the high rates ensure the reaching of an equilibrium ($\dot{Y} = 0$) we can obtain an expression for the ratio of the abundances between neighbouring nuclei:

$$\begin{aligned}\frac{Y(Z,A)}{Y(Z,A+1)} &= \frac{n_n\langle\sigma v(Z,A)\rangle}{\lambda_\gamma(Z,A+1)} = \\ &n_n\frac{G(Z,A+1)}{2G(Z,A)}\left(\frac{A+1}{A}\right)^{3/2}\left(\frac{2\pi\hbar^2}{m_u kT}\right)^{3/2}\exp\left[\frac{S_n(Z,A+1)}{kT}\right],\end{aligned} \quad (5.15)$$

where the last equality was obtained using Eq. (5.13). Eq. (5.15) provides a very interesting result regarding the abundances distribution during the r-process. For each proton number Z, the abundance maxima can be found by approximating $Y(Z,A+1)/Y(Z,A)$ to one. Neglecting differences in the ratio of the partition functions and the mass number we get that the abundance maxima only depend on the neutron densities n_n, the temperature T and the neutron separation energy S_n. This means that for fixed thermodynamic conditions there is only one abundance maximum for each isotopic chain, and its neutron separation energy has to be the same for all the isotopic chains. The nucleus corresponding to the maximum is also known as waiting point (and the $(n,\gamma) \rightleftarrows (\gamma,n)$ equilibrium as waiting point approximation), since the material flow has to wait for this nucleus to β decay before proceeding towards heavier regions. The set of all the waiting points forms the so-called r-process path. Furthermore, by replacing T and ρ in Eq. (5.15) with typical conditions of r-process one gets that the r-process path proceeds along nuclei with constant neutron separation energy $S_n \approx 2-3$ MeV [80].

So far we have neglected β decays and consequently the connection between different isotopic chains. This can be easily taken into account by defining the total abundance for each isotopic chain $Y(Z)$:

$$Y(Z) = \sum_A Y(Z,A), \quad Y(A,Z) = P(Z,A)Y(Z)\,, \quad (5.16)$$

where $P(Z,A)$ are the individual population coefficients given by Eq. (5.15). Considering β-decays we can then express the (isotopic) abundance evolution as [100]:

$$\begin{aligned}\frac{dY(Z)}{dt} &= Y(Z-1)\sum_A P(Z-1,A)\lambda_\beta(Z-1,A) - Y(Z)\sum_A P(Z,A)\lambda_\beta(Z,A) \\ &= Y(Z-1)\lambda_\beta^{\text{eff}}(Z-1) - Y(Z)\lambda_\beta^{\text{eff}}(Z)\,,\end{aligned} \tag{5.17}$$

being $\lambda_\beta^{\text{eff}}(Z)$ an effective isotopic β-decay rate. One has that Eq. (5.17) solely allows to keep track of changes in nuclear abundances, since the abundances of the individual isotopes can be obtained using Eq. (5.15).

5.2.2 The steady flow approximation

If the r process occurring in $(n,\gamma) \rightleftarrows (\gamma,n)$ equilibrium lasts longer than the β-decay lifetimes of the involved nuclei, the abundances will reach a steady state known as β flow [101]:

$$Y(Z-1)\lambda_\beta^{\text{eff}}(Z-1,A) = Y(Z)\lambda_\beta^{\text{eff}}(Z,A)\,. \tag{5.18}$$

This equilibrium between nuclei with charge number Z and $Z+1$ is always reached if the variations on neutron densities are much slower than the β-decay lifetimes and even without $(n,\gamma) \rightleftarrows (\gamma,n)$ equilibrium. The peaks around $A = 130$ and 195 observed in the solar r-process abundances are an example of accumulation of material due to the long β-decay lifetimes of nuclei with magic neutron numbers $N = 82$ and 126 [80].

5.2.3 Dynamic calculations

In realistic scenarios one finds large variations of neutron densities during the r-process nucleosynthesis, that do not allow the application of the waiting point approximation. Also neutron captures and beta decays may have an impact in r-process dynamics, which cannot be taken into account in the steady flow approximation. More sophisticated network calculations spanning a larger range of astrophysical conditions can be carried out by means of dynamic calculations. In dynamical models the r-process path is given by the competition between neutron captures and beta decay rates calculated for each nucleus as a function of the baryon density, temperature and neutron density of the system. This means that in order to perform dynamic calculations we need a detailed knowledge of the nuclear cross sections for the whole range of astrophysical conditions where the r process takes place.

In dynamic calculations one has to solve the discretized version of the network equations (5.12):

$$\frac{d\vec{Y}}{dt} = F(\vec{Y})\,, \tag{5.19}$$

where $\vec{Y} = \{Y_i\}$ is the abundances vector at a given time t:

$$\begin{aligned} t_0 &\longrightarrow \vec{Y}_0\,, \\ t_0 + \Delta t &\longrightarrow \vec{Y}_0 + \delta\vec{Y}\,. \end{aligned} \tag{5.20}$$

The main problem in solving Eq. (5.19) is that the large variety of timescales spanned by the electromagnetic, strong and weak interactions makes the network system of equations extremely stiff.

Therefore one has to use an implicit scheme in order to solve the system of equations like for instance the Euler-backward-differentiation, where the evolution of the abundances is expressed as:

$$\frac{\delta\vec{Y}}{\Delta t} = F(\vec{Y} + \delta\vec{Y})\,. \tag{5.21}$$

Since we do not know the quantity $\delta\vec{Y}$ we have to solve this set of non-linear equations by finding the zeros of the function

$$G(\delta\vec{Y}) = F(\vec{Y} + \delta\vec{Y}) - \frac{\delta\vec{Y}}{\Delta t} = 0\,. \tag{5.22}$$

In practice purposes this is done by making a linear approximation at each single step:

$$F(\vec{Y}) + \frac{\partial F(\vec{Y})}{\partial \vec{Y}}\delta\vec{Y} - \frac{\delta\vec{Y}}{\Delta t} = 0\,, \tag{5.23}$$

and this system of linear equations is solved until the solutions convergence within the required precision $|\delta Y| < \epsilon$. This method is equivalent to the Newton-Raphson method where the change in the abundances is found iteratively:

$$\delta Y_{n+1} = \delta Y_n - \frac{G(\delta Y_n)}{G'(\delta Y_n)}\,, \tag{5.24}$$

but the verbatim usage of the equation above is avoided since it requires the inversion of the G matrix which is not efficient. Obviously, the larger the network is the bigger the matrix equation to be solved becomes. In most of the cases the Jacobian matrix $\partial F_i / \partial Y_k$ used in the Newton-Raphson method is rather sparse even though fission jeopardizes this sparseness by connecting species with different mass and charge number.

5.3 Energy generation

The energy liberated by a nuclear reaction is the difference in the rest mass energy between reactants and products inducing a change in the total kinetic energy. Thus we can compute the total nuclear energy released in the astrophysical plasma by computing the change in the abundances of all the single species, which in turn allows to write the thermonuclear energy rate as:

$$\dot{q} = -\sum_i \frac{m_i c^2}{m_u} \frac{dY_i}{dt}\,, \tag{5.25}$$

with $m_i c^2$ being the rest mass energy of the i-th species. The first law of thermodynamics allows to rewrite the equation above in terms of the change of the energy per nucleon ε and the nucleon density $n = \rho / m_u$:

$$\dot{q} = \frac{d\varepsilon}{dt} - \frac{P}{n^2}\frac{dn}{dt} = c_V \frac{dT}{dt} + \left(\frac{d\varepsilon}{dn} - \frac{P}{n^2}\right)\frac{dn}{dt}\,, \tag{5.26}$$

where $c_V = d\varepsilon / dT$ is the specific heat per nucleon at constant temperature. From this last equation we get that the evolution of the temperature with time is given by the expression:

$$\frac{dT}{dt} = \frac{1}{c_V}\left[\dot{q} - \frac{1}{\tau_n}\left(\frac{P}{n} - n\frac{d\varepsilon}{dn}\right)\right]\,, \tag{5.27}$$

where $\tau_n = 1/\lambda_d = n dt/dn$ is the expansion timescale. One see therefore that the change of the energy balance induced by nuclear reactions can affect the dynamics of the r process by changing the temperature of the system, and this should be consistently taken into account at each step of the evolution.

5.4 Characteristic quantities in r-process nucleosynthesis

In r-process calculations we track the evolution of the abundances from the initial nuclear statistical equilibrium until most of the material has decayed back to stability ($\sim$ Gy). As time evolves we want to keep track of variations in the thermodynamic and nuclear properties of the material, which poses the problem of identifying the most relevant quantities describing our system besides the neutron density n_n and the electron fraction Y_e already introduced before.

We will start defining the averaged proton and neutron number as:

$$\langle Z \rangle = \frac{\sum_{Z,A} Z Y(A,Z)}{\sum_{Z,A} Y(A,Z)}, \quad \langle A \rangle = \frac{\sum_{Z,A} A Y(A,Z)}{\sum_{Z,A} Y(A,Z)}, \tag{5.28}$$

where the sum is restricted to "heavy" nuclei with $Z > 2$ and $A > 4$ (i.e., all nuclei heavier then ^{4}He). Both quantities determine the most representative nucleus at a certain stage of the evolution. Besides that, one can determine the number of times that the material reaches the fissioning region and decay back to lighter nuclei (fission cycles) by studying the evolution of $\langle Z \rangle$ with time. From the previous definition of heavy nuclei one defines the abundance of heavy (or "seed") nuclei as:

$$Y_h = \sum_{\substack{A>4 \\ Z>2}} Y(A,Z), \tag{5.29}$$

which leads to another crucial quantity in r-process calculations, the so-called neutron-to-seed ratio:

$$R_{n/s} = \frac{Y_n}{Y_h}. \tag{5.30}$$

This quantity indicates how many free neutrons can be captured in averaged by a seed nucleus, and together with the neutron densities determines whether the r process can successfully proceed to heavy nuclei. For example, if we want to produce ^{238}U starting from ^{52}Fe we will need a neutron-to-seed ratio of the order of $R_{n/s} = 186$. At the time when $R_{n/s}$ is equal to one we say that the r-process freezes out, since seed nuclei on average cannot capture more than neutron each.

Other important quantities are the averaged rates, that are helpful for establishing which decay is dominating at each stage of the evolution. The average rate for a reaction of type i can be defined as:

$$\langle \lambda_i \rangle \equiv \left\langle \frac{1}{\tau_i} \right\rangle = \frac{\sum_{Z,A} \lambda_i(Z,A) Y(Z,A)}{\sum_{Z,A} Y(Z,A)}, \tag{5.31}$$

being $\lambda_i(Z,A)$ the rate of the nucleus $^A Z$ (where for the case of neutron captures one has that $\lambda_{n,\gamma} = n_n \langle \sigma v(Z,A) \rangle_{n,\gamma}$). Obviously we can trivially defined an averaged timescale for a certain type of reaction τ_i as the inverse of its averaged rate λ_i. The averaged reaction timescales allow to define the end of the r process as the time when the beta decay rate equals the averaged neutron capture rate $\tau_{\lambda,n} = \tau_\beta$. After this moment the beta decay becomes the dominating decay channel and the material starts to decay towards the valley of stability.

5.5 Hydrodynamical trajectories

In standard r-process calculations the evolution of $\sim$ 6000 nuclei is obtained by solving the system of equations described in Sec. 5.2.3 assuming a variation in temperature and density with time. These can be obtained from simple analytical expressions, steady state approximation or full hydrodynamical simulations. In this thesis we followed the last approach and performed *r*-process calculations based on fluid trajectories extracted from three-dimensional relativistic hydrodynamical simulations of neutron star (NS) mergers.

We studied the case of two neutron stars with gravitational masses of $1.35 \mathrm{M}_\odot$. In this configuration most of the unbound material is ejected from the contact interface, being the extremely neutron-rich ejecta originating from the inner NS crust. The evolution of the ejecta could be followed only up to a time t_0 (of the order of tens of milliseconds) due to the time-step limitations of the simulations. Thus, after t_0 we assumed an homologous expansion of the form:

$$\rho(t) = \rho_0 \left(\frac{t_0}{t} \right)^3 , \tag{5.32}$$

with $\rho_0 = \rho(t = t_0)$.

The NS mergers (NSM) trajectories obtained from these simulations were extensively studied in [102] for a wide range of initial densities. In this work the authors found that the trajectories can be classified depending on the resulting competition between the depletion rate (λ_n) due to neutron captures on seed nuclei and the hydrodynamical expansion rate (λ_d):

$$\lambda_n = \frac{d(\ln Y_n)}{dt} \approx \frac{\rho Y_n}{m_u R_{n/s}} \overline{\langle \sigma v \rangle}_{n,\gamma} , \quad \lambda_d = -\frac{d(\ln \rho)}{dt} = \frac{3}{t} , \tag{5.33}$$

where $\overline{\langle \sigma v \rangle}_{n,\gamma}$ is the neutron-capture rate averaged over the seed nuclei and $R_{n/s}$ the neutron to seed ratio. For trajectories with $\lambda_n \gtrsim \lambda_d$ during the whole duration of the *r*-process ("slow trajectories"), all the initial neutrons can be captured resulting in rather robust final abundances. Conversely, trajectories where the material expands extremely fast (and therefore called "fast trajectories") result in $\lambda_d \gtrsim \lambda_n$, leaving free neutrons at the end of the *r* process and producing a large spread in the final abundances distribution. In this thesis we will present results obtained using slow trajectories, since they are the most relevant for *r*-process calculations.

6 Benchmark against experimental data

One of the main aims of this thesis was to study the fission properties of superheavy nuclei, with a particular focus to those that play a relevant role during the r-process nucleosynthesis. But before exploring the superheavy landscape in the region far from stability where the r process takes place, we want to estimate the quality of our results in comparison to the available experimental data. An important point to address is the sensitivity of our calculations to variations in the fission barriers, collective inertias and the rest of ingredients entering in the estimation of the reaction rates within the Hauser-Feshbach statistical model. The study of these variations can help to determine which models better reproduce the experimental data but also to understand the nuclear inputs that may have a larger impact during the r-process nucleosynthesis. Thus in this Chapter we will perform an exhausting benchmarking of our results against the available experimental data and we will assess the level of accuracy achieved in our calculations using different energy density functionals, collective inertia schemes, nuclear level densities and gamma-ray strengths. The first part of this Chapter is dedicated to the binding energies and neutron separation energies. Later we will discuss the agreement of fission barriers and spontaneous fission lifetimes. Finally, in the last sections we will present the results for the calculation of the neutron induced cross sections and the alpha decay properties of superheavy nuclei.

6.1 General considerations on fission observables

It is important to notice that there are only two observables related to fission: the spontaneous fission lifetimes and the induced fission cross sections. The former describe the fissioning of a nucleus in its ground state while the cross sections characterize the probability to penetrate the fission barrier from an excited state. Since fission is a tunnelling process its probability depends exponentially on the fission barrier height and the collective inertia. In general when the fission probabilities are small one has that the lifetimes and induced fission cross sections are very sensitive to variations in the different quantities used for the calculation of the fission probability. As we will see during this chapter, this is the case for the spontaneous fission lifetimes of light actinides, where the high stability of the nucleus leads to a large span in the theoretical predictions. But in r-process calculations we are interested in nuclei where fission is a competing decay with neutron captures, which means that the fission probabilities are large because nuclei are excited close to the fission barrier. The theoretical description of systems fissioning close to the fission barrier is much simpler, because the number of degrees of freedom that have a relevant impact in the fission probability is rather small compared to nuclei that are stable against fission.

It is important to explicitly state that the fission barrier, a crucial quantity in all fission theoretical calculations, is not an observable. This is because the experimental value of the fission barrier is extracted from induced fission cross sections (mainly photo-induced, neutron-induced and electron capture delayed fission) assuming a particular level density and shape of the fission barrier (see [104] for a recent review on experimental techniques). This means that the experimental fission barrier is a model dependent quantity and therefore not an observable.

6.2 Binding energies

We computed the binding energies of nuclei with $84 \leq Z \leq 120$ and $118 \leq N \leq 250$ using the BCPM EDF and the D1S, D1N and D1M Gogny parametrizations within the Perturbative Nucleon

---

Some of the results presented in this Chapter are extracted from Ref. [103].

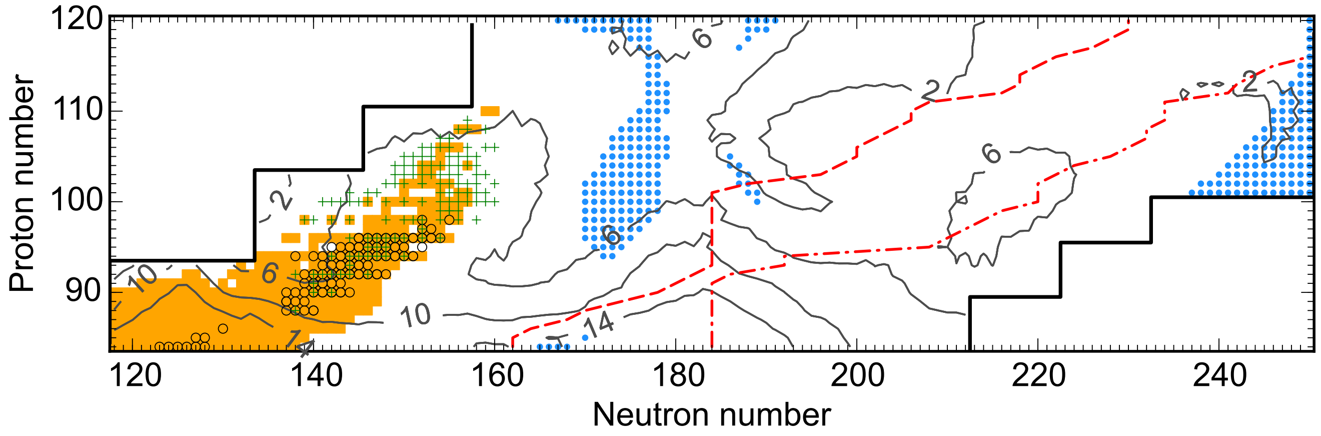

Figure 6.1: Region of the nuclear landscape explored in this thesis. Nuclei present in the AME2012 mass table evaluation [105] are depicted with orange squares. Nuclei with experimentally measured fission barriers [89, 106] and spontaneous fission lifetimes [107, 108] are marked with open circles and crosses, respectively. Nuclei for which the BCPM interaction predicts an oblate-deformed ground state are depicted with solid circles. Dashed and dot-dashed lines represent the heaviest isotope of each element with $S_n \gtrsim 2$ and $S_n \gtrsim 0$ MeV, respectively. Contour lines show the highest predicted fission barrier predicted by the BCPM EDF in MeV. Figure taken from Ref. [103].

Addition Method (PNAM) described in Sec. 2.4. Fig. 6.2 shows the differences between theoretical and experimental [105] binding energies obtained for the four functionals as a function of mass number (upper panels) and neutron excess $N - Z$ (lower panels). In these plots the D1S EDF shows a drift of the binding energies with increasing mass number and neutron excess. This trend is cured in the D1N and D1M EDF's by fitting the functionals to very-neutron rich systems that in turn fixes the symmetry energy. The final result is a flatter pattern, where the deviations are less sensitive to increasing mass number and neutron excess. Thus, one interesting consequence of computing fission barriers using different EDF's is that we can study possible correlations between the shape of fission barriers and the symmetry energy. This aspect will be addressed in Sec. 6.3 exploring the variations in the fission barriers predicted by the different EDF's.

It is important to recall that r-process calculations are more sensitive to changes in neutron separation energies (S_n) rather than absolute binding energies, since the former ones enter in the calculation of the reaction cross sections. It is therefore useful to look at the differences in the predictions of S_n. For this purpose, Fig. 6.3 shows the two-neutron separation energies as a function of the neutron number and Fig. 6.4 shows the same quantity but as a function of the proton number. In Fig. 6.4 the lines connecting nuclei in the same isotopic chain show some disconnections between $186 \leq N \leq 200$, representing unstable nuclei in the corresponding model. An example of such nuclei is given in Fig. 6.5, where the binding energy as a function of the deformation predicted by the BCPM EDF is plotted for four different nuclei. These nuclei have a vanishing or very small fission barrier and can be considered unstable against fission. They are placed in a region of transition between spherical and superdeformed prolate nuclei, where the spherical minimum has disappeared and the prolate minimum is still not developed.

Fig. 6.3 and 6.4 show that all the models predict jumps in the neutron separation energies at the shell closures $N = 126$ and 184 and, in smaller magnitude, around neutron numbers $N = 152$ and $N = 162$ (see dashed vertical lines in Fig. 6.3). These jumps in the neutron separation energies can be very important for the accumulation of material during the r-process nucleosynthesis. This is because the neutron capture cross sections of these nuclei decrease dramatically due to the sudden decrease in the neutron separation energies. Due to this, nuclei in these regions suffer multiple beta decays moving the neutron captures and the r-process path closer to stability where the half-lives are longer and material

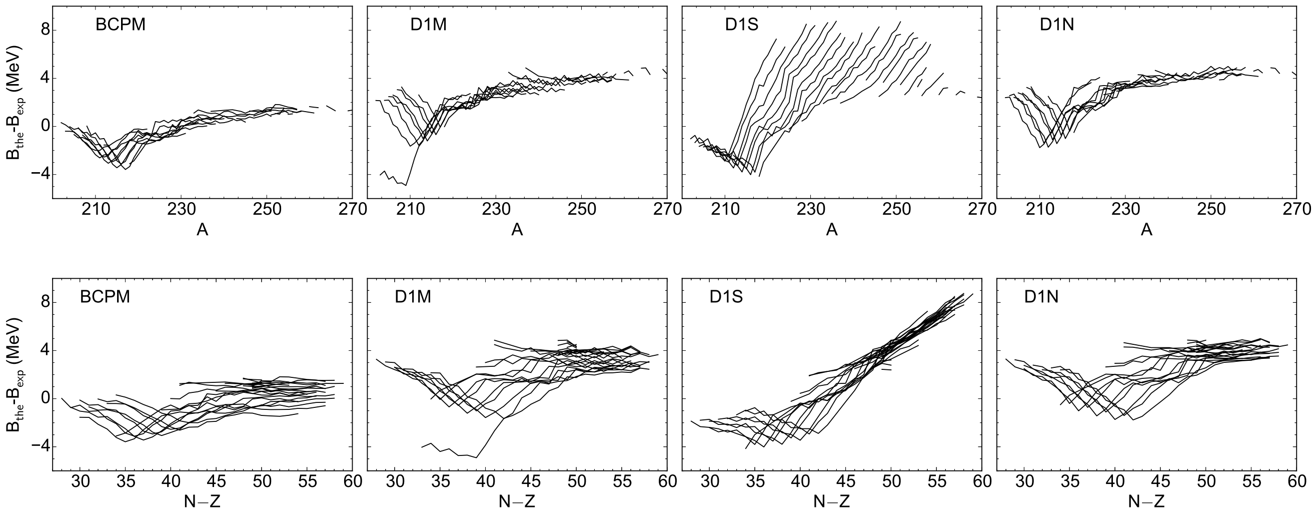

Figure 6.2: Binding energies differences $B_{\text{the}} - B_{\text{exp}}$ in MeV for the four energy density functionals as a function of the mass number A (upper plots) and the neutron excess $N - Z$ (lower plots). Lines connect nuclei in the same isotopic chain.

Functional	$\sigma(Be)_{ee}$ (MeV)	$\sigma(Be)$ (MeV)	$\sigma(S_n)_{ee}$ (MeV)	$\sigma(S_n)$ (MeV)
BCPM	1.207	1.288	0.304	0.280
D1M	2.787	2.846	0.391	0.432
D1S	4.152	4.237	0.542	0.610
D1N	3.147	3.149	0.431	0.431

Table 6.1: Root mean square deviations in MeV between the atomic mass evaluation AME2012 [105] and predictions for BCPM, D1M, D1S and D1N models for nuclei with $84 \leq Z \leq 120$ and $118 \leq N \leq 250$. The first pair of columns refer to the binding energies (Be), the second pair to the neutron separation energies (S_n). The first and the third column refer only to even-even nuclei.

accumulates. In order to get an estimation of the magnitude of the jump in the two-neutron separation energy one can compute the shell gap, defined as the difference in the two-neutron separation energies of two neighbouring nuclei $\Delta_{2n}(Z,N) = S_{2n}(Z,N) - S_{2n}(Z,N+2)$. In Fig. 6.6 we compare the energy shell gap predicted by the four functionals as a function of proton number for neutron numbers 152, 162 and 184. We conclude that the four functionals predict very similar trends of the two-neutron separation energies, with comparable values of the energy shell gaps and a rather smooth behaviour of S_{2n}. It is worth to mention that all the models predict the disappearance of the shell closure $N = 184$ around $Z = 102$, that is reflected in the reduction of the gap at $N = 184$ in Fig. 6.4.

For a more quantitative comparison Table 6.1 shows the rms deviations for binding energies and neutron separation energies between the four functionals and the atomic mass table evaluation AME2012 [105]. From this table and Fig. 6.2 one can conclude that BCPM gives the best agreement with experimental data and that the D1N and D1M EDF's provide very similar results of binding energies. As we already mentioned before, it will be interesting to see if this agreement is somehow reflected also in the fission properties predicted by these functionals.

For some nuclei around the shell closure $N = 184$ the models predict a strange behaviour of the neutron separation energies visible in Fig. 6.4. The two-neutron separation energies show an irregular staggering that is reflected in sudden changes of the energy gap plotted in the right panel of Fig. 6.6. Looking in detail to our calculations we traceback these irregularities to the rotational energy correction computed using the approximation described in Sec. 2.3.5. In turn this approximation overestimates

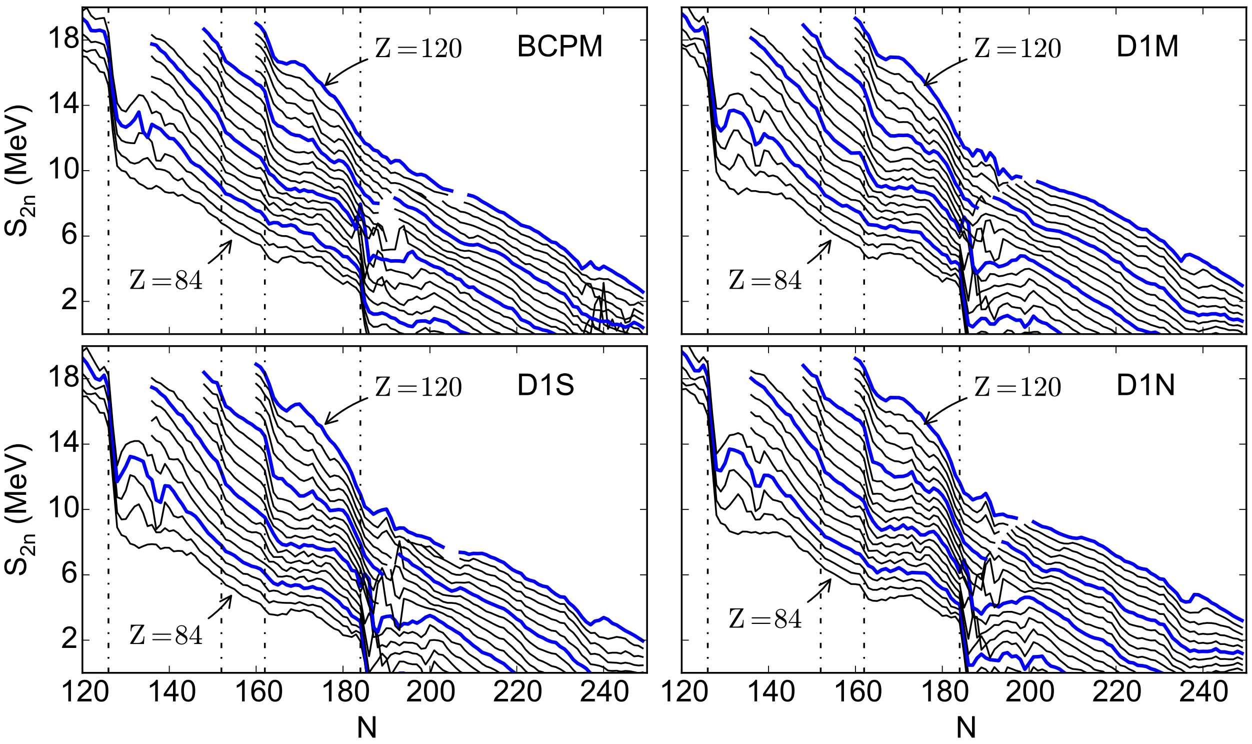

Figure 6.3: Two-neutron separation energies in MeV as a function of the neutron number predicted by the different energy density functionals. Solid lines connect nuclei with the same proton number. Nuclei with a proton number equal to 90, 100, 110 and 120 are depicted with thick blue lines. Dashed vertical lines denote the neutron number 126, 152, 162 and 184.

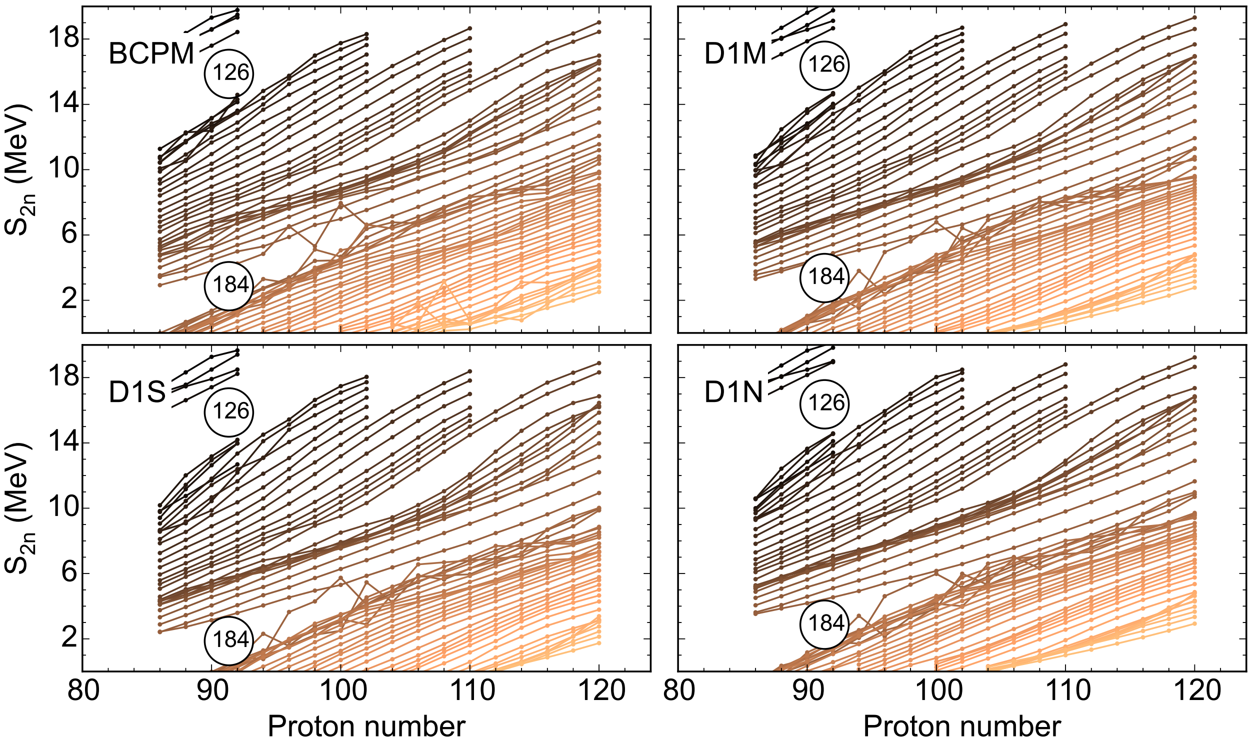

Figure 6.4: Two-neutron separation energies in MeV as a function of the proton number predicted by the different energy density functionals. The shell closures $N = 126$ and $N = 184$ are also indicated.

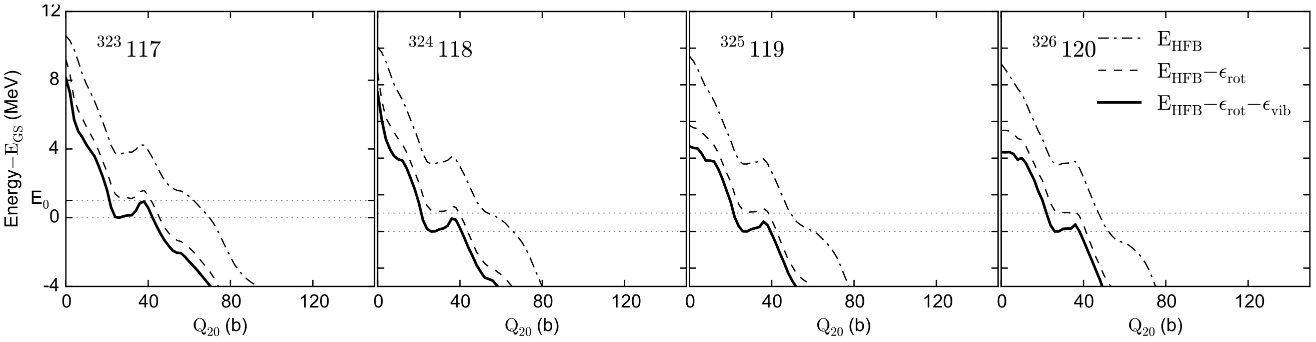

Figure 6.5: Fission barrier n MeV as a function of the quadrupole deformation of nuclei ^{323}117, ^{324}118, ^{325}119, ^{326}120 computed with the BCPM interaction. The lines show the different contributions to the potential energy surface $\mathcal{V}(Q_{20})$ of Eq. (3.52).

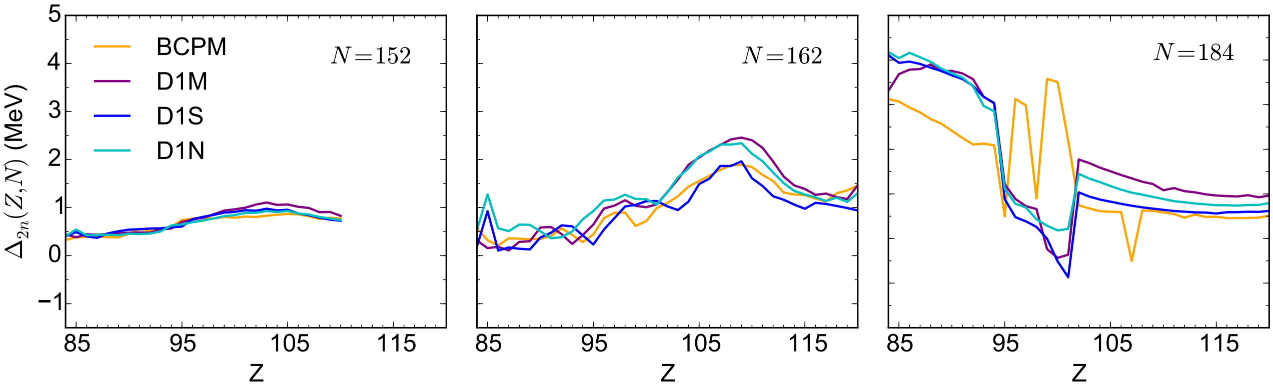

Figure 6.6: Energy shell gap $\Delta_{2n}(Z,N) = S_{2n}(Z,N) - S_{2n}(Z,N+2)$ in MeV as a function of the proton number predicted by the different energy density functionals for nuclei with $N = 152$ (left panel), $N = 162$ (middle panel) and $N = 184$ (right panel).

the rotational correction at small deformations ($Q_{20} = 0 - 200$ fm^2) by 1 MeV or more in nuclei above $N = 184$. This overestimation is induced by octupole deformations in the ground state of the nucleus that increase the rotational energy correction producing a staggering in the neutron separation energies and the shell gaps. These irregularities disappear when the nucleus is constraint to a spherical shape or when the binding energies are computed without rotational correction. This is shown in Fig. 6.7, where the shell gaps predicted by BCPM and D1M with the rotational energy correction are compared to those obtained without including the correction. It is interesting to notice that the rotational correction does not have any relevant impact in the energy gap of deformed nuclei ($N = 152$ and 162), while it strongly reduces Δ_{2n} in spherical ones with $N = 184$. From this study we conclude that the staggering observed in the neutron separation energies and shell gaps around the shell closure is an artifact induced by our approximate treatment of the rotational correction.

This spurious contribution of the rotational energy opens the more general discussion regarding the limits of HFB theory in describing nuclei close to shell closures. The HFB model is known for its capability to describe deformed nuclei, where the large level densities around the Fermi level allow for pairing correlations. For nuclei with protons and/or neutrons close to magic numbers the HFB picture reduces to HF and calculations become very sensitive to the predictions of single-particle energies, that in general are rather poor described in energy density functionals. In Chapter 8 we will see that these nuclei play an important role during the *r*-process nucleosynthesis. For example the magic neutron number $N = 184$ is responsible for the accumulation of material in the fissioning region at $A \sim 280$. Our models predict that this shell closure disappears for nuclei with $Z \gtrsim 96$, that is the region where

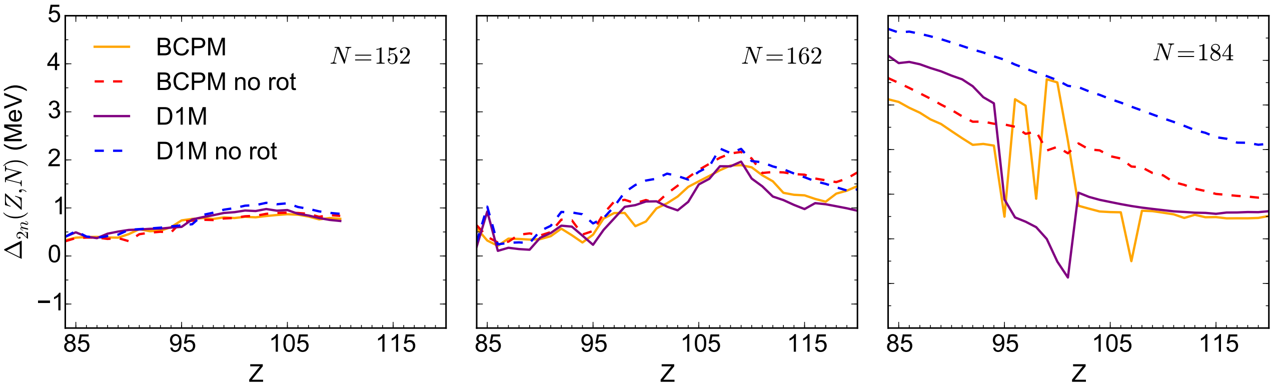

Figure 6.7: Energy gap in MeV as a function of the proton number predicted by BCPM and D1M for nuclei with $N = 152$ (left panel), $N = 162$ (middle panel) and $N = 184$ (right panel). Dashed lines show the results obtained without rotational correction.

Functional	$\sigma(Be)$ (MeV)	$\sigma(Be)_{\mathrm{WR}}$ (MeV)	$\sigma(S_n)$ (MeV)	$\sigma(S_n)_{\mathrm{WR}}$ (MeV)
BCPM	1.288	2.372	0.280	0.365
D1M	2.846	5.489	0.432	0.579
D1S	4.237	6.468	0.610	0.715
D1N	3.149	5.826	0.431	0.581

Table 6.2: Root mean square deviations in MeV between the atomic mass evaluation AME2012 [105] and predictions for BCPM, D1M, D1S and D1N models for nuclei with $84 \leq Z \leq 120$ and $118 \leq N \leq 250$. The first pair of columns refer to the binding energies (Be), the second pair to the neutron separation energies (S_n). The second and the fourth column are the results obtained without rotational corrections (WR).

we predict the r-process path to be terminated by the neutron-induced fission. Thus in order to avoid a propagation of the artifacts in the neutron separation energies into the r-process abundances it is necessary to remove them. A possibility would be to go beyond the mean-field prescription and make a projection into good angular momentum. These type of calculations are beyond the scope of this work, but they should deserve further efforts if we want to improve the quality of the nuclear input in r-process calculations. Concerning the results of this thesis, we opted for computing the neutron induced reaction rates using the neutron separation energies obtained without the rotational correction. For a quantitative estimation of the impact of removing the rotational correction Table 6.2 summarizes the deviations between experimental data and theoretical calculations of binding and neutron separation energies. The removal of the rotational correction worsen the quality of the results, but we notice that the impact in the neutron separation energies is relatively small which in turn gives a certain confidence in the use of these masses for the computation of neutron induced reaction rates.

6.3 Fission barriers and isomer excitation energies

We move now to the comparison between theoretical fission barriers and experimental data. Even though the fission barriers are not observable but model dependent quantities, the comparison can still provide a rough evaluation of the agreement between theory and experiment regarding the shape of the fission barrier. The fission barrier height is defined as the energy difference between the saddle point and the ground state. For a double humped barrier, the barrier closer to the ground state is defined as inner fission barrier while the farer is the outer fission barrier. The minimum between these two saddle points

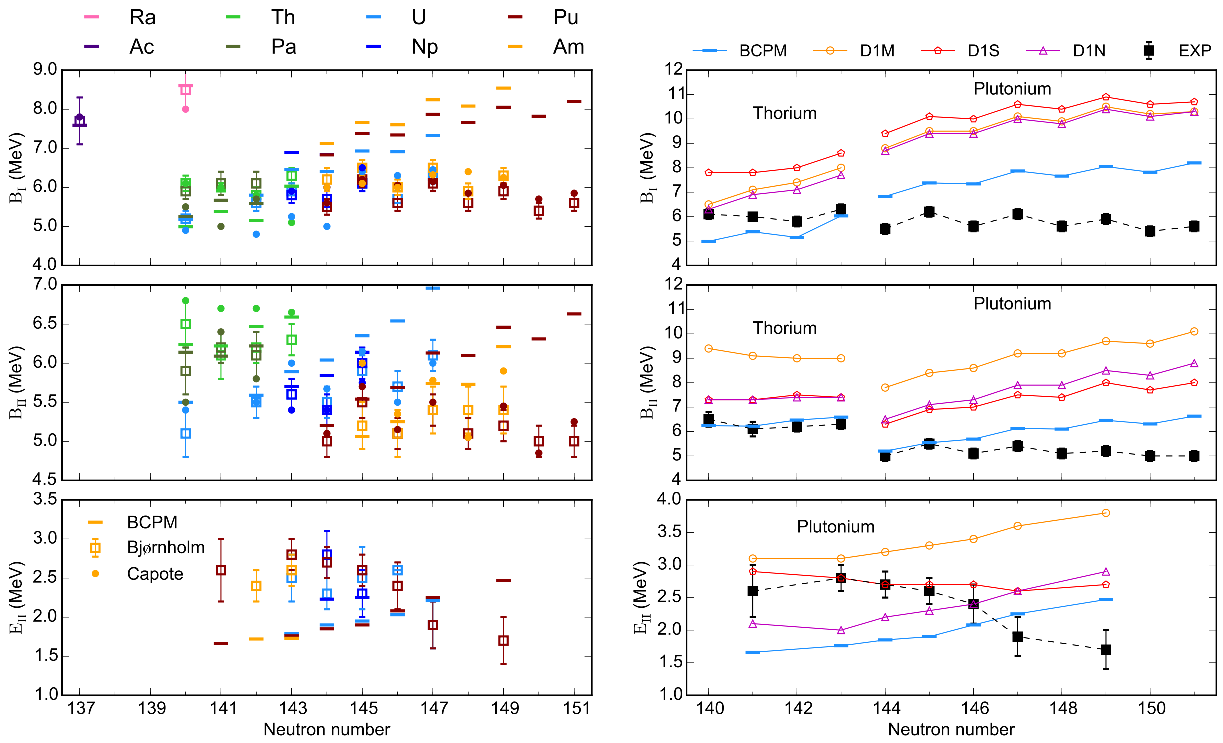

(a) **(b)**

Figure 6.8: Left panels: inner fission barrier height (upper panels), outer fission barrier (middle panel) and isomer excitation energies (lower panel) of six experimental known isotopic chains. The results from BCPM (horizontal lines) are compared with experimental data of Bjørnholm [89] (open squares) and Capote [106] (bullets). Right panels: same as left panels but comparing predictions from the different functionals with experimental data of Bjørnholm [89] for the Plutonium and Thorium isotopic chains.

is referred as isomer excitation energy. Fig. 6.8 shows the comparison between the theoretical predictions of barriers heights and isomer excitation energies with the available experimental data of Bjørnholm and Lynn [89] and Capote *et al.* [106]. The left panels of Fig. 6.8 show the comparison between the BCPM and experimental data for the inner (B_I) and outer (B_{II}) fission barrier height and the isomer excitation energy (E_{II}). We find that BCPM reproduces the B_I, B_{II} and E_{II} experimental values of Bjørnholm and Lynn [89] with a rms deviation of 1.29, 0.81 and 1.22 MeV respectively. The discrepancies with the data set of Capote *et al.* [106] are slightly larger: 1.51 MeV for B_I and 0.97 MeV for B_{II}, while no data is available for E_{II}. The differences in these values and in the experimental data plotted in Fig. 6.8 reiterate the model dependency in the value of the experimental fission barriers.

In all the models the largest differences are found in the uranium, plutonium and americium isotopes. For these nuclei the EDF's tend to describe a marked increase of the three parameters with increasing neutron number, while experimental data show a flatter trend. In general we find that all the models predict very similar trends of the fission barriers heights and with a spread around 3 MeV. This is shown in the right panels of Fig. 6.8, where the fission barrier heights and isomer excitation energies of two isotopic chains are plotted as a function of the neutron number. In the picture of a nucleus as a liquid drop the evolution of the energy with deformation is governed by the competition between the Coulomb repulsion of protons in the nucleus and the increasing surface energy, the latter one given by the surface energy coefficient in semi-infinite nuclear matter a_s [109]. Functionals with a larger value of a_s are then expected to predict higher fission barriers heights due to their larger surface energy [44]. Regarding the models employed in this thesis, the functional with the largest a_s is D1S (20 MeV [110]) followed by D1N (19.3 MeV [45]) and BCPM (17.7 MeV [50]). We notice that the Gogny values meet the empirical data $a_s = 21 \pm 2$ MeV[111] extracted from the parametrization of the experimental binding energies using the semiempirical mass formula [112]. For the D1M model there is no available a_s because semi-infinite nuclear matter calculations using this interaction have not been performed yet. Looking at inner fission barrier heights in Fig. 6.8 we notice that indeed the differences between the functionals reflect the hierarchy of a_s: D1S predict the highest barrier, BCPM the lowest ones and D1N is somewhat in between. However, this is not the case for the outer barrier, where D1N predict larger barriers than D1S for the heaviest Plutonium isotopes. A possible explanation for this failure of the surface argument is that since the outer fission barriers are placed at high deformations, the quantum shell effects play an important role and therefore the classical argument of Coulomb repulsion versus surface energy does not apply anymore. Indeed, it would be very interesting to perform semi-infinite nuclear matter calculations as those presented in [109] using the D1M EDF and extract its a_s value. D1M predicts B_I very similar to D1N and lower than D1S but its B_{II} are the highest ones. Therefore a value of a_s similar to the D1N functional will confirm this decoupling between the semiclassical regime of the inner fission barrier and the quantum effects governing the height of the outer fission barrier.

The symmetry energies of the models are rather different: 32.0 MeV for D1S [110], 31.9 MeV for BCPM [50], 29.3 for D1N [45] and 28.554 MeV for D1M [46]. With the exception of D1M the other functionals predict a value of the symmetry energy in agreement with the empirical range of $29.0 - 32.7$ MeV obtained in Ref. [113]. Comparing these values with the plot of the fission barriers 6.8 we cannot conclude that there is a clear correlation between these two quantities. For example, neither the D1S and BCPM nor D1M and D1N predict similar fission barriers despite the fact that they have similar symmetry energies. Also all the functionals predict exactly the same trend with neutron number, despite the fact that some of them have a very different symmetry energy. It seems therefore that there is not a correlation between the symmetry energy and the fission barrier that goes beyond the correlation between the symmetry energy and the surface coefficient (see [114] for a discussion regarding the correlation between these two quantities in the context of EDF). We have to mention that the range of nuclei taken in this study is rather small and one should explore a larger set of nuclei in order to extract more solid conclusion. Therefore in Sec. 7.1 and 7.2 we will come back to this discussion of the surface and symmetry energy while studying the fission properties of nuclei in the superheavy landscape .

It is important to notice that none of the models used in this work is able to reproduce the experimental trend of the E_{II}. The magnitude and location of these superderfomed minima depend on details of single particle states, the strength of pairing energy and spin-orbit interaction as well as Coulomb and the surface energy [115]. Moreover some recent studies show that the fission isomer is also sensitive to the surface symmetry energy [35, 116]. It is therefore difficult to understand which part of the functional is responsible for the wrong trend of the isomer (and if there is only one...), as it is testified by the difficulties in reproducing this observable even when experimental data is explicitly included in the parametrization of the functional [35].

Regarding the agreement between experimental fission barriers heights and theoretical predictions, we notice that the PNAM method produces a staggering in the fission barrier heights that is present also in the experimental results. We also notice that the inner fission barriers are systematically overestimated in our calculations. This is probably due to the fact that we are imposing axial symmetry in all the calculations, since several studies showed that triaxiality can reduce the inner fission barrier height up to 2 MeV [31, 33, 72], that in our case will improve the agreement with the experimental data.

6.4 Spontaneous fission lifetimes

After discussing the binding energies and fission barriers we will compare the spontaneous fission lifetimes predicted by our models with the experimental data. Before starting the discussion we briefly recall how spontaneous fission lifetimes are computed within the WKB method. All the equations presented here were detailed described in Chapter 3. The spontaneous fission lifetimes t_{sf} are given by the expression (3.5):

$$t_{\mathrm{sf}}[s] = 2.86 \times 10^{-21}(1 + \exp(2S)) \,, \tag{6.1}$$

being S the integral action computed along the fission path $L(Q_{20})$ between the classical turning points a and b:

$$S(L) = \int_a^b dQ_{20} \sqrt{2\mathcal{M}(Q_{20})[\mathcal{V}(Q_{20}) - (E_0 + E_{\mathrm{GS}})]} \,. \tag{6.2}$$

In the equation above $\mathcal{V}(Q_{20}) - E_{\mathrm{GS}}$ is the fission barrier, $E_0 = 0.5$ MeV [117] the energy of the collective ground state and $\mathcal{M}(Q_{20})$ the collective inertia. The latter one can be computed using either the ATDHFB or the GOAGCM schemes. Within the perturbative cranking approximation the expression of the collective inertias for the different schemes is given by Eqs. (3.28) and (3.42):

$$\mathcal{M}_{\mathrm{ATDHFB}}(Q_{20}) = \frac{\mathrm{M}_{-3}}{2(\mathrm{M}_{-1})^2} \,, \tag{6.3}$$

$$\mathcal{M}_{\mathrm{GOAGCM}}(Q_{20}) = \frac{(\mathrm{M}_{-2})^2}{2(\mathrm{M}_{-1})^3} \,. \tag{6.4}$$

$\mathrm{M}_{(-n)}(Q_{20})$ is the energy-weighted momentum of the quadrupole generating field that can be expressed in terms of the two-quasiparticle excitations $|\alpha\beta\rangle$:

$$\mathrm{M}_{(-n)}(Q_{20}) = \sum_{\alpha>\beta} \frac{|\langle\alpha\beta|Q_{20}|0\rangle|^2}{(E_\alpha + E_\beta)^n} \,, \tag{6.5}$$

being E_α and E_β the one quasiparticle energies. The collective inertias can be also computed using the semiempirical formula [68]:

$$\mathcal{M}_{\mathrm{SEMP}} = \mu \left(\frac{d\beta_{20}}{dQ_{20}}\right)^2 = \frac{0.065}{A^{5/3}} \ \mathrm{MeV}^{-1}\mathrm{fm}^{-4} \,, \tag{6.6}$$

which so far has been the only scheme used for the calculation of cross sections for r process. These equations show that there are two types of model dependencies in the spontaneous fission lifetimes, one that is related to the choice of the collective inertia scheme and the other to the choice of the functional. Actually not only the fission barrier depends on the energy density functional but also the microscopic collective inertias, since the quasiparticle energies are very sensitive to pairing correlations. In this section we want to study the level of agreement between theory and experiment when different functionals and collective inertias schemes are used for the calculation of the spontaneous fission lifetimes.

The spontaneous fission is a tunneling problem and the decay probability depends exponentially on the barrier height and the collective inertia. One has therefore that variations in these two quantities can modify the spontaneous fission lifetimes by several orders of magnitude which in turn complicates the comparison between different theoretical predictions. During this thesis we will follow the prescription of Ref. [118] and compare the logarithm of the ratio of theory to experiment:

$$R_\tau = \log\left(\frac{t_{\mathrm{sf}}^{\mathrm{model}}}{t_{\mathrm{sf}}^{\mathrm{exp}}}\right) . \tag{6.7}$$

The target performance $\bar{R}_\tau$ and variance σ_τ are then obtained as:

$$\bar{R}_\tau = \frac{1}{N}\sum_{i=1}^{N} R_{\tau,i} \,, \tag{6.8}$$

$$\sigma_\tau = \frac{1}{N}\left(\sum_{i=1}^{N}(R_{\tau,i} - \bar{R}_\tau)^2\right)^{1/2} , \tag{6.9}$$

	$\bar{R}_\tau$			σ_τ		
	ATDHFB	GCM	SEM	ATDHFB	GCM	SEM
BCPM	11.583	4.691	2.036	6.447	4.236	6.126
D1M	10.030	4.728	22.779	4.405	3.177	11.448
D1S	3.622	-0.748	8.423	3.585	4.050	6.325
D1N	5.460	0.771	12.480	3.388	3.249	6.993
BCPM-r	-0.007	-0.006	0.004	3.403	3.339	5.231

Table 6.3: Target performances ($\bar{R}_\tau$) and variances (σ_τ) of the spontaneous fission lifetimes obtained with ATDHFB, GCM and semiempirical collective inertias described in Sec. 3.2 for the different models. The last row shows the results obtained by multiplying the BCPM collective inertias by a renormalization factor (0.497 for ATDHFB, 0.731 for GCM and 0.868 for SEMP, see Sec. 6.4 for more details.) Experimental values extracted from Ref. [107, 108].

being N the number of nuclei used in the benchmark. Table 6.3 compares the experimental spontaneous fission half-lives and theoretical calculations employing different functionals and collective inertias schemes. The best results considering all the interactions employing microscopic collective inertias are obtained with the D1S functional. This is because the D1S interaction predict the lowest collective inertias, which compensates the overestimation of the fission barriers described in Sec. 6.3 and improves the agreement with the experimental data. The lower inertias predicted by D1S are due to the its higher pairing correlations, which in turn decrease the collective inertias $\mathcal{M}$ by increasing the quasiparticle energies in the denominator of Eq. (6.5). The opposite argument applies to the BCPM EDF predicting the lowest pairing correlations. Due to this, its microscopic collective inertias as well as the spontaneous fission lifetimes are very high, even though the fission barriers are smaller compared to the other energy density functionals. On the other hand, when comparing the lifetimes predicted by the semiempirical formula we are only sensitive to the shape of the fission barrier, and therefore BCPM has the smallest t_{sf} since its barriers are the smallest ones (see Fig. 6.8). This explains why BCPM predicts the highest t_{sf} with the GCM and ATDHFB inertias and the smallest ones for the semiempirical formula, as it is also shown in Fig. 6.9 where the spontaneous fission lifetimes are plotted as a function of the fissibility parameter Z^2/A.

We find that the spread among different collective inertias schemes within the same interaction is similar to the spread obtained using different interactions with the same collective inertias scheme. This is shown in Table 6.3, Fig. 6.9 and 6.10, where the latter shows the lifetimes as function of Z^2/A obtained with the BCPM EDF for different collective inertias. From this plot we notice that the spread among theoretical lifetimes and the discrepancy with experimental data are larger for light actinides, while for heavier nuclei predictions become more accurate and precise. This convergence of theoretical calculations can be understood by looking at the fission barriers plotted in Fig. 6.11. The left panel shows the fission path of the nucleus ^{232}Th giving the largest half-live difference between theory and experiment. This nucleus presents a broad fission barrier together with a large collective inertia, resulting in a large action integral $S(L)$ where variations in the collective inertias have a strong impact in the spontaneous fission lifetimes. On the other hand, the nucleus ^{262}No has a much shorter barrier with relatively small inertia between the classical turning points. This configuration reduces the value of the action integral and the impact of different collective inertias schemes in the absolute magnitude of t_{sf}, all converging towards the experimental value. This decreasing relevance of the collective inertias with increasing fission probability brings two interesting conclusions:

- during the r-process we are interested in nuclei were fission is a competitive channel (mainly via neutron induced fission), like the ^{290}No and ^{316}Ds plotted in Fig. 6.11. These nuclei must have a narrow and/or low fission barrier and small collective inertias, bringing to a level of precision in the estimation of the fission probability closer to the one obtained for the ^{262}No rather than the

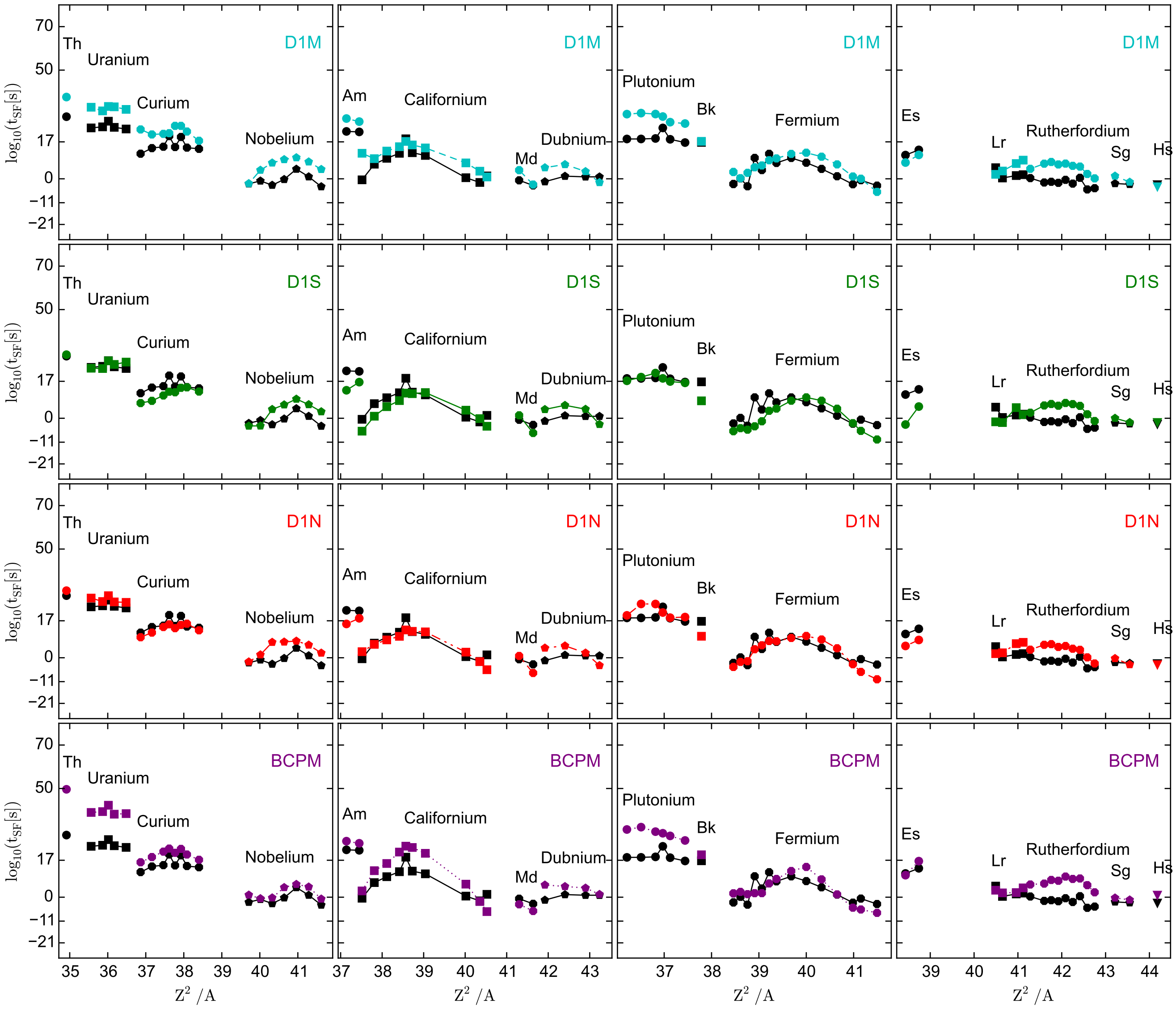

Figure 6.9: Comparison between experimental spontaneous fission lifetimes [107, 108] (black markers) and theoretical predictions from BCPM, D1M, D1S and D1N functionals employing the GOAGCM collective inertias (Eq. (6.4)). Nuclei are plotted as a function of the fissibility parameter Z^2/A, isotopic chains are connected by lines.

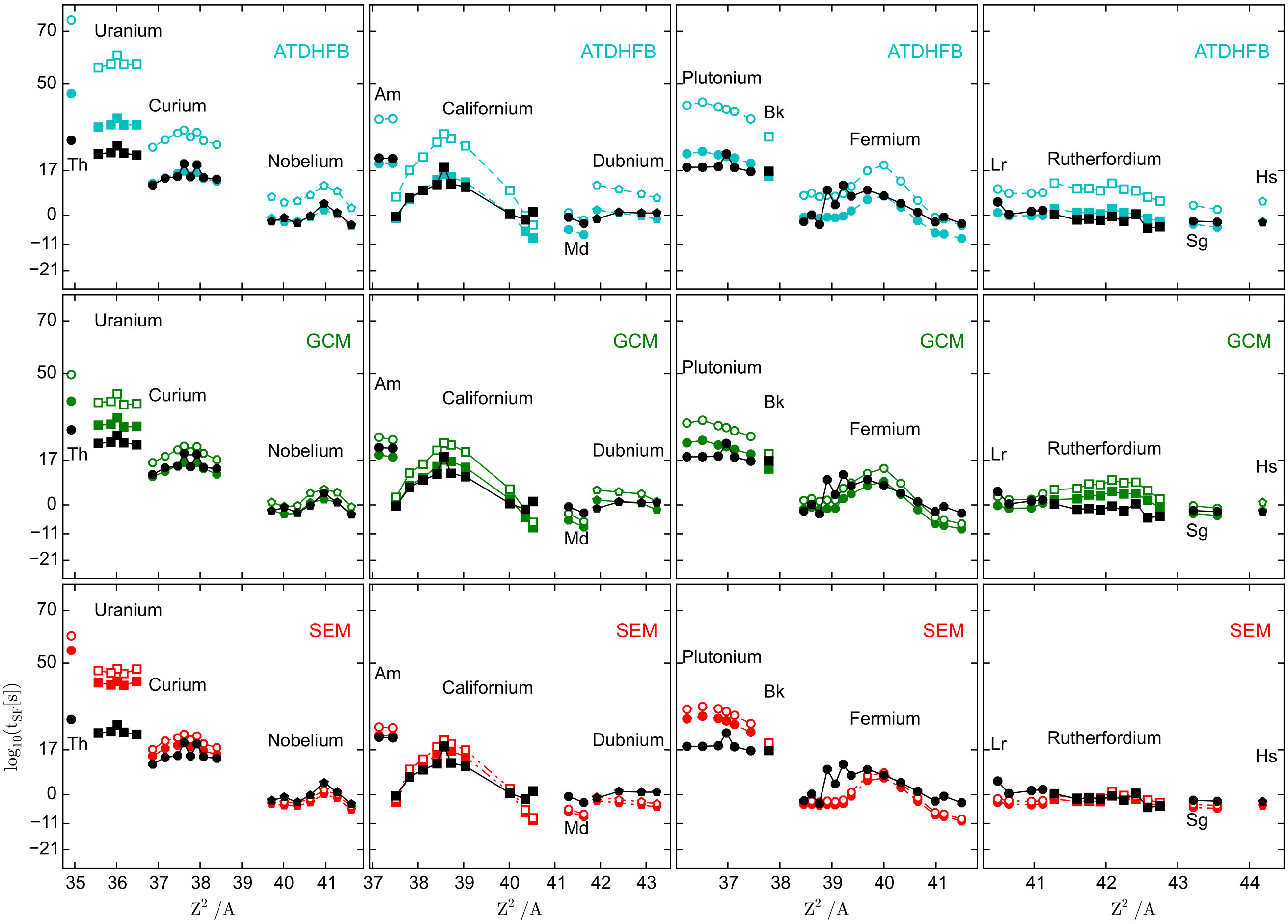

Figure 6.10: Comparison between experimental spontaneous fission lifetimes [107, 108] (black markers) and BCPM predictions employing different collective inertia schemes: ATDHFB (Eq. (6.3)), GOAGCM (Eq. (6.4)) and semiempirical formula (Eq. (6.6)). Solid symbols are the results obtained with the renormalized collective inertias. Nuclei are plotted as a function of the fissibility parameter Z^2/A, isotopic chains are connected by lines.

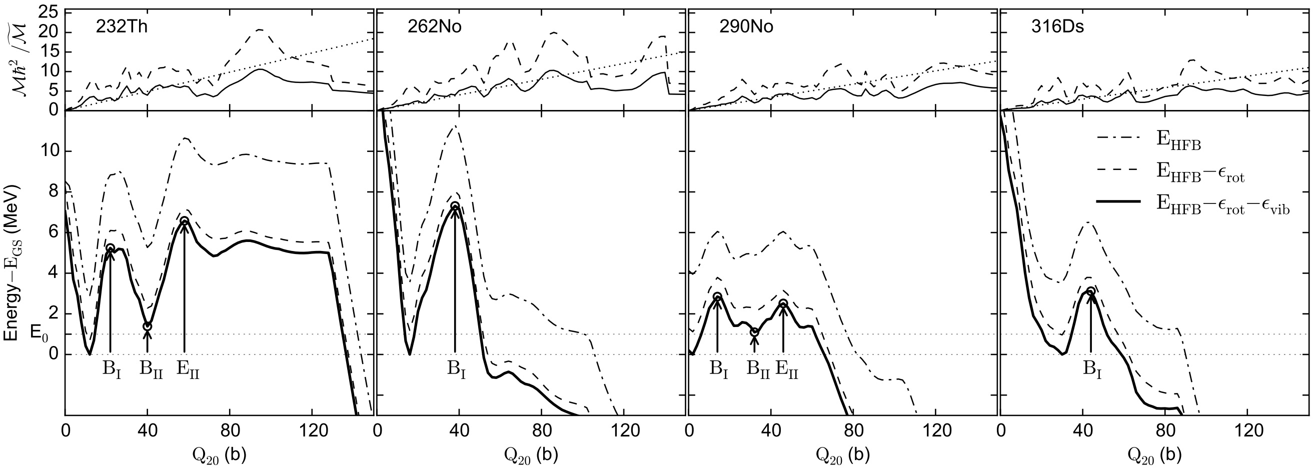

Figure 6.11: Collective fission properties of ^{232}Th, ^{262}No, ^{290}No and ^{316}Ds as a function of the quadrupole moment computed with the BCPM EDF. Lower panels show different contributions to the potential energy surface $\mathcal{V}(Q_{20})$ of Eq. (3.52). Upper panels show collective inertias $\mathcal{M}(Q_{20})$ computed with the ATDHFB (dashed line), GCM (solid line) and semiempirical inertia formula (dotted line), renormalized to the semiclassical inertia $\widetilde{\mathcal{M}}(Q_{20}) = m_n/4Q_{20}$.

^{232}Th. This means that r-process nuclei will be weakly affected by the collective inertias.

- Since nuclei with small t_{sf} are rather insensitive to the collective inertias, we can globally renormalize them in order to improve the agreement of the t_{sf} for the light nuclei without worsening the comparison in the heavier isotopes. This normalization will be further discussed in the next section.

Before discussing the renormalization of the collective inertias we want to make the last considerations regarding the comparison between theoretical results and experimental data of t_{sf}. In Fig. 6.9 and 6.10 we notice that the odd-even staggering of the fission barriers is reflected in the lifetimes in a rather good agreement with experimental data. However it is important to notice that this staggering is more pronounced in the experimental t_{sf}, suggesting for a missing mechanism enhancing the collective inertias in odd nuclei as discussed in Sec. 2.4. Also considering the differences in the functionals is quite surprising the level of precision achieved in the prediction of the lifetimes. For nuclei beyond Nobelium the level of agreement among models and experimental data is very high, bringing a certain optimism in the calculation of fission probabilities in nuclei far from stability. Comparing our results with previous studies of the spontaneous fission lifetimes, we find that the variations in t_{sf} obtained in our models are similar to the variations obtained with different Skyrme energy density functionals [30, 31] and the ATDHFB collective inertia scheme. Ref. [30] shows that Skyrme functionals with higher effective mass ($m^* \approx 0.9$) reproduce better the experimental data of fission barriers and spontaneous fission lifetimes. The authors relate this result to the fact that a low effective mass lead to low density of single particle states, yielding higher shell corrections and in turn higher fission barriers. Therefore, Skyrme interactions with low effective masses ($m^*/m \sim 0.6$) tend to overestimate the fission barriers and consequently the spontaneous fission lifetimes. In our models, the functional with the highest effective mass is BCPM ($m^*/m = 1$) while D1S has the lowest one ($m^*/m = 0.7$). We see therefore that this criteria does not apply in our study of the spontaneous fission lifetimes, since for the ATDHFB inertias we have that D1S is the functional giving the best result for the spontaneous fission lifetimes.

Renormalization of collective inertias

For simplicity in this study we will restrict our discussion to the BCPM EDF, but the considerations made here also apply to the other functionals. In the previous sections we concluded that the overestimation of the spontaneous fission lifetimes can be related to an overestimation of both the fission barrier heights (Fig. 6.8) and the collective inertias (Table 6.3, Fig. 6.9 and Fig. 6.10). While the discussion of the fission barriers has already been approached and can be related with the imposition of axial symmetry, the discussion regarding the collective inertias is more complicated.

When discussing the absolute value of the collective inertias along the fission path one has to consider three different aspects: the dependence of the collective inertias on the functional, the approximations used in the computation of the collective inertias and the approach employed to compute the fission path. We will now explain how these three aspects impact the collective inertias and their interplay in the fission process. We already mentioned before that the overestimation of the spontaneous fission lifetimes can be related to low pairing correlations that increase the collective inertias by reducing the quasiparticle energies. As already suggested in [32], one could try to improve the agreement with experimental data by including the t_{sf} data in the fitting protocol of the pairing interaction. This could be done for example by modifying the pairing strength in Eq. (2.69) in order to match the experimental data. On the other hand, one should also consider the approximations employed in the derivation of Eqs. (6.3) and (6.4). In principle the perturbative cranking approximation employed in our calculations (see discussion in Sec. 3.3.1 and 3.3.2) is expected to underestimate the collective inertias. A recent study [119] showed that a more "exact" calculation of the mass tensor involving the exact numerical differentiation of the energy kernels leads to larger collective inertias. In our case such kind of calculation will clearly worsen the agreement with experimental data. This apparent contradiction arises from the fact that in our model we are exploring only one degree of freedom, namely the quadrupole mass operator Q_{20} as it is sketched in Fig. 6.11, and this bring us to the last point mentioned before: the calculation of the fission path. The overestimation of the spontaneous fission lifetimes can be cured by computing the fission path by means of the minimum action principle in a multidimensional space including pairing as a collective degree of freedom. As it was shown in several recent papers [73, 74, 76] and in Sec. 3.5 of this thesis the dynamic approach has a strong impact in the penetration probability and it can drastically reduce the t_{sf} improving the agreement with experimental data. However such method requires multidimensional calculations exploring multiple collective variables, that unfortunately is too demanding for being applied in systematic calculations like those presented in this paper.

For this reason we propose a renormalization of the collective inertias aimed to take into account for all those effects neglected in the static one-dimensional picture and improve the agreement with experimental data. The renormalization of the collective inertias shall be considered as an alternative to other approaches like, for instance, the renormalization of the fission barriers proposed in Ref. [29]. The advantage of renormalizing the inertias is that we do not sensibly modify the fission probabilities in nuclei that are relevant for the *r*-process nucleosynthesis while renormalizing the barriers will do it. Having a renormalization method that is less "invasive" allows to maintain the predictability of our functionals when study regions far from stability. Of course, if there is an intrinsic problem with the functional prediction one will need to readjust the functional. The last row of Table 6.3 shows that by multiplying the ATDHFB, GCM and SEMP collective inertias by a factor 0.497, 0.731 and 0.868 respectively we can drastically improve the agreement of the predicted t_{sf} with experimental data and achieve the minimum possible deviation within these models. The main impact of the normalization is the reduction of the spontaneous fission lifetimes of light actinides (thorium, uranium and plutonium), where the high stability against fission produced by the large values of the action integral leads to large discrepancies with the experimental data. On the other hand, as we move towards heavier nuclei there is a general decrease of the fission stability and therefore a smaller impact of the renormalization in the absolute value of the fission lifetimes.

6.5 Neutron induced cross sections

Since the *r*-process is driven by the neutron captures one has to describe the competition between the different decays of the compound nucleus. Thus the comparison between experimental data and our theoretical predictions of cross sections is an important test to verify the quality of our calculations. In this section we will discuss the results of neutron capture and neutron-induced fission cross sections obtained employing the statistical model and the nuclear input of the BCPM EDF. We will analyze the sensitive to the different ingredients entering in the calculation of the cross sections in order to estimate which quantities could bring the largest uncertainties in our calculations.

Using the Hauser-Feshbach statistical theory discussed in Chapter 4 the cross section of a neutron induced reaction can be computed using Eq. (4.8). As we discussed in Chapter 4 the theoretical estimation of cross sections depend on several parameters (optical potentials, nuclear level densities, gamma-ray strengths…) that can be computed using multiple approaches. We decided thus to focus our discussion to those quantities that could be more relevant for neutron capture and neutron induced fission, namely the fission barriers, collective inertias, nuclear level densities and gamma-ray strengths. The calculations were performed using the TALYS 1.8 reaction code[1], which provides different schemes to compute the ingredients required by the statistical model [87]. The code was explicitly modified in order to compute the neutron induced cross sections using the microscopic collective inertias obtained with the BCPM EDF. By varying the model used in the calculation of the quantities described before, we will quantify the sensitivity of the cross sections to the main ingredients entering in the statistical calculation and get a qualitative estimation of the goodness of our results.

---

[1] `http://www.talys.eu/`

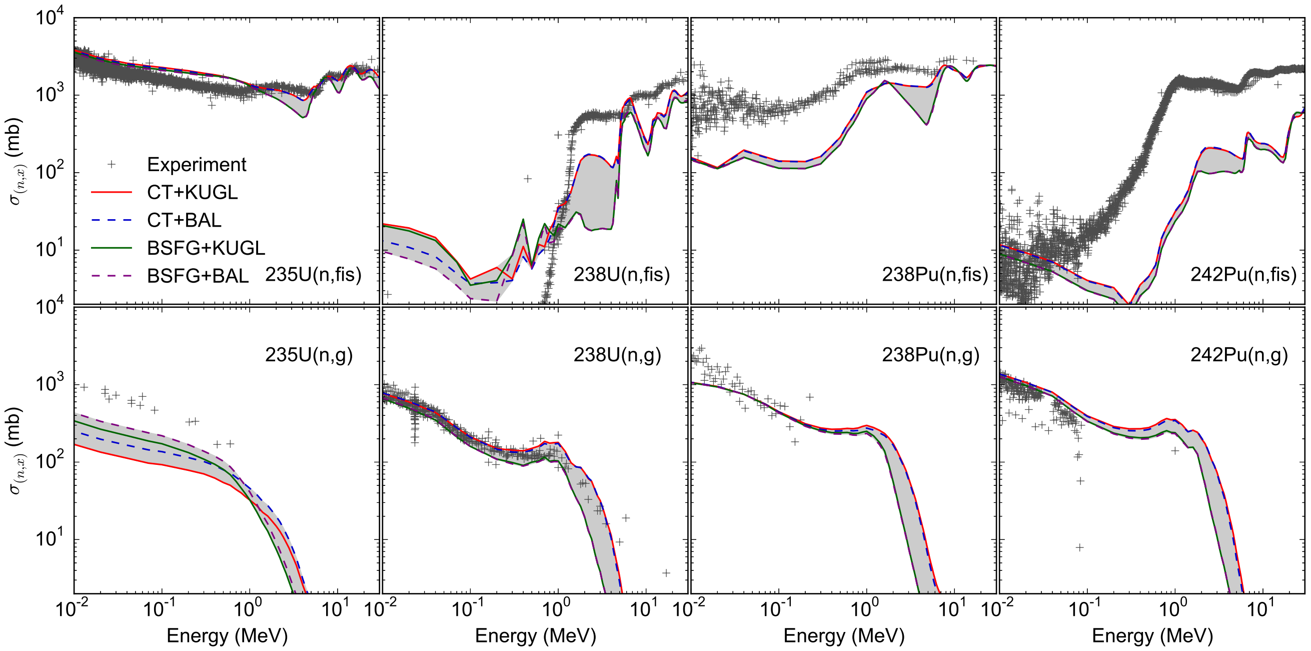

Figure 6.12: Neutron-induced fission (upper panels) and radioactive capture (lower panels) cross sections as a function of the incident neutron energy for four different nuclei. The lines show different combinations of level densities (Back-Shifted Fermi Gas Model and Constant Temperature) and gamma ray-strength (Kopecky-Uhl generalized Lorentzian and Brink-Axel Lorentzian) described in Sec. 4.2.

6.5.1 Sensitivity to level densities and gamma-ray strengths

Fig. 6.12 shows the comparison between experimental data from the EXFOR library [120] and our calculations of the neutron induced cross sections for four different nuclei as a function of the incident neutron energy. These nuclei are chosen in order to show the different level of accuracy achieved in our calculations respect to experimental data and they are commonly used in theoretical studies of neutron-induced fission cross sections [29, 121]. Upper panels display the cross sections for neutron-induced fission and lower panels for radioactive capture. The results were obtained using the GCM collective inertias and different combinations of nuclear level densities and gamma-ray strengths. The typical temperatures at which the r-process takes place is in the range of $0.8 - 1.0$ GK [102], which correspond to an energy of the incident neutrons below 100 keV.

From this plot one can already see that there are different levels of agreement depending on the nucleus and the type of reaction. For example, the neutron-induced fission cross sections are well reproduced for the ^{235}U but they are overestimated for the lower energy range of the ^{238}U and underestimated in the ^{238}Pu and ^{242}Pu. We conclude from this result that a general improvement in the description of the cross sections cannot be obtained by a global renormalization of the fission barriers and/or collective inertias: enhancing(reducing) the neutron-induced fission cross sections on one nucleus will also increase(decrease) those of the other nuclei, without any sensitive betterment. On the other hand, the relative magnitude between both reactions seems to be well reproduced, at least for the region around 100 keV. Radioactive captures are in very good agreement with experimental data (except for a slight underestimation in the case of the ^{235}U) which gives a certain confidence regarding the quality of our calculations. It seems that for the ^{242}Pu there is a decrease of the (n,γ) cross section at 80 keV that is not reproduced in our calculations. Unfortunately the experimental information for (n,γ) at high energies is extremely scarce and (for this nucleus) contradictory, and therefore it is not possible to extract more solid conclusions.

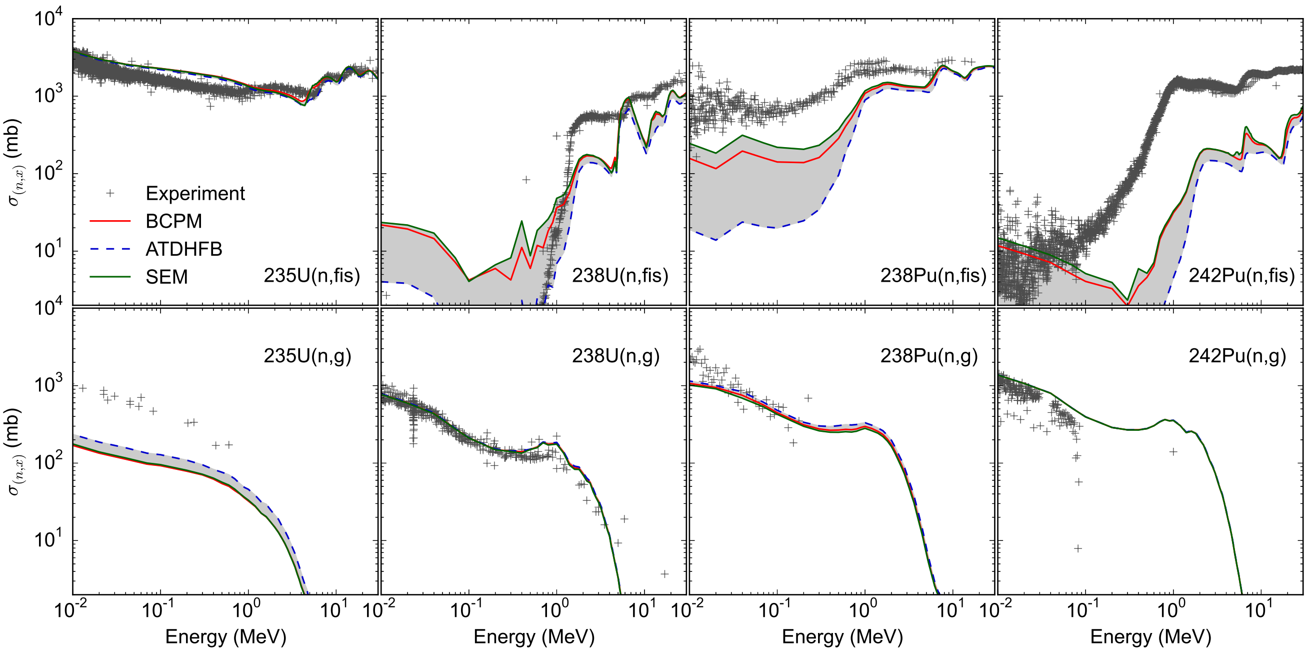

Figure 6.13: Neutron-induced fission (upper panels) and radioactive capture (lower panels) cross sections as a function of the incident neutron energy for four different nuclei. The lines show the results for different collective inertias schemes: ATDHFB (Eq. (6.3)), GOAGCM (Eq. (6.4)) and semiempirical formula (Eq. (6.6)). All the calculations were performed using the BSFGM level densities and the KUGL gamma-ray strengths.

From Fig. 6.12 we can also study the sensitivity of the cross sections to the level densities and gamma-ray strengths. From the upper panels one can see that using the constant temperature level densities increases the prediction of the neutron-induced cross sections compared to the BSFGM, and vice versa for the radioactive capture. Conversely, both type of cross sections seem to be rather insensitive to the gamma-ray strengths. The average spread in this case is around a factor two, even though variations in the cross section increase around the saddle points of the fission barrier, specially at energies around the outer fission barrier.

6.5.2 Sensitivity to collective inertias

The ATDHFB, GCM and semiempirical collective masses were used for the calculation of fission probabilities (Eq. (4.14)) entering in the transmission coefficients (Eq. (4.15)). To our knowledge, this is the first time that microscopic schemes of the collective inertias are used for the calculation of reaction cross sections. Fig. 6.13 shows the variations of the neutron induced fission and radioactive cross sections when these different schemes are applied. It is clear that collective inertias have a large impact in the region where the neutron induced fission cross section are small, which means small values of the fission transmission coefficients. This result is not surprising and actually can be related to the discussion of the spontaneous fission lifetimes addressed in Chapter 7: if the fission transmission coefficient (i.e. the fission probability) is small the integral action has to be large and therefore any variation in the collective inertia will have a large impact in the fission probability (see Eq. (4.15) and (4.14)). This is consistent with the decreasing variations at higher incident neutron energies, since as we increase the excitation energy of the compound nucleus the probability of fissioning will increase and therefore the collective inertias will have a smaller impact. This variation on the spread has two main consequences for the neutron induced cross section:

- for nuclei where the neutron induced fission is the dominating channel, we do not expect any

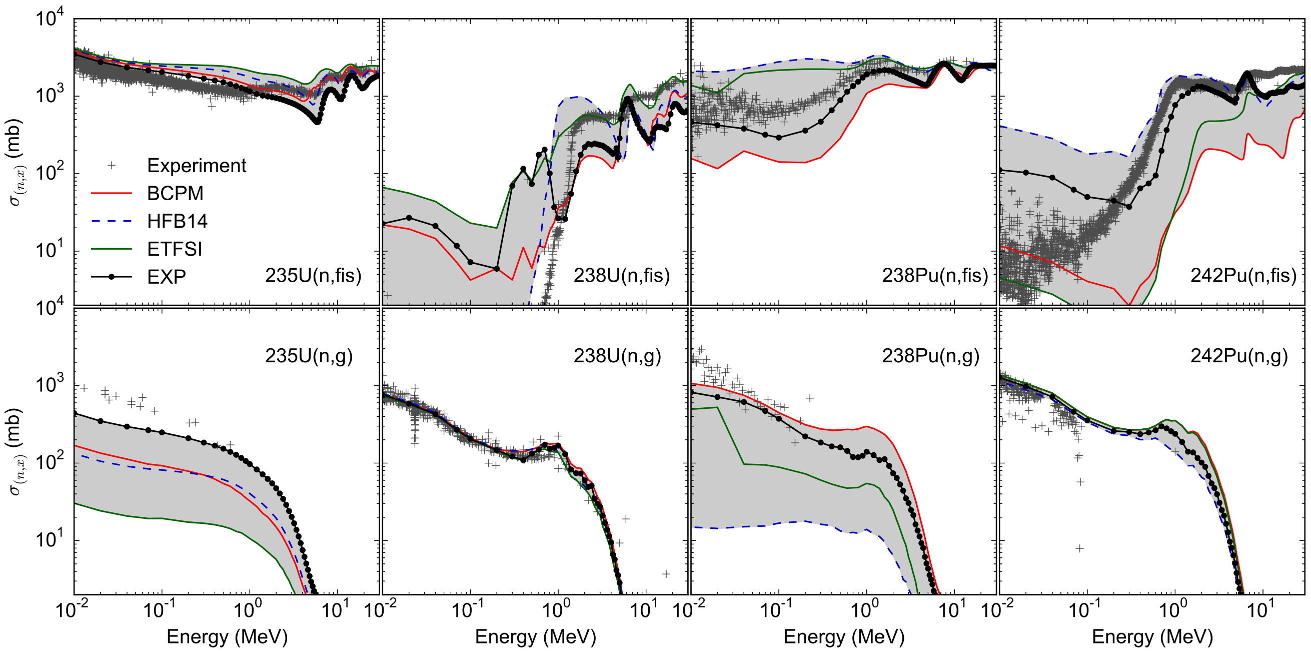

Figure 6.14: Neutron-induced fission (upper panels) and radioactive capture (lower panels) cross sections as a function of the incident neutron energy for four different nuclei. Lines show the results obtained using four different sets of fission barriers: BCPM EDF (with GCM collective inertias), the HFB14 EDF [29], the Extended Thomas-Fermi plus Strutinsky Integral model [122] and experimental fission barriers [106]. All the calculations were performed using the BSFGM level densities and the KUGL gamma-ray strengths.

dependence on the collective inertias. This can be seen in the case of the ^{235}U, where the neutron separation energy of ^{236}U is already larger than the maximum height of the fission barrier. Since the nucleus after capturing the neutron is excited close (or even above) the fission barrier the collective inertia cannot impact the cross sections.

- The collective inertias barely change the neutron capture cross sections. This is because only small fission transmission coefficients are modified, and therefore there is almost no impact in the total transmission coefficient T_{tot} entering in $\sigma_{(n,\gamma)}$.

Finally, looking at the low energy spectra of the ^{238}U, ^{238}Pu and ^{242}Pu one can see that GCM and the semiempirical inertias predict very similar neutron-induced fission cross sections while ATDHFB returns much smaller values, in agreement with what observed in Sec. 6.4 for the spontaneous fission lifetimes.

6.5.3 Sensitivity to fission barriers

The last part of this section is devoted to a comparison of the cross sections obtained using different set of fission barriers. This study has the double purpose of assessing the sensitivity to barrier shapes as well as benchmarking the results obtained from BCPM against other theoretical models. Fig. 6.14 shows the cross sections that we calculated using the fission barriers from BCPM, the Skyrme HFB14 EDF [29] and the Extended Thomas-Fermi plus Strutinsky Integral model [122] (ETSFI), together with the results obtained using experimental fission barriers [106]. The spread on the predictions obtained from different barriers is by far the largest among all the quantities studied in this section, with variations up to two order of magnitudes. This is also due to the fact that the transmission coefficients are computed in different ways: BCPM and HFB14 use the full integral action in Eq. (4.14), while for the ETFSI and the experimental sets the barriers are approximated by a double inverted parabola, leading to the analytical

Hill-Wheeler expression $P_{HW}(E) = 1/(1+\exp[2\pi(V_0 - E)/\hbar\omega])$ where V_0 and ω are the height and curvature of the parabolic barrier. Respect to the other models BCPM tends to predict lower neutron induced fission cross sections, mainly related to its higher barriers. Fig. 6.14 also shows that modifying the fission barriers can have a huge impact in the r-process nucleosynthesis, since it not only modifies the region where fission operates but also affects the neutron capture cross sections.

Finally, it is important to notice that the experimental barriers better reproduce the neutron induced fission cross sections, but the agreement is in many cases around a factor two compared to the experimental cross sections (or even higher in the case of the ^{238}Pu). This is because the values of the experimental fission barriers are extracted from the neutron-induced fission cross sections, and therefore a particular level density and shape of the barrier has to be assumed. This result agrees with the previous discussion regarding the nature of the experimental fission barriers, confirming that they are model dependent and should not be regarded as pure observables.

6.6 α decay of superheavy nuclei

So far we have restricted our discussion to neutron captures and neutron-induced fission, but in r-process calculations also β and α decays play a relevant role. β decays lifetimes determine the speed along the r-process path and consequently the regions where the material accumulates during the r-process nucleosynthesis. α decay plays a relevant role at later stages of the evolution by determining the abundances of nuclei with $A \sim 200$ [102]. Moreover, both decays are an important source of readioactive energies at timescales relevant for macronova observations (see Ref. [123] and discussion in Sec. 8.4). Both decays require a specific microscopic description that we did not use in this thesis due to our focus on describing the fission process. But if for β-decay rates we have to rely in experimental data and the theoretical calculations available in the literature, in the case of α decay we can compute the half-lives using the phenomenological Viola-Seaborg formula [124]:

$$\log_{10}(t_\alpha[s]) = \frac{aZ+b}{\sqrt{Q_\alpha[\text{MeV}]}} + cZ + d + h_{\log}\,, \tag{6.10}$$

where Z is the proton number of the parent nucleus. The Q_α value is obtained from the binding energies of the alpha particle, parent and daughter nuclei as:

$$Q_\alpha(Z,N) = Be(Z,N) - Be(Z-2,N-2) - Be(^4\text{He})\,, \tag{6.11}$$

with $Be(^4\text{He}) = -28.296$ MeV. In this thesis we will employ the coefficients of the recent parametrization of Ref. [125], that were obtained through a least-square fit to α-decay experimental data [48]:

$$a = 1.64062, \quad b = -8.54399, \tag{6.12}$$
$$c = -0.19430, \quad d = -33.9054, \tag{6.13}$$

with the hindrance factor

$$h_{\log} = \begin{cases} 0, & \text{for Z even and N even;} \\ 0.8937, & \text{for Z even and N odd;} \\ 0.5720, & \text{for Z odd and N even;} \\ 0.9380, & \text{for Z odd and N odd}\,. \end{cases} \tag{6.14}$$

Functional	$\sigma(Q_\alpha)$ (MeV)	$\sqrt{\sigma^2}$	$\langle\sigma\rangle$	$\bar{R}_\tau$	σ_τ
BCPM	0.573	2.201	1.682	0.433	1.590
D1M	1.077	3.005	1.991	1.419	1.794
D1S	0.653	2.175	1.667	-0.127	1.649
D1N	0.697	2.268	1.722	1.766	1.612

Table 6.4: Deviations between predicted alpha decay properties and experimental data for nuclei with $84 \leq Z \leq 120$ and $118 \leq N \leq 250$. The second column shows the Q_α mean square deviations between the atomic mass evaluation AME2012 [105] and theoretical predictions. The next four columns show show the standard $\sqrt{\sigma^2}$ deviations, mean $\langle\sigma\rangle$ deviations, target performances $\bar{R}_\tau$ and variances σ_τ of the alpha decay half-lives.

In order to determine the agreement between theoretical half-lives and experimental data we follow the prescription of [125] and define the mean and standard deviation as:

$$\langle\sigma\rangle = \frac{\sum_{i=1}^{N} \left|\log_{10}(T^i_{\text{exp}}/T^i_{\text{the}})\right|}{N}, \tag{6.15}$$

$$\sqrt{\sigma^2} = \sqrt{\frac{\sum_{i=1}^{N} \left[\log_{10}(T^i_{\text{exp}}/T^i_{\text{the}})\right]^2}{N}}. \tag{6.16}$$

The main advantage of the Viola-Seaborg formula is that it only requires the Q_α value of the parental nucleus to compute the α-decay half-lives, which implicitly means that models giving the smallest deviations of the alpha-decay half-lives are those reproducing better the experimental Q_α. This correlation can be observed in Table 6.4 summarizing the deviations between theoretical estimations of Q_α and t_α and experimental data [105]. Surprisingly enough the smallest deviations are obtained with the D1S functional while D1M returns the worst description. This is a result that goes in the opposite direction of what suggested by the binding energies and neutron separation energies and collected in Tables 6.1 and 6.2. The problem is that D1M overbinds the astatine isotopes and underbinds the francium ones, which in turn results in a overestimation of the Q_α for the $^{207-214}_{87}$Fr isotopes between 3.5 and 6 MeV. For a better comparison Fig. 6.15 shows the Q_α predicted by the different models together with the available experimental [105] data for three isotopic chains. From this plot we see that around the neutron number $N = 127$ there is a transition in the theoretical predictions: the Q_α of nuclei with $N < 127$ are systematically underestimated, while those above $N > 127$ are overestimated. The large discrepancies in the vicinity of $N = 126$ points out once again the difficulties of mean field models to describe the region around shell closures. However one has to say that the experimental trend of Q_α is quite well reproduced by most of the models, and that the agreement in nuclei above and below the $N = 126$ shell closure is certainly satisfactory.

For the alpha-decay half-lives of nuclei with $Z \geq 84$, the logarithm of the mean and standard deviations are between 1.67 and 3.00, corresponding to deviations between theoretical half-lives and experimental data of factors 47 and 1000. These large deviations in the t_α reflect the difficulties of reaching accuracies beyond the logarithmic precision in lifetimes calculations involving tunneling processes, as it was already mentioned before in this Chapter. Actually the Viola-Seaborg formula itself reproduces the half-lives within a factor 6 [125], and by comparing the target performances and variances one can notice that the deviations obtained in the t_α are smaller than those obtained in the t_{sf} without renormalization of the collective inertias (see Table 6.3). In order to get a general overview of the competition between spontaneous fission (SF) and alpha decay Fig. 6.16 shows the dominating channel predicted by BCPM. The lower panels are the results obtained using the different collective inertias scheme of Sec. 6.3 and the

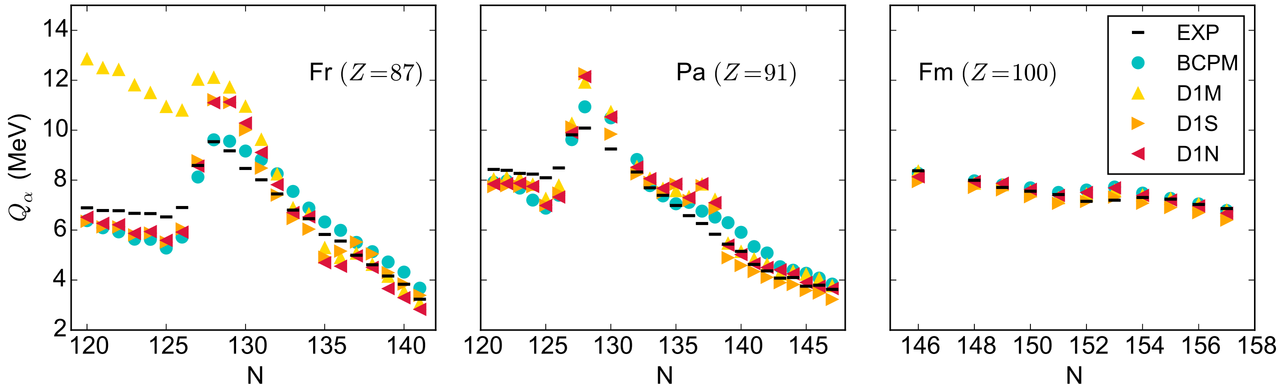

Figure 6.15: Experimental [105] and theoretical Q_α as a function of neutron number for three isotopic chains: francium (left panel), protactinium (middle panel) and fermium (right panel).

upper panel shows the experimental data extracted from Ref. [105]. All the inertia schemes predict α decay to be the dominating channel in the region $84 \leq Z \leq 98$ and $118 \leq N \leq 156$, in good agreement with experimental data. However, only the ATDHFB and GCM schemes succeed in reproducing the α-decay path that starting from the lighter region proceeds towards $Z/N = 110/172$. This path form the peninsula of stability that will be discussed in Sec. 7.1. In this region the semiempirical formula seems to underestimate the stability against the SF process, and the α decay path is interrupted by the SF already at $A = 254$. One should also notice that the increasing stability around the predicted magic neutron number $N = 184$ produces an island of nuclei dominated by α decay around $Z = 94$. Finally, the ATDHFB is the only scheme predicting the α decay to be the dominating channel of most of the nuclei in the island of stability placed around $^{300}_{120}$Uub.

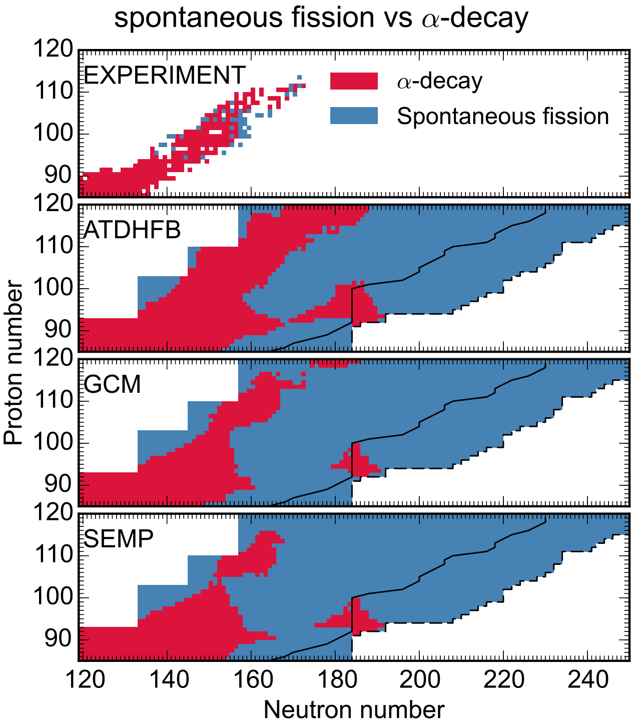

Figure 6.16: Dominating channel between α-decay and spontaneous fission predicted by BCPM for different collective inertias. For comparison, the upper panel shows the dominating channel for nuclei experimentally observed [105].

7 Fission properties of r-process nuclei

In the previous Chpater we benchmarked our theoretical calculations of binding energies, fission barriers, spontaneous fission lifetimes and neutron induced cross sections against experimental data. In these Chapter we provide the fission properties of nuclei throughout the whole superheavy landscape. The aim of this work is to quantify the variations in the fission properties of superheavy nuclei far from stability and use the calculations obtained from the energy density functionals (EDF) as a nuclear input in the estimation of neutron induced stellar reaction rates relevant for the r-process nucleosynthesis. The first section of this Chapter is devoted to the discussion of the fission barriers predicted by BCPM and the Gogny EDF's for nuclei in the region $84 \leq Z \leq 120$ and $118 \leq N \leq 250$. Later we will explore the sensitivity of the spontaneous fission lifetimes of these superheavy nuclei to variations in the quantities determining the fission probability. We will conclude this Chapter discussing the calculation of the neutron induced reaction rates and their sensitivity to the collective inertias and we will compare our results with previous theoretical calculations.

7.1 Fission barriers

By looking at the general trend of the fission barriers heights it is possible to get a crude estimation of the stability of nuclei against the fission process and the impact of shell closures in fission. It is therefore interesting to study the evolution of the fission barriers predicted by the models for nuclei far from stability and analyze the common features and differences in the results. Fig. 7.1 shows the maximum fission barrier height B_f as a function of proton and neutron number predicted by BCPM and the D1M, D1S and D1N parametrizations of the Gogny EDF. We notice that all the models predict a similar trend of the barrier height, with large variations related to the fluctuations in the shell structure. Actually, in the four models we find four different islands of local maximum placed around nuclei $^{210}_{84}$Po, $^{268}_{84}$Po, $^{250}_{100}$Fm, $^{320}_{102}$No and $^{300}_{120}$Ubn. The increase of fission barriers around $^{210}_{84}$Po and $^{268}_{84}$Po are related to the presence of the neutron magic numbers $N = 126$ and $N = 184$, leading to spherical nuclei with fission barriers up to 30 MeV in the case of the D1S interaction. These two islands are separated by prolate nuclei and a group of slightly oblate nuclei around $Z/N = 86/176$. Regions around $^{250}_{100}$Fm and $^{300}_{120}$Ubn are usually referred as "peninsula of known nuclei" and "island of stability", respectively [126]. The peninsula is formed by prolate-deformed nuclei and it extends up to $Z/N \approx 110/166$. On the other hand, nuclei in the island of stability are either oblate (for lower N) or spherical (higher N). The peninsula and the island are separated by a rather narrow region of prolate nuclei with $A \sim 280$ where the fission barriers usually decrease. Finally, the region around $^{320}_{102}$No is formed by strongly-deformed nuclei ($\beta_{20} \sim 0.25$). It is interesting to notice that all the models predict a region of vanishing fission barriers around $^{316}_{102}$Lv in correspondence of a transition between spherical and strongly deformed nuclei ($\beta_{20} \sim 0.4$). Nuclei in this region are the unstable nuclei described in Sec. 6.2 (see Fig. 6.5) that appear above the shell closure $N = 184$ when $Z \geq 100$. Since during the r-process nucleosynthesis the material is accumulated around this magic neutron number the presence of these unstable nuclei suggests a possible hindering in the production of nuclei with $N > 184$.

When comparing the results obtained from the different functionals we find that BCPM predict the lowest barriers throughout the whole superheavy landscape. This can be related to an higher value of the effective mass m^* compared to the Gogny functionals (see Table 7.1): higher m^* leads to higher density of single particle states and therefore smaller shell corrections, resulting in an reduction of the fission

---

Some of the results presented in this Chapter are extracted from Ref. [103].

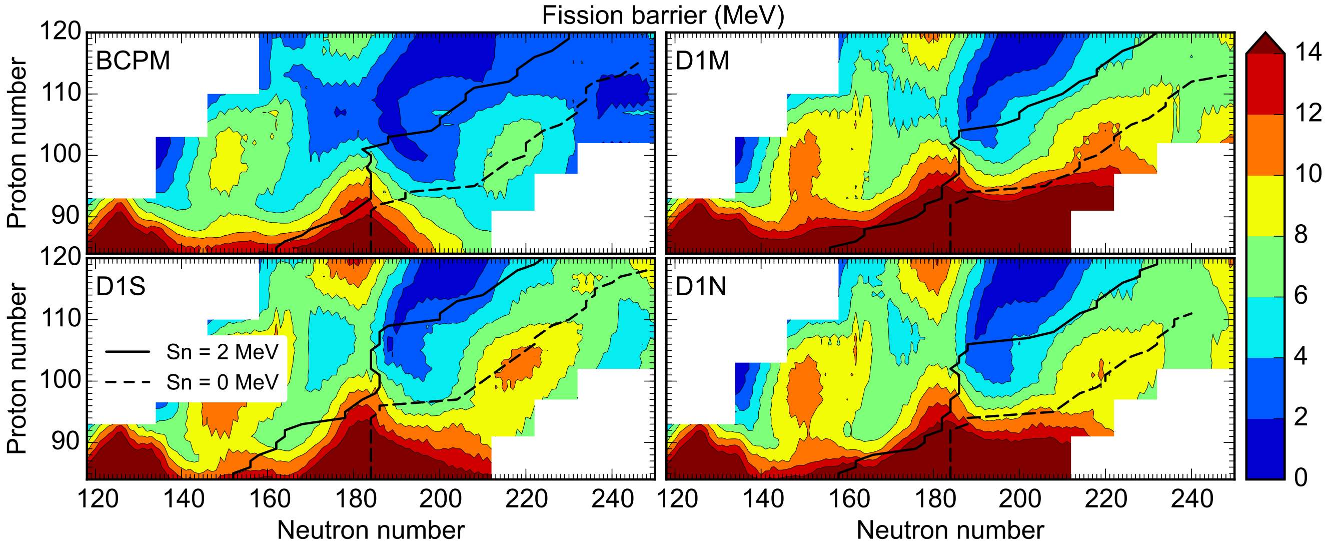

Figure 7.1: Maximum fission barrier height in MeV as a function of proton and neutron number predicted by the different energy density functionals. The drip line predicted by each model is represented by a dashed black line. The solid black lines show the heaviest isotope of each specie with $S_n \leq 2$ MeV.

	BCPM	D1S	D1N	D1M
m^*/m	1	0.7	0.75	0.746
a_s [MeV]	17.7	20	19.3	
E_{sym} [MeV]	31.9	32.0	29.3	28.554

Table 7.1: Effective mass m^*/m, surface energy and symmetry energy of BCPM, D1S, D1M and D1N energy density functionals.

barriers [72]. As already mentioned in Sec. 6.3 another possible explanation is the different competition between the surface energy and Coulomb repulsion predicted by BCPM, that has a smaller surface energy coefficient a_s compared to D1S and D1N. The smaller surface energy favours the deformation induced by the Coulomb repulsion of protons in the nucleus reducing the fission barriers [33]. Regarding the Gogny models we notice that they all predict very similar barriers for nuclei above $Z = 92$. Fig. 7.2 shows the spread in the prediction of B_f, defined as the maximum difference in the predictions of the fission barrier height of each nucleus. The left panel of Fig. 7.2 shows that the spread in the prediction of B_f between D1M, D1S and D1N is below 2 MeV, and actually except for the region around the peninsula and island of stability the differences are below 1 MeV. This result is in agreement with the fact that the value of m^* is very similar in the three functionals as well as the surface energy coefficient of D1N and D1S. However one has to notice that the differences in the fission barrier heights among Gogny functionals is rather large in nuclei below $Z = 92$, specially when comparing D1M with D1S. For all nuclei below $Z = 92$ D1M predicts the largest fission barriers, and the differences with D1S increase as we approach the neutron drip line at $N = 184$. These variations in the barriers cannot be explained by the effective mass, that is slightly larger in D1M. We conclude therefore that these differences in the predictions of the fission barriers arise from the treatment of loosely bound nuclei.

Concerning the implications for the r-process we notice that for the Gogny interactions the largest spread in B_f is obtained in the region of high fission barriers (Fig. 7.1 and left panel of Fig. 7.2), where we do not expect fission to play a relevant role. However, when comparing the spread in the predictions considering also the BCPM EDF we find that the differences are rather large for all the nuclei close to the r-process path (right panel of Fig. 7.2). It would be very interesting therefore to study the different

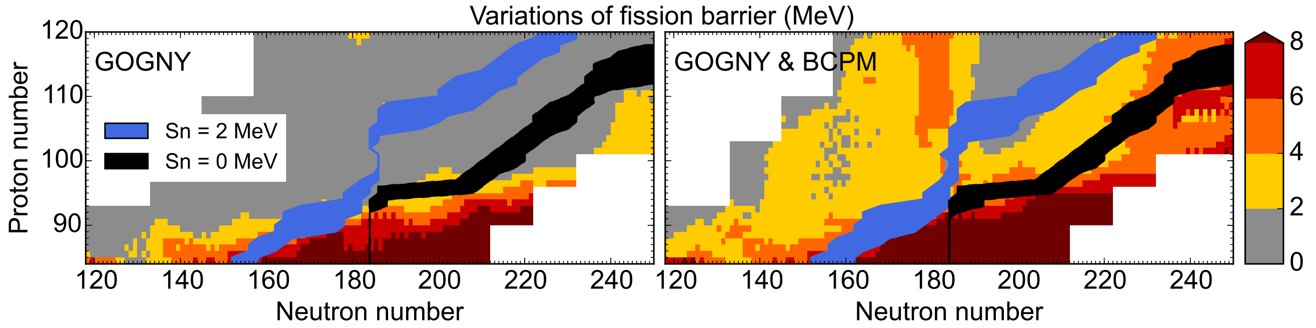

Figure 7.2: Maximum difference in the predictions of the highest fission barrier B_f obtained with the Gogny parametrizations (left panel) and including the BCPM interaction (right panel), in MeV. The shaded areas represent variations in the prediction of the drip-line (black) and nuclei with a neutron separation energy of 2 MeV (blue).

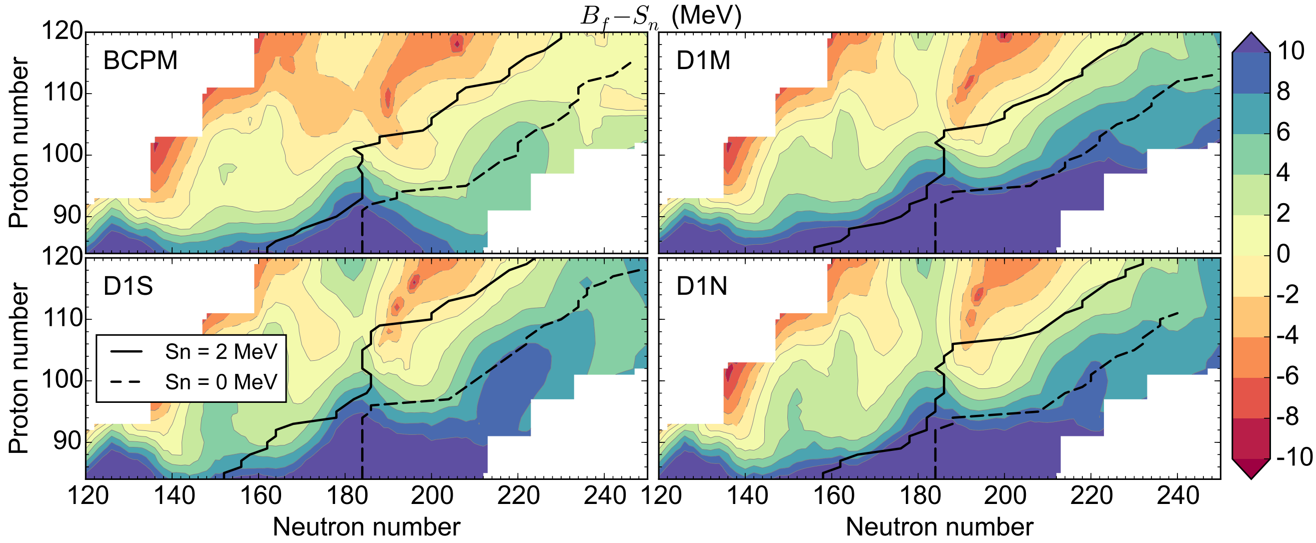

Figure 7.3: Energy window for the neutron induced fission of even-even nuclei in MeV as a function of proton and neutron number predicted by the different energy density functionals.

abundances predicted by BCPM and the Gogny functionals and quantify the impact of these variations of the fission barriers the r-process nucleosynthesis.

Energy window for neutron-induced fission

An important quantity for astrophysical calculations is the neutron induced fission energy window defined as the difference between the maximum fission barrier height and the neutron separation energy $B_f - S_n$. In the neutron capture during the r process the compound nucleus is excited with an energy roughly given by the neutron separation energy S_n. For a value of the neutron separation energy similar to the fission barrier height ($B_f - S_n \lesssim 2$ MeV) the compound nucleus will be excited close to the top of the fission barrier and fission. The neutron induced fission energy window gives then a first hint of the competition between (n, γ) and neutron-induced fission.

Fig. 7.3 shows the energy window for neutron induced fission predicted by BCPM and the three Gogny energy density functionals in even-even nuclei. Similarly to the study of the fission barrier, the neutron induced energy window shows the same general trends in all the models. For example, there is a clear increase of $B_f - S_n$ as we move from $S_n = 2$ MeV to the neutron drip line, due to the fact that the fission

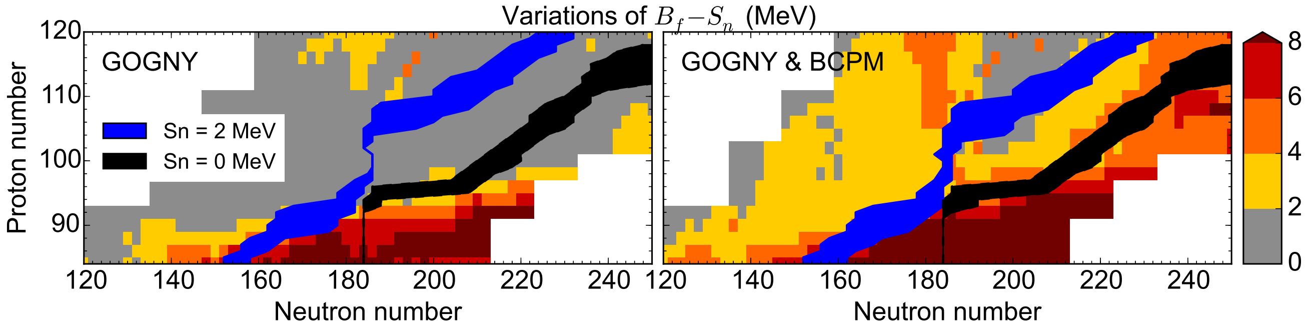

Figure 7.4: Maximum variation in the prediction of the energy window for the neutron induced fission $B_f - S_n$ obtained with the Gogny parametrizations (left panel) and including the BCPM interaction (right panel), in MeV. The shaded areas represent variations in the prediction of the drip-line (black) and nuclei with a neutron separation energy of 2 MeV (blue).

barriers tend to increase and the neutron separation energies decrease as we approach the neutron drip line. As it was already pointed out in [127], this trend tells us that if the r-process path proceeds close to the neutron drip line the neutron induced fission will be less dominant compared to the case when the r-process path proceeds closer to the valley of stability. This plot also shows that the predicted neutron magic number $N = 184$ plays an important role in determining the nucleosynthesis of superheavy elements, since the decrease in the neutron separation energies after $N = 184$ pushes the material towards nuclei with smaller $B_f - S_n$. Taking the nuclei with $S_n \approx 2$ MeV as rough approximation of the r-process path, we notice that all the models predict that after overcoming $N = 184$ the r-process path has to cross a region with negative $B_f - S_n$ values. This is shown in the right panel of Fig. 7.4 representing the spread in the predictions of the $B_f - S_n$ considering all the models. The r-process path, depicted as a blue region to include all the nuclei with $S_n \sim 2$ MeV predicted by the different models, crosses a grey region where all functionals predict low values of $B_f - S_n$. From this we conclude that the nucleosynthesis of nuclei beyond $N = 184$ will be highly hindered by the neutron-induced fission, in agreement with what already deduced from the trend of the fission barriers. Finally, it interesting to notice that the spread in the predictions for $B_f - S_n$ (Fig. 7.4) is not very different from the spread obtained for B_f (Fig. 7.2). This result confirms the similar neutron separation energies predicted by the different models and discussed in Sec. 6.2.

7.2 Spontaneous fission lifetimes

The trend of the fission barriers gives only a rough hint of the stability of the nucleus against the fission process. As it was already explained in Sec. 3.2, the probability of the system to penetrate the fission barrier is determined by a complex process where several ingredients must be taken into account and it can not be solely determined by the height of the barrier. A more complete picture can be obtained studying the trend of the spontaneous fission lifetimes

$$t_{\text{sf}}\,[s] = 2.86 \times 10^{-21}(1 + \exp(2S)) \tag{7.1}$$

and the contribution of the different terms entering in the action integral $S(L)$ computed along the fission path L:

$$S(L) = \int_a^b dQ_{20}\,\sqrt{2\mathcal{M}(Q_{20})[\mathcal{V}(Q_{20}) - (E_0 + E_{\text{GS}})]}\,. \tag{7.2}$$

We recall that $\mathcal{M}(Q_{20})$ are the collective inertias obtained from either the ATDHFB, GOAGCM or the semiempirical schemes, $E_0 = 0.5$ MeV is the energy of the collective ground state and $\mathcal{V}(Q_{20})$ is the

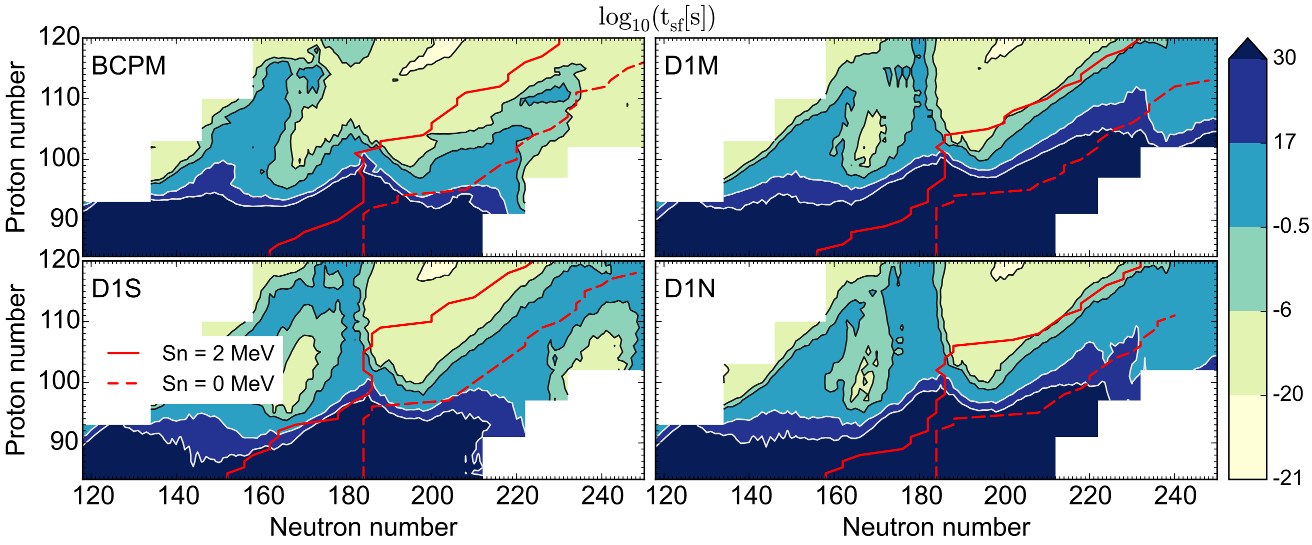

Figure 7.5: Decimal logarithm of the spontaneous fission lifetimes as a function of proton and neutron number predicted by the BCPM, D1M, D1S and D1M models using the GCM collective inertias. Dotted regions represent nuclei with $t_{\mathrm{sf}} \lesssim 3$ s.

effective potential energy obtained by subtracting the vibrational and rotational zero-point energies from the total HFB energy:

$$\mathcal{V}(Q_{20}) = E_{\mathrm{HFB}}(Q_{20}) - \epsilon_{\mathrm{vib}}(Q_{20}) - \epsilon_{\mathrm{rot}}(Q_{20})\,. \tag{7.3}$$

As we have already discussed in Sec. 6.4 there are two different types of model dependencies in the calculation of spontaneous fission lifetimes, one that is related to the choice of the collective inertia scheme and the other to the choice of the functional. After assessing the variations in the predictions of t_{sf} for nuclei with available experimental data we want to study how these differences propagates to nuclei far from stability. In order to do that we will perform a systematic calculation of t_{sf} using different energy density functionals and collective inertias schemes and study the sensitivity of the results to variations in these quantities. For completeness we will also explore the sensitivity of t_{sf} to variations in E_0, that mimics the effects of a renormalization of the fission barriers in the spontaneous fission lifetimes.

7.2.1 Sensitivity to different energy density functionals

We will start showing the sensitivity of the t_{sf} to different energy density functionals. It is important to keep in mind that the choice of the functional affects both the estimation of $\mathcal{V}$ as well as the collective inertias $\mathcal{M}$. Fig. 7.5 shows the t_{sf} predicted by the different models using the GCM collective inertias. The spread in the results is large, specially in nuclei with large values of t_{sf} like actinides below $Z \lesssim 98$. This is a consequence of the exponential dependence of the spontaneous fission lifetimes to the action integral in Eqs. (7.1) and (7.2) already discussed before in this thesis (see Sec. 6.4): large values of the action integral make the half-lives very sensitive to variations in any of the ingredients entering in the expression of the WKB formula. We notice that the spontaneous fission lifetimes plotted in Fig. 7.5 resembles to some extent the trend of the highest fission barriers in Fig. 7.1, indicating that the maximum height of the fission barrier is a reasonable first order estimator of the fission probability of a nucleus.

Fig. 7.6 shows the model predicting the shortest (left panels) and the longest ones (right panels) spontaneous fission lifetime of each nucleus for different collective inertia schemes. From this plot we could not identify a particular dominance of any model along the whole chart. For example, within the microscopic inertias BCPM predicts the largest spontaneous fission lifetimes for nuclei below $Z = 94$ and along the peninsula of stability, but its t_{sf} for r-process nuclei are the smallest among all the functionals.

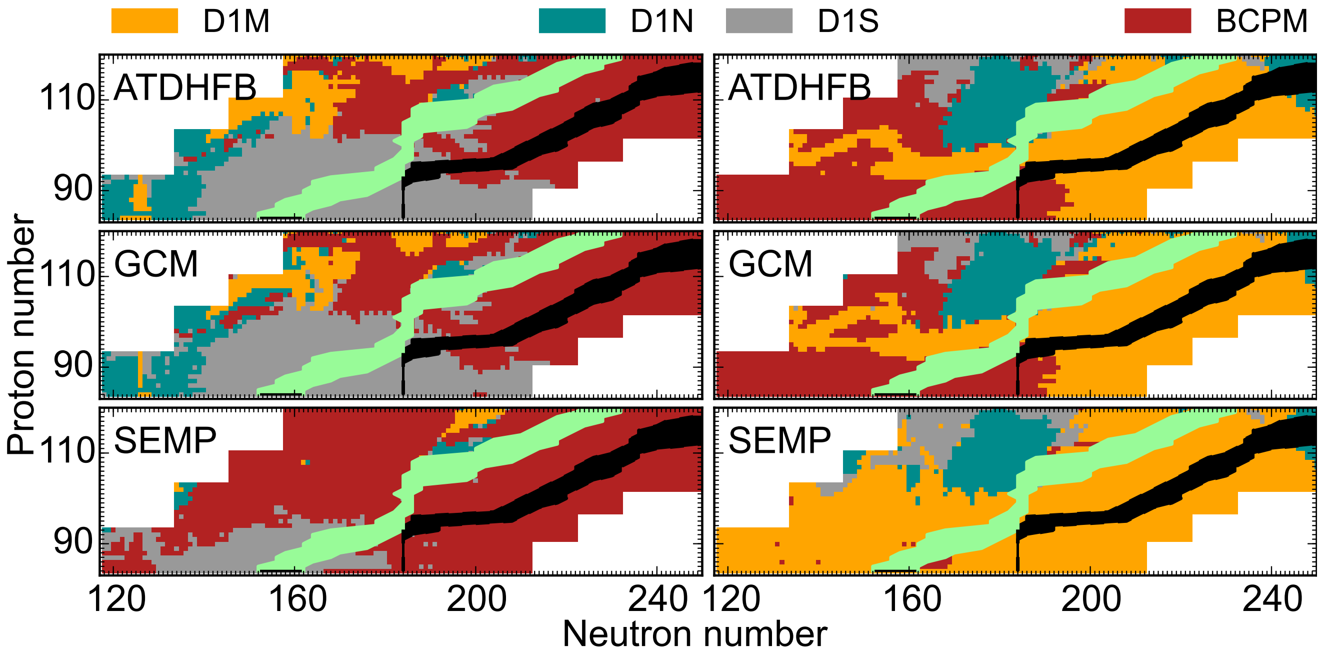

Figure 7.6: Map of the functional predicting the shortest (left panels) and longest (right panels) spontaneous fission lifetimes for each nucleus. The t_{sf} are obtained using the ATDHFB (upper panels), GCM (middle panels) and semiempirical (lower panels) collective inertias scheme.

On the other hand, D1M predicts the longest t_{sf} for neutron rich nuclei and the shortest ones for neutron-deficient superheavy nuclei. The reason of these variations in the dominance is related to the evolution of the fission barriers predicted by the models when we move towards larger proton and/or neutron number. When the fission barriers are high and/or large enough, the differences in the t_{sf} predicted by the models are mainly driven by the collective inertias. Therefore, for these nuclei BCPM predicts the longest half-lives because its collective inertias are the largest among all the functionals, as we already discussed in Sec. 6.4. For instance, this is the case of nuclei with a rather low Z and/or N. But as we move towards more neutron rich or heavier nuclei, the fission barriers become smaller and the impact of the collective inertias diminishes while the relevance of the barrier increases. Therefore for these nuclei BCPM predicts the smallest t_{sf} because all the Gogny interactions predict larger and wider barriers than BCPM. We have therefore that the superheavy landscape is decoupled in two regions: one where the fission barriers are high enough and the lifetimes are dominated by the collective inertias; and another one where the fission barriers are small and collective inertias play a minor role. In our calculations we find that the transition can be quite well identified around the mass number $A \sim 280$, above which BCPM predicts the smallest t_{sf} for the vast majority of nuclei.

Since the semiempirical inertias $\mathcal{M}_{\text{SEMP}} = 0.065A^{-5/3}$ MeV^{-1}fm^{-4} only depend on the mass number A the lifetimes obtained from the different models with $\mathcal{M}_{\text{SEMP}}$ reflect the differences in the barrier shape. We can therefore combine the lower panels in Fig. 7.6 together with the fission barriers plots of the previous section to extract more information about the shape of the fission barrier predicted by the different models. For example, in Sec. 7.1 we noticed that the Gogny interactions predict very similar fission barrier heights in nuclei above $Z = 92$, with an average spread below 1 MeV. But looking at the maximum spontaneous fission lifetimes predicted with the semiempirical formula (lower right panel in Fig. 7.6) it is evident that D1M has the longest t_{sf} for all the nuclei between $S_{2n} = 2$ MeV and the neutron dripline. This is because D1M predicts wider barriers than D1N and D1S as we increase the neutron number N. Larger fission barriers are classically related to higher values of the surface energy coefficient a_s, because when the surface energy is larger the nucleus is more stable against deformations and the decline of the barrier becomes. This result contradicts the smaller inner barrier height observed

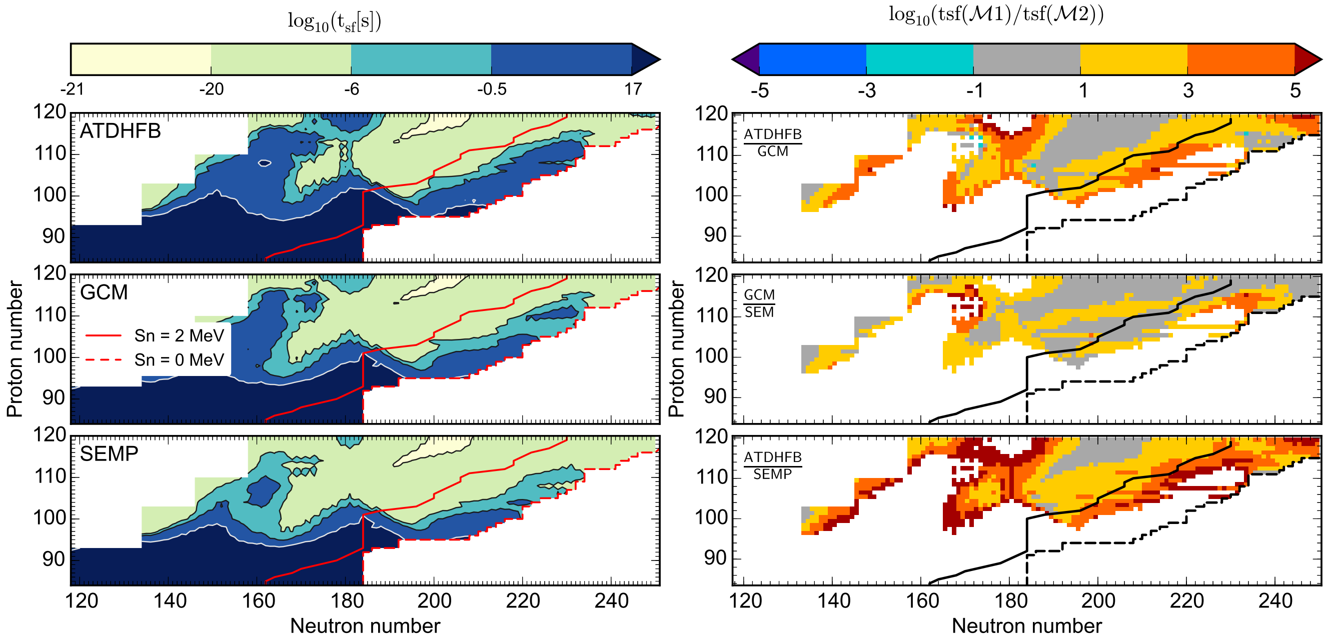

(a) **(b)**

Figure 7.7: Left panels: decimal logarithm of the spontaneous fission lifetimes predicted by BCPM using different collective inertia schemes: ATDHFB (upper panel), GCM (middle panel) and semiempirical formula (lower panel). Right panels: logarithm of the ratio of the spontaneous fission lifetimes of nuclei with $t_{\mathrm{sf}} \lesssim 3$ s for different combinations of collective inertias: $R^{\mathrm{ATDHFB}}_{\mathrm{GCM}}$ (upper panel); $R^{\mathrm{GCM}}_{\mathrm{SEMP}}$ (middle panel) and $R^{\mathrm{ATDHFB}}_{\mathrm{SEMP}}$ (lower panel). Figure taken from Ref. [103].

in Sec. 6.3 but agrees with the larger barriers predicted by D1M in nuclei below $N = 92$. Once again, it will be very interesting to determine the a_s of D1M, but we may affirm that the classical picture of describing the fission process as a competition between Coulomb and surface energy is too limited to properly describe the evolution of the fission barrier.

7.2.2 Sensitivity to collective inertias

After discussing the sensitivity of t_{sf} to different energy density functionals, we want to focus our attention to the variations induced by the choice in the collective inertias scheme. In order to do that we pick the BCPM EDF as a reference functional, but the conclusions obtained in this section can be generalized to the other models. Fig. 7.7 shows the t_{sf} predicted by BCPM using the ATDHFB, GCM and semiempirical collective inertias schemes described in Sec. 3.2. The vibrational energy corrections ϵ_{vib} are computed accordingly to inertia scheme, except for the semiempirical inertias where we arbitrarily choose the $\epsilon^{\mathrm{ATDHFB}}_{\mathrm{vib}}(Q_{20})$ scheme. Regarding the collective ground state energy, all the lifetimes are obtained with $E_0 = 0.5$ MeV. Due to a certain arbitrariness in the choice of these last two parameters, the next section will be devoted to study the sensitivity of the lifetimes on ϵ_{vib} and E_0.

We notice that independently of the collective inertias scheme the t_{sf} trend in Fig. 7.7 resembles the general trend of the maximum fission barrier height plotted in the upper left panel of Fig. 7.1, as we already pointed out with the GCM collective inertias employed in the previous section. This result confirms that quantities like collective inertias and the shape of the barrier are responsible for local variations in the stability of the nucleus against the fission process. Nevertheless, the choice of the collective inertias scheme has a clear impact on the absolute value of the spontaneous fission lifetimes. For example, the semiempirical inertias predict a substantial larger amount of nuclei with $t_{\mathrm{sf}} \lesssim 3\,$s, that is the timescale at which the r-process operates from the onset of neutron captures till the exhaustion of all neutrons. Due to the inclusion of the time-odd response of the nucleus to small perturbations of the deformation, the t_{sf} predicted by the ATDHFB scheme are systematically larger than the GCM ones. We also notice that the ATDHFB inertias are larger than those obtained with the semiempirical scheme for the vast majority of the nuclei. There is only a small set of nuclei where the lifetimes predicted by GCM are larger than the ATDHFB ones. These nuclei correspond to the most extreme case of instability, with almost vanishing fission barrier and $t_{\mathrm{sf}} \sim 10^{-21}$ s, where the rotational energy correction $\epsilon_{\mathrm{rot}}(Q_{20})$ plays a leading role in determining the SF lifetimes. For nuclei with $Z \leq 96$ semiempirical lifetimes lie in between of the ATDHFB and the GCM lifetimes, while for nuclei with $Z > 96$ the semiempirical lifetimes become smaller than the GCM ones.

The larger discrepancies among the different schemes are found in the region where the fission lifetimes are extremely high ($Z \lesssim 96$). Due to the stability of these nuclei against the fission process their fission decay will not play a relevant role during the r-process nucleosynthesis. Since we are interested in nuclei relevant for r-process calculations, in the following we will restrict the discussion to nuclei with $t_{\mathrm{sf}} \leq 3$ s. For a more detailed comparison the right panels of Fig. 7.7 show the ratio of the lifetimes computed with different collective inertia schemes: ATDHFB to GCM (upper panel), ATDHFB to semiempirical inertias (middle panel) and GCM to semiempirical inertias (lower panel). The values shown in this plot correspond to the quantity

$$R_{\mathcal{M}2}^{\mathcal{M}1} = \log\left(\frac{t_{\mathrm{sf}}(\mathcal{M}_1)}{t_{\mathrm{sf}}(\mathcal{M}_2)}\right), \tag{7.4}$$

being $t_{\mathrm{sf}}(\mathcal{M}_i)$ the spontaneous fission lifetimes computed using the collective inertia $\mathcal{M}_i$. For these nuclei the average difference in the SF lifetimes using different inertias schemes is between one and three orders of magnitude, which in principle may be related to the logarithmic precision of the half-lives obtained for tunneling decays. The largest differences are found between the ATDHFB and semiempirical schemes in nuclei lying between the r-process path and the neutron drip-line and around the shell closure $N = 184$. Since the former is a relevant region for r-process nucleosynthesis, one could expect that such variations in the penetrability may have an impact in the final r-process abundances. This hypothesis will be further explored in Chapter 8 while studying the sensitivity of the r-process abundances to different collective inertias.

7.2.3 Sensitivity to the collective ground state energy and zero-point energy correction

The collective ground state energy E_0 represents the true ground-state energy obtained after considering quantal fluctuations in the collective degrees of freedom. It plays an analog role to the zero-point energy $\hbar\omega/2$ of the harmonic oscillator and in principle could be computed as half of the square root of the potential energy curvature around the minimum divided by the collective inertia. However in several applications it is choose as a free parameter or kept fixed at some reasonable value. In this thesis we follow the last approach and set $E_0 = 0.5$ MeV. It is interesting to study the sensitivity of the spontaneous fission lifetimes to E_0 because we can explore with more detail the impact of variations in the fission barriers and mimic the effect of a renormalization the fission barriers. Fig. 7.8 shows the logarithm of the lifetimes ratio of 0.5 to 1.5 MeV computed with the ATDHFB, GCM and the semiempirical inertias. We notice that for many nuclei the sensitivity of t_{sf} to E_0 is comparable or even larger than the sensitivity to the collective inertias. This is because nuclei plotted in Fig. 7.8 have relatively short barriers and usually with a complex shape presenting multiple humps, like in the case of the ^{290}No plotted in Fig. 6.11. As it was already extensively studied in Ref. [128], the presence of a second fission isomer increases the spontaneous fission lifetimes by several orders of magnitude. By increasing the E_0 to 1.5 MeV the isomer can be shifted below the ground-state energy of the nucleus, and therefore the lifetimes are strongly reduced since the third hump does not contribute anymore to the penetration probability.

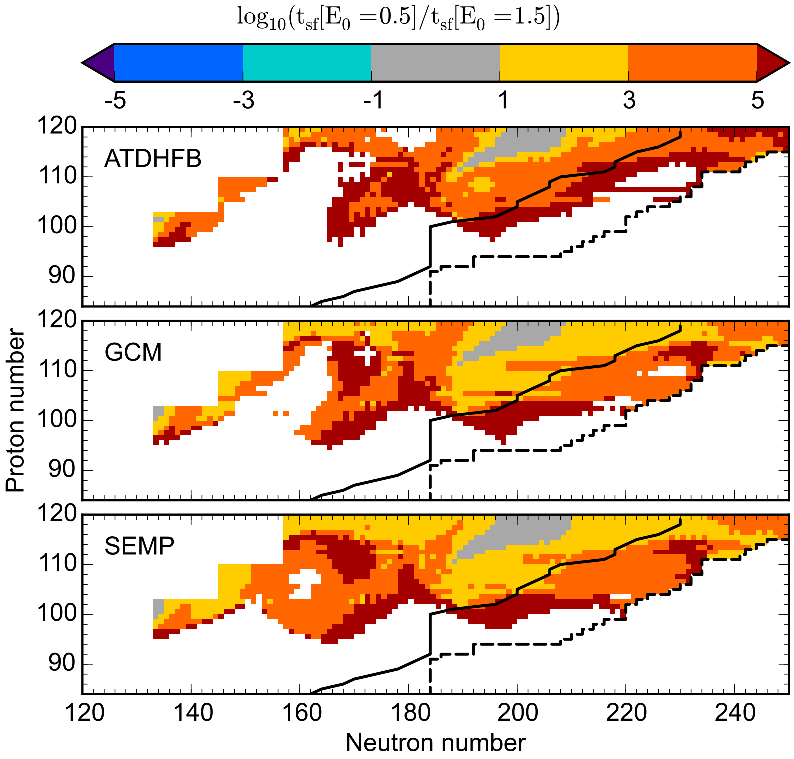

Figure 7.8: Sensitivity of the spontaneous fission lifetimes to different values of the collective ground-state energy $\log_{10}\left[t_{\mathrm{sf}}(E_0 = 0.5\,\mathrm{MeV})/t_{\mathrm{sf}}(E_0 = 1.5\,\mathrm{MeV})\right]$ computed with BCPM and different collective inertias: ATDHFB (upper panel), GCM (lower panel) and semiempirical inertia formula (lower panel). Figure taken from Ref. [103].

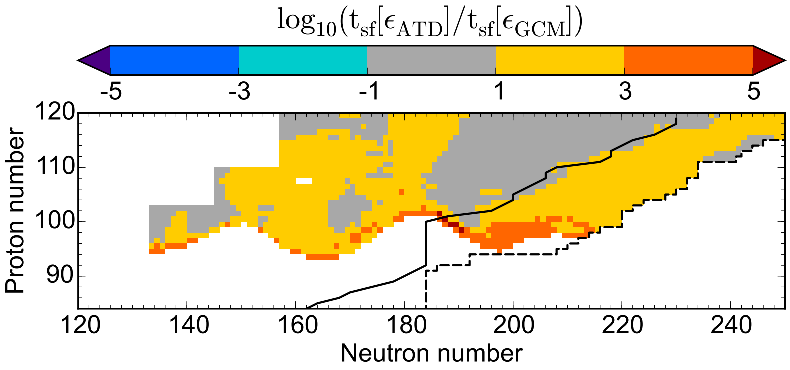

Figure 7.9: Logarithm of the ratio of the spontaneous fission lifetimes of ATDHFB to GCM vibrational energy correction ϵ_{vib} computed using the semiempirical collective inertias and the BCPM functional. Figure taken from Ref. [103].

More in general this result agrees with the study of Sec. 7.2 where we concluded that the spontaneous fission lifetimes of nuclei with small barriers are more sensitive to the topology of the barrier than to the collective inertias. It also suggests that the renormalization of the barriers may strongly influence the location of the region where the *r*-process path is terminated by the neutron-induced fission.

We conclude this discussion showing the impact of the vibrational zero-point energy correction ϵ_{vib} on the spontaneous fission lifetimes. Fig. 7.9 shows the logarithm of the ratio of t_{sf} computed with the same semiempirical inertias and two different ϵ_{vib} calculations, the ATDHFB and GCM scheme:

$$\epsilon_{\text{vib}}^{\text{ATDHFB}}(Q_{20}) = \frac{G(Q_{20})}{\mathcal{M}_{\text{ATDHFB}}(Q_{20})}, \tag{7.5}$$

$$\epsilon_{\text{vib}}^{\text{GOAGCM}}(Q_{20}) = \frac{G(Q_{20})}{\mathcal{M}_{\text{GOAGCM}}(Q_{20})}, \tag{7.6}$$

where $G(Q_{20})$ is the overlap width between two configurations with similar quadrupole deformations:

$$G(Q_{20}) = \frac{\text{M}_{-2}}{2(\text{M}_{-1})^2}. \tag{7.7}$$

$\text{M}_{(-n)}(Q_{20})$ is the energy-weighted momentum of the quadrupole generating field that can be expressed in terms of the two-quasiparticle excitations $|\alpha\beta\rangle$:

$$\text{M}_{(-n)}(Q_{20}) = \sum_{\alpha>\beta} \frac{|\langle\alpha\beta|Q_{20}|0\rangle|^2}{(E_\alpha + E_\beta)^n}. \tag{7.8}$$

We find that the t_{sf} computed with the ATDHFB ϵ_{vib} are usually between 1 and 2 orders of magnitude larger than the GCM ones, but these variations induced by the zero-point energy correction are small compared to the sensitivity of the lifetimes to different collective inertia schemes and collective ground-state energies. This is because the vibrational zero-point energy corrections depend weakly on Q_{20} and therefore the contribution of this quantity in Eq. (7.3) does not substantially modify the fission barrier.

7.3 Reaction rates

In order to study the impact of our results on the r-process nucleosynthesis we use the binding energies, fission barriers and collective inertias presented in this Chapter as a nuclear input for the calculation of stellar reaction rates. In this thesis the reaction rates are computed following the Hauser-Feshbach statistical model described in Chapter 4. We briefly recall that in astrophysical plasma nuclei exist in both their ground and excited states, where relative populations of the excited levels obey a Maxwell-Boltzmann distribution. For a neutron induced reaction, the stellar reaction rate is obtained by folding the (stellar) reaction cross section σ^* of Eq. (4.25) with a Maxwell-Boltzmann distribution of the relatives velocities between targets and neutrons [129]. In this thesis we want to derive a complete set of neutron induced reaction rates relevant for r-process calculations employing the nuclear input consistently computed from the same energy density functional. Ideally we would like to perform these calculations using all the functionals described along this thesis, and study the variations in the r-process nucleosynthesis obtained from the different sets of reaction rates. As a first step towards this systematic study of the role of superheavy nuclei in the r process, we computed the reaction rates using the nuclear outcome of the BCPM EDF. This section is thus devoted to explore the sensitivity of neutron induced reaction rates to different collective inertias schemes, employing for the first time microscopic collective inertias in the calculation of the fission transmission coefficients.

Fig. 7.10 shows the dominating decay channel, defined as the channel with the biggest decay rate, as a function of proton and neutron number for nuclei in the superheavy landscape. Panels a), b) and c) are the results obtained using the BCPM EDF and the ATDHFB, GCM and semiempirical collective inertias schemes, respectively. All the calculations are obtained employing the back shifted Fermi gas model [95] for the level densities and the Kopecky-Uhl generalized Lorentzian gamma-ray strengths [85]. For comparison, the results obtained using the HFB14 EDF [29, 130] are shown in panel d)[1]. The rates are obtained for typical conditions of r-process nucleosynthesis in neutron star mergers with $T = 0.9\,\text{GK}$ and $n_n = 1.0 \times 10^{28}\,\text{cm}^{-3}$ [102]. As it was already expected all the models predict that in the relevant region for the r-process nucleosynthesis, where the neutron separation energies are $S_n \sim 2$ MeV, the two competing channels are the neutron induced fission (n, f) and the radioactive capture (n, γ). Neutron captures dominate below $Z = 100$ but for higher proton numbers fission is the dominating decay. As already deduced from the neutron induced energy window (see the discussion in Sec. 7.1), the critical region for the termination of the r-process path is above the $N = 184$ shell closure, where the r-process path enters in a region with low fission barriers where all the models predict the neutron induced fission to be the dominating channel.

It is interesting to study the differences in the predictions obtained from the collective inertias schemes. In Sec. 6.4 and 7.2 we showed that the ATDHFB predict the largest collective inertias among all the models. The increase of the collective inertias reduces the fission probability yielding to lower fission cross sections and reaction rates. Thus, the reaction rates computed with the ATDHFB should reflected a larger dominance of the neutron capture over the neutron induced fission. However, along this thesis we discussed several times that the collective inertias have a relevant impact only in nuclei with relative small fission probabilities and that the sensitivity of the cross sections decrease as we increase the excitation energy of the compound nucleus. We deduce therefore that collective inertias will have a relevant impact only in those nuclei where the barriers are small enough allowing the fission decay to be a competing channel, but at the same they are large enough to reflect the impact of the collective inertias. One can check this hypothesis by looking at Fig. 7.10, where we notice that the difference in the BCPM predictions are mainly localized in the region between $S_n = 2$ MeV and the neutron drip-line, where $B_f - Sn = 2 - 4$ MeV, while the rest of the landscape does not show any relevant difference. The results obtained with both the GCM and the semiempirical inertias suggest the possibility that above

---

[1] Results in panel d) of Fig. 7.10 are available at the url `http://www.astro.ulb.ac.be/pmwiki/Brusslib/Talys`, except for the spontaneous fission rates. These are obtained using the fission barriers present in the TALYS 1.8 code [87] together with the semiempirical inertias [29]. Alpha-decays for this model are not considered in this plot.

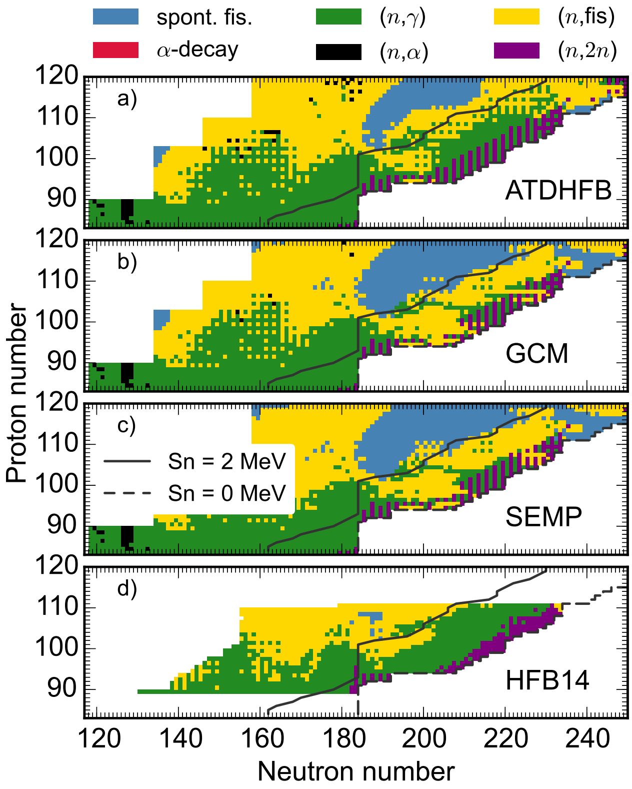

Figure 7.10: Dominating decay channel in the superheavy landscape: spontaneous fission, alpha-decay, neutron-capture, neutron-induced alpha emission, neutron-induced fission and two-neutron emission. Panels a), b) and c) shows the results obtained using the BCPM EDF for different collective inertias schemes. Panel d) shows the results obtained using the HFB14 EDF [29, 130].

nuclei with ~ 280 the fission path will be terminated by neutron induced fission. On the other hand, the ATDHFB masses allow for a corridor between the $S_n = 2$ MeV and the neutron dripline where neutron captures are dominating. However, the material may never reach this narrow corridor in which (n, γ) dominates over (n, f) due to the even larger $(n, 2n)$ rates predicted by the models. We can conclude then that independently of the computational scheme the production of nuclei heavier than $N > 184$ will be strongly hindered due to the dominance of neutron induced fission. Comparing our results with the HFB14 calculations, we notice that the latter are closer to the ATDHFB predictions since they predict a larger dominance of (n, γ) over (n, f). However, also in these results the production of superheavy nuclei above $N = 184$ may be limited by the presence of neutron induced fission and $(n, 2n)$.

Regarding the other decay channels we find that only spontaneous fission may play a relevant role for nuclei where the fission barriers are below 1 MeV. This conclusion however does not take into account the possible role played by beta-delayed fission decays, which in principle should overcome the spontaneous fission process when the material will start to move towards stability by means of beta decays. We also computed the rates for the photo-induced fission process (γ, f) but we find that it does not play any significant role. We will come back to this point during the discussion of the *r*-process calculations in the next Chapter.

8 Impact of fission on r-process nucleosynthesis in neutron star mergers

The final goal of this thesis was to study the impact of fission on the r-process nucleosynthesis occurring in neutron star mergers. As we will discuss during this Chapter, estimating the region in the nuclear chart where fission occurs and the amount of material accumulated in the fissioning region are two crucial ingredients in the prediction of r-process abundances. Ideally we would like to estimate how the uncertainties for the predicted fission properties affect the r-process nucleosynthesis by using several sets of fission and neutron-induced rates, each of them consistently computed from the same model. We are currently working towards this major goal, and in this Chapter we will present the nucleosynthesis calculations obtained using two different calculations of reaction rates, one of which is the BCPM set introduced in the previous Chapter. We will start giving a general overview of the role played by fission during the r-process and discussing those features that are commonly observed in recent network calculations. Afterwards we will present the r-process nucleosynthesis calculations predicted with the BCPM rates and compare our results with those obtained using a different set of reaction rates. Finally the last part of this Chapter is devoted to analyze the impact of our calculations in the production of radioactive energy at timescales relevant for macronova observations. Since several of the results presented in this Chapter are still preliminary, we will also discuss which aspects of this study should be further explored.

8.1 The role of fission in r-process nucleosynthesis

The rapid neutron capture process, or r-process, is responsible for the production of roughly half of the nuclei heavier than iron that are observed in the Universe [1]. Despite the fact that its astrophysical site is still unknown, recent simulations suggest the merger of two neutron stars (NSM) as a likely candidate for the occurrence of this process [131]. In NSM a large amount of material, between 10^{-3} and $10^{-2} M_{\odot}$ [20, 21, 132], can be ejected during the dynamical (prompt) phase from the contact interface of the neutron stars and the surface regions close to the orbital plane. This material is extremely neutron rich and the largest part of it ($\sim 90\% - 95\%$) is converted in r-process nuclei with a distribution resembling the pattern observed in the solar system [102, 133]. The radioactive decay of this r-process nuclei is expected to trigger electromagnetic transients in the optical and infrared bands, also known as "macronova" or "kilonova", that if observed would represent the first detection of r-process material in situ [14, 16, 134].

In the last years there have been several studies exploring the sensitivity of the r-process abundances in NSM to different astrophysical scenarios [19–21] and variations in the nuclear input [102, 135–137]. All these calculations show that if NSM is the actual site for the r-process nucleosynthesis, the appearance of fission is unavoidable. This is a natural consequence of the large neutron-to-seed ratio required during the r-process that allows the seed nuclei to become heavier and heavier until they become unstable against fission. Once the r-process path reaches this fissioning region the material decay back to lighter nuclei, where the fission fragments can capture neutrons giving rise to the so-called fission cycling. The number of fission cycles occurring during the r-process can be estimated by looking at the temporal evolution of the average mass number $\langle A \rangle$ as it is shown in Fig. 8.1. From this plot we can see that during the first second after the ejecta the material reaches the fissioning region and is cycled back to lighter nuclei a total of three times. Over time the neutron density (n_n) decreases yielding to a fall in the neutron-to-seed ratio (n_n/s). When $n_n/s = 1$, seed nuclei can not capture on average more than

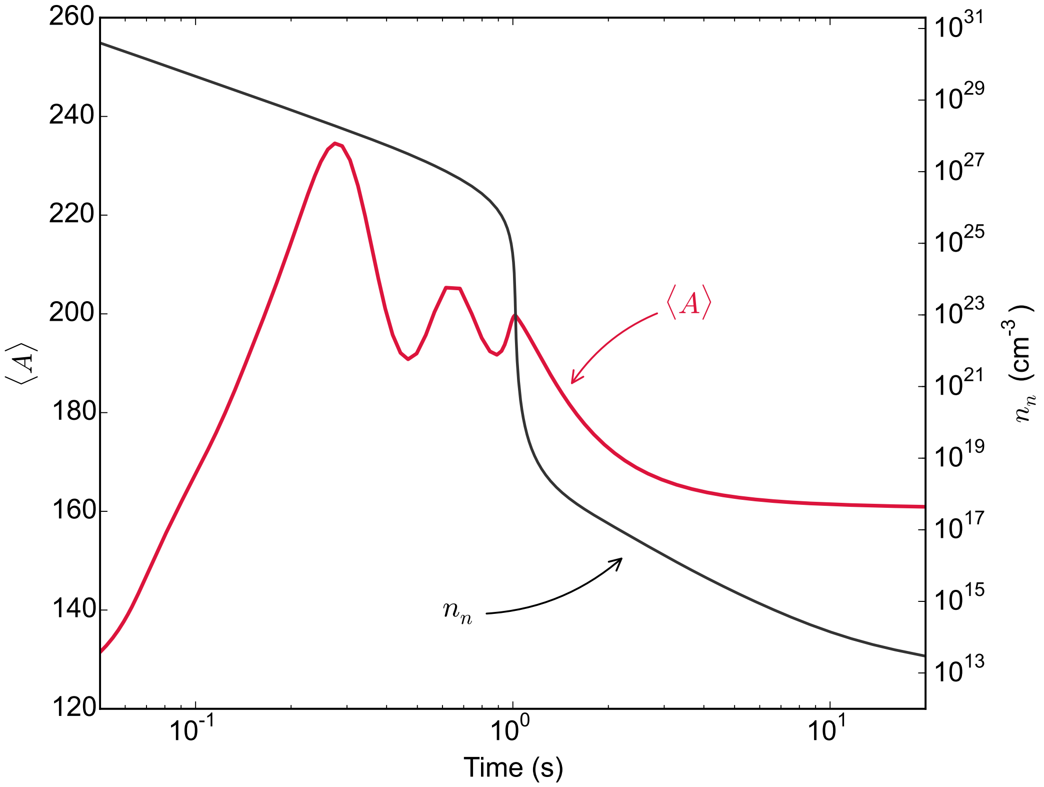

Figure 8.1: Time evolution of the averaged mass number $\langle A \rangle$ (red line, left axis) and neutron densities (black line, right axis) in cm^{-3}, for a representative trajectory of the merger of two NS with $1.35 M_{\odot}$.

one neutron each, and one says that the r-process freezes out. After this moment the cycling is halted and the material starts to β decay to stability and fission to light nuclei. Even though these results correspond to a particular trajectory based on a three dimensional relativistic simulation of the merger of two NS with $1.35 M_{\odot}$, the evolution described before is a common feature in all the simulations of r-process nucleosynthesis occurring in the dynamical ejecta of NSM. The typical number of fission cycles is estimated to be around two and three, depending on the initial neutron-to-seed ratio.

Considering the scenario presented before it is clear that fission plays a crucial role during the evolution of the r-process nucleosynthesis in NSM. In Ref. [102] it was shown that when the amount of material accumulated in the fissioning region at the freeze-out is much larger than the amount of material accumulated around the second peak, the final abundances below the third peak are insensitive to the initial astrophysical conditions. The reason for this is that fission yields are virtually insensitive to particular thermodynamic conditions, and therefore the spread in the abundances pattern produced by fissioning nuclei is very small. This robustness of the r-process abundances is a very appealing feature since it could explain the presence of nuclei with $Z \geq 40$ in proportions similar to solar observed in metal poor stars [22]. In Chapter 7 we showed that the fissioning region relevant for the r-process is located above the neutron shell closure $N = 184$, in agreement with other recent studies [102, 136]. The amount of material accumulated in this region depends on the shell gap and the beta decay half-lives of nuclei with $N = 184$. Once the r-process path overcomes this waiting point it enters in a region where nuclei are predicted to decay by fission populating the region around mass number $120 \leq A \leq 140$. The distribution of fission fragments is therefore a crucial ingredient in the shaping of the r-process abundances, also because it provides a non-negligible source of free neutrons that can be captured by seed nuclei at the latest times of the evolution shifting the position of the peak at $A \sim 195$ [135]. These neutrons are emitted by the fission yields having a Z/A ratio similar to the one of the parental nucleus.

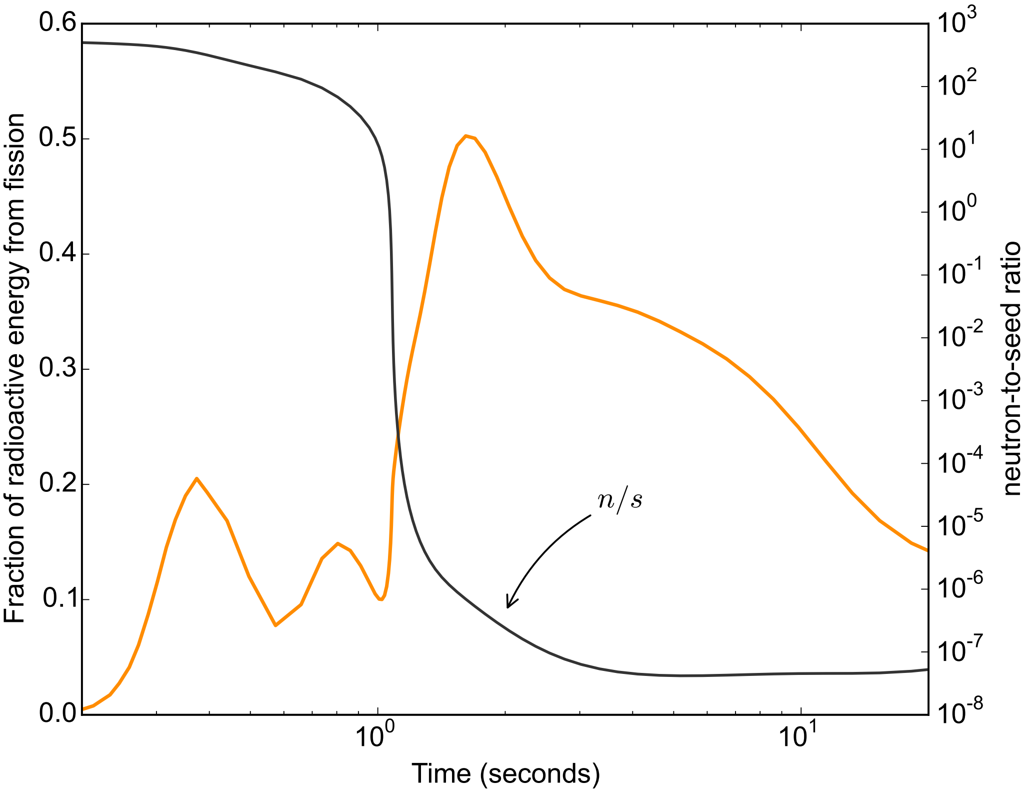

Figure 8.2: Fraction of the total radioactive energy emitted by fission (orange line, left axis) and neutron-to-seed ratio (black line, right axis) as a function of time for a representative trajectory of the merger of two NS with $1.35M_\odot$.

Finally, fission can be an important source of energy generation during the neutron irradiation and when the material starts to β decay to stability [136]. Fig. 8.2 shows the contribution of fission to the total radioactive energy during the first tens of seconds after the ejecta. Before reaching the freeze-out fission contributes up to a 20% to the total radioactive energy, and this contributions increases up to a 50% after the freeze-out when the material starts to β decay triggering β-delayed fission. As the material moves closer to the stability the fission contribution diminishes, and it does not seem to sensibly contribute at timescales relevant for macronova observation ($\sim$ days to weeks). This aspect will be further studied in Sec. 8.4 of this Chapter.

Fig. 8.3 shows the density and temperature profile of the trajectory used in this Chapter. As discussed in Ref. [102], the evolution of the temperature is driven by the fact that at high densities the equation of state (EoS) is dominated by the ideal gas component of nuclei. At early times the temperature decreases due to the fast expansion timescale, which in turn determines when the temperature reaches its minimum. After that, the temperature starts to increase until the point when the EoS becomes dominated by radiation. The dominance of the radiation implies a large specific heat, that reduces the efficiency at which the energy generation contributes to the temperature increase flattering the maximum in temperature [102].

8.2 *r*-process abundances from BCPM rates

We will now present the results of our *r*-process nucleosynthesis calculations for matter dynamically ejected in NSM. Before analyzing the outcome obtained from our simulations we briefly introduce the nuclear physics inputs of the reaction network used in this thesis (for further details regarding the reaction network we refer to the discussion in Chapter 5). We employ the reaction network of

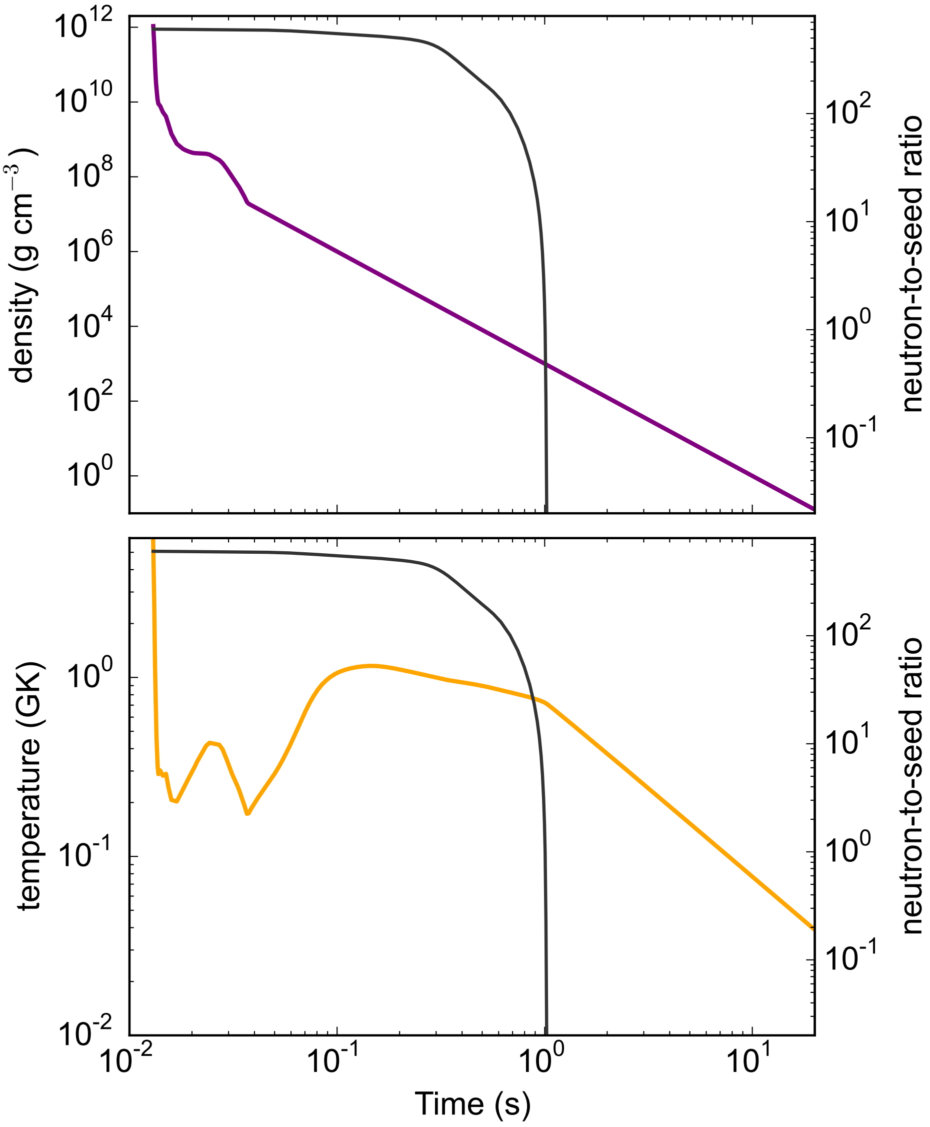

Figure 8.3: Evolution of the density (upper plot, purple line, left axis) and temperature (lower plots, orange line, left axis) for the trajectory used in this study. The black line in both plots shows the evolution of the neutron-to-seed ratio.

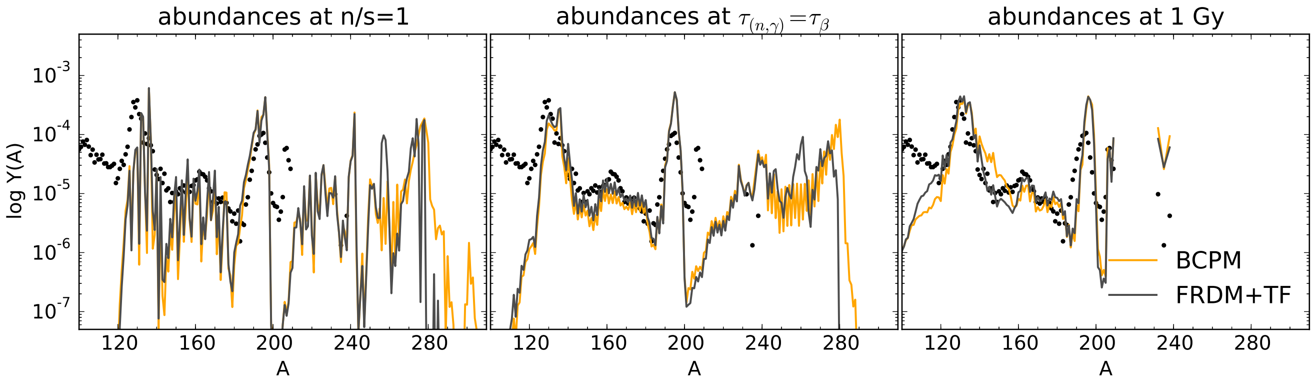

Figure 8.4: r-process abundances from matter dynamically ejected in NSM as a function of the mass number obtained using the BCPM (orange line) and FRDM+TF [121] (gray line) stellar reaction rates. The three panels show different phases of the evolution: when the neutron-to-seed ratio becomes equal to one (left panel); the time when the beta-decay rate equals the neutron-capture rate (middle panel); and at 1 Gyr, when most of the material has decayed back to stability (right panel). The solar r-process relative abundances are plotted as solid circles to guide the eye.

Ref. [102] covering the nuclear chart up to $^{270}_{120}$Uub. For nuclei above $Z \geq 84$ we use the neutron captures, photo-induced fission, spontaneous fission and alpha-decay rates obtained from the BCPM EDF and presented in Chapter 7. The photodissociation rates are obtained from the neutron-captures rates using the detailed balance discussed in Sec. 4.3.2. Nuclei below polonium are not expected to contribute via fission decay [136], and we use the neutron-induced reaction rates from Ref. [121], that are based on the Finite Range Droplet Model (FRDM) nuclear masses [138] and the Thomas-Fermi (TF) fission barriers [139]. From now on we will refer to this set of neutron-induced rates as FRDM+TF. We use the compilation of beta-decay and beta-delayed neutron emission rates of Ref. [140] derived from QRPA calculations on top of the FRDM nuclear mass model. These beta-decay rates were used in Ref. [127] to compute the beta-delayed fission rates employed in our calculations. In the first part of this study we will focus the discussion on the BCPM results obtained using the ATDHFB collective inertias and the comparison with the predictions obtained using the FRDM+TF rates, and we keep the analysis of the sensitivity to different collective inertias schemes for the last section.

8.2.1 BCPM vs FRDM+TF

We have performed nucleosynthesis calculations based on a smoothed-particle trajectory extracted from a three-dimensional relativistic simulation of a binary system of two neutron stars with $1.35 M_\odot$ (see discussion in Sec. 5.5). The initial composition of the material is determined by nuclear statistical equilibrium with an initial temperature of 6 GK, $\rho = 1.2 \times 10^{12}$ g cm^{-3} and electron fraction $Y_e = 4.73 \times 10^{-2}$, and we follow the evolution of the system until all nuclei decay to stability. Fig. 8.4 shows the r-process abundances as a function of the mass number A obtained from the BCPM reaction rates at three different times: when the r-process freezes out (left panel), defined as the moment when the neutron-to-seed ratio becomes one and seed nuclei cannot capture in average more than one neutron each; the time when the averaged beta-decay rate equals the neutron capture rate (middle panel) and the material starts to decay back to stability; and finally at 1 Gyr (right panel), when the nuclei that are left can be considered to be stable. The BCPM abundances are compared with those obtained using the FRDM+TF neutron capture rates, and the solar r-process abundances are plotted to guide the eye. We stress once again that for nuclei below $Z = 84$ the nuclear input is the same in both calculations, which allows to study the role that nuclei above bismuth play in the r-process nucleosynthesis.

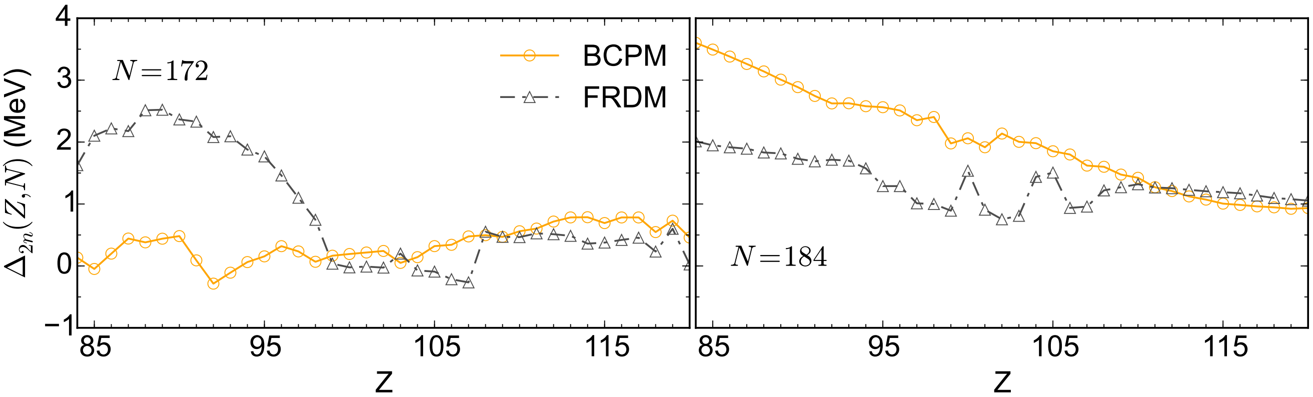

Figure 8.5: Shell gap $\Delta_{2n}(Z,N) = S_{2n}(Z,N) - S_{2n}(Z,N+2)$ in MeV as a function of the proton number predicted by BCPM (orange line) and FRDM [138] (gray line) mass models for nuclei with $N = 172$ (left panel) and $N = 184$ (right panel).

Before analyzing the differences between both calculations we will discuss the general features in the evolution of the *r*-process abundances and introduce some of the nomenclature used in the following sections. Distributions at freeze out show one sharp peak at $A \sim 195$ (the so-called third peak) produced by nuclei with a magic neutron number $N = 126$. These nuclei have beta-decay half-lives that are long enough to allow the accumulation of material already at this stage of the evolution. On the other hand, the second peak ($A \sim 130$) produced by nuclei at shell closure $N = 82$ is only shaped at later times, when the material coming from fission yields starts to populate this region. The main contribution from fission is given by nuclei with $N = 184$ at $A \sim 280$, as testified by the peak in the abundances present at the freeze-out and when $\tau_{(n,\gamma)} = \tau_\beta$. Finally, the rare-earth peak at $A \sim 160$ and the lead peak at $A \sim 208$ produced by the α-decay of heavier nuclei are also visible in the final abundances.

Regarding the differences in the abundances predicted by BCPM and FRDM+TF in Fig. 8.4 we notice the following aspects. At the freeze-out the predictions start to differ at $A = 256$, where the dominant contribution comes from the $^{256}_{84}$Po. The neutron number of this nucleus reflects the extreme neutron rich conditions achieved by the material at this early stage of the evolution. After this point the BCPM abundances show a strong odd-even staggering, specially at the time when $\tau_{(n,\gamma)} = \tau_\beta$. The reason of this staggering is related to an odd-even effect in the neutron-capture rates arising from the opening of the $(n, 2n)$ channel. The neglection of this channel in the network calculations produce a pile up of the odd-even effect in the abundances as a function of the mass number, that is reflected in the strong odd-even staggering visible in Fig. 8.4. We are currently working to include this channel in our calculations, but this study was not finished by the time of writing this thesis.

The two calculations also differ in the region where the material accumulates. Looking at the time when $\tau_{(n,\gamma)} = \tau_\beta$ we notice that FRDM+TF shows a peak around $A = 257$ related to the larger shell gap predicted by the FRDM mass model at $N = 172$ (see left panel of Fig. 8.5). The decay of this material produces an enhancement of the abundances below the second peak ($A \sim 120$) visible in the pattern at 1 Gyr. Conversely, at the freeze-out the abundances predicted by BCPM show a larger peak around $A = 280$ corresponding to nuclei around the neutron magic number $N = 184$. We notice that around this shell closure BCPM predicts fission barriers that are in average 2 MeV higher than those predicted by TF. The higher fission barriers combined with a larger shell gap (see right panel of Fig. 8.5) allow for a larger accumulation of material in this heavy region. Later these nuclei decay by fission increasing the abundances above the second peak $A \sim 130$. In Fig. 8.6 we can see in more detail how the abundances predicted by BCPM reach heavier nuclei compared to FRDM+TF at the time when the neutron-to-seed ratio is equal to one. These nuclei correspond to the corridor described in Sec. 7.3 where neutron captures dominate over the neutron induced fission. However, a larger accumulation of material in this region is inhibited by the rather narrow neck at $Z/N = 100/190$ that the *r*-process path has to pass in order to

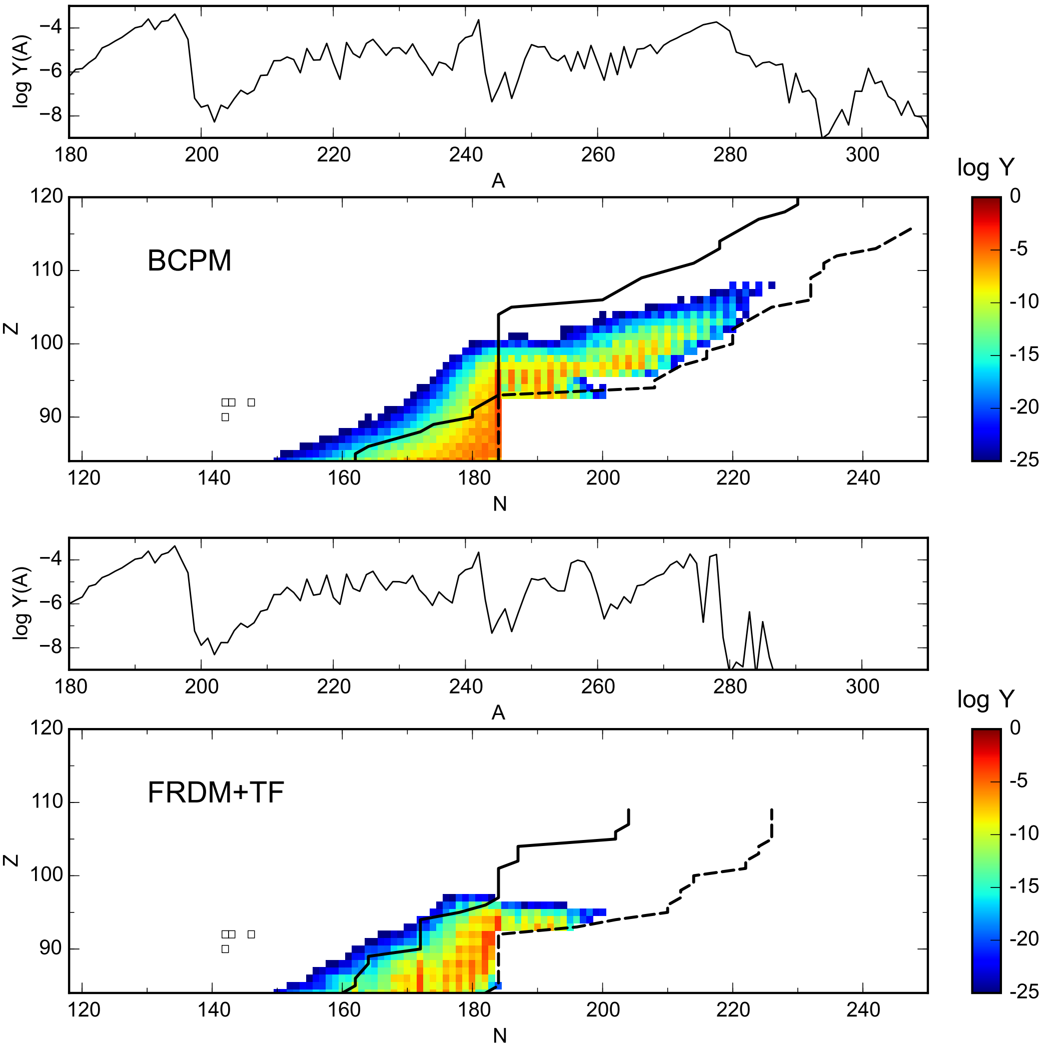

Figure 8.6: r-process abundances at the freeze-out predicted by BCPM (upper plots) and FRDM+TF models (lower plots). Contour plots show the abundances as a function of the neutron and proton number, where empty boxes represent stable nuclei.

reach the (n, γ) corridor (see upper panel of Fig. 7.10).

From the previous results we conclude that the evolution of the r-process abundances is more sensitive to local variations in the neutron separation energies rather than in the global trend of the binding energies. This is an important point that one has to keep in mind while exploring the sensitivity of the r-process abundances to different theoretical predictions of nuclear masses. The critical issue in the usage of energy density functionals is the fact that the most relevant regions for the r-process nucleosynthesis are around the shell closures, that is where sudden changes in the neutron separation energy manifest more prominently. As we already extensively discussed in Sec. 6.2, EDF's calculations at mean-field level have severe difficulties to properly describe the nuclear properties around these regions. Therefore, systematic evaluations of binding energies using beyond mean-field approaches would be a very valuable nuclear input for r-process nucleosynthesis calculations.

It is interesting to notice that the ratio of ^{232}Th and ^{238}U at 1 Gyr is very similar in both calculations. These nuclides have half lives that are comparable to the cosmic age ($t_{1/2}(^{232}\text{Th}) = 14.0$ Gyr and $t_{1/2}(^{238}\text{U}) = 4.47$ Gyr) and have been used as a cosmochronometers. However, in order to perform realistic estimations of the galactic age it is necessary to understand the production of these nuclei and quantify the variations related to uncertainties in the nuclear physics inputs [141, 142]. The predicted

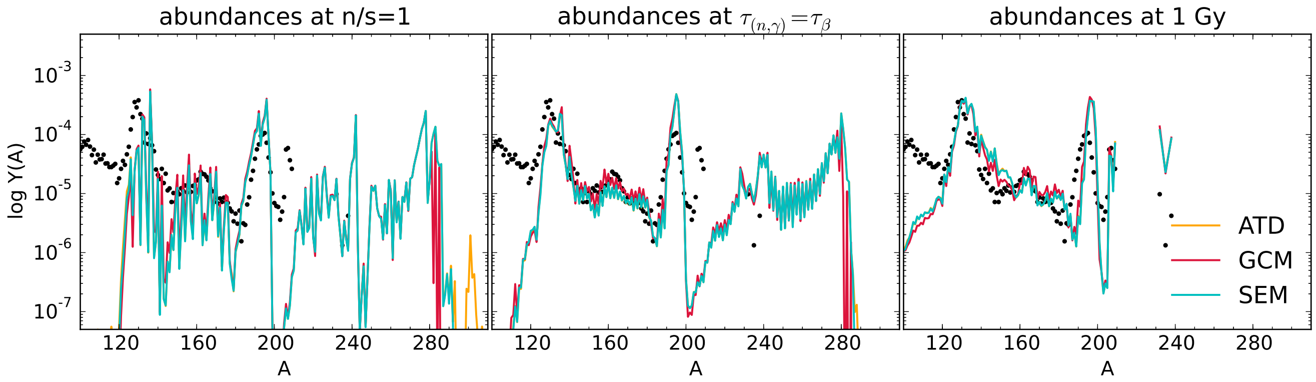

Figure 8.7: r-process abundances as a function of the mass number at different phases of the evolution (see Fig. 8.4 and text for more details) predicted by BCPM for different collective inertias schemes: ATDHFB (Eq. (3.42)), GOAGCM (Eq. (3.28)) and semiempirical formula (Eq. (3.44)).

^{238}U/^{232}Th ratio is 0.873 for BCPM and 0.866 for FRDM. The similar values obtained in both calculations show that the production of ^{232}Th and ^{238}U is mainly determined by the nuclear physics below $Z = 84$. The slight variation in the absolute value of the ^{232}Th and ^{238}U abundances can be traced-back to the alpha decay of nuclei surviving to fission after the freeze out. In Sec. 8.4 we will see that the insensitivity of the abundances to the nuclear physics above $Z = 84$ can be extended to all the actinides produced during the r-process nucleosynthesis, which may have interesting consequences for the electromagnetic counterparts of compact object mergers.

8.2.2 Sensitivity to collective inertias

So far we have restricted our discussion to the r-process abundances obtained using the ATDHFB collective inertias. Fig. 8.7 shows sensitivity of our results to different collective inertias schemes, and clearly the variations are rather small during all the phases. This result was already expected from the analysis of the fission cross sections in Sec. 6.5.2, where it was shown that variations in the collective inertias only have relevant impact when the fission probabilities are small, which means in nuclei stable against the fission process. However, some interesting conclusions can be drawn from this comparison. First of all, the ATDHFB are the only collective inertia scheme predicting a r-process path proceeding beyond $A = 290$ and reaching the (n, γ) corridor discussed before. From the analysis of the experimental fission lifetimes in Chapter 7 we concluded that the ATDHFB masses are probably too high, coming out against a real possibility of reaching such heavy nuclei. On the other hand, for lower masses the semiempirical and ATDHFB schemes predict very similar abundances, justifying to some extent the usage of the phenomenological formula in the calculation of the fission cross sections for r-process nuclei. Finally, the results in Fig. 8.7 were obtained using the binding energies including the rotational energy correction. The staggering in the shell gaps caused by this corrections (see the discussion in Sec. 6.2) produces a depletion in the abundances at $A = 278$, that disappears when the binding energies are calculated without rotational correction. This result highlight once again the crucial role that local variations in the neutron separation energy play for the r-process nucleosynthesis.

8.3 Competition between fission channels

To further explore the dependence to nuclear input Fig. 8.8 shows the temporal evolution of the averaged rates (5.31) for different fission channels obtained with the BCPM and FRDM+TF models of Sec. 8.2.1. In this plot there are several aspects that are worth mentioning. At the earliest stages of the evolution the dominating channel is the neutron-induced fission. The prediction from both models

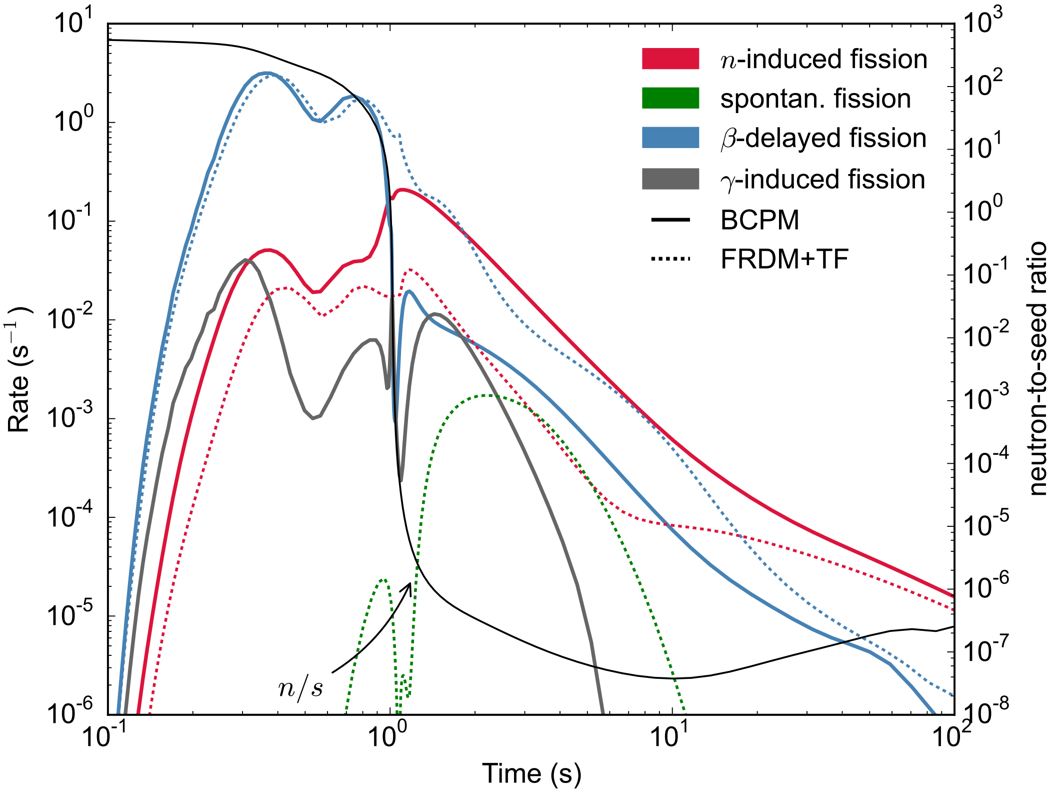

Figure 8.8: Evolution of different fission channels predicted by BCPM (solid lines) and FRDM+TF (dotted lines). The black solid line shows the evolution of the neutron-to-seed ratio (n/s).

is practically identical until the time when the neutron-to-seed ratio becomes one and the r-process freezes out. At this point, nuclei start to beta-decay towards stability emitting beta-delayed neutrons and giving rise to beta-delayed fission. We can see that in the FRDM calculations the neutron-induced fission remains the dominating channel after the freeze-out and it is maintained by the free neutrons emitted by the fission fragments until the density becomes too low to sustain this process. Conversely, after the freeze-out the BCPM neutron-induced fission rates strongly decrease and the beta-delayed fission becomes the dominant decay channel. Shortly after the freeze-out there is a revival of the neutron induced fission feed by the beta-delayed neutrons, but the increase is not large enough to recover the dominance. This drastic decrease of the neutron-induced fission is due to the fact that the beta-delayed fission rates are not consistently computed from the BCPM barriers, and therefore we are overestimating the amount of nuclei decaying via this channel. This is reflected in a large bump of the beta-delayed fission rates after the freeze-out. From this result we conclude that a consistent calculation of all the fission channels is crucial to obtain reliable r-process nucleosynthesis calculations.

Another interesting result is the emerging role of the photo-induced fission, that was not considered in the calculation of the FRDM+TF rates [121]. At early times the contribution of this channel is lower than the neutron-induced fission but larger than the beta-delayed fission. For times after freeze-out is difficult to make reliable conclusions because the outcome may be affected by the artificially low beta-delayed fission rates, but what seems to be certain is that the contribution of this channel is larger than the spontaneous fission. This result was somehow expected, since the fission from the excited state produced after a photon capture should always be more favourable than fissioning from the ground state. What is more subtle is the reason why the photo-induced fission is subdominant compared to the neutron-induced fission. Actually, what is preventing the photo-induced fission to be competitive is the fact that in order to excite a nucleus above the fission barrier the neutron-separation energy has to be higher than the fission barrier, otherwise the neutron emission will dominate. However, the

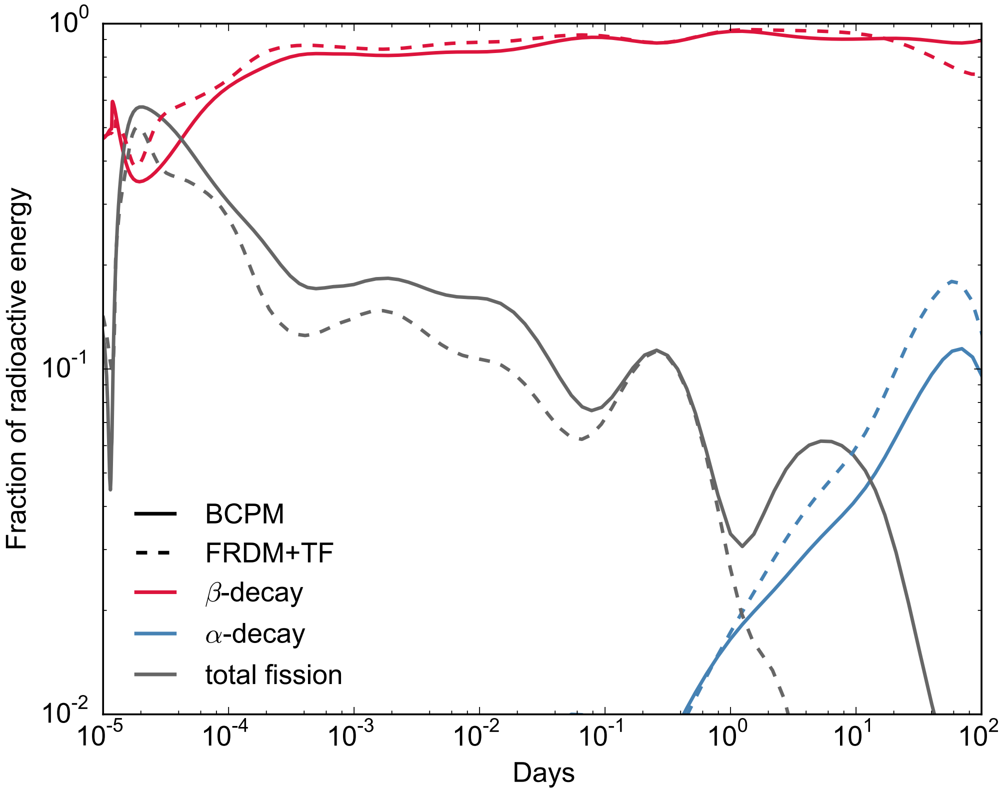

Figure 8.9: Fraction of the total radioactive energy emitted by β-decays, α-decays and fission predicted in BCPM (solid lines) and FRDM+TF (dashed lines) models.

presence of nuclei with fission barriers lower than neutron separation energies is strongly hindered by the neutron-induced fission, which in turn decreases the average photo-induced rates.

8.4 Production of radioactive energy

We will now explore the impact of our calculations in the production of radioactive energy, that is a crucial aspect in macronova modeling. Macronovae are electromagnetic transients powered by the radioactive decay of r-process elements in compact object mergers peaking days to week after the merger [14, 16]. The energy emitted by the radioactive decay products is transfered to the thermal background and re-radiated as thermal energy powering the light curve. A possible recent observation of this transient associated to a short γ-ray burst GRB130603B [17, 18] triggered several studies aiming to improve the macronova light curve modeling. In this section we will focus on the radioactive decay dominating at each stage of the evolution, which is a relevant piece of information for the modeling of kilonova light curves since the efficiency in the thermalization of the radioactive energy depends on the decay producing it [123].

Fig. 8.9 shows the fraction of the total radioactive energy emitted by β-decays, α-decays and fission predicted by BCPM and the FRDM+TF model. There are some interesting conclusions that can be deduced from this plot. The most important one is that both models predict substantially the same features during the whole evolution. For most of the time β-decay is the dominating channel while fission only contributes at early times that are not relevant for macronova observations. While the contribution from fission decreases with time, the fraction of radioactive energy produced by α-decays increases. In a recent paper [123] the contribution of single decay channels to the total radioactive energy and their thermalization efficiencies were extensively studied. The authors show that the choice in the nuclear mass model modifies the estimation of the energy release by α-decays, affecting the total energy generated by the decay of r-process isotopes at times relevant for macronova observation. Our results show that the radioactive energy is rather insensitive to the nuclear physics of isotopes above $Z = 83$, which is related to the fact that the released radioactive energy is mainly determined by the amount of actinides decaying in the ejecta. As we already pointed out in Sec. 8.2.1, these isotopes are produced by the beta-decay of nuclei below $Z = 84$, and for these reason the outcome of BCPM and FRDM+TF is very similar.

8.5 Further work to be addressed

This Chapter contains several results that are preliminary. Here we want to collect the work that remains to be done.

- The r-process calculations obtained from the BCPM rates do not include the $(n, 2n)$ decay channel. This is an important issue to address due to the large rates predicted for this channels in our calculations.
- The impact of collective inertias in the r-process abundances (Sec. 8.2.2 and Fig. 8.7) was obtained using the binding energies including the rotational correction (see Sec. 6.2). The study should be repeated removing this correction in order to ensure the validity of our conclusions.
- The β-delayed fission rates are obtained from [140], but this is not consistent with the rest of fission reaction rates. In order to proceed further in this study, the β-delayed fission rates should be calculated using the fission barriers and collective inertias presented in this thesis.

9 Conclusions & Outlook

In this thesis we studied the fission properties of superheavy nuclei and the impact of fission in the r-process nucleosynthesis in neutron star mergers (NSM). Fission can be described as a tunneling process where the decay probability depends on the evolution of the energy with deformation and the inertia produced by the "movement" of the nucleus in the collective coordinates. Despite its key role the sensitivity of the r-process to different fission predictions has not been explored. One of the reasons is that only few sets of fission rates suited for r-process calculations are nowadays available. Furthermore these stellar reaction rates are based on an approximated description of fission, assuming parabolic shapes of the fission barriers and/or simple formulas for the estimation of the collective inertias.

In this thesis we go beyond these approximations and compute the fission properties of 3642 nuclei in the super heavy landscape using four different energy density functionals (EDF): BCPM, D1S, D1N and D1M. The binding energy, fission barrier and collective inertia of each nucleus are consistently obtained from microscopic calculations by minimizing the potential energy as a function of the quadrupole deformation. The spontaneous fission lifetimes are obtained following the WKB method employing three different schemes for the calculation of the collective inertias. By performing an extensive benchmark against the available experimental data we find that our accuracy is comparable to Skyrme EDF's commonly used in fission calculations. The theoretical predictions tend to overestimate the fission barriers and this effect can be related to the imposition of axial symmetry in our calculations. Since the models have very different effective masses, symmetry and surface energies the estimated height of the fission barrier along the landscape can differ up to 6 MeV but the general trend is very similar for all the functionals.

Looking at the variations of spontaneous fission lifetimes across the superheavy landscape we find that those nuclei that are stable against spontaneous fission are very sensitive to changes in the collective inertias. The comparison between different EDF's shows that the longest half-lives are obtained for the models predicting the highest collective inertias and not from those predicting the highest fission barriers. This sensitivity of the spontaneous fission lifetime to the collective inertia diminishes as the fission barrier decreases, until the point when the fission probability is mainly driven by the height of the fission barrier. In our calculations we find that the transition between these two regimes occurs around the mass number $A \approx 280$. Following this trend of the spontaneous fission lifetimes we propose a renormalization of the collective inertias aimed to improve the agreement with experimental data. Compared to a renormalization of the fission barriers, this method has the advantage that it does not modify the fission properties of r-process nuclei. Using the collective inertia as an adjustable parameter we are able to sensibly improve the agreement of spontaneous fission lifetimes in light actinides keeping the good accuracy achieved in heavier nuclei.

We find that our calculations of neutron capture and neutron-induced fission cross sections obtained from the statistical Hauser-Feshbach model fairly agree with the experimental data in the energy window relevant for r-process calculations. Using the BCPM functional and three different collective inertia schemes we compute the neutron induced stellar reaction rates and study the competition between different decays, including α and photo-induced fission. We find that above $Z = 100$ all the rates predict fission to be the dominating decay channel for typical thermodynamic conditions in NSM. The rates turn out to be rather insensitive to collective inertias, mainly due to the fact that they impact the fission probability of nuclei that are stable against fission. However, some differences are appreciable in the region above the nuclear shell closure at $Z \approx 95$. One collective inertia scheme predicts a region where the neutron capture dominates over the neutron induced fission, opening the possibility for the r-process to reach nuclei with mass number $A \approx 330$. However, the r-path may never reach this region due to the large $(n, 2n)$ rates. We conclude therefore that independently of the model the production of superheavy nuclei above $A = 280$ is hindered due to neutron induced fission.

We use these stellar reaction rates to perform r-process nucleosynthesis calculations for matter dynamically ejected in neutron star mergers, and we compare our results with those obtained from a set of neutron induced reaction rates based on a traditional description of fission. We notice modest differences in the final abundance distributions around the second peak produced by the fission decay of nuclei with $A \approx 260 - 280$. The amount of material accumulated in this region is mainly determined by the shell gaps and fission barriers of nuclei with $N \approx 170 - 190$. We find that the impact of collective inertias for the evolution of the r-process is small and therefore we conclude that our calculations are not sensitive to the collective inertias. Within our model, we notice that the progenitors of the actinides produced at the latest stages of the evolution are mainly nuclei with $Z \leq 84$. This is an important result for estimating the uncertainties in the production of cosmochronometers in metal poor stars and for the radioactive energy emitted by the r-process nuclei at timescales relevant for macronova observations.

Finally, we have also explored the impact on spontaneous fission lifetimes of recent advances in the theoretical description of the fission process. Using the dynamical approach where the fission path is determined by minimizing the action integral, we find that the inclusion of collective degrees of freedom that modify the amount of pairing correlations in the nucleus strongly reduces the spontaneous fission lifetimes of light actinides. The possible impact of this approach for the neutron-induced fission is not clear and should be addressed in future studies.

Suggestions for future work

- An important aspect to address is the consistent calculation of β-delayed fission rates using our fission barriers. In this thesis we have adopted the β-delayed fission rates from [140], but in Sec. 8.3 we found that a consistent calculation of all the fission decay channels is required in order to properly study the impact of fission in the r-process nucleosynthesis. Since in the r process we are dealing with neutron-rich nuclei, the relevant β-delayed processes to consider are fission and neutron emission. The β-delayed rates of these two reactions can be computed using a compilation of β-strengths distributions covering the relevant nuclei for the r-process, like for instance the one presented in Ref. [143]. It would be advisable therefore to start a collaboration with a group that could provide the β-strength distributions of r-process nuclei.

- A rather simple but extremely interesting continuation of this work will be the extension of the calculation of the stellar reaction rates to the Gogny EDF's. In Chapter 7 it was shown that the Gogny functionals predict larger fission barriers than BCPM, and this may allow for the production of heavier nuclei than those obtained in this work. Therefore this study could be very helpful to understand if the uncertainties in fission predictions allow the r-process to proceed beyond the neutron number $N = 184$. Of course the extension of this calculations to a set of trajectories exploring larger astrophysical conditions would be useful to extract more definitive conclusion.

- In this work we only changed the neutron-induced rates of nuclei with $Z \geq 84$, that is the relevant region for studying fission. However, it would be interesting to extend the calculation of the rates to nuclei below polonium and explore the impact on the production of actinides after the freeze-out. The results could be an important piece of information for the modeling of macronova light curves as explored in Ref. [123], and may help to understand if fission can be a relevant decay channel in the production of radioactive energy at timescales relevant for macronova observations.

- From the point of view of the nuclear input, it would be important to study the impact of calculations beyond the mean-field level. In Sec. 6.2 we found that the approximated treatment of the rotational correction led to artifacts in the shell gap of nuclei around the shell closure $N = 184$. We avoided this problem by removing the rotational correction from the calculation of the binding energies, but it would be better to perform a projection of the wavefunction onto good angular momentum. More in general, it would be interesting to study if beyond-mean field effects may have an impact on the *r*-process nucleosynthesis. These techniques can lead to substantial differences in the predictions of binding energies [144] that in turn may modify the location of the *r*-process path.

- Finally, it would interesting to continue the development of theoretical description of the fission process. We showed in Sec. 3.5 the large impact that dynamic calculation can have for the spontaneous fission. This study underlines the important role of collective inertias in light actinides, and therefore an important aspect would be the improvement of the theoretical calculation of the collective masses. Following the lines of Ref. [119] one could try to numerically compute the derivatives of the density respect to the collective degrees of freedom in both the GCM and the ATDHFB scheme and see how they compare. These calculations would be helpful to understand the role that collective degrees of freedom like triaxiality play in the fission process and to check the validity of the adiabatic hypothesis at the ground of the theoretical description of the fission process. However, we do not expect a large impact on *r*-process nucleosynthesis, since nuclei in this scenario fission from energies close to the top of the fission barriers where collective inertias are less relevant.

List of Figures

1.1 r-process path . . . 2

3.1 Collective properties of the ^{244}U . . . 33
3.2 Collective inertia, potential energy and action as a function of $\langle \Delta N^2 \rangle$ . . . 35
3.3 Fission barriers of ^{234}U for the static and dynamic approach . . . 36

4.1 Illustration of effects of the class II states in the fission penetrability . . . 44

6.1 Superheavy landscape . . . 58
6.2 Binding energies deviances for BCPM, D1M, D1S and D1M EDF's . . . 59
6.3 Predicted two-neutron separation energies of superheavy nuclei as a unction of N . . . 60
6.4 Predicted two-neutron separation energies of superheavy nuclei as a function of Z . . . 60
6.5 Binding energy of unstable nuclei . . . 61
6.6 Shell gaps for nuclei with $N = 152$, $N = 162$ and $N = 184$ . . . 61
6.7 Impact of rotational correction in the energy gaps . . . 62
6.8 Experimental fission barriers heights and isomer excitation energies . . . 63
6.9 Experimental spontaneous fission lifetimes and theoretical values for different EDF's . . 67
6.10 Experimental spontaneous fission lifetimes and theoretical values for different collective inertias . . . 68
6.11 Collective fission properties of ^{232}Th, ^{262}No, ^{290}No and ^{316}Ds . . . 68
6.12 Cross sections for different level densities and gamma-ray strengths . . . 71
6.13 Cross sections for different collective inertias . . . 72
6.14 Cross sections for different fission barriers . . . 73
6.15 Experimental and theoretical Q_α of Fr, Pa and Fm isotopes. . . . 76
6.16 Dominating decay: spontaneous fission versus alpha decay . . . 77

7.1 Maximum fission barrier height B_f . . . 80
7.2 Spread of B_f . . . 81
7.3 Energy window for neutron induced fission $B_f - S_n$ . . . 81
7.4 Spread of $B_f - S_n$ . . . 82
7.5 Spontaneous fission lifetimes of superheavy nuclei from different models . . . 83
7.6 Functional predicting the shortest and longest spontaneous fission lifetimes. . . . 84
7.7 Spontaneous fission lifetimes of r-process nuclei for different collective inertias . . . 85
7.8 Spontaneous fission lifetimes of r-process nuclei for different collective ground-state energies 87
7.9 Spontaneous fission lifetimes of r-process nuclei for different zero-point energies . . . 88
7.10 Dominating decay channels of superheavy nuclei . . . 90

8.1 Time evolution of averaged mass number and neutron density . . . 94
8.2 Time evolution of the radioactive energy emitted by fission . . . 95
8.3 Profile of the trajectory . . . 96
8.4 r-process abundances from BCPM and FRDM+TF rates . . . 97
8.5 BCPM and FRDM shell gaps . . . 98
8.6 BCPM and FRDM abundances at freeze-out . . . 99
8.7 Sensitivity of r-process abundances on collective inertias . . . 100
8.8 Evolution of fission rates . . . 101

8.9 Radioactive energy emitted by different channels 102

List of Tables

2.1 Values of the parameters of the D1S, D1N and D1M interactions 14
2.2 Values of the parameters of the BCPM EDF 16

3.1 Spontaneous fission lifetimes in static and dynamic calculations 36

6.1 Deviations of binding energies and neutron separation energies to experimental data . . 59
6.2 Impact of the rotational correction in the deviations of binding and neutron separation energies. 62
6.3 Target perfomances and variances of spontaneous fission lifetimes 66
6.4 Deviations of predicted alpha decay properties to experimental data 75

7.1 Effective mass, surface and symmetry energy of BCPM, D1N, D1M and D1M 80

Bibliography

[1] E. M. Burbidge, G. R. Burbidge, W. A. Fowler, and F. Hoyle, Rev. Mod. Phys. **29**, 547 (1957).

[2] A. G. W. Cameron, *Stellar evolution, nuclear astrophysics, and nucleogenesis*, Tech. Rep. (Atomic Energy of Canada Ltd. Chalk River Project, Chalk River, Ontario (Canada), 1957).

[3] A. S. Eddington, The Observatory **43**, 341 (1920).

[4] H. Schatz, J. Phys. G **43**, 064001 (2016).

[5] K. Langanke and G. Martínez-Pinedo, Rev. Mod. Phys. **75**, 819 (2003).

[6] M. Arnould, S. Goriely, and K. Takahashi, Phys. Rep. **450**, 97 (2007).

[7] S. E. Woosley, J. R. Wilson, G. J. Mathews, R. D. Hoffman, and B. S. Meyer, Astrophys. J. **433**, 229 (1994).

[8] H.-T. Janka, Annu. Rev. Nucl. Part. Sci. **62**, 407 (2012).

[9] J. M. Lattimer and D. N. Schramm, Astrophys. J. **192**, L145 (1974).

[10] J. M. Lattimer and D. N. Schramm, Astrophys. J. **210**, 549 (1976).

[11] E. Symbalisty and D. N. Schramm, Astrophys. Lett. **22**, 143 (1982).

[12] J. Abadie and et al. (LIGO Scientific Collaboration and Virgo Collaboration), Phys. Rev. D **82**, 102001 (2010).

[13] B. Paczynski, Astrophys. J. **308**, L43 (1986).

[14] L.-X. Li and B. Paczyński, Astrophys. J. **507**, L59 (1998).

[15] E. Nakar and T. Piran, Nature **478**, 82 (2011).

[16] B. D. Metzger, G. Martínez-Pinedo, S. Darbha, E. Quataert, A. Arcones, D. Kasen, R. Thomas, P. Nugent, I. V. Panov, and N. T. Zinner, MNRAS **406**, 2650 (2010).

[17] Tanvir N. R., Levan A. J., Fruchter A. S., Hjorth J., Hounsell R. A., Wiersema K., and Tunnicliffe R. L., Nature **500**, 547–549 (2013).

[18] E. Berger, W. Fong, and R. Chornock, Astrophys. Lett. **774**, L23 (2013).

[19] S. Goriely, A. Bauswein, and H.-T. Janka, Astrophys. Lett. **738**, L32 (2011).

[20] O. Korobkin, S. Rosswog, A. Arcones, and C. Winteler, MNRAS **426**, 1940 (2012).

[21] A. Bauswein, S. Goriely, and H.-T. Janka, Astrophys. J. **773**, 78 (2013).

[22] C. Sneden, J. J. Cowan, and R. Gallino, Annu. Rev. Astron. Astrophys. **46**, 241 (2008).

[23] C. Wagemans, *The Nuclear fission process* (CRC Press, Boca Raton, 1991).

[24] M. Bolsterli, E. O. Fiset, J. R. Nix, and J. L. Norton, Phys. Rev. C **5**, 1050 (1972).

[25] M. Brack, J. Damgaard, A. Jensen, H. Pauli, V. Strutinsky, C. Wong, and A. S. Jen, Rev. Mod. Phys. **44**, 320 (1972).

[26] P. Möller, A. J. Sierk, T. Ichikawa, A. Iwamoto, and M. R. Mumpower, Phys. Rev. C **91**, 024310 (2015).

[27] P. Jachimowicz, M. Kowal, and J. Skalski, Phys. Rev. C **95**, 014303 (2017).

[28] H. Flocard, P. Quentin, D. Vautherin, M. Veneroni, and A. Kerman, Nucl. Phys. A **231**, 176 (1974).

[29] S. Goriely, S. Hilaire, A. J. Koning, M. Sin, and R. Capote, Phys. Rev. C **79**, 024612 (2009).

[30] J. Erler, N. Birge, M. Kortelainen, W. Nazarewicz, E. Olsen, A. M. Perhac, and M. V. Stoitsov, Nature **486**, 509 (2012).

[31] A. Staszczak, A. Baran, and W. Nazarewicz, Phys. Rev. C **87**, 024320 (2013).

[32] S. A. Giuliani and L. M. Robledo, Phys. Rev. C **88**, 054325 (2013).

[33] R. Rodríguez-Guzmán and L. M. Robledo, Phys. Rev. C **89**, 054310 (2014).

[34] M. Kortelainen, J. McDonnell, W. Nazarewicz, P.-G. Reinhard, J. Sarich, N. Schunck, M. V. Stoitsov, and S. M. Wild, Phys. Rev. C **85**, 024304 (2012).

[35] M. Kortelainen, J. McDonnell, W. Nazarewicz, E. Olsen, P.-G. Reinhard, J. Sarich, N. Schunck, S. M. Wild, D. Davesne, J. Erler, and A. Pastore, Phys. Rev. C **89**, 054314 (2014).

[36] N. Schunck and L. M. Robledo, Reports Prog. Phys. **79**, 116301 (2016).

[37] M. Bender, G. F. Bertsch, and P.-H. Heenen, Phys. Rev. C **73**, 034322 (2006).

[38] H. Krappe and K. Pomorski, *Theory of Nuclear Fission*, Vol. 838 (Springer-Verlag, 2012) pp. 1–320.

[39] P. Ring and P. Schuck, *The nuclear many-body problem* (Springer-Verlag, New York, 1980).

[40] P. Hohenberg and W. Kohn, Phys. Rev. **136**, B864 (1964).

[41] D. Gogny, Nucl. Phys. A **237**, 399 (1975).

[42] T. H. R. Skyrme, Philos. Mag. **1**, 1043 (1956).

[43] T. Skyrme, Nucl. Phys. **9**, 615 (1958).

[44] J. Berger, M. Girod, and D. Gogny, Nucl. Phys. A **428**, 23 (1984).

[45] F. Chappert, M. Girod, and S. Hilaire, Phys. Lett. B **668**, 420 (2008).

[46] S. Goriely, S. Hilaire, M. Girod, and S. Péru, Phys. Rev. Lett. **102**, 242501 (2009).

[47] B. Friedman and V. Pandharipande, Nucl. Phys. A **361**, 502 (1981).

[48] G. Audi, A. H. Wapstra, and C. Thibault, Nucl. Phys. A **729**, 337 (2003).

[49] W. Kohn and L. J. Sham, Phys. Rev. **140**, A1133 (1965).

[50] M. Baldo, L. M. Robledo, P. Schuck, and X. Viñas, Phys. Rev. C **87**, 064305 (2013).

[51] M. Baldo and C. Maieron, J. Phys. G Nucl. Part. Phys. **34**, R243 (2007).

[52] Tondeur F., Nucl. Phys. A **315**, 353–369 (1979).

[53] E. Garrido, P. Sarriguren, E. Moya de Guerra, and P. Schuck, Phys. Rev. C **60**, 064312 (1999).

[54] M. Anguiano, J. Egido, and L. Robledo, Nucl. Phys. A **683**, 227 (2001).

[55] J. L. Egido and L. M. Robledo, in *Ext. Density Funct. Nucl. Struct. Phys.*, Vol. 641 (2004) pp. 269–302.

[56] R. E. Peierls and J. Yoccoz, Proc. Phys. Soc., Sec. A **70**, 381 (1957).

[57] H. Mang, Phys. Rep. **18**, 325 (1975).

[58] T. Duguet, P. Bonche, P.-H. Heenen, and J. Meyer, Phys. Rev. C **65**, 014310 (2001).

[59] L. M. Robledo, R. Bernard, and G. F. Bertsch, Phys. Rev. C **86**, 064313 (2012).

[60] D. J. Griffiths, *Introduction to Quantum Mechanics (2nd Edition)* (Pearson Prentice Hall, 2004).

[61] A. Baran, Phys. Lett. B **76**, 8 (1978).

[62] A. Baran, K. Pomorski, A. Lukasiak, and A. Sobiczewski, Nucl. Phys. A **361**, 83 (1981).

[63] F. R. Xu, E. G. Zhao, R. Wyss, and P. M. Walker, Phys. Rev. Lett. **92**, 252501 (2004).

[64] C. Fiolhais, F. Nogueira, and M. Marques, *A Primer in Density Functional Theory*, Lecture Notes in Physics, Vol. 620 (Springer Berlin Heidelberg, 2003).

[65] N. Onishi and T. Une, Progr. Theor. Exp. Phys. **53**, 504 (1975).

[66] P. A. M. Dirac, Math. Proc. Cambridge Philos. Soc. **26**, 376–385 (1930).

[67] M. Baranger and M. Vénéroni, Ann. Phys. **114**, 123 (1978).

[68] S. G. Nilsson, J. R. Nix, A. Sobiczewski, Z. Szymański, S. Wycech, C. Gustafson, and P. Möller, Nucl. Phys. A **115**, 545 (1968).

[69] D. A. Varshalovich, A. N. Moskalev, and V. K. Khersonskii, *Quantum Theory Of Angular Momemtum* (World Scientific, 1988).

[70] R. Rodríguez-Guzmán and L. M. Robledo, Eur. Phys. J. A **50**, 142 (2014).

[71] R. Rodríguez-Guzmán and L. M. Robledo, Eur. Phys. J. A **52**, 12 (2016).

[72] J. Erler, K. Langanke, H. P. Loens, G. Martínez-Pinedo, and P.-G. Reinhard, Phys. Rev. C **85**, 025802 (2012).

[73] J. Sadhukhan, J. Dobaczewski, W. Nazarewicz, J. A. Sheikh, and A. Baran, Phys. Rev. C **90**, 061304 (2014).

[74] J. Zhao, B.-N. Lu, T. Nikšić, D. Vretenar, and S.-G. Zhou, Phys. Rev. C **93**, 044315 (2016).

[75] L. G. Moretto and R. P. Babinet, Phys. Lett. B **49**, 147 (1974).

[76] S. A. Giuliani, L. M. Robledo, and R. Rodríguez-Guzmán, Phys. Rev. C **90**, 054311 (2014).

[77] N. López Vaquero, T. R. Rodríguez, and J. L. Egido, Phys. Lett. B **704**, 520 (2011).

[78] G. Bertsch and H. Flocard, Phys. Rev. C **43**, 2200 (1991).

[79] S. Hilaire, (2000), lecture given at the Workshop on Nuclear Data and Nuclear Reactors.

[80] G. Martínez-Pinedo, Eur. Phys. J. Spec. Top. **156**, 123 (2008).

[81] P. Fröbrich and R. Lipperheide, *Theory of nuclear reactions* (Clarendon Press, 1996).

[82] W. Hauser and H. Feshbach, Phys. Rev. **87**, 366 (1952).

[83] N. Bohr, Nature **137**, 344 (1936).

[84] P. E. Hodgson, *Nuclear reactions and nuclear structure* (Oxford : Clarendon Press, 1971).

[85] J. Kopecky and M. Uhl, Phys. Rev. C **41**, 1941 (1990).

[86] A. J. Koning and J. P. Delaroche, Nucl. Phys. **A713**, 231 (2003).

[87] A. J. Koning, S. Hilaire, and S. Goriely, "Talys 1.8 user manual," (2015).

[88] B. B. Back, O. Hansen, H. C. Britt, and J. D. Garrett, Phys. Rev. C **9**, 1924 (1974).

[89] S. Bjørnholm and J. E. Lynn, Rev. Mod. Phys. **52**, 725 (1980).

[90] W. D. Myers and W. J. Swiatecki, Ark. Fys. **36**, 343 (1967).

[91] M. Sin, R. Capote, A. Ventura, M. Herman, and P. Obložinský, Phys. Rev. C **74**, 014608 (2006).

[92] A. J. Koning, S. Hilaire, and S. Goriely, Nucl. Phys. **A810**, 13 (2008).

[93] A. Bohr and B. R. Mottelson, *Nuclear Structure - Volume I: Single-Particle Motion* (Benjamin, 1969).

[94] A. Gilbert and A. G. W. Cameron, Can. J. Phys. **43**, 1446 (1965).

[95] W. Dilg, W. Schantl, H. Vonach, and M. Uhl, Nucl. Phys. **A217**, 269 (1973).

[96] M. K. Grossjean and H. Feldmeier, Nucl. Phys. A **444**, 113 (1985).

[97] P. Demetriou and S. Goriely, Nucl. Phys. A **695**, 95 (2001).

[98] T. Rauscher, F.-K. Thielemann, and K.-L. Kratz, Phys. Rev. C **56**, 1613 (1997).

[99] W. A. Fowler, G. R. Caughlan, and B. A. Zimmerman, Ann. Rev. Astron. Astrophys. **5**, 525 (1967).

[100] J. J. Cowan, F.-K. Thielemann, and J. W. Truran, Phys. Rep. **208**, 267 (1991).

[101] A. G. W. Cameron, J. J. Cowan, H. V. Klapdor, J. Metzinger, T. Oda, and J. W. Truran, Astrophys. Space Sci. **91**, 221 (1983).

[102] J. J. Mendoza-Temis, M.-R. Wu, K. Langanke, G. Martínez-Pinedo, A. Bauswein, and H.-T. Janka, Phys. Rev. C **92**, 055805 (2015).

[103] S. A. Giuliani, G. Martinez-Pinedo, and L. M. Robledo, arXiv:1704.00554 [nucl-th] .

[104] F. P. Heßberger, Eur. Phys. J. A **53**, 75 (2017).

[105] M. Wang, G. Audi, A. H. Wapstra, F. Kondev, M. MacCormick, X. Xu, and B. Pfeiffer, Chinese Phys. C **36**, 1603 (2012).

[106] R. Capote, M. Herman, P. Obložinský, P. G. Young, S. Goriely, T. Belgya, V. Ignatyuk, A. J. Koning, S. Hilaire, V. Plujko, M. Avrigeanu, O. Bersillon, M. B. Chadwick, T. Fukahori, Z. Ge, Y. Han, S. Kailas, J. Kopecky, V. M. Maslov, G. Reffo, M. Sin, E. Soukhovitskii, and P. Talou, Nucl. Data Sheets **110**, 3107 (2009).

[107] N. E. Holden and D. C. Hoffman, Pure Appl. Chem. **72**, 1525 (2000).

[108] J. Khuyagbaatar, S. Hofmann, F. P. Heßberger, D. Ackermann, H. G. Burkhard, S. Heinz, B. Kindler, I. Kojouharov, B. Lommel, R. Mann, J. Maurer, K. Nishio, and Y. Novikov, Eur. Phys. J. A **37**, 177 (2008).

[109] M. Centelles, M. D. Estal, and X. Viñas, Nucl. Phys. A **635**, 193 (1998).

[110] J. Berger, M. Girod, and D. Gogny, Comput. Phys. Commun. **63**, 365 (1991).

[111] C. Mahaux and R. Sartor, in *Advances in Nuclear Physics* (Springer US, 1991) pp. 1–223.

[112] K. S. Krane, *Introductory Nuclear Physics* (Wiley, New York, 1987).

[113] J. M. Lattimer and Y. Lim, Astrophys. J. **771**, 51 (2013).

[114] W. Nazarewicz, P. G. Reinhard, W. Satuła, and D. Vretenar, Eur. Phys. J. A **50**, 20 (2014).

[115] M. A. Hooshyar, F. B. Malik, and I. Reichstein, *Nuclear Fission and Cluster Radioactivity* (Springer-Verlag, 2005).

[116] N. Nikolov, N. Schunck, W. Nazarewicz, M. Bender, and J. Pei, Phys. Rev. C **83**, 034305 (2011).

[117] S. G. Nilsson, C. F. Tsang, A. Sobiczewski, Z. Szymański, S. Wycech, C. Gustafson, I.-L. Lamm, P. Möller, and B. Nilsson, Nucl. Phys. A **131**, 1 (1969).

[118] G. F. Bertsch, W. Loveland, W. Nazarewicz, and P. Talou, J. Phys. G Nucl. Part. Phys. **42**, 077001 (2015).

[119] A. Baran, J. A. Sheikh, J. Dobaczewski, W. Nazarewicz, and A. Staszczak, Phys. Rev. C **84**, 054321 (2011).

[120] "Experimental Nuclear Reaction Data (EXFOR)," `https://www-nds.iaea.org/exfor/exfor.htm`.

[121] I. V. Panov, I. Y. Korneev, T. Rauscher, G. Martínez-Pinedo, A. Kelić-Heil, N. T. Zinner, and F.-K. Thielemann, Astron. Astrophys. **513**, 14 (2010).

[122] A. Mamdouh, J. M. Pearson, M. Rayet, and F. Tondeur, Nucl. Phys. A **679**, 337 (2001).

[123] J. Barnes, D. Kasen, M.-R. Wu, and G. Martínez-Pinedo, Astrophys. J. **829**, 110 (2016).

[124] V. Viola and G. Seaborg, J. Inorg. Nucl. Chem. **28**, 741 (1966).

[125] T. Dong and Z. Ren, Eur. Phys. J. A **26**, 69 (2005).

[126] P. R. Chowdhury, C. Samanta, and D. N. Basu, Phys. Rev. C **77**, 47 (2008).

[127] I. Petermann, K. Langanke, G. Martínez-Pinedo, I. V. Panov, P.-G. Reinhard, and F.-K. Thielemann, Eur. Phys. J. A **48**, 122 (2012).

[128] M. Warda, J. L. Egido, L. M. Robledo, and K. Pomorski, Phys. Rev. C **66**, 014310 (2002).

[129] W. A. Fowler, QJRAS **15**, 82 (1974).

[130] S. Goriely, S. Hilaire, and A. J. Koning, Astron. Astrophys. **487**, 767 (2008).

[131] C. Freiburghaus, S. Rosswog, and F.-K. Thielemann, Astrophys. Lett. **525**, L121 (1999).

[132] S. Goriely, S. Hilaire, A. J. Koning, and R. Capote, J. Korean Phys. Soc. **59**, 979 (2011).

[133] B. D. Metzger, A. Bauswein, S. Goriely, and D. Kasen, MNRAS **446**, 1115 (2015).

[134] L. F. Roberts, D. Kasen, W. H. Lee, and E. Ramirez-Ruiz, Astrophys. J. Lett. **736**, L21 (2011).

[135] M. Eichler, A. Arcones, A. Kelic, O. Korobkin, K. Langanke, T. Marketin, G. Martínez-Pinedo, I. V. Panov, T. Rauscher, S. Rosswog, C. Winteler, N. T. Zinner, and F.-K. Thielemann, Astrophys. J. **808**, 30 (2015).

[136] S. Goriely, Eur. Phys. J. A **51**, 22 (2015).

[137] D. Martin, A. Arcones, W. Nazarewicz, and E. Olsen, Phys. Rev. Lett. **116**, 121101 (2016).

[138] P. Möller, J. R. Nix, W. Myers, and W. Swiatecki, At. Data Nucl. Data Tables **59**, 185 (1995).

[139] W. D. Myers and W. J. Swiatecki, Phys. Rev. C **60**, 014606 (1999).

[140] P. Möller, B. Pfeiffer, and K.-L. Kratz, Phys. Rev. C **67**, 055802 (2003).

[141] S. Goriely and M. Arnould, Astron. Astrophys. **379**, 1113 (2001).

[142] H. Schatz, R. Toenjes, B. Pfeiffer, T. C. Beers, J. J. Cowan, V. Hill, and K.-L. Kratz, Astrophys. J. **579**, 626 (2002).

[143] T. Marketin, L. Huther, and G. Martínez-Pinedo, Phys. Rev. C **93**, 025805 (2016).

[144] T. R. Rodríguez, A. Arzhanov, and G. Martínez-Pinedo, Phys. Rev. C **91**, 044315 (2015).

Index

Action integral, 22, 23, 43
Alpha decay, 74, 76
    half-lives, 74, 75
    Q-value, 74, 75

Barcelona-Catania-Paris-Madrid (BCPM), 13, 14
Beta decay, 74
    rates, 97
Bogolyubov trasformation, 9

Class states effects, 43
Collective inertias
    ATDHFB, 28, 65
    cranking approximation, 26, 28, 65
    GCM, 24, 26, 65
    perturbative approximation, 25, 28, 65
    reduced, 29
    semiempirical, 28
Cross section, 40, 70–73
    stellar, 46

Effective mass, 15, 79

Generalised density matrix $\mathcal{R}$, 10
Generator Coordinate Method (GCM), 23
    Gaussian Overlap Approximation (GOA), 24
Gogny force, 13

Hartree-Fock-Bogolyubov (HFB)
    equation, 10
    matrix, 10
    TDHFB, 26
Hauser-Feshbach statistical theory, 39
Height, fission barrier, 62
Hill-Wheeler equation, 24

Isomer excitation energy, 63

Neutron induced fission energy window, 81
Neutron-to-seed ratio $R_{n/s}$, 55
Nuclear level density (NLD), 44, 46
    Back-shifted Fermi gas model (BSFGM), 45
    Constant temperature model (CTM), 45
    Fermi gas model (FGM), 44
Nuclear statistical equilibrium (NSE), 49

One-body density matrix ρ_{ij}, 10

Pairing tensor κ_{ij}, 10
Perturbative nucleon addition method (PNAM), 18
Potential energy surface, 12, 29
Projection, 62
    Projection after variation (PAV), 17
    Variation after projection (VAP), 17

Q-value, 40
Quasiparticle, 9
    basis, 11

r process, 1
    abundances, 1
    freeze-out, 55, 97
    path, 52, 82

Second quantization, 6
Shell gap Δ, 59
Spontaneous fission lifetime, 22
Stellar reaction rate, 46

Target performance $\bar{R}_{\tau}$, 65
Transmission coefficient, 40, 41
    fission, 42
    gamma, 41
    particle, 42

Variance σ_{τ} 65
Viola-Seaborg formula, 74

Waiting point, 1, 52
    approximation, 52
WKB approximation, 21, 22, 43

Zero-point energy, 13, 17, 32
    ATDHFB, 28
    GCM, 25, 26

Acknowledgments

It seems that I am at the end of this long trip, which suddenly became incredibly short. It was like living on a roller coaster with continuous ups and downs. But if for the downs I should only blame myself, I want to acknowledge all the people that during these three years helped me in this wonderful journey.

Foremost, I want to thank my supervisor Gabriel Martínez-Pinedo for giving me the opportunity to work on my PhD and for all the time he took to me. During these years I worked in something that I really enjoyed, had a lot of discussions with extremely interesting people and traveled around the world; and nothing of this would have be possible without his support. Only now I start to understand how much patience he had with me and how much I learnt from his advises. And above all, I can not thank him enough for transmitting me this passion that I have for physics.

I owe my deepest gratitude to Luis Robledo for his invaluable collaboration during all these years and for pushing me to start this adventure. I feel really lucky to have benefited from his advises and I am grateful to him for his willingness to help me so many times during my PhD.

A special thanks goes to Hans Feldmeier, whose advise motivated me to widen my knowledge with the hope that at some point I will understand something about fission.

I would also like to express my gratitude to prof. Robert Roth, who accepted to be my doctoral advisor and whose availability was very helpful in this last stage of my PhD.

I am in debt with Meng-Ru Wu for initiating me to the network calculations and for his willingness every time I had a problem. Besides that, he was an extremely enjoyable company during many years, specially while skiing.

A very special thanks goes to all my group mates who bore me during these years: André for being such a pleasant person in every situation, Andreas for his invaluable discussions and company, Alexander for all those trips where we shared a room, Andrea for being the funniest guy from Milan I have ever met, Dag for making me laugh until the very last days of my thesis, Gang for his contagious laugh and Heiko for being so Heiko that we all miss him from the very first moment he left.

I owe my thanks to Ms. Genette Kluckner, who was simply marvelous during these years. I cannot count all the times she helped me with administrative issues.

Many thanks to Gabriel Martínez-Pinedo, André and Andreas for proof-reading parts of this thesis.

I am grateful to all the free and/or open-source community, that made the PhD and the writing of this thesis much easier. In particular I would like to thank the developers from the LaTeX, Python and Debian community.

I would also like to thank the other awesome guys that I met at the institute and GSI during these years. Specially Marius and Sofija, who where an amazing company in all the trips we did together; Victoria and Toño for being such a cheerful persons and the first Spanish speaker friends that never made fun of my Italian accent; Guillermo for hosting me at his place when I did not have an home; Lukas, Marc and Albino for their impossible humor that makes laugh so much; and Arianna, who is the most amazing thing I ever found in Frankfurt. A special thanks goes to Enrico, whose friendship made Darmstadt a special place.

It seems like it was a decade ago but at some point I had a life outside this institute, and there are some friends with whom I am in debt. Foremost my flatmates Valentina and Diana, whose love literally fed me in these last days of my thesis. If I did not starve is just because I was extremely lucky in having them under my same roof. And a special thanks goes also to Andreas, who had to bear the Latino ambient of the house. I am also grateful to all those guys who gave me the opportunity to enjoy playing football in Darmstadt, specially Alexander, Samuel #1 and Julio, whose friendship I will hardly forget.

I owe a special thanks to those friends that are shuffling across Europe and hosted me at some point during these last three years: Marco, who brought me for the first time to Chile and ~~convinced~~ deceived me into thinking that I could hike volcanoes of 6900 meters; Moni y Richi, whose friendship was one of the biggest things I ever had in Madrid and it remained so when we moved to Germany; Rata, for hosting me every time that I went to Madrid, making me so joyful to be there again; I Boys a Roma, who every day remember me how much I can miss Rome; and Naps, to whom I wish to never, never leave Rome again.

And then I would like to thank my family for supporting me during these years. Time passes and I am away from you, but there is nothing that makes so happy as come back home. Papà, Mamma, Sole, Giulia, Alice, Viola, Nando, Ilaria, non sapete quanto vi voglio bene.

Y aunque no creo que jamás llegarás a leer estas líneas, quiero que sepas que te he llegado a querer como nada en este Mundo.

And somewhere in the World, thank you Explosions in the Sky for keeping me company during these days.

Samuel A. Giuliani | Curriculum Vitæ

Institut für Kernphysik (Theorie-Zentrum)
Schlossgartenstraße 2, 64289 Darmstadt, Germany
☎ +49 (0)176 3609 7372 • ☎ +49 (6151) 16 21544
✉ giuliani@theorie.ikp.physik.tu-darmstadt.de

Education

Technische Universität Darmstadt **Darmstadt**
Ph.D. candidate in Theoretical Nuclear Astrophysics *December 2013*
Fission and r-process nucleosynthesis in neutron star mergers - Supervisor: G. Martínez Pinedo

Universidad Autónoma de Madrid **Madrid**
Interuniversitary Nuclear Physics M.Sc. *2012 – 2013*
Fission properties of superheavy nuclei - Supervisor: L. M. Robledo

Universidad Complutense de Madrid **Madrid**
Licenciado en Ciencias Físicas *2012*

Universidad de Barcelona **Barcelona**
SICUE exchange student *2011–2012*

Liceo Español Cervantes **Rome**
Diploma di Maturità (Italian High School Degree) *2006*

Liceo Español Cervantes **Rome**
Science and Nature Spanish High School Degree *2006*

Teaching

Assistant for exercises in ”Nuclear Astrophysics” **WS 2016**
Technische Universität Darmstadt

Assistant for exercises in ”Nuclear Astrophysics” **WS 2015**
Technische Universität Darmstadt

Publications

[1] S. A. Giuliani, G. Martinez-Pinedo, and L. M. Robledo, arXiv:1704.00554 [nucl-th] .

[2] S. A. Giuliani, L. M. Robledo, and R. Rodríguez-Guzmán, Phys. Rev. C **90**, 054311 (2014).

[3] S. A. Giuliani and L. M. Robledo, Phys. Rev. C **88**, 054325 (2013).

[4] S. A. Giuliani, G. Martínez-Pinedo, L. M. Robledo, and M.-R. Wu, Acta. Phys. Pol. B **48**, 299 (2017).

[5] S. A. Giuliani, G. Martínez-Pinedo, and L. M. Robledo, in *PoS (NIC XIII)*, Vol. 095 (2015).

Talks

Invited talks

The impact of fission on r-process nucleosynthesis in neutron star mergers,
Arbeitstreffen Kernphysik, March 2017, Schleching (Germany).

Spontaneous fission: pairing impact and the least action approach,
FUSTIPEN Topical Meeting, October 2014, GANIL - Caen (France).

Contributed talks

Impact of fission in the r-process nucleosynthesis: an energy density functional study,
JINA-CEE Frontiers in Nuclear Astrophysics, February 2017, Lansing (Michigan).

Impact of fission on r-process nucleosynthesis within the energy density functional theory,
Neutron star mergers: from gravitational waves to nucleosynthesis, January 2017, Hirschegg (Austria).

r-process calculations with a microscopic description of the fission process,
Extremes of the Nuclear Landscape, August 2016, Zakopane (Poland).

The role of nuclear inputs in r-process nucleosynthesis,
DPG Spring Meeting, March 2016, Darmstadt (Germany).

Fission properties of superheavy nuclei within the EDF theory,
IIIrd Topical Workshop on Modern Aspects of Nuclear Structure, February 2016, Bormio (Italy).

Fission properties of r-process nuclei,
NAVI Physics Days, January 2016, GSI - Darmstadt (Germany).

Systematic of the fission properties of superheavy nuclei,
XXXIV Mazurian Lakes Conference on Physics, September 2015, Piaski (Poland).

Microscopic description of fission properties of r-process nuclei,
IOP Nuclear Physics in Astrophysics Conference VII, May 2015, York (United Kingdom).

Microscopic description of nuclear fission properties in the superheavy region,
DPG Spring Meeting, March 2015, Heidelberg (Germany).

Fission barriers for r-process nuclei,
NAVI Physics Days, February 2015, GSI - Darmstadt (Germany).

Fission properties of the Barcelona-Catania-Paris-Madrid energy-density functional,
DPG Spring Meeting, March 2014, Frankfurt (Germany).

Large deformation properties of nuclear interactions and superheavy nuclei stability,
XXXIVth Biannual Meeting of the Royal Spanish Society of Physics, July 2013, Valencia (Spain).

Attended Schools & Workshops

Lecture Week on Gamma Ray Spectroscopy **Laubach**
Helmholtz Graduate School for HIRe *November 2016*

3rd Astrophysical Nuclear Reaction Network School **Schmitten**
NAVI & JINA-CEE *August 2016*

Lecture Week on Nuclear Structure **Bad Münster**
Helmholtz Graduate School for HIRe *June 2015*

Course on Density Functional Theory and Self-Consistent Methods **Trento**
ECT Nuclear TALENT School* *July 2014*

Nuclei in the Cosmos Summer School **Debrecen**
Institute for Nuclear Research *June 2014*

Power Week on Neutron Stars **Herborn**
Helmholtz Graduate School for HIRe *February 2014*

Scholarships

HGS-HIRe grant for research stay abroad **Darmstadt – Madrid**
Helmholtz Graduate School for Hadron and Ion Research *April 2015*

Doctoral participantship **Germany**
Helmholtz Graduate School for Hadron and Ion Research *2014 – now*

Ayudas para Inicio de Estudios en Programas de Posgrado (Predoctoral scholarship) **Madrid**
Universidad Autónoma de Madrid *2012 – 2013*

Ayudas de residencia a deportistas universitarios **Madrid**
Universidad Complutense de Madrid *2008 –2009, 2010 – 2011*

Ministerio de Educación, Cultura y Deporte **Spain**
Beca de carácter General y de Movilidad *2008 – 2009*

Languages

Italian: Mother tongue

Spanish: Native speaker

English: Fluent

German: Basic

Catalan: Basic

Computer skills

Scripting: Python, Bash

Programming: Fortran

OS: Unix, GNU/Linux (Ubuntu), Windows

Markup: LaTeX

Volunteering

Associazione Arciragazzi **Terni - Rome**
Campsite leader *2004–2007*
Volunteering in an educational environment camping with 6–12 y.o. children.

Lega Navale Italiana **Ostia (Rome)**
Sailing instructor *2004–2007*
Instructor in Italian Navy summer sailing courses with 8–15 y.o. children.

Erklärung zur Dissertation

Hiermit versichere ich, die vorliegende Dissertation ohne Hilfe Dritter nur mit den angegebenen Quellen und Hilfsmitteln angefertigt zu haben. Alle Stellen, die aus Quellen entnommen wurden, sind als solche kenntlich gemacht. Diese Arbeit hat in gleicher oder ähnlicher Form noch keiner Prüfungsbehörde vorgelegen.

Darmstadt, den 13. Juni 2017

(Samuel Andrea Giuliani)